

Novel theoretical tools in jet quenching



Johannes Hamre Isaksen

Thesis for the degree of Philosophiae Doctor (PhD)
University of Bergen, Norway
2023

UNIVERSITY OF BERGEN



Novel theoretical tools in jet quenching

Johannes Hamre Isaksen



Thesis for the degree of Philosophiae Doctor (PhD)
at the University of Bergen

Date of defense: 13.06.2023

© Copyright Johannes Hamre Isaksen

The material in this publication is covered by the provisions of the Copyright Act.

Year: 2023

Title: Novel theoretical tools in jet quenching

Name: Johannes Hamre Isaksen

Print: Skipnes Kommunikasjon / University of Bergen

Scientific environment

This research was conducted in the Theoretical Physics Group at the Institute for Physics and Technology at the University of Bergen. More specifically I have worked closely with the heavy-ion part of the theory group. The group leader is my PhD advisor Konrad Tywoniuk. The other current and former members of the heavy ion group that I have worked and discussed with are Adam Takacs, Alexandre Falcão, Daniel Pablos and Yilun Du.

This research has been part of the project "Thermalizing jets", which was funded by the Trond Mohn Foundation (BFS2018REK01).

Acknowledgements

I would like to express my sincere gratitude to my supervisor, Konrad Tywoniuk, for his guidance and support throughout my doctoral studies at the University of Bergen. His immense knowledge of our field of research has been invaluable in shaping the direction of my work. I am indebted to him for the time and effort he has invested in me, and for being a kind and insightful presence throughout my journey as a PhD student.

I would also like to extend my gratitude to the rest of the theoretical heavy ion group at UiB. These include Adam Takacs, Alexandre Falcão, Yilun Du, and Daniel Pablos. Without their presence, my time at UiB would have been much less enjoyable. I would also like to mention our heavy-ion colleagues in other universities around the world, whom I have had the great pleasure of getting to know at various conferences.

Furthermore, I would like to thank my colleagues and friends at UiB for making my time here more fun and interesting. I would especially like to mention Simon Huiberts and Helge Henjum, who have always been there to offer a welcome distraction when I needed one, such as playing in a band. I would also like to thank Laurence Hogan for his insightful advice regarding differential geometry.

I owe a special debt of gratitude to my family, who have been a constant source of support and encouragement throughout my academic journey. I am sure they will appreciate that in my next job they might finally have some understanding of what I do at work.

Finally, I would like to express my heartfelt appreciation to my girlfriend Johanne, who has made my life much better throughout the time spent working on my PhD.

Abstract in English

Jet quenching is the study of how the properties of a QCD jet change as it traverses hot nuclear matter. This is relevant for heavy ion collisions at the LHC and RHIC, as such collisions produce a droplet of quark-gluon plasma (QGP) that jets have to pass through before reaching the detector. This thesis is about the theoretical treatment of jet quenching.

One of the main effects the medium has on jets is energy loss through medium-induced emissions. The jets will interact with the medium in such a way as to induce the partons in the jet to emit even more partons. These emitted partons can go outside of the jet cone, and will not be counted as part of the jet in an experiment. The energy of these emitted partons is hence lost, and in general jets in heavy ion collisions have a lower energy than in proton-proton collisions. The main contribution to jet energy loss is medium-induced radiation, and the theoretical description of medium-induced emissions is also the principal topic of my thesis.

In our first paper [1] we found a general method of calculating correlators of any number of Wilson lines in a thermal medium. These Wilson lines are present in most theoretical calculations of medium-induced emissions. Researchers usually rely on using approximations like the large- N_c limit to calculate Wilson line correlators. Although this approximation continues to be very useful, we showed how one can do these calculations in general at $N_c = 3$. We also showed that the large- N_c approximation always leads to a simplified system that allows for an analytic solution.

In the second paper [2] we derived a way of calculating the energy spectrum of medium-induced emissions at all energies and medium lengths. This is usually calculated by using one of two approximations, called the opacity expansion and the harmonic oscillator approximation. However, these two approaches work in different parts of the phase space, and none of them can be used to calculate the full energy spectrum. We showed that by introducing a third expansion, coined the resummed opacity expansion, one can through a union of these three approaches cover the full phase space of medium-induced emissions.

Finally, in our third paper [3] we calculated the medium-induced emission spectrum as a function of energy and transverse momentum. This is usually calculated in the large- N_c limit, or in the eikonal limit, as we did in [1]. In [3] we relaxed both of these approximations and, extending the methods derived in [1] to also describe transverse motion, we simulated the full spectrum numerically at finite- N_c . We then compared this result to the various approximations that usually are employed to quantify the error introduced by using these approximations.

We found that going from the solution at finite N_c to large- N_c is associated with only a small error. The large- N_c solution is made up of two terms, called the factorizable and non-factorizable pieces. The non-factorizable part is complicated and is often dropped in calculations, as the main contribution to the spectrum comes from the factorizable term. We found, through our numerical simulation, that the non-factorizable term is indeed insignificant at a small splitting fraction z , but its contribution can be sizable for more balanced splittings $z \sim 0.5$. Finally, we found that the eikonal approximation does not work particularly well in the cases studied in the paper.

Abstract in Norwegian

Jet quenching er studiet av hvordan egenskapene til en QCD-jet endrer seg når den passerer gjennom varmt nukleært materiale. Dette er relevant for kollisjoner av tunge ioner ved LHC og RHIC, da slike kollisjoner produserer en dråpe av kvark-gluon plasma (QGP) som jetene må passere gjennom før de når detektorene. Denne avhandlingen omhandler den teoretiske behandlingen av jet quenching.

En av de viktigste effektene mediumet har på jetene, er energitap gjennom medium-indusert stråling. Jetene vil samhandle med mediumet på en måte som induserer partiklene i jeten til å utsåle enda flere partikler. Disse utstrålte partiklene kan gå utenfor jetkjeglen og vil ikke bli telt som en del av jeten i et eksperiment. Energien til disse utstrålte partiklene går dermed tapt, og generelt har jetene i kollisjoner mellom tunge ioner lavere energi enn i kollisjoner mellom protoner. Hovedbidraget til jetenes energitap skyldes medium-indusert stråling, og den teoretiske beskrivelsen av medium-indusert stråling er også hovedtemaet i min avhandling.

I vår første artikkel [1] fant vi en generell metode for å beregne korrelatorer av et hvilket som helst antall Wilson-linjer i et termisk medium. Disse Wilson-linjene er til stede i enhver teoretisk beregning av medium-induserte utslipp. Forskere pleier vanligvis å bruke approksimasjoner som høy- N_c -approksimasjonen for å beregne korrelatorer av Wilson-linjer. Selv om denne tilnærmingen fremdeles er veldig nyttig, viste vi hvordan man kan gjøre disse beregningene generelt ved $N_c = 3$. Vi viste også at høy- N_c -approksimasjonen alltid leder til et forenklet system som tillater en analytisk løsning.

I den andre artikkelen [2] utledet vi en måte å beregne energispektret til medium-indusert stråling ved alle energier og mediumlengder. Dette beregnes vanligvis ved å bruke en av to tilnærminger, kalt opasitetsutvidelsen og harmonisk oscillator-tilnærmingen. Disse to tilnærmingene fungerer bra i forskjellige deler av faseområdet, og ingen av dem kan brukes til å beregne det fulle energispektret. Vi viste at ved å introdusere en tredje utvidelse, kalt den resumerte opasitetsutvidelsen, kan man gjennom en forening av disse tre tilnærmingene dekke hele faseområdet til medium-indusert stråling.

Til slutt, i vår tredje artikkel [3], beregnet vi spekteret for medium-indusert stråling som en funksjon av energi og tverrgående bevegelsesmengde. Dette beregnes vanligvis i høy- N_c -approximasjonen eller i eikonal-approximasjonen, slik vi gjorde i [1]. I [3] brukte vi ingen av disse approximasjonene og utvidet metodene som ble utviklet i [1] til også å beskrive tverrgående bevegelse, og simulerte deretter det fulle spekteret numerisk ved endelig N_c . Vi sammenlignet deretter dette resultatet med de ulike tilnærmingene som vanligvis brukes for å kvantifisere feilen som innføres ved å bruke disse approximasjonene.

Vi fant ut at å gå fra løsningen ved endelig N_c til høy- N_c er forbundet med liten feil. Høy- N_c -løsningen består av to ledd, kalt de faktoriserbare og ikke-faktoriserbare ledd. Det ikke-faktoriserbare leddet er komplisert og blir ofte droppet i beregninger, siden hovedbidraget til spekteret kommer fra det faktoriserbare leddet. Vi fant gjennom vår numeriske simulering at det ikke-faktoriserbare leddet er ubetydelig ved små splittingsfraksjoner z , men bidraget kan være betydelig for mer balanserte splittings hvor $z \sim 0.5$. Til slutt fant vi at eikonal-approximasjonen ikke fungerer spesielt bra i tilfellene som ble studert i artikkelen.

List of publications

1. J. H. Isaksen and K. Tywoniuk,
“Wilson line correlators beyond the large- N_c ,”
Published in: Journal of High Energy Physics, vol. 11, p. 125, 2021
2. J. H. Isaksen, A. Takacs, and K. Tywoniuk,
“A unified picture of medium-induced radiation,”
Published in: Journal of High Energy Physics, vol. 02, p. 156, 2023.
3. J. H. Isaksen and K. Tywoniuk,
“Precise description of medium-induced emissions,”
Submitted to Journal of High Energy Physics, 2023.

These articles are distributed under the terms of the Creative Commons Attribution License (CC-BY 4.0), which permits any use, distribution and reproduction in any medium, provided the original authors and source are credited.

Contents

Scientific environment	i
Acknowledgements	iii
Abstract in English	v
Abstract in Norwegian	vii
List of publications	ix
1 Introduction	1
1.1 The Standard Model and quantum field theory	3
1.1.1 Symmetries and groups	3
1.2 Quantum Chromodynamics	5
1.2.1 QCD Feynman rules	6
1.2.2 Confinement and asymptotic freedom	8
2 Heavy ion physics	11
2.1 Heavy ion collisions	11
2.1.1 Motivation for colliding heavy ions	11
2.1.2 Features of a heavy ion collision	12

2.1.3	Evolution after the collision	15
2.2	Experimental signatures of the QGP	17
3	Jet quenching	21
3.1	Basics of jet quenching theory	24
3.1.1	The medium interaction	25
3.1.2	The medium propagator	27
3.1.3	Transverse momentum broadening	32
3.2	Medium-induced radiation	34
3.2.1	The quadrupole at large- N_c	38
3.3	Calculating the splitting kernel	47
3.4	Multiple emissions	52
4	Conclusion and outlook	55
A	Different forms of the medium propagator	59
B	The non-factorizable part of the large-N_c limit	63
	Scientific articles	73
	Article I	73
	Article II	112
	Article III	171

Chapter 1

Introduction

The goal of theoretical physics is to be able to describe all the physical phenomena in nature using the language of mathematics. This quest has been extremely successful, and now only a few mysterious phenomena elude us completely. The field of theoretical physics is roughly divided into two parts: those who try to solve the few remaining mysteries, and those who try to refine our current knowledge and make measurable predictions. The first part has led to exciting theories like string theory, that hope to one day produce a framework that encapsulates even more physics than the one we currently use. However, these theories have not as far had any success in providing predictions that can be measured in experiments. I work on the second part, called phenomenology. Our goal is to use the already well-tested theories to better describe the ever-growing amount of experimental data. Even though the underlying theories have been known for a long time, using them to their full power still poses a great and exciting challenge.

The data that we want to describe comes from particle accelerator experiments. The biggest one is the Large Hadron Collider (LHC) at CERN, but there are also other ones like the Relativistic Heavy Ion Collider (RHIC) in Brookhaven. At the LHC they collide protons together at extremely high energies. The energy is high enough to produce exotic particles that will not be produced in any other process on earth. These can then be measured at great precision, leading to the discovery of new physics, like the Higgs boson in 2012.

However, not only protons are collided. Another part of the experiment at the LHC is to produce collisions of so-called heavy ions, like gold or lead nuclei. These contain an abundance of protons and neutrons bound together by the strong nuclear force. Colliding so many particles at the same time gives rise to collective effects that cannot be studied

when colliding singular protons. In my PhD, I have worked on describing different phenomena that happen in heavy ion collisions.

The protons and neutrons that make up the heavy ions are made up of fundamental particles called quarks and gluons. When colliding heavy ions all of these quarks and gluons break free from nucleons and create a fluid called the quark-gluon plasma (QGP). This is an exotic phase of matter that was dominant in the very early universe, but after some time passed and the universe cooled down it is no longer produced from natural processes. A huge part of the motivation for doing heavy ion collisions is to map out the properties of the QGP. This is both an experimental effort and a theoretical one. It turns out that it is extremely hard to directly calculate the properties of the QGP with the theoretical tools currently available.

When you want to learn the properties of some liquid a common method is to design a probe that you can put inside of the liquid and measure different characteristics of it. However, it is impossible to create an external probe that can be put into a heavy ion collision to measure the properties of the QGP. The whole process takes place on a very short time scale and has an extremely small spatial extent. You therefore have to rely on so-called internal probes, which are produced in the collision itself. In heavy ion collisions the internal probes have to travel through the QGP to reach the detector. This passage changes the properties of the probe, and there can therefore be a measurable difference between the same probe in proton-proton collisions and heavy ion collisions. This provides valuable information about the QGP. There are several such internal probes. In my thesis I have focused on a specific subset, called *jets*.

In a subset of collision events very energetic particles are produced. These will start radiating more particles, and in the end you measure a spray of particles close together. This is a jet. Jets are produced both in proton-proton collisions and in heavy ion collisions. In proton-proton collisions the jets go unhindered to the detector. However, the QGP created in the heavy ion collisions will interact with the jet as it goes through it. The jet then loses energy and changes its momentum transverse to the direction of travel. This is called *jet quenching* and is the topic of my thesis. Jet quenching poses a great challenge, both on the experimental and the theory side, and is an active field of research.

The thesis is structured as follows: First, in Sec. 1.1 I will present a short review of the Standard Model of particle physics, which is the current framework we use to make calculations. I will in Sec. 1.2 put special emphasis on the part of the Standard Model that is relevant for jets, namely quantum chromodynamics (QCD). After the theoretical introduction, I will in chapter 2 write about heavy ion collisions in general. Then finally

in chapter 3 I will arrive at the main topic of the thesis, jet quenching. Here I will present the theory of jet quenching and note where my papers have contributed to the advancement of the field.

1.1 The Standard Model and quantum field theory

Most of the fundamental particles and interactions in the universe can be described through a framework called the Standard Model of particle physics. This includes all the fundamental forces except for gravity, as well as all the particles that make up visible matter. We know that the Standard Model is not complete, as it does not include gravity, dark matter, or dark energy. Nevertheless, it is an exceptionally successful theory and is able to describe natural phenomena with remarkable precision.

The Standard Model is an example of a quantum field theory (QFT). Quantum field theory is a way to combine quantum mechanics and special relativity, which were the two pinnacles of theoretical physics in the early 20th century. I will in the following present a short introduction to the parts of QFT most relevant to my thesis. This will in no way constitute a comprehensive review of QFT, and for those interested in more details I would recommend reading one of the many textbooks on the subject [4, 5].

In a QFT every particle and interaction correspond to a quantized field. The properties of the particles, and how they interact with each other are formulated in a Lagrangian density \mathcal{L} .

The possible terms in the Lagrangian are given by the symmetries of the theory. The particles in the Standard Model are symmetric under global space-time transformations and local gauge transformations.

1.1.1 Symmetries and groups

A symmetry simply means that the theory is invariant under some transformation. The natural way to describe these transformations is in the context of group theory. All the groups we will consider are Lie groups, which are groups whose elements form a differentiable manifold. In our context it is more useful to think of the elements of a Lie group as matrices. A group transformation is then given by $\phi \rightarrow M\phi$, where ϕ is some field, and M is some matrix contained in the group. This is a symmetry group for the theory if the Lagrangian is invariant under this transformation.

A Lie group is closely related to its Lie algebra, which describes infinitesimal transformations. The matrix can in general be written as an exponential $M = e^{i\alpha}$ for some matrix α . For an infinitesimal transformation we then have $M \simeq \mathbb{1} + i\alpha$, where α is a member of the Lie algebra. One can show that if α_1 and α_2 are members of the Lie algebra then the commutator $i[\alpha_1, \alpha_2]$ is also a member.

It is in general useful to define a basis of the algebra. The group generators t^a constitute a basis for the algebra if all the members of the algebra can be written as $\alpha = \alpha^a t^a$, where α^a is some number. Using that $i[\alpha_1, \alpha_2]$ is a member of the algebra leads to the following relation between the generators

$$[t^a, t^b] = i f^{abc} t^c, \quad (1.1)$$

where f^{abc} are some real coefficients called the structure constants.

It is possible to find several different sets of matrices t^a that satisfy the algebra (1.1). Each such set constitutes a different *representation* of the algebra. The original set of matrices t^a that we used to define the group is called the fundamental representation. Another representation is provided by the structure constants themselves: $(T^a)^{bc} = -i f^{abc}$. This is called the adjoint representation. These two representations are of special importance in QFT. We will for example see that in quantum chromodynamics, which has gauge group SU(3), the quarks transform in the fundamental representation, while the gluons transform in the adjoint representation.

Let us now summarize the symmetry groups in the Standard Model.

Another way to say that the Standard Model follows the rules of special relativity is to say that it is symmetric under the Lorentz group. The Lorentz group encompasses rotations and boosts. In fact, the Standard Model is invariant under transformations of the bigger Poincaré group, which contains the Lorentz group but also includes space-time translations.

Demanding that your theory is invariant under the Poincaré group severely limits the kind of fields your theory can include. In fact, one can show that the unitary irreducible representations of the Poincaré group are classified by two numbers: the mass m and the spin J , where the spin is a non-negative half-integer.

Invariance under the Poincaré group is a so-called global symmetry. Local symmetries are also important. The difference is that for local symmetries the transformation is position-dependent: $\phi \rightarrow M(x)\phi$. Local symmetries necessitate the introduction of a gauge field A_μ to make the theory invariant under group transformations. Local symmetries are

therefore often known as gauge symmetries. The gauge field is invariant under transformations corresponding to some arbitrary function $A_\mu \rightarrow A_\mu + \frac{1}{g}\partial_\mu\alpha^a(x) - f^{abc}\alpha^b(x)A_\mu^c$. The fact that this function $\alpha(x)$ can be chosen as we wish is called gauge freedom. In many cases one can choose a specific form of the function $\alpha(x)$ to simplify calculations, which is called gauge fixing.

The gauge symmetry group of the Standard Model is $SU(3) \times SU(2) \times U(1)$. The $SU(2) \times U(1)$ part is responsible for electromagnetic force and the weak interaction. It is spontaneously broken $SU(2) \times U(1) \rightarrow U(1)$ through the Higgs mechanism, which is responsible for giving mass to all the particles in the Standard Model.

The $SU(3)$ part of the Standard Model is called quantum chromodynamics (QCD), which is the theory of quarks and gluons. In our research we mainly work with QCD, so we study this theory in more detail in the next section.

1.2 Quantum Chromodynamics

In this section, we will go into more detail about quantum chromodynamics, as this is the main theory used in this thesis. QCD has gauge group $SU(3)$ and consists of vector fields (spin 1) called gluons, and spinors (spin 1/2) called quarks. The conserved charge in $SU(3)$ is called color. There are N_c different colors in a $SU(N_c)$ gauge theory, so in the case of QCD $N_c = 3$.

There are two important representations of $SU(3)$: the fundamental representation and the adjoint representation. In this thesis, we will adopt the convention to use $T_F^a \equiv t^a$ for fundamental generators and $T_A^a \equiv T^a$ for adjoint generators.

The fundamental representation is the smallest non-trivial representation, and it consists of $N_c \times N_c$ Hermitian matrices with determinant 1. In QCD where $N_c = 3$ it is common to define $t_{ij}^a = \frac{1}{2}\lambda_{ij}^a$, where λ^a are the eight Gell-Mann matrices. The index a signifies the number of generators, which is $N_c^2 - 1 = 8$, while the indices i, j are color indices that run to $N_c = 3$. In QCD the quarks transform under the fundamental representation $\psi_i \rightarrow \psi_i + i\alpha^a(x)t_{ij}^a\psi_j$ for an infinitesimal $\alpha(x)$.

The other important representation is the adjoint representation, where the generators are made up of the structure constants $(T^a)^{bc} = -if^{abc}$. In $SU(3)$ these are 8×8 matrices. The adjoint representation is important for physics because that is the representation under which the gluons transform: $A_\mu \rightarrow A_\mu + \frac{1}{g}\partial_\mu\alpha^a(x) - f^{abc}\alpha^b(x)A_\mu^c$.

It is useful to calculate the index $T(R)$ and quadratic Casimir C_R of a representation R ,

which are given by

$$\begin{aligned}\mathrm{tr}[T_R^a T_R^b] &= T(R)\delta^{ab} \\ T_R^a T_R^a &= C_R \mathbb{1},\end{aligned}\tag{1.2}$$

where $\mathbb{1}$ is the identity matrix. For the fundamental representation we have $T(F) = \frac{1}{2}$ and $C_F = \frac{N_c^2 - 1}{2N_c} = \frac{4}{3}$, while for the adjoint representation we have $T(A) = C_A = N_c = 3$.

The QCD Lagrangian is¹

$$\mathcal{L}_{\mathrm{QCD}} = \bar{\psi}_i (i \not{D}_{ij} - m \delta_{ij}) \psi_j - \frac{1}{4} G_{\mu\nu}^a G_a^{\mu\nu}.\tag{1.3}$$

We have used the covariant derivative $D_\mu = \partial_\mu - ig A_\mu^a t^a$, and the slash notation $\not{D} = \gamma^\mu D_\mu$. The gluon field strength tensor is $G_{\mu\nu}^a = \partial_\mu A_\nu^a - \partial_\nu A_\mu^a + g f^{abc} A_\mu^b A_\nu^c$.

1.2.1 QCD Feynman rules

Most observables in QCD are calculated by using the QCD Feynman rules. In some cases it is impossible to use the Feynman rules to do calculations, in which case one can use a numerical technique called lattice QCD. We will discuss this point more in later sections.

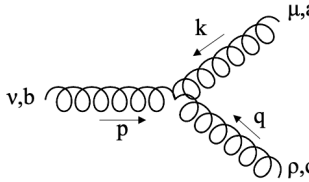
The Feynman diagrams consist of the gluon and quark propagators, as well as the interaction vertices. The quarks can interact with gluons, and the gluons can also self-interact. The Feynman rules can be derived from the Lagrangian.

The Lagrangian has some gauge freedom, and the best way to fix the gauge is dependent on the problem on hand. The choice of gauge will, among other things, change the form of the gluon propagator. In many QCD calculations it is useful to choose a covariant gauge, where the gluon propagator is

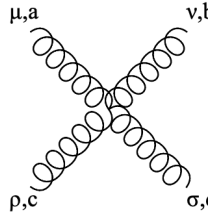
$$i\Pi_{\mathrm{covariant}}^{\mu\nu ab} = i \frac{-g^{\mu\nu} + (1 - \xi) \frac{p^\mu p^\nu}{p^2}}{p^2 + i\epsilon} \delta^{ab}.\tag{1.4}$$

The parameter ξ represents some additional gauge freedom and is usually chosen to be 0 (Lorenz gauge) or 1 (Feynman gauge). However, when choosing a covariant gauge you introduce some unphysical degrees of freedom, which can be canceled by adding

¹This is simplified somewhat from how it appears in the Standard Model, for the sake of clarity. One should sum over the six flavors. We have also neglected the Faddeev-Popov ghosts, as they do not appear in the lightcone gauge that we will use. In addition, the mass term actually comes from the Higgs mechanism.



$$= g f^{abc} [g^{\mu\nu} (k - p)^\rho + g^{\nu\rho} (p - q)^\rho + g^{\rho\mu} (q - k)^\nu] \quad (1.8)$$



$$= -ig^2 [f^{abe} f^{cde} (g^{\mu\rho} g^{\nu\sigma} - g^{\mu\sigma} g^{\nu\rho}) + f^{ace} f^{bde} (g^{\mu\nu} g^{\rho\sigma} - g^{\mu\sigma} g^{\nu\rho}) + f^{ade} f^{bce} (g^{\mu\nu} g^{\rho\sigma} - g^{\mu\rho} g^{\nu\sigma})] \quad (1.9)$$

These diagrams make up the starting point for computing QCD processes.

Most calculations in QFT rely on an approach called perturbation theory. To calculate a process where $a \rightarrow b$, where a is some initial collection of particles and b is some final state, we have to sum up all of the possible ways this can happen. There is an infinite number of such combinations, so it is not possible to calculate all of them. One can order the diagrams in complexity, so that the diagrams with the fewest interaction vertices come first, and then the number of vertices increases. Each interaction vertex comes with the coupling constant g , so if $g < 1$ the least complex diagrams will give the biggest contributions, and the more complex diagrams will give small corrections to this. One can then calculate the first few diagrams, and stop when the desired level of precision is reached. This is called perturbation theory, and crucially only works for weak coupling $g < 1$.

1.2.2 Confinement and asymptotic freedom

When doing calculations you will notice that when trying to calculate diagrams containing loops the result will diverge. This problem is solved through the process of renormalization, which results in the "bare" coupling g being replaced with the renormalized coupling $g_R(\mu)$. This is no longer a constant, but changes (runs) with the energy scale μ . The manner of running is encapsulated in a differential equation called the β -function, given as $\mu \frac{d}{d\mu} g_R = \beta(g_R)$. The form of $\beta(g_R)$ is defined through loop calculations.

Actually, when people mention the QCD coupling constant they usually rather refer to $\alpha_s \equiv g^2/4\pi$, as this appears more frequently in QCD calculations. At 1-loop order the

solution to the β -function is

$$\alpha_s(\mu) = \frac{2\pi}{7} \frac{1}{\ln \frac{\mu}{\Lambda_{\text{QCD}}}}. \quad (1.10)$$

From this, it is clear that the coupling α_s is small at high energies $\mu \gg \Lambda_{\text{QCD}}$, but grows large at low energies as $\mu \sim \Lambda_{\text{QCD}} \simeq 200$ MeV. The parameter Λ_{QCD} is the so-called Landau pole of QCD, where the coupling blows up.

At low energies the interaction is strong, and quarks bind together in colorless objects called hadrons, which are what can be observed in nature. The hadrons are grouped into mesons, which consist of a quark and an antiquark, and baryons, which consist of three quarks. The inability to observe quarks by themselves at low energies is a phenomenon called *confinement*. Confinement of Yang-Mills theory is an open mathematical problem, although lattice calculations shed light on various aspects of its appearance, not to mention that the overwhelming experimental evidence supporting it.

Since perturbation theory cannot be used the only reliable method of calculation at low energies is through lattice QCD, which is based on solving QCD on a discretized grid. This has some applications, but also some important limitations. We will discuss this more in later sections. Lattice QCD is extremely computationally expensive and requires very powerful computers to perform calculations.

In the high energy regime the coupling α_s is small, which means that one can use perturbative QCD (pQCD) to calculate observables. It is interesting to note that for very high energies $\mu \rightarrow \infty$ the coupling $\alpha_s \rightarrow 0$. This phenomenon is referred to as *asymptotic freedom*, as the quarks and gluons stop interaction at extremely high energy scales.

In heavy ion collisions nuclei are collided at very high energy. The nuclei consist of a collection of quarks and gluons, which we will collectively refer to as *partons*, a term coined by Feynman. As the partons in the nuclei gain energy the interaction between them becomes weak, and they will break out from their confinement and form a plasma of interacting quarks and gluons. This state of matter is called the quark-gluon plasma (QGP). The QGP has been an area for a lot of both theoretical and experimental efforts, which we will discuss in more detail in the next section.

Chapter 2

Heavy ion physics

2.1 Heavy ion collisions

The current data we have from heavy ion collisions is from RHIC in Brookhaven and the LHC in CERN. In these experiments heavy nuclei like Pb or Au are accelerated and made to collide at ultra-relativistic energies.

2.1.1 Motivation for colliding heavy ions

In heavy ion collisions you collide nuclei containing many protons and neutrons. Such collisions will have many binary collisions of nucleons happening at the same time, as opposed to only one in a proton-proton collision. Hence it provides an opportunity to study collective effects introduced by having many collisions happening in a small area. The effects of these collective phenomena are then compared to benchmark measurements that are not expected to exhibit collectivity, for example proton-proton collisions.

One of these collective phenomena that are produced in heavy ion collisions is the quark-gluon plasma, which is produced when nuclear matter is heated to very high temperatures. The finite temperature properties of QCD were largely unknown, and it is therefore a very interesting field to study. The heavy ion experiments at RHIC were largely done in the hope to see some signatures of the QGP, which they succeeded at [6, 7]. The LHC then started colliding heavy ions at higher energies, and also produces an abundance of interesting experimental results [8–12].

The QGP is only one part of the larger QCD phase diagram, seen in Fig. 2.1. At low temperatures T and baryon chemical potential μ_B the quarks and gluons are confined

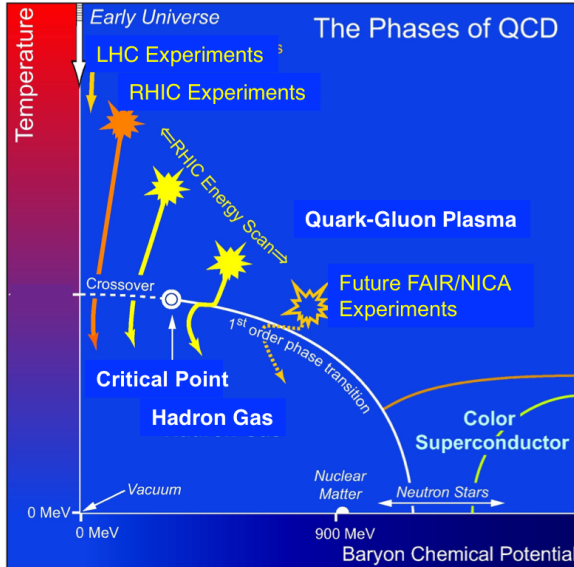


Figure 2.1: The QCD phase diagram. Figure from [13].

into hadrons. As the temperature increases there is a continuous crossover to the QGP phase at temperature $T_c \sim 155$ MeV [14].

The baryon chemical potential μ_B is in general small in heavy ion collisions, and it decreases with increasing collision energy. This is because the total baryon number in the collision is always two times the number of nucleons in each nucleus, while the total number of produced particles increases as the collision energy increases. Hence, the ~ 400 baryons are highly diluted in the final state, which contains thousands of hadrons.

Colliding heavy ions is the primary way of producing QGP, and thus our most important approach to studying this particular phase of QCD. In the following sections, we will describe the different aspects of heavy ion collisions in more detail.

2.1.2 Features of a heavy ion collision

There are several parameters that are used to describe a collision event. The center-of-mass energy per pair of colliding nucleons is referred to as $\sqrt{s_{NN}}$, and can go up to 5 TeV the LHC.

An abundance of particles is produced in each collision event, and they will fly out to hit the detector. The position of where the particle hits the detector can be described by the polar angle θ and the azimuthal angle ϕ compared to the beam direction. However, it is

usually more common to use the rapidity y or pseudorapidity η instead of θ . Defining the first component of momentum p_1 so its direction is along the beam direction, the rapidity is given as $y = \frac{1}{2} \ln \frac{E+p_1}{E-p_1}$, where the energy is $E = p_0$. The pseudorapidity is given by $\eta = -\log \tan(\theta/2)$, so that $\eta = 0$ in the direction perpendicular to the beam $\theta = \pi/2$. Lastly, it is common to define p_T as the particle's momentum perpendicular to the beam direction $p_T = \sqrt{p_2^2 + p_3^2}$.

The nuclei collide at a speed very close to the speed of light, and their length in the direction of travel is therefore Lorentz contracted. Their shape is therefore more like very thin discs, with a diameter of around 14 fm perpendicular to the direction of travel, and a thickness of around $14/\gamma$ fm in the direction of travel. For the RHIC and LHC energies the relativistic Lorentz factor γ is around 100 and 2500, respectively [15].

As the nuclei collide they create an area of high density and temperature. This results in a large yield of particles in the final state. At the LHC around 15000 charged particles are created for central collisions [16]. This abundance of particles is clearly produced by an initial state of very high density, simply from conservation of energy, as the detected particles typically have a few hundred MeV of energy each.

It is interesting to study the measured momentum of the produced particles. From the momentum spectrum it is clear that most of the produced particles are soft, meaning they have low energy. Hard particles, over around 5 GeV, are also produced but are comparatively rare. At high energy the spectrum falls steeply as a power of p_T , see Fig 2.2. These rare hard particles are of special interest as their high energy makes perturbation theory viable as a tool to calculate their journey through the QGP.

There are several methods of modeling the initial dense state that is reached right after the collision takes place. A relatively simple and well-known approach is called the Glauber model, see for example [18]. In the Glauber model, the energy density in the region of the collision is proportional to the thickness of the two colliding nuclei. Another more sophisticated model for the initial state is called the color-glass condensate (CGC), see e.g. [19]. The CGC is based on the physics of gluon saturation in the colliding nuclei. One can translate this model of the colliding nuclei into an energy density in the collision region after the collision has occurred.

Using one of the models for the initial state one can estimate the energy density in the collision region. Doing this one will find that it more than overshoots the critical energy density of QCD found by lattice QCD simulations $\epsilon_c \simeq 1 \text{ GeV}/\text{fm}^3$, where there is a crossover from hadronic matter to quark-gluon plasma [20]. This makes us confident that quark-gluon plasma has indeed been produced in the collision event.

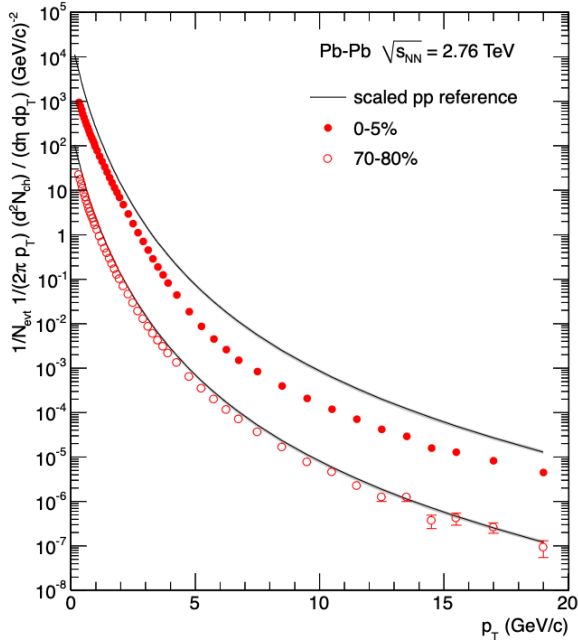


Figure 2.2: Charged particle multiplicity as a function of p_T for central and peripheral Pb-Pb collisions at $s_{NN} = 2.76$ TeV. Figure from the ALICE Collaboration [17].

Of course, not all of the nuclei will hit each other head-on. If the two nuclei hit each other off-center then not all of the nucleons will collide, and the rest are called spectators. The nucleons that are involved in the collisions are referred to as participants, and one participant can be involved in several binary collisions. In an idealized setting this is described by the impact parameter b , which is the transverse distance between the centers of the two nuclei in a collision.

The impact parameter cannot be measured directly, so in experiments the events are rather grouped into different centrality classes. The centrality of a collision can be inferred event-by-event by statistical data. More central collisions generally produce a higher yield of particles. For example, the 10% of collisions with the highest particle multiplicities will be put in the 0% – 10% centrality class and referred to as central collisions. Collisions with a large impact parameter are called peripheral collisions. An illustration of a peripheral collision can be seen in Fig. 2.3. In some experiments it is also possible to directly detect the beam remnants, which also gives a good indication of the centrality.

Since it is not possible to measure the number of spectators, participants, and binary collisions in an event these numbers must be inferred from some model, like the Glauber

model. The beam remnants can also be useful in this regard. The measured yield of charged particles is approximately proportional to the number of participants. Colorless probes such as photons and weak bosons are unaffected by the QGP and provide a good test for these models. This makes us confident of our starting point when studying colored probes.

2.1.3 Evolution after the collision

The collision results in a system with very high density and temperature, which means that the quarks and gluons no longer are confined in hadrons. In the current experiments the energy is not high enough to create truly free quarks and gluons. Rather they are in a state where they still interact strongly with each other, and form a collective fluid. This is, as already mentioned, referred to as the quark-gluon plasma. In the phase diagram Fig. 2.1 this corresponds to moving vertically towards higher temperatures, while keeping the baryon chemical potential μ_B relatively low.

For a weakly coupled plasma one can use perturbative hard thermal loop calculations to compute the properties of the plasma. However, at strong coupling this cannot be used. Lattice QCD is the only method we currently know of that can be used to compute the thermodynamical properties of a strongly coupled QGP. However, lattice QCD can only be used to compute static properties, when the system is at global equilibrium. In addition, if one wants to go to non-zero baryon chemical potential μ_B then lattice QCD runs into the so-called sign problem, where the probability interpretation breaks down. Going beyond zero μ_B is an important ongoing problem, that lies outside the scope of this thesis, see e.g. [21] for a review.

The current theory best suited to describing the evolution of the QGP is through relativistic hydrodynamics. As this thesis is about hard probes of the QGP we will not review the mathematics of hydrodynamics. For a review see for example [22].

In collisions that are not completely central the collision area will exhibit an almond shape, see Fig. 2.3 for a visual representation. This spatial anisotropy of the initial shape of the drop of QGP leads to differing pressure gradients in different directions. The pressure is greatest at the center of the collision and zero on its border. This implies that the pressure gradient will be biggest in the direction where the extent of the almond is the shortest. The QGP will expand hydrodynamically faster in the directions with bigger gradients, leading to a subsequent momentum anisotropy in the measured particles. This can be seen in Fig. 2.4. The azimuthal momentum anisotropy can be quantified by measuring the angular distribution of the final state hadrons.

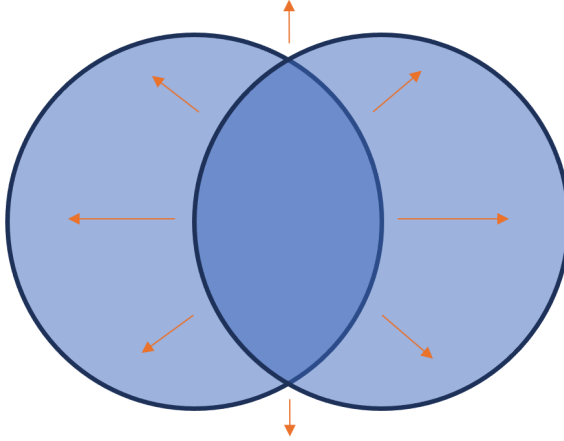


Figure 2.3: A visual representation of two colliding nuclei in a peripheral collision. The almond-shaped collision area is in the middle. The pressure gradients are noted by arrows.

The fact that the QGP can be described as a fluid is not a given. If this was not the case then the above argument would not be valid, and the azimuthal dependence of the measured hadrons would be different. It is the fact that we indeed see evidence of anisotropy in collision data that makes us confident that the QGP can be modeled using hydrodynamics.

The experimental data suggest that the ratio of the shear viscosity η over the entropy density s is small, close to the theoretical bound of $1/4\pi$ [24]. This means that QGP is almost an ideal fluid. This sets it clearly apart from most other fluids in nature, which typically have an $\eta/s > 1$. An $\eta/s \sim 1/4\pi$ is an indicator of strong coupling, as we know from calculations using the AdS/CFT correspondence [25]. All in all this fact indicates that the QGP produced at RHIC and LHC energies is a strongly coupled fluid with very low viscosity.

As the QGP expands, its pressure and temperature drop. When the QGP has cooled sufficiently the hydrodynamical picture is no longer valid, and we reach an energy density where hadrons are formed. This is called the chemical freeze-out. After this happens the relative abundances of the different hadron species are fixed for the rest of the evolution. However, the hadrons are still interacting with each other. The chemical freeze-out provides interesting insight into this stage of the event. One can fit the abundances of the different hadron species with a thermal distribution to extract the temperature T and chemical potential μ_B at the time of freeze-out. The extracted temperature at RHIC energies is close to the critical temperature at ~ 155 MeV [26].

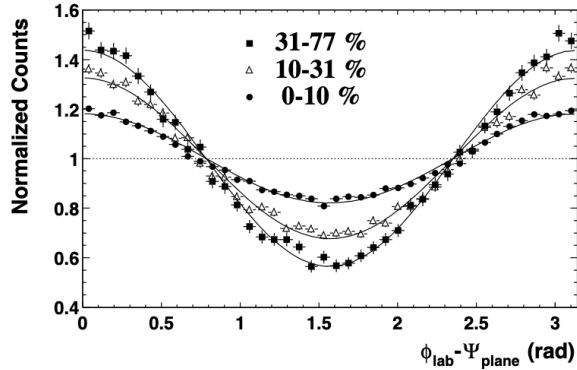


Figure 2.4: Normalized charged particle multiplicity as a function of the azimuthal angle ϕ for central and peripheral collisions. Figure from the STAR Collaboration [23].

Immediately after their formation the hadrons will interact. After the system has cooled down further the kinetic freeze-out occurs, meaning that the hadrons stop interacting and stream freely to the detector.

In rare cases, the collision will involve a hard interaction between two partons. This creates a particle of high virtuality that will move through the QGP. If the created particle is colored it will interact with the medium through QCD interactions. This provides an opportunity to study the QGP, because the parton's evolution through the medium is different than the corresponding process in the vacuum. The good thing about these hard probes is that because of their hardness, the interaction with the medium will be of higher energy, which means that the coupling will be weaker. This means that one can use perturbative techniques to perform calculations and to learn about a phase of matter that is non-perturbative in nature.

2.2 Experimental signatures of the QGP

Heavy ion collisions are the primary experiments to study the quark-gluon plasma. There are several types of experimental signatures that can be used to study the QGP. These can roughly be divided into

- correlation of low- p_T hadrons
- heavy quarks
- hard probes

In this section, we will review these signatures. In our research we focus on the hard probes of the QCD, so that will be our focus in later sections.

Correlation of low- p_T hadrons An important observable is the flow, which is a measure of how the QGP behaves like a fluid. It is related to the pressure anisotropy described in the previous section. We want to quantify the azimuthal dependence of the charged particle multiplicity. This is shown in Fig. 2.4. The shape of the azimuthal distribution seen in the plot suggests an expansion in cosines

$$\frac{dN}{d\mathbf{p}^2 dy} = \frac{1}{2\pi p_T} \frac{dN}{dp_T dy} [1 + 2v_1 \cos(\phi - \Psi_1) + 2v_2 \cos(2(\phi - \Psi_2)) + \dots]. \quad (2.1)$$

The second flow coefficient v_2 is referred to as elliptic flow, and it is an important observable describing the asymmetry of the collision. Experimentally, one finds sizable v_2 in heavy ion collisions [27].

The v_2 is smaller for central collisions than for peripheral collisions. This can be explained by the fact that a completely head-on collision creates a circular collision area, with no asymmetry. When the impact parameter is bigger the collision area will be less circular and have more of an asymmetric almond shape. This leads to differing pressure gradients in different directions, see Fig. 2.3. The pressure gradients make the fluid expand rapidly outwards towards the detector, but in an unequal manner in different directions. The degree of this asymmetry is what is described by the v_2 .

It is worth noting that the multiplicity of different particle species is dominated by low- p_T particles, as energetic particles are relatively rare. This can be seen in Fig. 2.2.

Heavy quarks Another signature of the presence of a thermal medium is the suppression of heavy quark bound states. The potential between a $c\bar{c}$ pair is screened in the medium, which will prevent the pair from finally forming a hadron. In contrast, the abundance of hadrons with strange quarks is higher in heavy ion collisions than in p-p collisions. This is because the QGP has high enough temperature to create strange quarks. This effect is called strangeness enhancement.

We will not go into details about heavy quarks as a probe of the QGP, see e.g. [28] for a review.

Hard probes An important class of observables is referred to as hard probes. In a subset of collisions, a hard process happens in the initial interaction, creating a hard

parton. This will fragment and leads to a spray of hadrons, called a jet. These jets are created both in p-p collisions and heavy ion collisions, and one can therefore compare the two to extract the modification of jets due to the presence of the thermal medium. These jet modification because of the thermal medium is referred to as *jet quenching*. The most important jet quenching effect is energy loss, which simply means that jets lose energy as they traverse the medium. We will cover jets and jet quenching in more detail in the next section.

One of the most commonly used observables in heavy ion collisions is the nuclear modification factor R_{AA} , which characterizes how many jets of a certain momentum are produced in a heavy ion (AA) collision, compared to in proton-proton collisions. It is given by the formula

$$R_{AA}(p_T, \eta) = \frac{dN^{AA \rightarrow X}/dp_T d\eta}{\langle N_{\text{coll}} \rangle dN^{pp \rightarrow X}/dp_T d\eta}. \quad (2.2)$$

The nuclear modification factor R_{AA} is a very useful observable, and its use is not limited to jets. One can also measure the R_{AA} of charged hadrons or heavy quarks states.

In the R_{AA} the p-p spectrum must be multiplied by the average number of binary collisions of nucleons happening in the specific AA collision. This can be estimated by for example using the Glauber model. Then an R_{AA} of 1 would imply that a heavy ion collision is more or less equivalent to many separate p-p collisions, meaning there would be no collective phenomena. If the R_{AA} deviates from 1 it means that either the initial state or the final state evolution is different than in p-p collisions. R_{AA} is measured at RHIC and the LHC, and the results show $R_{AA} < 1$ for charged hadrons, which means that these particles are suppressed. The measurements also show a strong centrality dependence of the R_{AA} , where the R_{AA} is less than 1 for central collisions, and closer to 1 for peripheral collisions [17]. This is readily interpreted as a sign that the partons lose energy as they go through and interact with the QGP.

On the other hand, the R_{pA} , which one can measure from proton-ion collisions, is consistent with a modification factor of 1, or slightly greater than 1 [29]. This implies that initial state effects, given by how much the nuclear PDFs differ from proton PDFs, are not very important for the measurement. It also suggests that there is not a sizable amount of QGP, and hence energy loss, in small systems. Additionally, the R_{AA} of colorless probes such as photons, Z's and W's is consistent with 1 [30]. This is expected, as colorless particles do not interact with the colored QGP, and is a good check of the interpretation of R_{AA} .

When a hard parton is created its momentum must, from conservation laws, be balanced

by an equal amount of momentum going in the opposite direction. A so-called dijet event is when there are two jets going back-to-back, in their center-of-mass frame. If the jets are created in a manner where they have to go through different lengths of QGP the amount of quenching will be different for each jet. This is called dijet asymmetry, and one expects the effect to be greater in central collisions than peripheral ones, since the amount of QGP created is greater in more central collisions. This effect is indeed observed in experiments [31].

Another class of jet observables is jet substructure. There are several ways to quantify the internal structure of a jet, and the difference in the substructure between vacuum and medium jets can provide information about the QGP and the quenching process. We will not go into details about this, see e.g. [32, 33] for reviews on this class of observables.

The main topic of this thesis is the theoretical treatment of jet quenching, with special emphasis on medium-induced radiation, which is the dominant process governing jet energy loss. We do not directly calculate any of the observables mentioned in this section. Rather, we have made contributions to the theoretical foundations that underpin jet quenching. These results must be integrated into a program like a Monte-Carlo simulation that takes into account all of the different effects that play a role between the collision and the measurement.

Chapter 3

Jet quenching

A jet is a collimated spray of hadrons. In a fraction of all collision events a highly energetic parton (quark or gluon) will be produced. This will start radiating and create a collection of partons close together. These partons will subsequently hadronize and show up in the detector as a jet.

Formally a jet is inherently linked with a jet-finding algorithm that describes how the final state particles are grouped together in a jet. Different jet definitions and algorithms exist in the literature. For a detailed discussion on jet definitions see [34].

Jets appear both in vacuum (p-p collisions) and in the medium (heavy ion collisions). The jets are created through the same processes in vacuum and in the medium, but the medium jets are modified by the passage through the QGP. In the vacuum the theory of jets is well understood, and vacuum jets hence provide a baseline for comparison to the more complex medium jets.

The modification of jets due to medium effects is, as already mentioned, known as jet quenching. Jet quenching is a broad term that not only refers to energy loss and the suppression of jet spectra, but to a range of jet observables, like jet substructure.

Vacuum jets

The theory of jets in p-p collisions has been studied for a long time and is under good theoretical control. See for example [35, 36] for more details.

The theory is based on a picture where the hard and soft processes are factorized. In the factorized picture the production of a final state X from the collision of two protons

can be written as

$$\sigma^{h_1 h_2 \rightarrow X}(p_1, p_2) = f_i^{h_1}(x_1, Q^2) \otimes f_j^{h_2}(x_2, Q^2) \otimes \sigma^{ij \rightarrow k}(x_1 p_1, x_2 p_2, Q^2) \otimes D_{k \rightarrow X}(z, Q^2). \quad (3.1)$$

The final state X can be a number of different objects, but here we will let it be a jet. The above equation describes how two partons i and j , one from each proton, interact and create a parton k that subsequently fragments and hadronizes. The process is factorized into three parts: the initial conditions of the protons that lead to the hard scattering, the hard scattering itself, and the evolution of the produced parton to the final observed jet X .

The initial conditions are described by the parton distribution functions (PDF) $f(x, Q^2)$, which give the probability of finding a parton of momentum x and virtuality Q^2 in an incoming proton. The PDFs are process-independent and non-perturbative objects that must be inferred from experiments. Their evolution in Q^2 is governed by the Dokshitzer-Gribov-Lipatov-Altarelli-Parisi (DGLAP) equations [37–39].

The hard scattering that produces a hard parton k from the initial partons i and j is described by the cross section $\sigma^{ij \rightarrow k}$. Since the scattering is hard this is a perturbative object, and it can be calculated to order of α_s using pQCD.

Finally, the fragmentation function $D_{k \rightarrow X}$ describes how the parton k evolves and ends up in a jet. Actually, this step involves two processes: partonic branching and hadronization. The partonic branching describes how a single parton of the scale Q^2 undergoes multiple splittings, and we end up with a collection of many partons at some lower scale Q_0^2 . This branching process is essential to understand to be able to calculate how jets are formed.

In vacuum the probability for one parton to branch into two contains both a soft and collinear divergence:

$$dP = \frac{\alpha_s}{2\pi} \frac{dk^2}{k^2} P_{ba}(z) dz. \quad (3.2)$$

Here the $P_{ba}(z)$ is the process-dependent Altarelli-Parisi splitting function. This means that most of the emitted partons will be soft, and be emitted with a small angle θ compared to the parent partons. The collinear divergence is when $k^2 \rightarrow 0$, where $k = |\mathbf{k}|$ is the transverse momentum. The soft divergence is when $z \rightarrow 0$, where z is the splitting fraction, and the splitting function goes as $P_{ba}(z) \sim 1/z$.

The evolution of the system from a high energy scale Q^2 to a lower one Q_0^2 is described by the DGLAP equation

$$\frac{\partial D(x, Q)}{\partial \ln(Q^2/Q_0^2)} = \int_0^1 \frac{dz}{z} \frac{\alpha_s(\mathbf{k})}{2\pi} P_{ba}(z) D(x/z, Q). \quad (3.3)$$

The DGLAP equation can be used to resum successive branchings. They are ideal for use in Monte-Carlo generators, where the DGLAP equation is used to produce parton showers.

One feature that is not captured by this picture is that of color coherence [40]. After a splitting there will take some finite time before the two partons are resolved, meaning that they are indistinguishable from a single colored object. This leads to the concept of angular ordering, where each successive branching has a smaller angle than the one before it $\theta_{n+1} < \theta_n$. The DGLAP equation can be modified to include this effect.

When the partons reach a certain energy threshold $Q_0 \sim \Lambda_{QCD}$ they hadronize. The resulting hadrons are then measured in the detector. Hadronization is a non-perturbative process, and can therefore not be calculated from pQCD. It must hence be inferred from data. Fortunately, it seems like a simple model of hadronization is enough to capture the most important effects [41].

Medium jets

Jets that are produced in the medium have to go through the quark-gluon plasma before they can escape to the detectors. The interaction with the medium changes the properties of the jet, which is called jet quenching. Because of this jets are an important probe of the QGP. However, the theory of jets in the thermal medium is more complicated than in vacuum.

A jet consists of several partons. As a parton goes through the medium it will change its direction and lose some of its energy. The former effect is referred to as transverse momentum broadening, and means that the parton changes its momentum transverse to its original direction. It leads to a general broadening of the jet. The interaction with the medium also leads to the jet losing energy. The most important effect is inelastic energy loss. There the partons in the jet are knocked off-shell by collisions with the medium, leading to additional emissions that might go out of the jet cone. This emission will not be included in the jet, and the energy is lost.

The factorized picture still holds in heavy-ion collisions. The hard scattering happens over a very short time, meaning that it will not be modified significantly by the formation of the medium [42].

The PDFs will certainly be different in heavy ion collisions compared to pp collisions. The so-called nuclear parton distribution functions (nPDF) differ from the proton PDFs in several ways [43], and must be used to obtain correct results.

The fragmentation function is definitively modified in the presence of a thermal medium. The partons will go through and interact with the medium before they can hadronize and reach the detector.

To calculate observables that can be directly compared to experiments one has to take into account all of the different parts of a heavy ion collision, from the initial configuration of the nuclei to the eventual hadronization of the particles created in the collision. This is too complicated and has too many parts to be possible to calculate analytically. Fortunately, all of this can be implemented in Monte Carlo simulations that aim to describe every step of the process, see e.g. [44, 45]. The theoretical studies we have conducted as part of my thesis can be used to improve the parts of these Monte Carlo generators relating to parton splitting in the medium, leading to a somewhat more accurate estimate of physical observables.

3.1 Basics of jet quenching theory

In this section, we will introduce the theory of jet quenching. I certainly do not mean for this to be an extensive review of jet quenching. There have been written many reviews on jet quenching, see e.g. [28, 32, 46, 47] for reviews focusing more on experiments and [42, 48–50] for theoretical reviews.

Since jets are composed of partons we need to derive rules for how highly energetic partons propagate and interact when they are in the QGP. We assume that the following hierarchy of energy scales holds:

$$E \gg |\mathbf{k}| \gg T, \Lambda_{\text{QCD}}. \quad (3.4)$$

By this, we mean that the energy of the hard parton E is much bigger than the transverse momentum scales \mathbf{k} . We will assume that the interaction between the partons and the medium is weakly coupled, which means that the energy scales of the partons are greater than those of the strongly coupled thermal medium (T, Λ_{QCD}). These assumptions are necessary to perform pQCD calculations. We will not discuss the possibility of strong coupling between the parton and the medium, or how to describe a strongly coupled medium through a gravity dual. For a review on how to model strong coupling through the AdS/CFT correspondence see [50].

Now we will show how to do calculations of jet quenching. First, we will introduce the theory, and then we will discuss two different facets of jet quenching: transverse momentum broadening and energy loss. Transverse momentum broadening is a fundamental

calculation in jet quenching, and it is tightly linked with the jet quenching parameter \hat{q} . Jet energy loss comes from medium-induced emissions that go outside of the jet cone. My papers are largely about improving the calculation of medium-induced emissions, so we will present this in some detail in Sec. 3.2.

3.1.1 The medium interaction

We will consider highly energetic partons (light quarks or gluons) that travel close to the light cone. In this regime the energy is much higher than their mass, so the mass can safely be neglected.

In this regime it is convenient to work with light-cone coordinates, defined by

$$\begin{aligned} x^+ &= \frac{1}{2}(x^0 + x^3) \\ x^- &= x^0 - x^3 \end{aligned} \tag{3.5}$$

The transverse coordinates are given by $\mathbf{x} = (x_1, x_2)$. We define the light-cone time as $t \equiv x^+$. The inner product in the light-cone coordinates is

$$x \cdot y = x^+ y^- + x^- y^+ - \mathbf{x} \cdot \mathbf{y}. \tag{3.6}$$

In momentum space the $+$ -component can be identified as the energy of the parton $E \equiv p^+$, while the p^- -component is negligible. The transverse coordinates are related to the transverse momentum through the Fourier transform¹

$$|\mathbf{p}\rangle = \int_{\mathbf{x}} e^{i\mathbf{p} \cdot \mathbf{x}} |\mathbf{x}\rangle. \tag{3.7}$$

The medium can be modeled as a classical colored gauge field $A^{\mu,a}$. In this context the word *classical* means that only tree-level diagrams involving the medium are considered. This approximation is valid since we assume weakly coupled interactions between the propagating parton and the medium.

One main assumption is to treat the subsequent scatterings on the medium field as independent. This assumption is valid when the mean free path is much larger than the range of the potential, $\lambda \gg \mu^{-1}$ [51]. In that case the only relevant correlator is the two-point correlator $\langle AA \rangle$. This also suppresses the contribution from the four-gluon interaction (1.9), so we will only consider three-gluon interactions (1.8).

¹We will use the convention $\int_{\mathbf{x}} = \int d^2\mathbf{x}$ and $\int_{\mathbf{p}} = \int \frac{d^2\mathbf{p}}{(2\pi)^2}$.

The medium field is sourced by a collection of independent color charges ρ^a spread out with a number density $n(t)$. The configuration of these color charges will follow a distribution centered around a net color charge of zero, so $\langle \rho^a \rangle = 0$. Since the color charges are assumed to be independent the correlation between two color charges is local in color and spacetime

$$\langle \rho^a(t, \mathbf{r}) \rho^b(t', \mathbf{r}') \rangle = n(t) \delta^{ab} \delta(t - t') \delta(\mathbf{r} - \mathbf{r}'). \quad (3.8)$$

This can for example be derived by assuming a Gaussian distribution for the color charges, as in the McLerran-Venugopalan (MV) model [52–54].

The gauge field A is related to the current $\mathcal{J}^\mu \simeq \rho^a t^a \delta^{\mu-}$ created by the color charges through the classical Yang-Mills equations $[D_\mu, F^{\mu\nu}] = \mathcal{J}^\nu$ [55]. In solving this it is convenient to use the light-cone gauge, where $A^{+,a} = 0$. After solving the Yang-Mills equations you find that the transverse components of the gauge field can be set to zero $A^{i,a} = 0$ [56]. This means that the remaining relevant component of the external field is the minus component, so we define $A^a \equiv A^{-,a}$. The field's relation to the color charges ρ is also given through solving the Yang-Mills equations, and is

$$A^a(t, \mathbf{r}) = \int_{\mathbf{q}} \frac{e^{-iq \cdot \mathbf{r}}}{\mathbf{q}^2} \rho^a(t, \mathbf{q}). \quad (3.9)$$

Combining this with Eq. (3.8) we find the correlator of two medium fields

$$\langle A^a(t, \mathbf{r}) A^b(t', \mathbf{r}') \rangle = \delta^{ab} n(t) \delta(t - t') \gamma(\mathbf{r} - \mathbf{r}'), \quad (3.10)$$

where

$$\gamma(\mathbf{r}) = g^2 \int_{\mathbf{q}} \frac{e^{-iq \cdot \mathbf{r}}}{\mathbf{q}^4}. \quad (3.11)$$

In reality, the potential will be Debye screened in the infrared because of the presence of the thermal medium. This screening depends on the microscopic properties of the medium and can be implemented through several different models. In general, we write

$$\gamma(\mathbf{r}) = \int_{\mathbf{q}} e^{-iq \cdot \mathbf{r}} \frac{d^2 \sigma_{\text{el}}}{d^2 \mathbf{q}}. \quad (3.12)$$

In many cases it is useful to define the difference

$$\sigma(\mathbf{r}) = g^2 [\gamma(\mathbf{0}) - \gamma(\mathbf{r})]. \quad (3.13)$$

We will mainly use the Gyulassy-Wang (GW) potential [57], which assumes static scat-

tering centers. It is given by

$$\frac{d^2\sigma_{\text{el}}}{d^2\mathbf{q}} = \frac{g^2}{(\mathbf{q}^2 + \mu^2)^2}, \quad (3.14)$$

where μ is the GW screening mass.

Another model can be found from hard thermal loops (HTL) calculations in a thermal medium with temperature T [58]. This HTL model differs from the GW model in how the IR screening is implemented

$$\frac{d^2\sigma_{\text{el}}}{d^2\mathbf{q}} = \frac{m_D^2 T}{n(t)} \frac{1}{\mathbf{q}^2(\mathbf{q}^2 + m_D^2)}, \quad (3.15)$$

where m_D is the Debye mass.

At this point we can start to describe a parton traversing the thermal medium. It is possible to derive in-medium Feynman rules, which can be used to calculate different processes happening in the medium. As the parton traverses the medium it gets small "kicks" from the background field, causing it to change its transverse direction. The fact that only the transverse momentum changes can be seen from (3.10), as there is a delta function in time (conjugate with energy).

3.1.2 The medium propagator

We will now derive the medium propagator, which describes a parton's propagation through and interaction with a thermal medium. This has been derived before, see e.g. [42] for a different derivation.

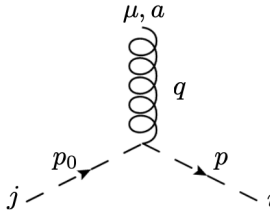
As the parton goes through the medium it can get any number of kicks from the scattering centers. The propagator therefore has to include an arbitrary number of such medium interactions. The medium interactions are separated in time. They will also, as we have already mentioned, only change the transverse momentum \mathbf{p} of the partons, while the energy p^+ stays constant. We therefore want a propagator that is a function of time and transverse momentum/position, and sums up an arbitrary number of interactions. Symbolically, we will represent a parton propagating from time t_0 to t , with transverse momentum going from \mathbf{p}_0 to \mathbf{p} as $(\mathbf{p}|\mathcal{G}(t, t_0)|\mathbf{p}_0)$. We will now show how this can be derived.

We will do the derivation for a scalar particle, as it makes the calculations simpler and more clear. The derivation for a quark or a gluon is very similar. Each case involves some different factors that relate to the spin of the parton, but since a scalar particle has spin 0 it is trivial. In the medium Feynman rules these spin factors are stripped from

the propagators and put into the vertices. The remaining propagator is the same in all three cases, and deriving it for a scalar particle is just the least complicated way. We will derive the internal propagator. The derivation for the external propagator is again very similar.

The QCD Feynman rules for a scalar in the fundamental representation are

$$j \text{ --- } \text{---} \text{---} \xrightarrow{p} \text{---} \text{---} \text{---} i = \delta^{ij} G_0(p) = \frac{i\delta^{ij}}{p^2 + i\epsilon}, \quad (3.16)$$



$$= V_{ij}^{\mu,a}(p+p_0) = ig(p^\mu + p_0^\mu) T_{ij}^a. \quad (3.17)$$

We use the high energy approximation, where the mass is zero.

We will denote the scalar medium propagator $(p|G_{\text{scal}}|p_0)$. We will first derive this as a function of four-momenta, and then change to the coordinates we want.

The propagator should sum up an arbitrary number of scatterings. The first possibility is there are no scatterings. In that case the medium propagator just reduces to the vacuum one

$$(p|G_{\text{scal},0}^{ij}|p_0) = (2\pi)^4 \delta(p-p_0) \delta^{ij} G_0(p). \quad (3.18)$$

The next term will then contain one medium interaction, namely

$$(p|G_{\text{scal},1}^{ij}|p_0) = G_0(p) V_{ij}^{\mu,a}(p+p_0) A^{\mu,a}(p-p_0) G_0(p_0). \quad (3.19)$$

The one after that will have two interactions etc. The sum of all of these interactions can be neatly written in terms of a Dyson-Schwinger expansion

$$\begin{aligned} (p|G_{\text{scal}}^{ij}|p_0) &= (2\pi)^4 \delta(p-p_0) \delta^{ij} G_0(p) \\ &+ \int \frac{d^4 p_1}{(2\pi)^4} G_0(p) V_{ij}^{\mu,a}(p+p_1) A^{\mu,a}(p-p_1) (p_1|G_{\text{scal}}^{kj}|p_0). \end{aligned} \quad (3.20)$$

This is a recursive relation for the propagator, as the term we are after is present at both sides of the equation. One can check by iterating this equation a few times that it contains the cases of zero and one medium interactions, which we already have calculated. In fact, it sums up an arbitrary number of medium interactions, in accordance with the Feynman rules. See Fig. 3.1 for a visual representation.

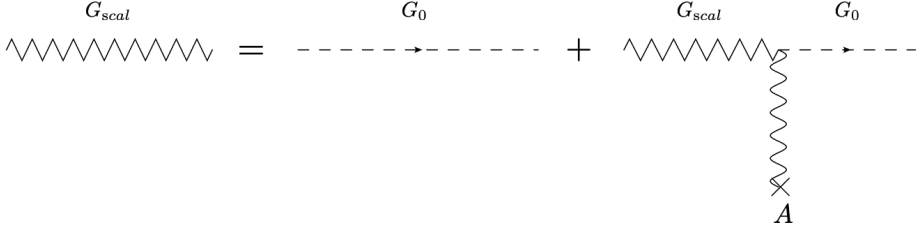


Figure 3.1: A visual representation of the Dyson-Schwinger expansion of the propagator.

Now let us calculate the product of the vertex and the external field A . As we have already shown only the $-$ -component of the field is relevant, so we get

$$\begin{aligned}
 V_{ik}^{\mu,a}(p+p_1)A^{\mu,a}(p-p_1) &= V_{ik}^{+,a}(p+p_1)A^{-,a}(p-p_1) \\
 &= ig(p^+ + p_1^+)A^a(p-p_1)T_{ik}^a \\
 &= 2p^+ ig\mathcal{A}_{ik}(p-p_1).
 \end{aligned} \tag{3.21}$$

In the last line we have used the fact that the medium interaction does not change the $+$ -component of the momentum, and defined $\mathcal{A} \equiv A^a T^a$. The Dyson-Schwinger expansion then becomes

$$\begin{aligned}
 \langle p|G_{\text{scal}}^{ij}|p_0\rangle &= (2\pi)^4 \delta(p-p_0) \delta^{ij} G_0(p) \\
 &\quad + 2p^+ \int \frac{d^4 p_1}{(2\pi)^4} G_0(p) ig\mathcal{A}_{ik}(p-p_1) \langle p_1|G_{\text{scal}}^{kj}|p_0\rangle.
 \end{aligned} \tag{3.22}$$

The quark and gluon cases can be derived in a similar way, but with some spin-dependent factors in front.

We want a process-independent propagator that covers all cases. In most calculations it is convenient to write the propagator as a function of time and either transverse momentum or transverse position, instead of the full 4-vector. The $+$ -component of the momentum is conserved in each interaction, so we would like our propagator to be independent of this. Hence, we define the medium propagator as

$$2\pi\delta(p^+ - p_0^+) \frac{1}{2p^+} \langle \mathbf{p}|\mathcal{G}(t, t_0)|\mathbf{p}_0\rangle = \int \frac{dp^- dp_0^-}{(2\pi)^2} e^{-ip^- t + ip_0^- t_0} \langle p|G_{\text{scal}}|p_0\rangle. \tag{3.23}$$

The Dyson-Schwinger expansion for the new propagator is then

$$\begin{aligned}
 \langle \mathbf{p}|\mathcal{G}(t, t_0)|\mathbf{p}_0\rangle &= (2\pi)^2 \delta(\mathbf{p} - \mathbf{p}_0) \mathcal{G}_0(\mathbf{p}, t - t_0) \\
 &\quad + \int_{t_0}^t ds \int_{\mathbf{q}} \mathcal{G}_0(\mathbf{p}, t - s) ig\mathcal{A}(\mathbf{q}, s) \langle \mathbf{p} - \mathbf{q}|\mathcal{G}(s, t_0)|\mathbf{p}_0\rangle.
 \end{aligned} \tag{3.24}$$

Here we have suppressed the color indices to make it more general. In cases where we want to make the representation explicit, we will write \mathcal{G}_R and T_R , where the representation R can be fundamental or adjoint. One can check that the free propagator in the mixed representation is

$$\begin{aligned} (\mathbf{p}|\mathcal{G}_0(t, t_0)|\mathbf{p}_0) &= (2\pi)^2 \delta(\mathbf{p} - \mathbf{p}_0) \mathcal{G}_0(\mathbf{p}, t - t_0) \\ &= (2\pi)^2 \delta(\mathbf{p} - \mathbf{p}_0) e^{-i\frac{p^2}{2E}(t-t_0)}. \end{aligned} \quad (3.25)$$

Here we have equated the energy with the $+$ -component of the momentum as $E \equiv p^+$.

It is often convenient to write this expansion in position space, which is reached through a Fourier transform

$$\begin{aligned} (\mathbf{x}|\mathcal{G}(t, t_0)|\mathbf{x}_0) &= \mathcal{G}_0(\mathbf{x} - \mathbf{x}_0, t - t_0) \\ &+ \int_{t_0}^t ds \int_{\mathbf{y}} \mathcal{G}_0(\mathbf{x} - \mathbf{y}, t - s) ig\mathcal{A}(\mathbf{y}, s) (\mathbf{y}|\mathcal{G}(s, t_0)|\mathbf{x}_0). \end{aligned} \quad (3.26)$$

The free propagator in position space is

$$(\mathbf{x}|\mathcal{G}_0(t, t_0)|\mathbf{x}_0) = \frac{E}{2\pi i(t - t_0)} e^{i\frac{E}{2} \frac{(\mathbf{x} - \mathbf{x}_0)^2}{(t - t_0)}}. \quad (3.27)$$

In position space it is possible to rewrite the Dyson-Schwinger expansion as a Schrödinger equation

$$\left[i\frac{\partial}{\partial t} + \frac{\partial^2}{2E} + g\mathcal{A}(\mathbf{x}, t) \right] (\mathbf{x}|\mathcal{G}(t, t_0)|\mathbf{x}_0) = i\delta(t - t_0)\delta(\mathbf{x} - \mathbf{x}_0). \quad (3.28)$$

The propagator can also be written in the path integral form

$$(\mathbf{x}|\mathcal{G}_R(t, t_0)|\mathbf{x}_0) = \int_{\mathbf{x}_0}^{\mathbf{x}} \mathcal{D}\mathbf{r} e^{i\frac{E}{2} \int_{t_0}^t ds \dot{\mathbf{r}}^2(s)} V_R(t, t_0; \mathbf{r}(t)), \quad (3.29)$$

where V_R is a Wilson line in the representation R

$$V_R(t, t_0; \mathbf{r}(t)) = \mathcal{P} e^{ig \int_{t_0}^t ds A^a(s, \mathbf{r}(s)) T_R^a}. \quad (3.30)$$

The path integral form is the most commonly used, as the propagator is written out in one compact expression. The form of the propagator can be interpreted in the following way: As the parton traverses the medium it can be kicked around many times, changing its path. The sum over all the possible paths leads to a path integral. In addition, the parton can change its color with every medium interaction. This color rotation is encapsulated in a Wilson line.

In App. A we explicitly show that the three ways to write the propagator, Eqs. (3.26), (3.28) and (3.29) are equivalent.

We could go on to calculate the full Feynman rules in the medium, with external and internal propagators for both quarks and gluons, and all the relevant vertices. However, this is beyond the scope of our thesis. The medium propagator will be used frequently in the subsequent chapters, which is why this was derived in detail. We refer to [59, 60] for the full medium Feynman rules.

The eikonal approximation If the energy of the parton traversing the medium is very high the changes in the transverse direction as it interacts with the medium will be negligible. This is called the eikonal approximation. Then the path integral in Eq. (3.29) becomes trivial, and the eikonal propagator is

$$(\mathbf{x}|\mathcal{G}_R^{\text{eik}}(t, t_0)|\mathbf{x}_0) = (\mathbf{x}|\mathcal{G}_0(t, t_0)|\mathbf{x}_0)V_R(t, t_0; \mathbf{x}_{\text{cl}}(t)), \quad (3.31)$$

and similarly in momentum space. Here the Wilson line is on the classical path between the two points.

$$\mathbf{x}_{\text{cl}}(s) = \frac{\mathbf{x} - \mathbf{x}_0}{t - t_0}(s - t_0) + \mathbf{x}_0. \quad (3.32)$$

Wilson lines In this thesis we will use $V_F \equiv V$ for fundamental Wilson lines and $V_A \equiv U$ for adjoint Wilson lines. The adjoint Wilson lines are related to the fundamental ones through the identity

$$U^{ab} = 2 \text{tr} [t^a V t^b V^\dagger] = U^{\dagger ba}. \quad (3.33)$$

From this discussion it is clear that phenomenological calculations will contain two Wilson lines for each parton existing in a process at a specific time, one in the amplitude and one in the complex conjugate amplitude. In addition each adjoint (gluon) Wilson line can be written in terms of two fundamental Wilson lines through Eq. (3.33). The maximum number of fundamental Wilson lines at any one time in a process is therefore

$$n = 2(n_q + 2n_g), \quad (3.34)$$

where n_q and n_g are the numbers of quarks and gluons, respectively. An important part of doing calculations in the medium is therefore calculating Wilson line correlators, on

the form

$$\langle |\mathcal{M}|^2 \rangle \sim \langle \text{tr}[V^\dagger V \dots V^\dagger V] \dots \text{tr}[V^\dagger V \dots V^\dagger V] \rangle. \quad (3.35)$$

In [1] we found a general method of calculating all Wilson line correlators on this form. We showed that they are given as solutions to differential equations. In addition, we showed in detail how the calculations simplify in the large- N_c limit.

3.1.3 Transverse momentum broadening

Transverse momentum broadening describes how the transverse momentum of a single parton changes as it traverses the medium. It is described by the distribution $\mathcal{P}(\mathbf{k})$, which gives the probability for a parton to pick up the transverse momentum \mathbf{k} after traveling a distance L in the medium. The mean transverse momentum picked up per unit length is called the jet quenching parameter \hat{q} , and is defined through

$$\hat{q} \equiv \frac{\langle \mathbf{k}^2 \rangle}{L} = \frac{1}{L} \int_{\mathbf{k}} \mathbf{k}^2 \mathcal{P}(\mathbf{k}). \quad (3.36)$$

The way to calculate the distribution $\mathcal{P}(\mathbf{k})$ is simply to calculate the process of a single parton propagating from an initial time t_0 to the end of the medium L . It therefore only involves the medium propagator, in the amplitude and in the complex conjugate amplitude. We therefore define

$$(\mathbf{p}_1; \mathbf{p}_1 | S^2(L - t_0) | \mathbf{p}_0; \bar{\mathbf{p}}_0) = (2\pi)^2 \delta(\mathbf{p}_0 - \bar{\mathbf{p}}_0) \mathcal{P}(\mathbf{p}_1 - \mathbf{p}_0 | L, t_0), \quad (3.37)$$

where the two-point function is

$$(\mathbf{p}_1; \mathbf{p}_1 | S^2(L - t_0) | \mathbf{p}_0; \bar{\mathbf{p}}_0) = \frac{1}{N_c} \text{tr} \langle (\mathbf{p}_1 | \mathcal{G}_F(L, t_0) | \mathbf{p}_0) (\bar{\mathbf{p}}_0 | \mathcal{G}_F^\dagger(L, t_0) | \mathbf{p}_1) \rangle. \quad (3.38)$$

Here we have chosen to study a quark. For gluons the only difference would be a factor $1/(N_c^2 - 1)$ in front and using gluon propagators. The propagators are usually written in position space, see Eq. (3.29), so after Fourier transforming we get

$$(\mathbf{p}_1; \mathbf{p}_1 | S^2(L - t_0) | \mathbf{p}_0; \bar{\mathbf{p}}_0) = \int_{\mathbf{x}_1 \mathbf{x}_0 \bar{\mathbf{x}}_1 \bar{\mathbf{x}}_0} e^{-i\mathbf{p}_1 \cdot (\mathbf{x}_1 - \bar{\mathbf{x}}_1) + i\mathbf{p}_0 \cdot \mathbf{x}_0 - i\bar{\mathbf{p}}_0 \cdot \bar{\mathbf{x}}_0} (\mathbf{x}_1; \bar{\mathbf{x}}_1 | S^2(L - t_0) | \mathbf{x}_0; \bar{\mathbf{x}}_0), \quad (3.39)$$

where in position space we have

$$\begin{aligned} (\mathbf{x}_1; \bar{\mathbf{x}}_1 | S^2(L - t_0) | \mathbf{x}_0; \bar{\mathbf{x}}_0) &= \frac{1}{N_c} \text{tr} \langle (\mathbf{x}_1 | \mathcal{G}_F(L, t_0) | \mathbf{x}_0) (\bar{\mathbf{x}}_0 | \mathcal{G}_F^\dagger(L, t_0) | \bar{\mathbf{x}}_1) \rangle \\ &= \int_{\mathbf{x}_0}^{\mathbf{x}_1} \mathcal{D}\mathbf{r} \int_{\bar{\mathbf{x}}_0}^{\bar{\mathbf{x}}_1} \mathcal{D}\bar{\mathbf{r}} e^{i\frac{E}{2} \int_{t_0}^L ds (\dot{\mathbf{r}}^2 - \dot{\bar{\mathbf{r}}}^2)} \frac{1}{N_c} \text{tr} \langle V(\mathbf{r}) V^\dagger(\bar{\mathbf{r}}) \rangle. \end{aligned} \quad (3.40)$$

The Wilson line correlator acts as the potential term of the path integral. In [1] we found a general method of calculating all Wilson line correlators through differential equations. This case of only two Wilson lines is trivial, but we will show the calculation using our method for illustrative purposes. Using the main result in [1] the differential equation for this is

$$\frac{d}{dt} \langle V(\mathbf{r}) V^\dagger(\bar{\mathbf{r}}) \rangle = -\frac{1}{2} n(t) \left(N_c - \frac{1}{N_c} \right) \sigma(\mathbf{r} - \bar{\mathbf{r}}) \langle V(\mathbf{r}) V^\dagger(\bar{\mathbf{r}}) \rangle. \quad (3.41)$$

This is separable, and the solution is simply

$$\frac{1}{N_c} \langle V(\mathbf{r}) V^\dagger(\bar{\mathbf{r}}) \rangle = e^{-C_F \int_{t_0}^L ds n(s) \sigma(\mathbf{r} - \bar{\mathbf{r}})}. \quad (3.42)$$

Inserting this into the equation for the two-point function gives

$$(\mathbf{x}_1; \bar{\mathbf{x}}_1 | S^2(L - t_0) | \mathbf{x}_0; \bar{\mathbf{x}}_0) = \int_{\mathbf{x}_0}^{\mathbf{x}_1} \mathcal{D}\mathbf{r} \int_{\bar{\mathbf{x}}_0}^{\bar{\mathbf{x}}_1} \mathcal{D}\bar{\mathbf{r}} e^{i \int_{t_0}^L ds \left[\frac{E}{2} (\dot{\mathbf{r}}^2 - \dot{\bar{\mathbf{r}}}^2) + i C_F n(s) \sigma(\mathbf{r} - \bar{\mathbf{r}}) \right]}. \quad (3.43)$$

Noticing that the potential only depends on the difference $\mathbf{r} - \bar{\mathbf{r}}$ one can change coordinates to $\mathbf{u} = \mathbf{r} - \bar{\mathbf{r}}$ and $\mathbf{v} = 1/2(\mathbf{r} + \bar{\mathbf{r}})$. The potential is now independent of the variable \mathbf{v} , and the path integral over \mathbf{v} can be done immediately. This has the effect of forcing \mathbf{u} to be on the classical path $\mathbf{u}_{\text{cl}}(t) = \frac{\mathbf{u}_1 - \mathbf{u}_0}{\Delta t} (t - t_0) + \mathbf{u}_0$, where $\Delta t = L - t_0$. Going back to momentum space we now have, after changing coordinates and doing the path integrals

$$\begin{aligned} (\mathbf{p}_1; \bar{\mathbf{p}}_1 | S^2(L - t_0) | \mathbf{p}_0; \bar{\mathbf{p}}_0) &= \left(\frac{E}{2\pi\Delta t} \right)^2 \int_{\mathbf{u}_1 \mathbf{u}_0 \mathbf{v}_1 \mathbf{v}_0} e^{i\mathbf{v}_0 \cdot (\mathbf{p}_0 - \bar{\mathbf{p}}_0) - i\mathbf{u}_1 \cdot \mathbf{p}_1 + \frac{1}{2} i\mathbf{u}_0 \cdot (\mathbf{p}_0 + \bar{\mathbf{p}}_0)} \\ &\times e^{i\frac{E}{\Delta t} (\mathbf{u}_1 - \mathbf{u}_0) \cdot (\mathbf{v}_1 - \mathbf{v}_0) - C_F \int_{t_0}^L ds n(s) \sigma(\mathbf{u}_{\text{cl}})}. \end{aligned} \quad (3.44)$$

The integrals over \mathbf{v}_1 , \mathbf{v}_0 and \mathbf{u}_1 can be done immediately, leading to Dirac deltas setting $\mathbf{u}_1 \rightarrow \mathbf{u}_0$ and $\bar{\mathbf{p}}_0 \rightarrow \mathbf{p}_0$. After extracting the overall momentum-conserving delta function you get the broadening distribution

$$\mathcal{P}(\mathbf{p}_1 - \mathbf{p}_0 | L, t_0) = \int_{\mathbf{u}} e^{-i\mathbf{u} \cdot (\mathbf{p}_1 - \mathbf{p}_0)} e^{-C_F \int_{t_0}^L ds n(s) \sigma(\mathbf{u})}, \quad (3.45)$$

and equivalently in position space

$$\mathcal{P}(\mathbf{u}|L, t_0) = e^{-C_F \int_{t_0}^L ds n(s) \sigma(\mathbf{u})}. \quad (3.46)$$

The calculation for gluons is very similar, and the general case is given by changing the color factor from C_F to the general C_R .

To continue we need a model for the potential $\sigma(\mathbf{u})$. For now, let us assume that the potential can be approximated as a harmonic oscillator with some arbitrary constant A

$$C_R n(t) \sigma(\mathbf{r}) = A r^2. \quad (3.47)$$

Then we calculate the mean broadening per unit length \hat{q}_R for a parton of representation R , given by

$$\begin{aligned} \hat{q}_R &= \frac{1}{L} \int_{\mathbf{k}} \mathbf{k}^2 \mathcal{P}(\mathbf{k}) \\ &= \frac{1}{L} \int_{\mathbf{k}} \int_{\mathbf{u}} \mathbf{k}^2 e^{-i\mathbf{u} \cdot \mathbf{k} - LAu^2} \\ &= 4A. \end{aligned} \quad (3.48)$$

In Sec. 3.3 we will see that a harmonic oscillator with constant $\hat{q}_R/4$ is indeed a valid approximation of the potential.

3.2 Medium-induced radiation

A parton traversing a quark-gluon plasma can lose energy in two different ways: collisional energy loss and radiative energy loss. In collisional energy loss, the parton scatters elastically on the medium and loses energy in the process. However, in radiative energy loss, the parton scatters inelastically on the medium, meaning that the scattering induces the parton to emit a gluon. For high-energy partons the energy loss is dominated by radiative processes, and hence this is what we will focus on in this section [49].

To start out we will keep the notation as general as possible, and consider a parton a with energy E splitting into two partons b and c with energies zE and $(1-z)E$, respectively. This discussion is mainly taken from [3], see also [59, 61, 62]. The inclusive cross section for this process is given by

$$\frac{d\sigma}{d\Omega_q d\Omega_k} = 2E 2\pi \delta(E - k^+ - q^+) \int d\Omega_{p_0} \mathcal{P}_2(\mathbf{k}, \mathbf{q}; \mathbf{p}_0) \frac{d\sigma_0}{d\Omega_{p_0}}, \quad (3.49)$$

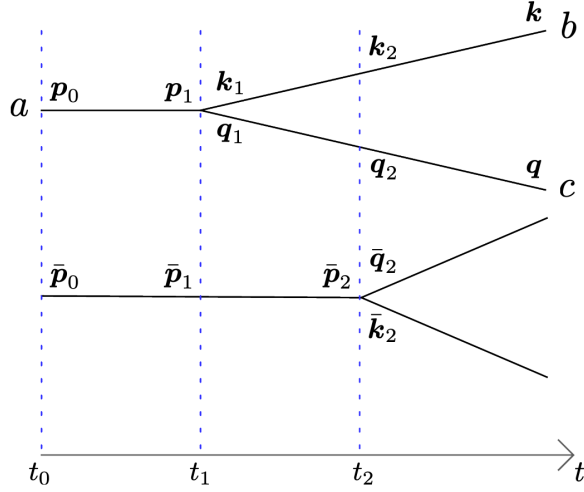


Figure 3.2: A parton splitting into two daughter partons at time t_1 in the amplitude and t_2 in the complex conjugate amplitude. Figure from [3].

where the phase space element is $d\Omega_p = dE d^2\mathbf{p}/(2E(2\pi)^3)$. The generalized splitting function $\mathcal{P}_2(\mathbf{k}, \mathbf{q}; \mathbf{p}_0)$ is given by

$$\begin{aligned} \mathcal{P}_2(\mathbf{k}, \mathbf{q}; \mathbf{p}_0) &= \frac{g^2}{z(1-z)E^2} P_{a \rightarrow bc}(z) \text{Re} \int_0^\infty dt_1 \int_{t_1}^\infty dt_2 \int_{\bar{\mathbf{p}}_0 \mathbf{p}_1 \bar{\mathbf{p}}_1 \mathbf{k}_2 \mathbf{q}_2 \bar{\mathbf{p}}_2 \bar{\mathbf{k}}_2} \\ &\times (\mathbf{k}_1 - z\mathbf{p}_1) \cdot (\bar{\mathbf{k}}_2 - z\bar{\mathbf{p}}_2) (\mathbf{k}, \mathbf{q}; \mathbf{k}, \mathbf{q} | S^{(4)}(t_\infty, t_2) | \mathbf{k}_2, \mathbf{q}_2; \bar{\mathbf{k}}_2, \bar{\mathbf{p}}_2 - \bar{\mathbf{k}}_2) \\ &\times (\mathbf{k}_2, \mathbf{q}_2; \bar{\mathbf{p}}_2 | S^{(3)}(t_2, t_1) | \mathbf{k}_1, \mathbf{p}_1 - \mathbf{k}_1; \bar{\mathbf{p}}_1) (\mathbf{p}_1; \bar{\mathbf{p}}_1 | S^{(2)}(t_1 - t_0) | \mathbf{p}_0; \bar{\mathbf{p}}_0). \end{aligned} \quad (3.50)$$

This might look complicated, but it is a convolution of three different objects with clear physical interpretations. The two-point, three-point and four-point functions are correlators of two, three and four propagators

$$\begin{aligned} (\mathbf{p}_1; \bar{\mathbf{p}}_1 | S^{(2)}(t_1, t_0) | \mathbf{p}_0; \bar{\mathbf{p}}_0) &\sim \langle (\mathbf{p}_1 | \mathcal{G}_a(t_1, t_0) | \mathbf{p}_0) (\bar{\mathbf{p}}_0 | \mathcal{G}_a^\dagger(t_0, t_1) | \bar{\mathbf{p}}_1) \rangle \\ (\mathbf{k}_2, \mathbf{q}_2; \bar{\mathbf{p}}_2 | S^{(3)}(t_2, t_1) | \mathbf{k}_1, \mathbf{p}_1 - \mathbf{k}_1; \bar{\mathbf{p}}_1) &\sim \langle (\mathbf{k}_2 | \mathcal{G}_b | \mathbf{k}_1) (\mathbf{q}_2 | \mathcal{G}_c | \mathbf{p}_1 - \mathbf{k}_1) (\bar{\mathbf{p}}_1 | \mathcal{G}_a^\dagger | \bar{\mathbf{p}}_2) \rangle \\ (\mathbf{k}, \mathbf{q}; \mathbf{k}, \mathbf{q} | S^{(4)}(L, t_2) | \mathbf{k}_2, \mathbf{q}_2; \bar{\mathbf{k}}_2, \bar{\mathbf{p}}_2 - \bar{\mathbf{k}}_2) &\sim \langle (\mathbf{k} | \mathcal{G}_b | \mathbf{k}_2) (\mathbf{q} | \mathcal{G}_c | \mathbf{q}_2) (\bar{\mathbf{p}}_2 - \bar{\mathbf{k}}_2 | \mathcal{G}_c^\dagger | \mathbf{q}) (\bar{\mathbf{k}}_2 | \mathcal{G}_b^\dagger | \mathbf{k}) \rangle, \end{aligned} \quad (3.51)$$

Here we have neglected some process-dependent color factors, again see [3] for more details.

The two-point function $S^{(2)}$ describes the broadening of the parent parton before the splitting. The splitting itself is encoded in the three-point function $S^{(3)}$. Lastly, the four-point function $S^{(4)}$ describes the evolution and broadening of the two-parton system

after the splitting has happened. In general one can calculate $S^{(2)}$ and $S^{(3)}$ analytically. However, the four-point function $S^{(4)}$ poses a challenge.

We have already shown that the 2-point function is given by Eqs. (3.37) and (3.45).

In [3] we showed that one can use conservation of energy to simplify the three-point and four-point functions to

$$(\mathbf{k}_2, \mathbf{q}_2; \bar{\mathbf{p}}_2 | S^{(3)}(t_2, t_1) | \mathbf{k}_1, \mathbf{p}_1 - \mathbf{k}_1; \bar{\mathbf{p}}_1) = (2\pi)^2 \delta(\mathbf{p}_1 - \bar{\mathbf{p}}_1) S^{(3)}(\mathbf{k}_2 - z\bar{\mathbf{p}}_2, \mathbf{k}_1 - z\mathbf{p}_1, \mathbf{p}_1 - \bar{\mathbf{p}}_2 | t_2, t_1), \quad (3.52)$$

and

$$\begin{aligned} (\mathbf{k}, \mathbf{q}; \mathbf{k}, \mathbf{q} | S^{(4)}(t_\infty, t_2) | \mathbf{k}_2, \mathbf{q}_2; \bar{\mathbf{k}}_2, \bar{\mathbf{p}}_2 - \bar{\mathbf{k}}_2) = \\ \equiv (2\pi)^2 \delta^2(\mathbf{q}_2 + \mathbf{k}_2 - \bar{\mathbf{p}}_2) S^{(4)}((1-z)\mathbf{k} - z\mathbf{q}, \mathbf{k}_2 - z\bar{\mathbf{p}}_2, \bar{\mathbf{k}}_2 - z\bar{\mathbf{p}}_2, \bar{\mathbf{p}}_2 - \mathbf{k} - \mathbf{q} | t_\infty, t_2). \end{aligned} \quad (3.53)$$

Then you end up with

$$\begin{aligned} \mathcal{P}_2(\mathbf{p}, \mathbf{P}; \mathbf{p}_0) = \frac{g^2}{z(1-z)E^2} P_{a \rightarrow bc}(z) \text{Re} \int_0^\infty dt_1 \int_{t_1}^\infty dt_2 \\ \times \int_{\mathbf{p}_1 l_1 l_2 \bar{\mathbf{p}}_2 \bar{l}_2} \mathbf{l}_1 \cdot \bar{\mathbf{l}}_2 S^{(4)}(\mathbf{p}, l_2, \bar{l}_2, \bar{\mathbf{p}}_2 - \mathbf{P} | t_\infty, t_2) \\ \times S^{(3)}(l_2, l_1, \mathbf{p}_1 - \bar{\mathbf{p}}_2 | t_2, t_1) \mathcal{P}(\mathbf{p}_1 - \mathbf{p}_0 | t_1, t_0). \end{aligned} \quad (3.54)$$

Here we have changed momentum variables to $l_1 = \mathbf{k}_1 - z\mathbf{p}_1$, $l_2 = \mathbf{k}_2 - z\bar{\mathbf{p}}_2$, $\bar{l}_2 = \bar{\mathbf{k}}_2 - z\bar{\mathbf{p}}_2$, $\mathbf{p} = (1-z)\mathbf{k} - z\mathbf{q}$ and $\mathbf{P} = \mathbf{q} + \mathbf{k}$. Usually, we are not interested in the total momentum \mathbf{P} , in which case this can be integrated out. This simplifies the expression to

$$\begin{aligned} \mathcal{P}_2(\mathbf{p}) = \int_{\mathbf{P}} \mathcal{P}_2(\mathbf{p}, \mathbf{P}; \mathbf{p}_0) = \frac{g^2}{z(1-z)E^2} P_{a \rightarrow bc}(z) \text{Re} \int_0^\infty dt_1 \int_{t_1}^\infty dt_2 \\ \times \int_{l_1 l_2 \bar{l}_2} \mathbf{l}_1 \cdot \bar{\mathbf{l}}_2 \mathcal{Q}(\mathbf{p}, l_2, \bar{l}_2 | t_\infty, t_2) \mathcal{K}(l_2, l_1 | t_2, t_1). \end{aligned} \quad (3.55)$$

Here we have introduced the splitting kernel $\mathcal{K}(l_2, l_1 | t_2, t_1) \equiv \int_{\bar{\mathbf{p}}_2} S^{(3)}(l_2, l_1, \mathbf{p}_1 - \bar{\mathbf{p}}_2 | t_2, t_1)$ and the quadrupole $\mathcal{Q}(\mathbf{p}, l_2, \bar{l}_2 | t_\infty, t_2) \equiv \int_{\mathbf{P}} S^{(4)}(\mathbf{p}, l_2, \bar{l}_2, \bar{\mathbf{p}}_2 - \mathbf{P} | t_\infty, t_2)$, and used that $\int_{\mathbf{p}_1} \mathcal{P}(\mathbf{p}_1 - \mathbf{p}_0 | t_1, t_0) = 1$.

It is convenient to write the differential cross section defined in (3.49) using these variables

$$\frac{d\sigma}{d\Omega_q d\Omega_k} = (2\pi)^6 4z(1-z)E \frac{d\sigma}{dz dE d^2\mathbf{p} d^2\mathbf{P}} \quad (3.56)$$

After integrating out \mathbf{P} the splitting function \mathcal{P}_2 does not depend on the initial transverse

momentum \mathbf{p}_0 anymore, so the right-hand side of (3.49) can be simplified. The emission spectrum $\frac{dI}{dzd^2\mathbf{p}}$ is then given in terms of the splitting function as

$$\begin{aligned} (2\pi)^2 \frac{dI}{dzd^2\mathbf{p}} &= \frac{1}{4\pi z(1-z)} \mathcal{P}_2(\mathbf{p}) \\ &= \frac{\alpha_s}{\omega^2} P_{a \rightarrow bc}(z) \text{Re} \int_0^\infty dt_1 \int_{t_1}^\infty dt_2 \int_{\mathbf{l}_1 \mathbf{l}_2 \bar{\mathbf{l}}_2} \mathbf{l}_1 \cdot \bar{\mathbf{l}}_2 \mathcal{Q}(\mathbf{p}, \mathbf{l}_2, \bar{\mathbf{l}}_2 | t_\infty, t_2) \mathcal{K}(\mathbf{l}_2, \mathbf{l}_1 | t_2, t_1), \end{aligned} \quad (3.57)$$

where we have defined $\omega \equiv z(1-z)E$ and

$$\frac{dI}{dzd^2\mathbf{p}} = \frac{d\sigma}{dzdE d^2\mathbf{p}} \bigg/ \frac{d\sigma_0}{dE} \quad (3.58)$$

The main result in [3] was solving (3.57) numerically. It was done in position space, where it is

$$\begin{aligned} (2\pi)^2 \frac{dI}{dzd^2\mathbf{p}} &= \frac{\alpha_s}{\omega^2} P_{a \rightarrow bc}(z) \text{Re} \int_0^\infty dt_1 \int_{t_1}^\infty dt_2 \\ &\quad \times \int_{\mathbf{u}_2 \bar{\mathbf{u}}_2} e^{-i(\mathbf{u}-\bar{\mathbf{u}})\cdot\mathbf{p}} (\partial_{\mathbf{u}_1} \cdot \partial_{\bar{\mathbf{u}}_2}) \mathcal{Q}(\mathbf{u}, \bar{\mathbf{u}}, \mathbf{u}_2, \bar{\mathbf{u}}_2 | t_\infty, t_2) \mathcal{K}(\mathbf{u}_2, \mathbf{u}_1 | t_2, t_1) \Big|_{\mathbf{u}_1 = \bar{\mathbf{u}}_2 = 0}. \end{aligned} \quad (3.59)$$

In position space the quadrupole and splitting kernel are given as path integrals

$$\mathcal{Q}(\mathbf{u}_f, \bar{\mathbf{u}}_f, \mathbf{u}_2, \bar{\mathbf{u}}_2 | t_f, t_2) = \int_{\mathbf{u}_2}^{\mathbf{u}_f} \mathcal{D}\mathbf{u} \int_{\bar{\mathbf{u}}_2}^{\bar{\mathbf{u}}_f} \mathcal{D}\bar{\mathbf{u}} e^{i\frac{\omega}{2} \int_{t_2}^{t_f} ds (\dot{\mathbf{u}}^2 - \dot{\bar{\mathbf{u}}}^2)} \mathcal{C}^{(4)}(\mathbf{u}, \bar{\mathbf{u}}), \quad (3.60)$$

$$\mathcal{K}(\mathbf{u}_2, \mathbf{u}_1 | t_2, t_1) = \int_{\mathbf{u}_1}^{\mathbf{u}_2} \mathcal{D}\mathbf{u} e^{i\frac{\omega}{2} \int_{t_1}^{t_2} ds \dot{\mathbf{u}}^2} \mathcal{C}^{(3)}(\mathbf{u}). \quad (3.61)$$

The potential terms $\mathcal{C}^{(n)}$ are correlators of Wilson lines

$$\begin{aligned} \mathcal{C}^{(3)} &\sim \langle V_b V_c V_a^\dagger \rangle \\ \mathcal{C}^{(4)} &\sim \langle V_b V_c V_c^\dagger V_b^\dagger \rangle. \end{aligned} \quad (3.62)$$

Again, these include some process-dependent color factors that we have omitted. The three-point correlator has an analytic solution

$$\mathcal{C}^{(3)}(\mathbf{u} | t_2, t_1) = e^{-\int_{t_1}^{t_2} ds v_{ba}(\mathbf{u})}, \quad (3.63)$$

where the potential $v_{ba}(\mathbf{u})$ for a splitting process $a \rightarrow bc$ is given by

$$v_{ba}(\mathbf{r}, t) = n(t) \left[\frac{C_{cba}}{2} \sigma(\mathbf{r}, t) + \frac{C_{acb}}{2} \sigma(z\mathbf{r}, t) + \frac{C_{bac}}{2} \sigma((1-z)\mathbf{r}, t) \right]. \quad (3.64)$$

The color factors are $C_{cba} \equiv C_c + C_b - C_a$ and they can be C_F for quarks and C_A for gluons.

In [3] we showed that if we define the object

$$F(\mathbf{u}, \bar{\mathbf{u}}|t) = \int_0^t dt_2 \int_0^{t_2} dt_1 \int_{\mathbf{u}_2} \times (\partial_{\mathbf{u}_1} \cdot \partial_{\bar{\mathbf{u}}_2}) \mathcal{Q}(\mathbf{u}, \bar{\mathbf{u}}, \mathbf{u}_2, \bar{\mathbf{u}}_2|t, t_2) \mathcal{K}(\mathbf{u}_2, \mathbf{u}_1|t_2, t_1) \Big|_{\mathbf{u}_1=\bar{\mathbf{u}}_2=0}, \quad (3.65)$$

then this can be solved through a Schrödinger equation

$$\left[i\delta_{ij} \frac{\partial}{\partial t} + \delta_{ij} \frac{\partial_{\mathbf{u}}^2 - \partial_{\bar{\mathbf{u}}}^2}{2\omega} - i\mathbb{M}_{ij}(\mathbf{u}, \bar{\mathbf{u}}) \right] F_j(\mathbf{u}, \bar{\mathbf{u}}|t) = -i\mathbf{1}_i \partial_{\bar{\mathbf{u}}} \delta^2(\bar{\mathbf{u}}) \cdot \partial_{\mathbf{u}_1} \int_0^L dt_1 \mathcal{K}(\mathbf{u}, \mathbf{u}_1|L, t_1) \Big|_{\mathbf{u}_1=0}, \quad (3.66)$$

where the sum goes over all the possible color states of the quadrupole, and $\mathbf{1}_i = [1, 1, \dots, 1]$. The matrix potential \mathbb{M} relates all the different color states and can be calculated using the method derived in [1].

The splitting kernel \mathcal{K} is given by Eqs. (3.61) and (3.63), and can be calculated directly for a potential v_{ba} . This is certainly not trivial for a realistic potential. We will study this calculation in detail in Sec. 3.3.

Compared to the splitting kernel the quadrupole is a much more complicated object to calculate analytically. We will therefore spend the rest of this section showing how the quadrupole can be simplified, using the large- N_c limit as help.

3.2.1 The quadrupole at large- N_c

The quadrupole describes the evolution and broadening of the two-parton system after the splitting has happened. When the two-parton system is created the two partons are connected in color. The two partons will then interact with the medium, and we expect that after some time has passed they will have lost their color connection completely through the medium interactions. This is referred to as color decoherence [63]. After the two partons have decohered they will broaden independently, so one would expect that after a long time, the quadrupole will become a product of two broadening functions $\mathcal{Q} \rightarrow$

\mathcal{PP} . However, the situation is more complicated just after the splitting has occurred.

In this section, we will see that the quadrupole can indeed be written as a sum of two terms, where the first describes the independent broadening and the second describes the decoherence process. The two terms are usually called the factorizable and non-factorizable pieces $\mathcal{Q} = \mathcal{Q}^{\text{fac}} + \mathcal{Q}^{\text{non-fac}}$ [59]. We will do this using the large- N_c limit, where the calculations simplify and you can get analytical results.

Going back to (3.50) and taking the Fourier transform of the four-point function you get

$$\begin{aligned}
& (\mathbf{k}, \mathbf{q}; \mathbf{k}, \mathbf{q} | S^{(4)}(t_\infty, t_2) | \mathbf{k}_2, \mathbf{q}_2; \bar{\mathbf{k}}_2, \bar{\mathbf{p}}_2 - \bar{\mathbf{k}}_2) = \\
& \int_{\mathbf{x}_2 \mathbf{y}_2 \bar{\mathbf{y}}_2 \bar{\mathbf{x}}_2 \mathbf{x} \mathbf{y} \bar{\mathbf{y}} \bar{\mathbf{x}}} e^{i\mathbf{k}_2 \cdot \mathbf{x}_2 - i\bar{\mathbf{k}}_2 \cdot \bar{\mathbf{x}}_2 + i\mathbf{q}_2 \cdot \mathbf{y}_2 - i(\bar{\mathbf{p}}_2 - \bar{\mathbf{k}}_2) \cdot \bar{\mathbf{y}}_2 - i\mathbf{k} \cdot (\mathbf{x} - \bar{\mathbf{x}}) - i\mathbf{q} \cdot (\mathbf{y} - \bar{\mathbf{y}})} \\
& \times (\mathbf{x}, \mathbf{y}; \bar{\mathbf{x}}, \bar{\mathbf{y}} | S^{(4)}(t_\infty, t_2) | \mathbf{x}_2, \mathbf{y}_2; \bar{\mathbf{x}}_2, \bar{\mathbf{y}}_2).
\end{aligned} \tag{3.67}$$

In position space the four-point function is given as a path integral

$$\begin{aligned}
& (\mathbf{x}, \mathbf{y}; \bar{\mathbf{x}}, \bar{\mathbf{y}} | S^{(4)}(t_\infty, t_2) | \mathbf{x}_2, \mathbf{y}_2; \bar{\mathbf{x}}_2, \bar{\mathbf{y}}_2) \\
& = \int_{\mathbf{x}_2}^{\mathbf{x}} \mathcal{D}\mathbf{r}_1 \int_{\mathbf{y}_2}^{\mathbf{y}} \mathcal{D}\mathbf{r}_2 \int_{\bar{\mathbf{y}}_2}^{\bar{\mathbf{y}}} \mathcal{D}\bar{\mathbf{r}}_2 \int_{\bar{\mathbf{x}}_2}^{\bar{\mathbf{x}}} \mathcal{D}\bar{\mathbf{r}}_1 e^{i\frac{E}{2} \int_{t_2}^{\infty} ds [z(\hat{r}_1^2 - \hat{r}_1^2) + (1-z)(\hat{r}_2^2 - \hat{r}_2^2)]} \mathcal{C}^{(4)}(\mathbf{r}_1, \mathbf{r}_2, \bar{\mathbf{r}}_2, \bar{\mathbf{r}}_1).
\end{aligned} \tag{3.68}$$

We will now be more specific, and consider three processes: a photon splitting into a quark-antiquark pair, a quark emitting a gluon, and a gluon emitting a gluon. In terms of fundamental Wilson lines the correlators $\mathcal{C}^{(4)}$ for these processes are

$$\begin{aligned}
\gamma \rightarrow q\bar{q} : \quad \mathcal{C}_{q\bar{q}}^4 &= \frac{1}{N_c} \langle \text{tr}[V_1 V_2^\dagger V_2 V_1^\dagger] \rangle \\
q \rightarrow qg : \quad \mathcal{C}_{gq}^{(4)} &= \frac{1}{N_c^2 - 1} \langle \text{tr}[V_1^\dagger V_1 V_2^\dagger V_2] \text{tr}[V_2^\dagger V_2] - \frac{1}{N_c} \text{tr}[V_1^\dagger V_1] \rangle \\
g \rightarrow gg : \quad \mathcal{C}_{gg}^4 &= \frac{1}{N_c(N_c^2 - 1)} \langle \text{tr}[V_1^\dagger V_1] \text{tr}[V_2^\dagger V_2 V_1^\dagger V_1] \text{tr}[V_2^\dagger V_2] - \text{tr}[V_1^\dagger V_1 V_2^\dagger V_2 V_1^\dagger V_1 V_2^\dagger V_2] \rangle.
\end{aligned} \tag{3.69}$$

The main result of [1] was finding a general method of calculating such Wilson line correlators at finite N_c , and showing how they simplify in the large- N_c limit. After using

the large- N_c approximation this becomes

$$\begin{aligned}
\gamma \rightarrow q\bar{q} : \quad \mathcal{C}_{q\bar{q}}^4 &= \frac{1}{N_c} \langle \text{tr}[V_1 V_2^\dagger V_2 V_1^\dagger] \rangle \\
q \rightarrow qg : \quad \mathcal{C}_{qq}^{(4)} &\simeq \frac{1}{N_c^2} \langle \text{tr}[V_1 V_2^\dagger V_2 V_1^\dagger] \rangle \langle \text{tr}[V_2^\dagger V_2] \rangle \\
g \rightarrow gg : \quad \mathcal{C}_{gg}^4 &\simeq \frac{1}{N_c^3} \langle \text{tr}[V_1^\dagger V_1] \rangle \langle \text{tr}[V_1 V_2^\dagger V_2 V_1^\dagger] \rangle \langle \text{tr}[V_2^\dagger V_2] \rangle.
\end{aligned} \tag{3.70}$$

Notice how they all contain the same quadrupole $1/N_c \langle \text{tr}[V_1 V_2^\dagger V_2 V_1^\dagger] \rangle$. The two latter ones also contain dipoles, given in (3.42). In the large- N_c the dipoles are

$$\begin{aligned}
\mathcal{P}_F(\mathbf{r}_1 - \mathbf{r}_2 | t_\infty, t_2) &= \frac{1}{N_c} \langle \text{tr}[V_1 V_2^\dagger] \rangle \\
&\simeq e^{-\frac{N_c}{2} \int_{t_2}^\infty ds n(s) \sigma(\mathbf{r}_1 - \mathbf{r}_2)}.
\end{aligned} \tag{3.71}$$

We have added the subscript F to indicate that these are fundamental Wilson lines. In the large- N_c limit the quadrupole can be written as the sum of two terms[1, 59], namely

$$\begin{aligned}
\frac{1}{N_c} \langle \text{tr}[V_1 V_2^\dagger V_2 V_1^\dagger] \rangle &\simeq \mathcal{P}_F(\mathbf{r}_1 - \mathbf{r}_1 | t_\infty, t_2) \mathcal{P}_F(\mathbf{r}_2 - \mathbf{r}_2 | t_\infty, t_2) \\
&+ \int_{t_2}^\infty ds \mathcal{P}_F(\mathbf{r}_1 - \mathbf{r}_1 | t_\infty, s) \mathcal{P}_F(\mathbf{r}_2 - \mathbf{r}_2 | t_\infty, s) T(s) \mathcal{P}_F(\mathbf{r}_1 - \mathbf{r}_2 | s, t_2) \mathcal{P}_F(\mathbf{r}_1 - \mathbf{r}_2 | s, t_2),
\end{aligned} \tag{3.72}$$

where we have used the transition term $T(s) = -N_c n(s)/2[\sigma_{12} + \sigma_{\bar{1}\bar{2}} - \sigma_{1\bar{2}} - \sigma_{\bar{1}2}]$. These two terms constitute the so-called factorizable and non-factorizable pieces.

The factorizable piece

Using the fact that in the large- N_c we have $\mathcal{P}_A(\mathbf{r}_1 - \mathbf{r}_1 | t_\infty, t_2) = (\mathcal{P}_F(\mathbf{r}_1 - \mathbf{r}_1 | t_\infty, t_2))^2$, one can plug this into (3.70) and see that for all three processes the factorizable part becomes

$$\mathcal{C}_{ba,\text{fac}}^{(4)} = \mathcal{P}_b(\mathbf{r}_1 - \mathbf{r}_1 | t_\infty, t_2) \mathcal{P}_c(\mathbf{r}_2 - \mathbf{r}_2 | t_\infty, t_2). \tag{3.73}$$

Inserting this into (3.68) the four-point function separates into a product of a pair of two-point functions

$$\begin{aligned}
(\mathbf{x}, \mathbf{y}; \bar{\mathbf{x}}, \bar{\mathbf{y}} | S_{\text{fac}}^{(4)}(t_\infty, t_2) | \mathbf{x}_2, \mathbf{y}_2; \bar{\mathbf{x}}_2, \bar{\mathbf{y}}_2) &= (\mathbf{x}; \bar{\mathbf{x}} | S^2(t_\infty - t_2) | \mathbf{x}_2; \bar{\mathbf{x}}_2) \\
&\times (\mathbf{y}; \bar{\mathbf{y}} | S^2(t_\infty - t_2) | \mathbf{y}_2; \bar{\mathbf{y}}_2),
\end{aligned} \tag{3.74}$$

where the two-point functions are given in terms of path integrals (3.43). These we have already solved, see (3.43). The results from that section can then be used here, and we

get, in momentum space

$$\begin{aligned}
(\mathbf{k}, \mathbf{q}; \mathbf{k}, \mathbf{q} | S_{\text{fac}}^{(4)}(t_\infty, t_2) | \mathbf{k}_2, \mathbf{q}_2; \bar{\mathbf{k}}_2, \bar{\mathbf{p}}_2 - \bar{\mathbf{k}}_2) &= (2\pi)^4 \delta(\bar{\mathbf{k}}_2 - \mathbf{k}_2) \delta(\mathbf{q}_2 - (\bar{\mathbf{p}}_2 - \bar{\mathbf{k}}_2)) \\
&\times \mathcal{P}(\mathbf{k} - \mathbf{k}_2 | t_\infty, t_2) \mathcal{P}(\mathbf{q} - (\bar{\mathbf{p}}_2 - \bar{\mathbf{k}}_2) | t_\infty, t_2).
\end{aligned} \tag{3.75}$$

Inserting the simplified four-point function into (3.50), and following the same steps we end up with a simplified version of (3.54)

$$\begin{aligned}
\mathcal{P}_{2,\text{fac}}(\mathbf{p}, \mathbf{P}; \mathbf{p}_0) &= \frac{g^2}{z(1-z)E^2} P_{a \rightarrow bc}(z) \text{Re} \int_0^\infty dt_1 \int_{t_1}^\infty dt_2 \\
&\times \int_{\mathbf{p}_1 t_1 t_2 \bar{\mathbf{p}}_2} \mathbf{l}_1 \cdot \mathbf{l}_2 \mathcal{P}(z(\mathbf{P} - \bar{\mathbf{p}}_2) + \mathbf{p} - \mathbf{l}_2 | t_\infty, t_2) \mathcal{P}((1-z)(\mathbf{P} - \bar{\mathbf{p}}_2) - (\mathbf{p} - \mathbf{l}_2) | t_\infty, t_2) \\
&\times S^{(3)}(\mathbf{l}_2, \mathbf{l}_1, \mathbf{p}_1 - \bar{\mathbf{p}}_2 | t_2, t_1) \mathcal{P}(\mathbf{p}_1 - \mathbf{p}_0 | t_1, t_0).
\end{aligned} \tag{3.76}$$

If we are not interested in the total transverse momentum \mathbf{P} and integrate it out we get the emission spectrum

$$\begin{aligned}
(2\pi)^2 \frac{dI_{\text{fac}}}{dz d^2\mathbf{p}} &= \frac{\alpha_s}{\omega^2} P_{a \rightarrow bc}(z) \text{Re} \int_0^\infty dt_1 \int_{t_1}^\infty dt_2 \\
&\times \int_{\mathbf{l}_1 \mathbf{l}_2} \mathbf{l}_1 \cdot \mathbf{l}_2 \int_{\mathbf{u}} e^{-i(\mathbf{p} - \mathbf{l}_2) \cdot \mathbf{u}} \mathcal{P}(z\mathbf{u} | t_\infty, t_2) \mathcal{P}((1-z)\mathbf{u} | t_\infty, t_2) \mathcal{K}(\mathbf{l}_2, \mathbf{l}_1 | t_2, t_1).
\end{aligned} \tag{3.77}$$

It is clear that keeping only the factorizable piece of the four-point function is equivalent to saying that the two partons decohere immediately after the splitting, and broaden independently. Comparing this to (3.57) we see that in general the factorizable part of the four-point function is

$$\begin{aligned}
\mathcal{Q}_{\text{fac}}(\mathbf{p}, \mathbf{l}_2, \bar{\mathbf{l}}_2 | t_\infty, t_2) &= (2\pi)^2 \delta(\mathbf{l}_2 - \bar{\mathbf{l}}_2) \int_{\mathbf{u}} e^{-i(\mathbf{p} - \mathbf{l}_2) \cdot \mathbf{u}} \mathcal{P}(z\mathbf{u} | t_\infty, t_2) \mathcal{P}((1-z)\mathbf{u} | t_\infty, t_2) \\
&\equiv (2\pi)^2 \delta(\mathbf{l}_2 - \bar{\mathbf{l}}_2) \mathcal{P}_{\text{eff}}(\mathbf{p} - \mathbf{l}_2 | t_\infty, t_2).
\end{aligned} \tag{3.78}$$

In the last step we have defined the effective broadening function of the two-parton system \mathcal{P}_{eff} .

Let us consider the case of a gluon emitting a soft gluon, so $z \ll 1$. Then $\omega = z(1-z)E \simeq zE$ and the gluon splitting function becomes $P_{g \rightarrow gg}(z) \simeq 2N_c/z$. The 2 is a symmetry factor that comes from the fact that both $z \rightarrow 0$ and $z \rightarrow 1$ must be counted as a soft gluon emission.

In the soft limit the two broadening factors in (3.77) reduce to one broadening function

$$\begin{aligned} \int_{\mathbf{u}} e^{-i(\mathbf{p}-\mathbf{l}_2)\cdot\mathbf{u}} \mathcal{P}(z\mathbf{u}|t_\infty, t_2) \mathcal{P}((1-z)\mathbf{u}|t_\infty, t_2) &\simeq \int_{\mathbf{u}} e^{-i(\mathbf{p}-\mathbf{l}_2)\cdot\mathbf{u}} \mathcal{P}(\mathbf{u}|t_\infty, t_2) \\ &= \mathcal{P}(\mathbf{p}-\mathbf{l}_2|t_\infty, t_2). \end{aligned} \quad (3.79)$$

The emission spectrum in the soft limit is then

$$(2\pi)^2 \omega \frac{dI}{d\omega d^2\mathbf{p}} = \frac{2\pi\bar{\alpha}}{\omega^2} \text{Re} \int_0^\infty dt_1 \int_{t_1}^\infty dt_2 \int_{l_1 l_2} \mathbf{l}_1 \cdot \mathbf{l}_2 \mathcal{P}(\mathbf{p}-\mathbf{l}_2|t_\infty, t_2) \mathcal{K}(\mathbf{l}_2, \mathbf{l}_1|t_2, t_1). \quad (3.80)$$

We see that in this limit the only remaining contribution from the 4-point function is a broadening factor after the splitting has happened. As we shall see the non-factorizable term is negligible in the soft limit, and it does not contribute to (3.80).

The non-factorizable piece

In most calculations it is common to drop the non-factorizable term and keep only the factorizable one. This cannot be done on the basis of the large- N_c limit, as both terms are of the same order of N_c . However, it was argued in [59] that the non-factorizable piece can be neglected as long as the formation time is much smaller than the length of the medium $t_f/L \ll 1$, where $t_f = \sqrt{2\omega/\hat{q}}$. A large part of our work in [3] was calculating both terms numerically, and figuring out whether it is safe to drop the non-factorizable piece. Here we found that the relation governing the size of the non-factorizable term seems to be more complicated than previously thought, and that the non-factorizable piece can be important even when the medium is big.

We will now show the calculation of the non-factorizable piece. Comparing Eqs. (3.70) and (3.72) we see that the non-factorizable part of the four-point correlator is

$$\mathcal{C}_{ba, \text{non-fac}}^{(4)} = \int_{t_2}^\infty dt_3 \mathcal{P}_b(\mathbf{r}_1 - \mathbf{r}_1|t_\infty, t_3) \mathcal{P}_c(\mathbf{r}_2 - \mathbf{r}_2|t_\infty, t_3) T(t_3) e^{-C_F \int_{t_2}^{t_3} ds n(s) \sigma_{\text{eff}}(s)}. \quad (3.81)$$

The transition function is really a function of all the positions

$$T(\mathbf{r}_1, \mathbf{r}_2, \mathbf{r}_1, \mathbf{r}_2|t_3) = -\frac{N_c}{2} n(t_3) [\sigma(\mathbf{r}_1 - \mathbf{r}_2) + \sigma(\mathbf{r}_1 - \mathbf{r}_2) - \sigma(\mathbf{r}_1 - \mathbf{r}_2) - \sigma(\mathbf{r}_1 - \mathbf{r}_2)]. \quad (3.82)$$

The effective potential $\sigma_{\text{eff}}(s)$ is different for all three processes, and also depends on all

the positions

$$\begin{aligned}
\gamma \rightarrow q\bar{q}: \quad \sigma_{\text{eff}}(\mathbf{r}_1, \mathbf{r}_2, \mathbf{r}_1, \mathbf{r}_2|t_3) &= \sigma(\mathbf{r}_1 - \mathbf{r}_2) + \sigma(\mathbf{r}_1 - \mathbf{r}_2) \\
q \rightarrow qg: \quad \sigma_{\text{eff}}(\mathbf{r}_1, \mathbf{r}_2, \mathbf{r}_1, \mathbf{r}_2|t_3) &= \sigma(\mathbf{r}_1 - \mathbf{r}_2) + \sigma(\mathbf{r}_1 - \mathbf{r}_2) + \sigma(\mathbf{r}_2 - \mathbf{r}_2) \\
g \rightarrow gg: \quad \sigma_{\text{eff}}(\mathbf{r}_1, \mathbf{r}_2, \mathbf{r}_1, \mathbf{r}_2|t_3) &= \sigma(\mathbf{r}_1 - \mathbf{r}_2) + \sigma(\mathbf{r}_1 - \mathbf{r}_2) + \sigma(\mathbf{r}_2 - \mathbf{r}_2) + \sigma(\mathbf{r}_1 - \mathbf{r}_1).
\end{aligned} \tag{3.83}$$

This can be inserted into (3.68) to get

$$\begin{aligned}
(\mathbf{x}, \mathbf{y}; \bar{\mathbf{x}}, \bar{\mathbf{y}}|S_{\text{non-fac}}^{(4)}(t_\infty, t_2)|\mathbf{x}_2, \mathbf{y}_2; \bar{\mathbf{x}}_2, \bar{\mathbf{y}}_2) &= \int_{t_2}^{\infty} dt_3 \int_{\mathbf{x}_3 \mathbf{y}_3 \bar{\mathbf{x}}_3 \bar{\mathbf{y}}_3} \\
&\times (\mathbf{x}; \bar{\mathbf{x}}|S^2(t_\infty - t_3)|\mathbf{x}_3; \bar{\mathbf{x}}_3)(\mathbf{y}; \bar{\mathbf{y}}|S^2(t_\infty - t_3)|\mathbf{y}_3; \bar{\mathbf{y}}_3) \\
&\times T(t_3) \int_{\mathbf{x}_2}^{\mathbf{x}_3} \mathcal{D}\mathbf{r}_1 \int_{\mathbf{y}_2}^{\mathbf{y}_3} \mathcal{D}\mathbf{r}_2 \int_{\bar{\mathbf{y}}_2}^{\bar{\mathbf{y}}_3} \mathcal{D}\bar{\mathbf{r}}_2 \int_{\bar{\mathbf{x}}_2}^{\bar{\mathbf{x}}_3} \mathcal{D}\bar{\mathbf{r}}_1 e^{i \int_{t_2}^{t_3} ds \left[\frac{zE}{2} (\dot{\mathbf{r}}_1^2 - \dot{\mathbf{r}}_2^2) + \frac{(1-z)E}{2} (\dot{\mathbf{r}}_2^2 - \dot{\mathbf{r}}_3^2) + iC_F n(s) \sigma_{\text{eff}}(s) \right]}.
\end{aligned} \tag{3.84}$$

Here we have introduced the intermediate positions \mathbf{x}_3 etc. at time t_3 , which divide up the path integrals.

We actually want this in momentum space, given in (3.67). The derivation is quite complicated, and we refer to App. B for details.

In the end, the non-factorizable quadrupole becomes

$$\begin{aligned}
\mathcal{Q}_{\text{non-fac}}(\mathbf{p}, \mathbf{l}_2, \bar{\mathbf{l}}_2|t_\infty, t_2) &= \int_{t_2}^{\infty} dt_3 \int_{\mathbf{u}_3 \bar{\mathbf{u}}_3} e^{-i\mathbf{p} \cdot (\mathbf{u}_3 - \bar{\mathbf{u}}_3)} \\
&\times \mathcal{P}(z(\mathbf{u}_3 - \bar{\mathbf{u}}_3)|t_\infty, t_3) \mathcal{P}((1-z)(\mathbf{u}_3 - \bar{\mathbf{u}}_3)|t_\infty, t_3) \\
&\times T(\mathbf{u}_3, \bar{\mathbf{u}}_3|t_3) \int_{\mathbf{u}_2 \bar{\mathbf{u}}_2} e^{i\mathbf{u}_2 \cdot \mathbf{l}_2 - i\bar{\mathbf{u}}_2 \cdot \bar{\mathbf{l}}_2} \int_{\mathbf{u}_2}^{\mathbf{u}_3} \mathcal{D}\mathbf{u} \int_{\bar{\mathbf{u}}_2}^{\bar{\mathbf{u}}_3} \mathcal{D}\bar{\mathbf{u}} e^{i \int_{t_2}^{t_3} ds \left[\frac{z}{2} (\dot{\mathbf{u}}^2 - \dot{\bar{\mathbf{u}}}^2) + iC_F n(s) \sigma_{\text{eff}}(s) \right]}.
\end{aligned} \tag{3.85}$$

In these coordinates the transition function is

$$T(\mathbf{u}_3, \bar{\mathbf{u}}_3|t_3) = -\frac{N_c}{2} n(t_3) [\sigma(\mathbf{u}_3) + \sigma(\bar{\mathbf{u}}_3) - \sigma((1-z)\mathbf{u}_3 + z\bar{\mathbf{u}}_3) - \sigma(z\mathbf{u}_3 + (1-z)\bar{\mathbf{u}}_3)]. \tag{3.86}$$

From this, it is clear that in the soft limit $z \rightarrow 0$ we have $T(t_3) \rightarrow 0$, and the non-factorizable term becomes insignificant. This proves that the soft emission spectrum (3.80) is accurate in the soft and large- N_c limits.

Likewise, the effective potential in these coordinates is

$$\begin{aligned}
\gamma \rightarrow q\bar{q}: \quad \sigma_{\text{eff}}(\mathbf{u}, \bar{\mathbf{u}}|t_3) &= \sigma(\mathbf{u}) + \sigma(\bar{\mathbf{u}}) \\
q \rightarrow qg: \quad \sigma_{\text{eff}}(\mathbf{u}, \bar{\mathbf{u}}|t_3) &= \sigma(\mathbf{u}) + \sigma(\bar{\mathbf{u}}) + \sigma(z(\bar{\mathbf{u}} - \mathbf{u})) \\
g \rightarrow gg: \quad \sigma_{\text{eff}}(\mathbf{u}, \bar{\mathbf{u}}|t_3) &= \sigma(\mathbf{u}) + \sigma(\bar{\mathbf{u}}) + \sigma(z(\bar{\mathbf{u}} - \mathbf{u})) + \sigma((1-z)(\mathbf{u} - \bar{\mathbf{u}})). \quad (3.87)
\end{aligned}$$

In the photon case the path integrals over \mathbf{u} and $\bar{\mathbf{u}}$ decouple and can be done. For the two other cases there is an interaction term between \mathbf{u} and $\bar{\mathbf{u}}$, making the path integrals more difficult.

The two remaining path integrals in (3.85) should be interpreted as an initial quadrupole that the system starts out in, before it transitions at the intermediate time t_3 .

$$\mathcal{Q}_{\text{initial}}(\mathbf{u}_3, \bar{\mathbf{u}}_3, \mathbf{u}_2, \bar{\mathbf{u}}_2|t_3, t_2) = \int_{\mathbf{u}_2}^{\mathbf{u}_3} \mathcal{D}\mathbf{u} \int_{\bar{\mathbf{u}}_2}^{\bar{\mathbf{u}}_3} \mathcal{D}\bar{\mathbf{u}} e^{i \int_{t_2}^{t_3} ds \left[\frac{g}{2}(\dot{\mathbf{u}}^2 - \dot{\bar{\mathbf{u}}}^2) + iC_{Fn}(s)\sigma_{\text{eff}}(s) \right]}. \quad (3.88)$$

After Fourier transforming, this is

$$\int_{\mathbf{u}_2 \bar{\mathbf{u}}_2} e^{i\mathbf{u}_2 \cdot \mathbf{l}_2 - i\bar{\mathbf{u}}_2 \cdot \bar{\mathbf{l}}_2} \mathcal{Q}_{\text{initial}}(\mathbf{u}_3, \bar{\mathbf{u}}_3, \mathbf{u}_2, \bar{\mathbf{u}}_2|t_3, t_2) = \int_{\mathbf{l}_3 \bar{\mathbf{l}}_3} e^{i\mathbf{u}_3 \cdot \mathbf{l}_3 - i\bar{\mathbf{u}}_3 \cdot \bar{\mathbf{l}}_3} \mathcal{Q}_{\text{initial}}(\mathbf{l}_3, \bar{\mathbf{l}}_3, \mathbf{l}_2, \bar{\mathbf{l}}_2|t_3, t_2). \quad (3.89)$$

Inserting this into (3.85) you get

$$\begin{aligned}
\mathcal{Q}_{\text{non-fac}}(\mathbf{p}, \mathbf{l}_2, \bar{\mathbf{l}}_2|t_\infty, t_2) &= \int_{t_2}^{\infty} dt_3 \int_{\mathbf{u}_3 \bar{\mathbf{u}}_3} \int_{\mathbf{l}_3 \bar{\mathbf{l}}_3} e^{-i(\mathbf{p} - \mathbf{l}_3) \cdot \mathbf{u}_3 + i(\mathbf{p} - \bar{\mathbf{l}}_3) \cdot \bar{\mathbf{u}}_3} \\
&\times \mathcal{P}(z(\mathbf{u}_3 - \bar{\mathbf{u}}_3)|t_\infty, t_3) \mathcal{P}((1-z)(\mathbf{u}_3 - \bar{\mathbf{u}}_3)|t_\infty, t_3) \\
&\times T(\mathbf{u}_3, \bar{\mathbf{u}}_3|t_3) \mathcal{Q}_{\text{initial}}(\mathbf{l}_3, \bar{\mathbf{l}}_3, \mathbf{l}_2, \bar{\mathbf{l}}_2|t_3, t_2). \quad (3.90)
\end{aligned}$$

The quadrupole $\mathcal{Q}_{\text{non-fac}}$ can be inserted into the emission spectrum (3.57) to get the contribution from the non-factorizable part of the large- N_c solution.

The system starts out at time t_2 in a system defined by the initial quadrupole. Then at time t_3 it switches configuration, described by the transition function $T(t_3)$. We see that after t_3 the system has decohered and reached the same structure as the factorizable piece, where the partons broaden independently.

This simplifies even further if we assume that the transition function T is only a function of the difference between the two coordinates, namely $T(\mathbf{u}_3 - \bar{\mathbf{u}}_3|t_3)$. This is the case for example in the harmonic oscillator approximation, so it is a relevant assumption. Then

we can change coordinates to $\mathbf{u} = \mathbf{u}_3 - \bar{\mathbf{u}}_3$ and $\mathbf{v} = 1/2(\mathbf{u}_3 + \bar{\mathbf{u}}_3)$, and get

$$\begin{aligned}
\mathcal{Q}_{\text{non-fac}}(\mathbf{p}, \mathbf{l}_2, \bar{\mathbf{l}}_2 | t_\infty, t_2) &= \int_{t_2}^{\infty} dt_3 \int_{\mathbf{u}\mathbf{v}} \int_{\mathbf{l}_3 \bar{\mathbf{l}}_3} e^{-i(\mathbf{p} - \frac{1}{2}[\mathbf{l}_3 + \bar{\mathbf{l}}_3]) \cdot \mathbf{u} + i(\mathbf{l}_3 - \bar{\mathbf{l}}_3) \cdot \mathbf{v}} \\
&\times \mathcal{P}(z\mathbf{u} | t_\infty, t_3) \mathcal{P}((1-z)\mathbf{u} | t_\infty, t_3) T(\mathbf{u} | t_3) \mathcal{Q}_{\text{initial}}(\mathbf{l}_3, \bar{\mathbf{l}}_3, \mathbf{l}_2, \bar{\mathbf{l}}_2 | t_3, t_2) \\
&= \int_{t_2}^{\infty} dt_3 \int_{\mathbf{l}_3 \bar{\mathbf{l}}_3} (2\pi)^2 \delta(\mathbf{l}_3 - \bar{\mathbf{l}}_3) \int_{\mathbf{u}} e^{-i(\mathbf{p} - \mathbf{l}_3) \cdot \mathbf{u}} \\
&\times \mathcal{P}(z\mathbf{u} | t_\infty, t_3) \mathcal{P}((1-z)\mathbf{u} | t_\infty, t_3) T(\mathbf{u} | t_3) \mathcal{Q}_{\text{initial}}(\mathbf{l}_3, \bar{\mathbf{l}}_3, \mathbf{l}_2, \bar{\mathbf{l}}_2 | t_3, t_2). \tag{3.91}
\end{aligned}$$

By comparing the first part of the last line to the factorizable quadrupole (3.78) we see that $\mathcal{Q}_{\text{non-fac}} \sim \mathcal{Q}_{\text{fac}} T \mathcal{Q}_{\text{initial}}$. After doing the last momentum integral you end up with only two remaining integrals

$$\begin{aligned}
\mathcal{Q}_{\text{non-fac}}(\mathbf{p}, \mathbf{l}_2, \bar{\mathbf{l}}_2 | t_\infty, t_2) &= \int_{t_2}^{\infty} dt_3 \int_{\mathbf{l}_3} \int_{\mathbf{u}} e^{-i(\mathbf{p} - \mathbf{l}_3) \cdot \mathbf{u}} \\
&\times \mathcal{P}(z\mathbf{u} | t_\infty, t_3) \mathcal{P}((1-z)\mathbf{u} | t_\infty, t_3) T(\mathbf{u} | t_3) \mathcal{Q}_{\text{initial}}(\mathbf{l}_3, \mathbf{l}_3, \mathbf{l}_2, \bar{\mathbf{l}}_2 | t_3, t_2). \tag{3.92}
\end{aligned}$$

This is still not in most cases simple to calculate, as the initial quadrupole generally has a somewhat complex form.

The energy spectrum

If we are not interested in the transverse momentum at all one can integrate out \mathbf{p} from (3.57), leading to the energy spectrum

$$\frac{dI}{dz} = \frac{\alpha_s}{\omega^2} P_{a \rightarrow bc}(z) \text{Re} \int_0^\infty dt_1 \int_{t_1}^\infty dt_2 \int_{\mathbf{p}} \int_{\mathbf{l}_1 \mathbf{l}_2 \bar{\mathbf{l}}_2} \mathbf{l}_1 \cdot \bar{\mathbf{l}}_2 \mathcal{Q}(\mathbf{p}, \mathbf{l}_2, \bar{\mathbf{l}}_2 | t_\infty, t_2) \mathcal{K}(\mathbf{l}_2, \mathbf{l}_1 | t_2, t_1). \tag{3.93}$$

One can check that $\int_{\mathbf{p}} \mathcal{Q}(\mathbf{p}, \mathbf{l}_2, \bar{\mathbf{l}}_2 | t_\infty, t_2) = (2\pi)^2 \delta(\mathbf{l}_2 - \bar{\mathbf{l}}_2)$. This is true both at finite N_c and in the large- N_c limit. We will now use our results to show this at large- N_c .

In the large- N_c limit we have seen that the quadrupole can be written as a sum of a factorizable and non-factorizable piece. We also derived the explicit expressions for these, in Eqs. (3.78) and (3.90). We will now see how these simplify after integrating out the

transverse momentum, starting with the factorizable part

$$\begin{aligned}
\int_{\mathbf{p}} \mathcal{Q}_{\text{fac}}(\mathbf{p}, \mathbf{l}_2, \bar{\mathbf{l}}_2 | t_\infty, t_2) &= (2\pi)^2 \delta(\mathbf{l}_2 - \bar{\mathbf{l}}_2) \int_{\mathbf{u}} \int_{\mathbf{p}} e^{-i(\mathbf{p}-\mathbf{l}_2)\cdot\mathbf{u}} \mathcal{P}(z\mathbf{u} | t_\infty, t_2) \mathcal{P}((1-z)\mathbf{u} | t_\infty, t_2) \\
&= (2\pi)^2 \delta(\mathbf{l}_2 - \bar{\mathbf{l}}_2) \int_{\mathbf{u}} \delta(\mathbf{u}) \mathcal{P}(z\mathbf{u} | t_\infty, t_2) \mathcal{P}((1-z)\mathbf{u} | t_\infty, t_2) \\
&= (2\pi)^2 \delta(\mathbf{l}_2 - \bar{\mathbf{l}}_2), \tag{3.94}
\end{aligned}$$

where we have used that $\mathcal{P}(0) = 1$.

Now let us look at the non-factorizable term

$$\begin{aligned}
\int_{\mathbf{p}} \mathcal{Q}_{\text{non-fac}}(\mathbf{p}, \mathbf{l}_2, \bar{\mathbf{l}}_2 | t_\infty, t_2) &= \int_{t_2}^{\infty} dt_3 \int_{\mathbf{u}_3 \bar{\mathbf{u}}_3} \int_{\mathbf{l}_3 \bar{\mathbf{l}}_3 \mathbf{p}} e^{-i(\mathbf{p}-\mathbf{l}_3)\cdot\mathbf{u}_3 + i(\mathbf{p}-\bar{\mathbf{l}}_3)\cdot\bar{\mathbf{u}}_3} \\
&\times \mathcal{P}(z(\mathbf{u}_3 - \bar{\mathbf{u}}_3) | t_\infty, t_3) \mathcal{P}((1-z)(\mathbf{u}_3 - \bar{\mathbf{u}}_3) | t_\infty, t_3) \\
&\times T(\mathbf{u}_3, \bar{\mathbf{u}}_3 | t_3) \mathcal{Q}_{\text{initial}}(\mathbf{l}_3, \bar{\mathbf{l}}_3, \mathbf{l}_2, \bar{\mathbf{l}}_2 | t_3, t_2) \\
&= \int_{t_2}^{\infty} dt_3 \int_{\mathbf{u}_3} \int_{\mathbf{l}_3 \bar{\mathbf{l}}_3} e^{i(\mathbf{l}_3 - \bar{\mathbf{l}}_3)\cdot\mathbf{u}_3} T(\mathbf{u}_3, \mathbf{u}_3 | t_3) \mathcal{Q}_{\text{initial}}(\mathbf{l}_3, \bar{\mathbf{l}}_3, \mathbf{l}_2, \bar{\mathbf{l}}_2 | t_3, t_2) \\
&= 0. \tag{3.95}
\end{aligned}$$

In the first step we have used that the integral over \mathbf{p} makes a delta function setting $\mathbf{u}_3 = \bar{\mathbf{u}}_3$. The reason we get 0 in the end is because $T(\mathbf{u}_3, \mathbf{u}_3) = 0$, which follows from the definition (3.86).

Hence, the non-factorizable part of the four-point function does not contribute to the energy spectrum. Only the factorizable part is left, and the sole contribution is a delta function. This is because the quadrupole actually describes the momentum broadening of the system after the splitting has happened. When integrating out all of the transverse momenta this becomes trivial.

To show this at finite N_c one can go back to the definition of the four-point function (3.51) and integrate out the final momenta \mathbf{q} and \mathbf{k} .

Inserting these integrated quadrupoles into (3.93) we get the energy spectrum in the large- N_c limit

$$\frac{dI}{dz} = \frac{\alpha_s}{\omega^2} P_{a \rightarrow bc}(z) \text{Re} \int_0^\infty dt_1 \int_{t_1}^\infty dt_2 \int_{\mathbf{l}_1 \mathbf{l}_2} \mathbf{l}_1 \cdot \mathbf{l}_2 \mathcal{K}(\mathbf{l}_2, \mathbf{l}_1 | t_2, t_1). \tag{3.96}$$

3.3 Calculating the splitting kernel

The energy spectrum is often written in the soft limit $z \rightarrow 0$, where $\omega \simeq zE$. In momentum space and position space this is

$$\begin{aligned} \omega \frac{dI}{d\omega} &= \frac{2\pi\bar{\alpha}}{\omega^2} \text{Re} \int_0^\infty dt_1 \int_{t_1}^\infty dt_2 \int_{\mathbf{l}_1 \mathbf{l}_2} \mathbf{l}_1 \cdot \mathbf{l}_2 \mathcal{K}(\mathbf{l}_2, \mathbf{l}_1 | t_2, t_1) \\ &= \frac{2\pi\bar{\alpha}}{\omega^2} \text{Re} \int_0^\infty dt_1 \int_{t_1}^\infty dt_2 \partial_{\mathbf{x}} \cdot \partial_{\mathbf{y}} \mathcal{K}(\mathbf{x}, \mathbf{y} | t_2, t_1) |_{\mathbf{x}, \mathbf{y}=0}. \end{aligned} \quad (3.97)$$

The main result in [2] was calculating the medium-induced energy spectrum for all energies ω and medium lengths L . The tricky part is the splitting kernel \mathcal{K} . Here we will show how this can be calculated analytically. The same splitting kernel also shows up in the more general formulas (3.57) and (3.80), so it is a vital object to calculate in jet quenching.

The splitting kernel is given as a path integral, see Eq. (3.61) and (3.63)

$$\mathcal{K}(\mathbf{x}, \mathbf{y} | t_2, t_1) = \int_{\mathbf{y}}^{\mathbf{x}} \mathcal{D}\mathbf{u} e^{i \int_{t_1}^{t_2} ds \left[\frac{m}{2} \dot{\mathbf{u}}^2 + iv(\mathbf{u}) \right]}. \quad (3.98)$$

The potential v is given in a general form in (3.64), but for a soft gluon emission it becomes

$$v(\mathbf{r}, t) = N_c n(t) \sigma(\mathbf{r}), \quad (3.99)$$

where $\sigma(\mathbf{r})$ is defined in (3.13). The path integral for the splitting kernel can also be written as a Schrödinger equation and in terms of a Dyson-Schwinger expansion

$$\left[i\partial_t + \frac{\partial_{\mathbf{x}}^2}{2\omega} + iv(\mathbf{x}, t) \right] \mathcal{K}(\mathbf{x}, \mathbf{y} | t, t_1) = i\delta(t - t_1) \delta(\mathbf{x} - \mathbf{y}), \quad (3.100)$$

$$\begin{aligned} \mathcal{K}(\mathbf{x}, \mathbf{y} | t_2, t_1) &= \mathcal{K}_0(\mathbf{x}, \mathbf{y} | t_2, t_1) \\ &\quad - \int_{t_1}^{t_2} ds \int_{\mathbf{z}} \mathcal{K}_0(\mathbf{x}, \mathbf{z} | t_2, s) v(\mathbf{z}, s) \mathcal{K}(\mathbf{z}, \mathbf{y} | s, t_1). \end{aligned} \quad (3.101)$$

The Schrödinger equation is useful for solving the kernel numerically. For numerical solutions of the splitting kernel see [64–66]. The Dyson-Schwinger expansion lends itself better to reaching analytic solutions through the use of various approximations. This is what we explored in [2], and we will now summarize how this is done. The reason for using approximate analytical solutions is twofold: analytic results give deeper physical insights and analytic formulas are much faster to calculate on a computer than performing a full numerical simulation.

In the Dyson-Schwinger form the splitting kernel is expanded around the vacuum solution which is given by setting $v = 0$ in the path integral

$$\begin{aligned}\mathcal{K}_0(\mathbf{x}, \mathbf{y}|t_2, t_1) &= \int_{\mathbf{y}}^{\mathbf{x}} \mathcal{D}\mathbf{u} e^{i\frac{\omega}{2} \int_{t_1}^{t_2} ds \dot{\mathbf{u}}^2} \\ &= \frac{\omega}{2\pi i (t_2 - t_1)} e^{i\frac{\omega}{2} \frac{(\mathbf{x}-\mathbf{y})^2}{(t_2-t_1)}}.\end{aligned}\quad (3.102)$$

Going back to (3.14) and (3.15) we see that the potential is usually given in momentum space. The Fourier transform of the previous expression is

$$\begin{aligned}\mathcal{K}(\mathbf{p}, \mathbf{p}_0|t_2, t_1) &= (2\pi)^2 \delta(\mathbf{p} - \mathbf{p}_0) \mathcal{K}_0(\mathbf{p}|t_2 - t_1) \\ &\quad - \int_{t_1}^{t_2} ds \int_{\mathbf{q}} \mathcal{K}_0(\mathbf{p}|t_2 - s) v(\mathbf{q}, s) \mathcal{K}(\mathbf{p} - \mathbf{q}, \mathbf{p}_0|s, t_1),\end{aligned}\quad (3.103)$$

with the vacuum solution given by

$$\mathcal{K}_0(\mathbf{p}, t) = e^{-i\frac{\mathbf{p}^2 t}{2\omega}}.\quad (3.104)$$

Defining $V(\mathbf{q}, t) = N_c n(t) g^2 \frac{d^2 \sigma_{e1}}{d^2 \mathbf{q}}$ we see from Eqs. (3.13) and (3.99) that the potential v can be written as

$$v(\mathbf{r}, t) = \int_{\mathbf{q}} V(\mathbf{q}, t) (1 - e^{i\mathbf{q}\cdot\mathbf{r}}).\quad (3.105)$$

The momentum space version of the potential is then simply given as

$$v(\mathbf{q}, t) = (2\pi)^2 \delta(\mathbf{q}) \Sigma(t) - V(\mathbf{q}, t),\quad (3.106)$$

where we have defined $\Sigma(t) = \int_{\mathbf{q}} V(\mathbf{q}, t)$. It is customary to define the mean free path in the medium λ as $\lambda = 1/\Sigma$.

Opacity expansion Eq. (3.103) is usually referred to as the *opacity expansion* (OE) [67–70]. The idea is to expand the kernel around the vacuum solution, and keep as many terms as necessary to reach sufficient accuracy when calculating the emission spectrum. In the opacity expansion you expand in the number of scatterings with the medium. The n 'th order of the opacity expansion comes with a factor χ^n , where $\chi = L/\lambda$ is called the opacity of the medium. We therefore expect it to work well when $\chi < 1$, meaning at early times or for a dilute medium. Comparing to the numerical solution of the full kernel shows that the opacity expansion at first order does indeed provide an accurate approximation of the spectrum at early times.

However, as shown in [2] the opacity expansion does not converge for all values of ω and L . It converges at early times $L/\lambda < 1$ or when the energy is high $\omega > \chi \bar{\omega}_c$. Here we

have used the characteristic energy scale of the OE, which is $\bar{\omega}_c = \frac{1}{2}\mu^2 L$. The reason it doesn't work at late times is that you then have to take into account many scatterings with the medium, which the opacity expansion is not suited for. Our approach in [2] was therefore to try different expansions and see if they together can describe \mathcal{K} in the full phase space. We found that using a total of three expansion schemes did the trick. Those are the opacity expansion, the resummed opacity expansion, and the improved opacity expansion.

Resummed opacity expansion The *resummed opacity expansion* (ROE) is made by separating the two terms in (3.106). The first term is resummed, and the expansion is then only over the second term. The first term of the ROE was found in [71], however, the full expansion was defined first in [2]. The resummed opacity expansion can be defined as

$$\mathcal{K}(\mathbf{p}, \mathbf{p}_0 | t_2, t_1) = (2\pi)^2 \delta(\mathbf{p} - \mathbf{p}_0) \Delta(t_2, t_1) \mathcal{K}_0(\mathbf{p} | t_2 - t_1) \\ \int_{t_1}^{t_2} ds \Delta(t_2, s) \int_{\mathbf{q}} \mathcal{K}_0(\mathbf{p} | t_2 - s) V(\mathbf{q}, s) \mathcal{K}(\mathbf{p} - \mathbf{q}, \mathbf{p}_0 | s, t_1), \quad (3.107)$$

where we have defined the Sudakov form factor $\Delta(t_2, t_1) = e^{-\int_{t_1}^{t_2} ds \Sigma(s)}$. The resummed opacity expansion works really well for low energies, $\omega < \omega_{\text{BH}}$, where we have defined the energy scale $\omega_{\text{BH}} = \frac{1}{2}\mu^2 \lambda$. Surprisingly, when you are below this energy scale the ROE also works at late times, where the ordinary opacity expansion cannot be used. One would think that at late times $L \gg \lambda$ many scatterings must be taken into account, which the ROE is not suited for. The reason it still works is that the typical time it takes an emission to form, called the formation time $t_f = \sqrt{2\omega/\hat{q}}$ (also referred to as branching time by some authors), is very small at low ω . So during the very short formation time the parton does not have time to scatter many times on the medium. This is the reason why the ROE can be used at small energies, even at late times.

However, these two expansions are still not sufficient to cover the entire phase space of (ω, L) . A third expansion is needed, which is called the improved opacity expansion.

Improved opacity expansion The *improved opacity expansion* (IOE) was developed in [72–76], and comes from a clever manipulation of the splitting potential. For both the GW and HTL models (Eqs. (3.14) and (3.15)), at small \mathbf{r} , the potential is approximately equal to

$$v(\mathbf{r}, t) \simeq \frac{1}{4} \hat{q}_0(t) \mathbf{r}^2 \ln \frac{1}{\mu_*^2 \mathbf{r}^2}, \quad (3.108)$$

where $\hat{q}_0(t) = 4\pi\alpha_s^2 N_c n(t)$. The parameter μ_* is defined differently in the GW and HTL models. In the GW model $\mu_*^2 = \frac{1}{4}\mu^2 e^{-1+2\gamma_E}$, while for the HTL it is $\mu_*^2 = \frac{1}{4}m_D^2 e^{-2+2\gamma_E}$. In this approximation the two models therefore match if $\mu^2 = m_D^2/e$.

The potential can be separated into two parts by introducing the energy scale Q^2

$$\begin{aligned} v(\mathbf{r}, t) &\simeq \frac{1}{4}\hat{q}_0(t)\mathbf{r}^2 \ln \frac{Q^2}{\mu_*^2} + \frac{1}{4}\hat{q}_0(t)\mathbf{r}^2 \ln \frac{1}{Q^2\mathbf{r}^2} \\ &= \frac{1}{4}\hat{q}(t)\mathbf{r}^2 + \frac{1}{4}\hat{q}_0(t)\mathbf{r}^2 \ln \frac{1}{Q^2\mathbf{r}^2} \\ &\equiv v_{\text{HO}}(\mathbf{r}, t) + \delta v(\mathbf{r}, t). \end{aligned} \quad (3.109)$$

Here we have defined $\hat{q} \equiv \hat{q}_0(t) \ln \frac{Q^2}{\mu_*^2}$. The first term defines the harmonic oscillator (HO), or BDMPS-Z approach [51, 77]. The harmonic oscillator potential has the great advantage that it allows for an analytic solution of the splitting kernel

$$\begin{aligned} \mathcal{K}_{\text{HO}}(\mathbf{x}, \mathbf{y}|t_2, t_1) &= \int_{\mathbf{y}}^{\mathbf{x}} \mathcal{D}\mathbf{r} e^{i \int_{t_1}^{t_2} ds \left[\frac{\omega}{2} \dot{\mathbf{r}}^2 + i v_{\text{HO}}(\mathbf{r}, s) \right]} \\ &= \frac{\omega \Omega}{2\pi i \sin(\Omega \Delta t)} e^{\frac{i\omega\Omega}{2\sin(\Omega\Delta t)} [\cos(\Omega\Delta t) (\mathbf{x}^2 + \mathbf{y}^2) - 2\mathbf{x}\cdot\mathbf{y}]}, \end{aligned} \quad (3.110)$$

where $\Delta t \equiv t_2 - t_1$ and $\Omega = \frac{1-i}{2} \sqrt{\hat{q}/\omega}$ is the characteristic oscillator frequency. Since this is a full analytic solution of the path integral it describes a splitting caused by an arbitrary number of medium interactions. For this reason, it is very useful when the opacity L/λ is big, as multiple scatterings must then be accounted for. However, the harmonic oscillator potential resums many soft scatterings, and can hence only induce soft emissions, up to the energy scale $\omega_c = \frac{1}{2}\hat{q}L^2$.

Fortunately, harder emissions can be described by utilizing the second part of the potential δv . The expansion in δv is called the improved opacity expansion. It is given by

$$\begin{aligned} \mathcal{K}(\mathbf{x}, \mathbf{y}|t_2, t_1) &= \mathcal{K}_{\text{HO}}(\mathbf{x}, \mathbf{y}|t_2, t_1) \\ &\quad - \int_{t_1}^{t_2} ds \int_{\mathbf{z}} \mathcal{K}_{\text{HO}}(\mathbf{x}, \mathbf{z}|t_2, s) \delta v(\mathbf{z}, s) \mathcal{K}(\mathbf{z}, \mathbf{y}|s, t_1). \end{aligned} \quad (3.111)$$

The expansion is now around the harmonic oscillator kernel rather than the vacuum one.

Summary of the expansions We have now presented three different expansions of the splitting kernel that together can be used to calculate the emission spectrum (3.97) for all energies ω and medium lengths L . These are the opacity expansion (3.103), the resummed opacity expansion (3.107), and the improved opacity expansion (3.111). The

expansions come with three characteristic energy scales, $\bar{\omega}_c$, ω_{BH} and ω_c .

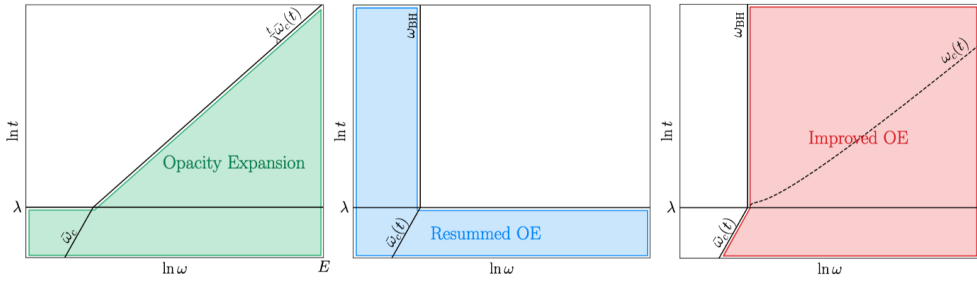


Figure 3.3: The regions of validity for the opacity expansion, the resummed opacity expansion, and the improved opacity expansion. Figure from [2].

In Fig. 3.3 we have shown the regions of validity for all three expansions. As one can see the IOE works well for most of the phase space, while only the ROE works for very low ω .

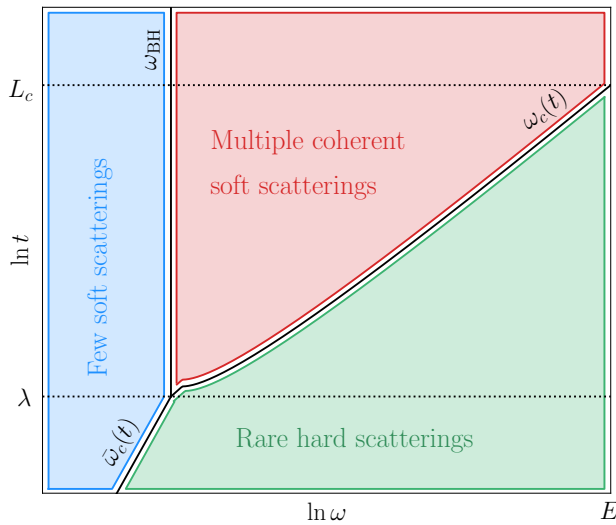


Figure 3.4: The scattering processes that lead to induced emissions. Figure from [2].

The physical processes that dominate the emission spectrum are shown in Fig 3.4. It is clear that at early times $t < \lambda$ the spectrum is dominated by few scatterings. This is well approximated by the opacity expansion, which indeed is an expansion in the number of scatterings with the medium. At later times the number of scatterings with the medium increases drastically, and the opacity expansion is no longer accurate. The harmonic oscillator approximation resums many soft scatterings, and can therefore be used at later times. At very low energies $\omega < \omega_{\text{BH}}$ the formation time t_f is so short that

the parton does not have time to scatter many times before an emission is induced. This low-energy region is therefore not suitable for the harmonic oscillator solution, but is well described by the resummed opacity expansion.

Using these three expansions of the splitting kernel \mathcal{K} , (3.103), (3.107) and (3.111) one can calculate a good approximation of the emission spectrum (3.97) in all regions of the phase space. Looking at the regions of validity in Fig. 3.3 one can deduce that the emission spectrum is well approximated by the formula

$$\frac{dI^{\text{Full}}}{d\omega} = \begin{cases} \frac{dI^{\text{ROE}}}{d\omega}, & \omega < \min(\omega_{\text{BH}}, \bar{\omega}_c(t)), \\ \frac{dI^{\text{IOE}}}{d\omega}, & \text{otherwise.} \end{cases} \quad (3.112)$$

The full derivations and the resulting formulas are shown in [2].

3.4 Multiple emissions

So far we have in Secs. 3.2 and 3.3 only considered a single medium-induced emission. However, the partons will typically split several times as they traverse the medium. This is a huge theoretical challenge, as these subsequent emissions can interfere with each other, which would necessitate the calculation of n-point functions even more complicated than the quadrupole. Fortunately, when considering soft gluon emissions these interference effects can safely be neglected [62, 78]. For soft emissions the formation time is short, and one can show that it is generally shorter than the time between two successive splittings. For more discussion about the effects of interference between subsequent emissions see e.g. [79–81].

Assuming that subsequent emissions are independent of each other is ideal for a Monte Carlo approach, where one can generate successive splittings and make a parton shower. It is also possible to derive analytical approaches to multiple emissions. These do not offer the same degree of accuracy as Monte Carlo simulations, but can still be useful in order to gain increased insight into the problem. Here we will present one such analytical approach, which we discussed in [2]. In this case, we ignore the dependence on transverse momentum and focus on the energy of the partons. We will also consider a fully gluonic cascade, although the generalization to also include quarks is straightforward.

Consider a parton going through the medium with initial energy E . It can undergo several independent splittings, and after some time t you end up with a collection of partons, where each of them will have a lower energy xE . The distribution of the energy

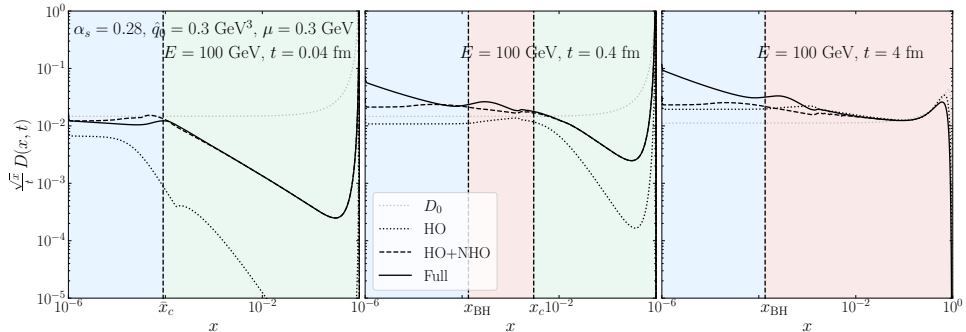


Figure 3.5: A numerical solution of the evolution equation (3.114) for the energy distribution $D(x, t)$ as a function of x for three different times. We have also included several approximate solutions. Figure from [2].

fraction x after a time t has passed can be defined as

$$D(x, t) \equiv x \frac{dN}{dx}. \quad (3.113)$$

One can show that this is governed by an evolution equation [62] given by

$$\frac{\partial}{\partial t} D(x, t) = \int_x^1 dz \mathcal{R}\left(z, \frac{x}{z}E, t\right) D\left(\frac{x}{z}, t\right) - \int_0^1 dz z \mathcal{R}(z, xE, t) D(x, t). \quad (3.114)$$

Here the function \mathcal{R} is called the splitting rate, and is related to the emission spectrum that we derived in Sec. 3.3

$$\mathcal{R}(z, E, t) = 2 \left. \frac{dI_{gg}}{dzdt} \right|_E. \quad (3.115)$$

The evolution equation (3.114) has an analytic solution for the harmonic oscillator solution of the emission spectrum [82, 83], which is given by

$$D_0(x, \tau) = \frac{\tau}{\sqrt{x(1-x)^{3/2}}} e^{-\pi \frac{\tau^2}{1-x}}, \quad (3.116)$$

with the re-scaled time variable τ defined as $\tau = \bar{\alpha} t \sqrt{\hat{q}_0/E}$.

However, as we argued in Sec. 3.3 the harmonic oscillator solution is only valid at late times and relatively low energies $\omega < \omega_c$. A more accurate splitting rate can be derived from the full spectrum, given in Eq. (3.112). In [2] we solved the evolution equation (3.114) numerically with the improved splitting rate. The result of the simulation is shown on [2].

In Fig. 3.5 we show different solutions of the energy distribution $D(x, t)$ at three different times. The full lines represent the numerical solution with the full splitting rate from

(3.112). The colors indicate which physical scattering process that leads to induced emissions for different splitting fractions x , and correspond to the colors in Fig. 3.4. As one can see, the distribution peaks at $x = 1$ at early times, as the initial parton has not yet had time to lose much of its energy. At later times the peak at $x = 1$ disappears, and the energy becomes distributed to low-energy modes at lower x .

There are also two other numerical solutions present in Fig. 3.5, referred to as HO and HO+NHO. The first is the harmonic oscillator solution, while the second includes the first correction to the HO solution through the IOE (3.111). The difference between HO+NHO and the full solution is that the full solution also includes the ROE at low energy fraction x . We see that the HO solution fails at early times, but becomes more accurate at late times. The HO+NHO solution is a good approximation at early and late times, except for at low x , where the ROE must be used to get an accurate result.

It is interesting to compare the full numerical solution to the analytical harmonic oscillator solution, given by (3.116). The difference between D_0 and HO in the plot is that in D_0 only the low-energy limit of the HO solution is used. The analytic solution is represented by the thin dotted line in Fig. 3.5. As is evident on the figure, D_0 does not work well at early times. This makes sense, as HO emissions are induced by many soft scatterings, which there has not been time for at early times. However, at late times we see that the energy distribution is dominated by HO emissions. The approximate distribution D_0 then provides a good approximation to the full result, except at very low energies, where the ROE spectrum must be used.

Chapter 4

Conclusion and outlook

In this thesis, we have reviewed the physics of jet quenching and showed how the papers we have written contribute to the field of research. In chapter 1 we introduced the theory we use to do all our calculations, namely the Standard Model of particle physics and more specifically QCD. In chapter 2 we wrote about heavy ion collisions in a broad sense, and their different experimental and theoretical aspects. Finally, in chapter 3 we arrived at the main topic for the thesis, which is the theory of jet quenching.

My work as a PhD student has been focused on improving the theoretical calculation of medium-induced emissions. These emissions constitute the main contribution to jet energy loss, which can be measured in experiments and hence is important to get under theoretical control. My three papers, [1], [2] and [3] all tackle different aspects of this calculation.

In [1] we derived a method for calculating correlators of Wilson lines in the medium at finite N_c . These Wilson lines are part of the medium propagator (3.29), and correlators of Wilson lines must hence be calculated in almost any calculation of partons going through the medium. The primary method of calculating these correlators is to invoke the large- N_c limit, which greatly simplifies the calculation. The method developed in [1] is therefore useful for controlling whether the large- N_c limit is a valid tool, and how big the error you get by using it is. We found that the large- N_c does work well, but we found errors up to around 15 % for $g \rightarrow gg$ splitting. The error seemed to increase with the color complexity of the system, as the error in $g \rightarrow gg$ was bigger than the error in $q \rightarrow qg$, which again was greater than the error in $\gamma \rightarrow q\bar{q}$.

In [3] we performed a similar study as in [1], but made it more precise. We calculated the medium-induced emission spectrum as a function of z and transverse momentum \mathbf{p} , see (3.57). In [1] we calculated the same, but used the eikonal approximation for all

the partons, meaning that we approximated their path through the medium as straight lines. In [3] we relaxed this approximation and provided the first calculation of a medium-induced emission without using either the soft, large- N_c , or eikonal approximations. We accomplished this by numerically simulating a system of Schrödinger equations that govern the time evolution of the system.

As in [1] we also found in [3] that the large- N_c approximation generally works well. The large- N_c approximation leads to a sum of two terms, called the factorizable and non-factorizable pieces, see (3.72). Usually, only the factorizable piece is kept in calculations. In [3] we checked whether it is valid to drop the non-factorizable term. We found that going from the large- N_c approximation to only the factorizable term involves a bigger error than going from the full solution at finite N_c to the large- N_c approximation. Dropping the non-factorizable piece is valid at small z , but for $z \sim 0.5$ there is a significant error involved. Interestingly, we also found that the fully eikonal approximation, as we used in [1], did not work particularly well for the cases we studied.

Finally, in [2] we calculated the emission spectrum as a function of energy, given in Eq. (3.97). The challenging part is calculating the splitting kernel, given in Eq. (3.98), for the full phase space of (ω, L) . We found that three different ways of expanding the kernel are sufficient to calculate the emission spectrum with high accuracy. The expansions are called the opacity expansion, the resummed opacity expansion, and the improved opacity expansion. They are useful at different energies and times, given in Fig. 3.3. The three expansions capture three different physical processes, shown in Fig. 3.4. At early times rare scatterings dominate, given by the opacity expansion (3.103). At late times the emissions are induced by multiple coherent soft scatterings, given by the harmonic oscillator approximation (3.110) or equivalently the improved opacity expansion (3.111). At very low energies the formation time is too short for multiple emissions, and this effect is captured by the resummed opacity expansion (3.107).

In [2] we also studied the energy distribution after multiple consecutive emissions, armed with our analytical results for the full splitting kernel. This is in a simplified model governed by an evolution equation (3.114). We found that the harmonic oscillator solution provides the most important effect at late times. However, at early times emissions induced by rare hard scatterings determine the energy distribution.

Finally, I would like to provide an outlook on how the work presented in this thesis can contribute to future research.

The result in [1] is very general, and can be used to compute Wilson line correlators of any size. This could be used to study for example two-gluon emissions [79], which could provide valuable insight into the interference between subsequent emissions.

The developments we made in [2] can be used to provide more precise splitting kernels to Monte Carlo simulations. An obvious extension is to calculate the transverse momentum dependent emission spectrum, instead of just the energy spectrum. This would make the result even more useful and could provide further insight into the splitting process.

Lastly, there are several interesting ways to extend the result from [3]. The most obvious one is perhaps to numerically calculate the emission spectrum for more complicated processes, like $q \rightarrow qg$ or $g \rightarrow gg$. This amounts to solving systems of differential equations of higher dimensions, which is more resource-expensive, but can be implemented. It is also straightforward to use a more general potential, rather than using the harmonic oscillator approximation. It is interesting that what we really study by calculating the spectrum at finite N_c is the impact of quantum effects on the splitting process. It would also be interesting to see what effect this could have on multiple splittings.

Appendix A

Different forms of the medium propagator

Here we will show that the three following ways to write the medium propagator are equivalent:

Dyson-Schwinger form:

$$\begin{aligned} (\mathbf{x}|\mathcal{G}(t, t_0)|\mathbf{x}_0) &= \mathcal{G}_0(\mathbf{x} - \mathbf{x}_0, t - t_0) \\ &+ \int_{t_0}^t ds \int_{\mathbf{y}} \mathcal{G}_0(\mathbf{x} - \mathbf{y}, t - s) ig\mathcal{A}(\mathbf{y}, s) (\mathbf{y}|\mathcal{G}(s, t_0)|\mathbf{x}_0), \end{aligned} \quad (\text{A.1})$$

Schrödinger equation form:

$$\left[i\frac{\partial}{\partial t} + \frac{\partial^2}{2E} + g\mathcal{A}(\mathbf{x}, t) \right] (\mathbf{x}|\mathcal{G}(t, t_0)|\mathbf{x}_0) = 0, \quad (\text{A.2})$$

Path integral form:

$$(\mathbf{x}|\mathcal{G}_R(t, t_0)|\mathbf{x}_0) = \int_{\mathbf{x}_0}^{\mathbf{x}} \mathcal{D}\mathbf{r} e^{i\frac{E}{2} \int_{t_0}^t ds \dot{\mathbf{r}}^2(s)} V_R(t, t_0; \mathbf{r}(t)). \quad (\text{A.3})$$

We will start with the path integral form and derive the Schrödinger equation from this. Start by discretizing the path integral with N time intervals with length ϵ . Let the whole path integral go to from (t_0, \mathbf{x}_0) to $(t + \epsilon, \mathbf{x})$, and we divide it into two parts: one from

t_0 to t and one from t to $t + \epsilon$. Then we have

$$\begin{aligned}
(\mathbf{x}|\mathcal{G}(t + \epsilon, t_0)|\mathbf{x}_0) &= \int_{\mathbf{x}_0}^{\mathbf{x}} \mathcal{D}\mathbf{r} \exp \left[i \frac{E}{2} \int_{t_0}^{t+\epsilon} ds \dot{\mathbf{r}}^2(s) \right] V(t + \epsilon, t_0) \\
&= \frac{1}{A} \int d\mathbf{r}_{N-1} \exp \left[i \frac{E}{2} \int_t^{t+\epsilon} ds \dot{\mathbf{r}}_N^2(s) \right] V(t + \epsilon, t) \\
&\times \int_{\mathbf{x}_0}^{\mathbf{r}_{N-1}} \mathcal{D}\mathbf{r} \exp \left[i \frac{E}{2} \int_{t_0}^t ds \dot{\mathbf{r}}^2(s) \right] V(t, t_0) \\
&= \frac{1}{A} \int d\mathbf{r}_{N-1} \exp \left[i \frac{E}{2} \epsilon \left(\frac{\mathbf{r}_N - \mathbf{r}_{N-1}}{\epsilon} \right)^2 + ig\epsilon \mathcal{A}(\mathbf{r}_N, s_N) \right] (\mathbf{r}_{N-1}|\mathcal{G}(t, t_0)|\mathbf{x}_0). \quad (\text{A.4})
\end{aligned}$$

Here A is a normalization factor. Using that $\mathbf{r}_N = \mathbf{x}$ we see that the integral over \mathbf{r}_{N-1} is dominated by terms where $\mathbf{x} - \mathbf{r}_{N-1}$ is small. We define a new variable through $\mathbf{r}_{N-1} = \mathbf{x} + \boldsymbol{\eta}$ so that the integration becomes

$$(\mathbf{x}|\mathcal{G}(t + \epsilon, t_0)|\mathbf{x}_0) = \frac{1}{A} \int d\boldsymbol{\eta} \exp \left[i \frac{E}{2\epsilon} \boldsymbol{\eta}^2 + ig\epsilon \mathcal{A}(\mathbf{x}, t) \right] (\mathbf{x} + \boldsymbol{\eta}|\mathcal{G}(t, t_0)|\mathbf{x}_0). \quad (\text{A.5})$$

Now we expand in ϵ and $\boldsymbol{\eta}$. As will be clear below all the contributions linear in $\boldsymbol{\eta}$ disappear, so we need to expand to second order

$$\begin{aligned}
&(\mathbf{x}|\mathcal{G}(t, t_0)|\mathbf{x}_0) + \epsilon \frac{\partial}{\partial t} (\mathbf{x}|\mathcal{G}(t, t_0)|\mathbf{x}_0) \\
&= \frac{1}{A} \int d\eta_1 d\eta_2 \exp \left[i \frac{E}{2\epsilon} (\eta_1^2 + \eta_2^2) \right] (1 + ig\epsilon \mathcal{A}(\mathbf{x}, t)) \\
&\times \left(1 + \eta_1 \frac{\partial}{\partial x_1} + \eta_2 \frac{\partial}{\partial x_2} + \frac{1}{2} \left(\eta_1^2 \frac{\partial^2}{\partial x_1^2} + 2\eta_1 \eta_2 \frac{\partial^2}{\partial x_1 \partial x_2} + \eta_2^2 \frac{\partial^2}{\partial x_2^2} \right) \right) (\mathbf{x}|\mathcal{G}(t, t_0)|\mathbf{x}_0). \quad (\text{A.6})
\end{aligned}$$

Now we use the Gaussian integral formulas

$$\begin{aligned}
\int dx e^{iax^2} &= \frac{\sqrt{\pi}}{\sqrt{-ia}} \\
\int dx x e^{iax^2} &= 0 \\
\int dx x^2 e^{iax^2} &= \frac{\sqrt{\pi}}{2(-ia^{3/2})}, \quad (\text{A.7})
\end{aligned}$$

and it is clear that all terms linear in $\boldsymbol{\eta}$ vanish. After doing the integrals we end up with

$$\begin{aligned}
&(\mathbf{x}|\mathcal{G}(t, t_0)|\mathbf{x}_0) + \epsilon \frac{\partial}{\partial t} (\mathbf{x}|\mathcal{G}(t, t_0)|\mathbf{x}_0) \\
&= \frac{1}{A} (1 + ig\epsilon \mathcal{A}(\mathbf{x}, t)) \left(\frac{2i\pi\epsilon}{E} - \frac{\pi\epsilon^2}{E^2} \left(\frac{\partial^2}{\partial x_1^2} + \frac{\partial^2}{\partial x_2^2} \right) \right) (\mathbf{x}|\mathcal{G}(t, t_0)|\mathbf{x}_0). \quad (\text{A.8})
\end{aligned}$$

The first two terms on the left and right sides have to match, meaning that the normal-

ization factor is

$$A = \frac{2i\pi\epsilon}{E}. \quad (\text{A.9})$$

Plugging this into the equation above we get

$$\begin{aligned} & (\mathbf{x}|\mathcal{G}(t, t_0)|\mathbf{x}_0) + \epsilon \frac{\partial}{\partial t} (\mathbf{x}|\mathcal{G}(t, t_0)|\mathbf{x}_0) \\ &= (\mathbf{x}|\mathcal{G}(t, t_0)|\mathbf{x}_0) + \epsilon \left(ig\mathcal{A}(\mathbf{x}, t) + \frac{i}{2E} \left(\frac{\partial^2}{\partial x_1^2} + \frac{\partial^2}{\partial x_2^2} \right) \right) (\mathbf{x}|\mathcal{G}(t, t_0)|\mathbf{x}_0) + \mathcal{O}(\epsilon^2). \end{aligned} \quad (\text{A.10})$$

Gathering all the terms linear in ϵ and defining $\partial_{\mathbf{x}}^2 \equiv \frac{\partial^2}{\partial x_1^2} + \frac{\partial^2}{\partial x_2^2}$ we get the Schrödinger equation (3.28).

Now we only need to show that the Dyson-Schwinger expansion is a solution to the Schrödinger equation. To do this it is more convenient to write it on an equivalent form

$$\begin{aligned} (\mathbf{x}|\mathcal{G}(t, t_0)|\mathbf{x}_0) &= \mathcal{G}_0(\mathbf{x} - \mathbf{x}_0, t - t_0) \\ &+ \int_{t_0}^t ds \int_{\mathbf{y}} (\mathbf{x}|\mathcal{G}(t, s)|\mathbf{y}) ig\mathcal{A}(\mathbf{y}, s) \mathcal{G}_0(\mathbf{y} - \mathbf{x}_0, s - t_0). \end{aligned} \quad (\text{A.11})$$

One can check that this is an equivalent expansion by simply iterating a few terms. Hitting this with the Schrödinger equation gives

$$\begin{aligned} & \left[i \frac{\partial}{\partial t} + \frac{\partial_{\mathbf{x}}^2}{2E} + g\mathcal{A}(\mathbf{x}, t) \right] (\mathbf{x}|\mathcal{G}(t, t_0)|\mathbf{x}_0) = g\mathcal{A}(\mathbf{x}, t) \mathcal{G}_0(\mathbf{x} - \mathbf{x}_0, t - t_0) \\ &+ i \int_{\mathbf{y}} \delta(\mathbf{x} - \mathbf{y}) ig\mathcal{A}(\mathbf{y}, s) \mathcal{G}_0(\mathbf{y} - \mathbf{x}_0, s - t_0) \\ &+ \int_{t_0}^t ds \int_{\mathbf{y}} \left[i \frac{\partial}{\partial t} + \frac{\partial_{\mathbf{x}}^2}{2E} + g\mathcal{A}(\mathbf{x}, t) \right] (\mathbf{x}|\mathcal{G}(t, s)|\mathbf{y}) ig\mathcal{A}(\mathbf{y}, s) \mathcal{G}_0(\mathbf{y} - \mathbf{x}_0, s - t_0) \\ &= g\mathcal{A}(\mathbf{x}, t) \mathcal{G}_0(\mathbf{x} - \mathbf{x}_0, t - t_0) - g\mathcal{A}(\mathbf{x}, t) \mathcal{G}_0(\mathbf{x} - \mathbf{x}_0, t - t_0) = 0. \end{aligned} \quad (\text{A.12})$$

This proves that all three ways of writing the propagator are equivalent.

Appendix B

The non-factorizable part of the large- N_C limit

Here we will go through the derivation of the non-factorizable quadrupole Eq. (3.85), starting with Eq. (3.84). Using that

$$\int_{\mathbf{x}\bar{\mathbf{x}}} e^{-i\mathbf{k}\cdot(\mathbf{x}-\bar{\mathbf{x}})}(\mathbf{x};\bar{\mathbf{x}}|S^2(t_\infty-t_3)|\mathbf{x}_3;\bar{\mathbf{x}}_3) = \int_{\mathbf{k}_3} e^{-i\mathbf{k}_3\cdot(\mathbf{x}_3-\bar{\mathbf{x}}_3)}\mathcal{P}(\mathbf{k}-\mathbf{k}_3|t_\infty,t_3), \quad (\text{B.1})$$

the non-factorizable four-point function can be written as

$$\begin{aligned} & (\mathbf{k}, \mathbf{q}; \mathbf{k}, \mathbf{q} | S_{\text{non-fac}}^{(4)}(t_\infty, t_2) | \mathbf{k}_2, \mathbf{q}_2; \bar{\mathbf{k}}_2, \bar{\mathbf{p}}_2 - \bar{\mathbf{k}}_2) = \\ & \int_{t_2}^{\infty} dt_3 \int_{\mathbf{k}_3 \mathbf{q}_3} \mathcal{P}(\mathbf{k}-\mathbf{k}_3|t_\infty, t_3) \mathcal{P}(\mathbf{q}-\mathbf{q}_3|t_\infty, t_3) \\ & \times T(t_3) \int_{\mathbf{x}_3 \mathbf{y}_3 \bar{\mathbf{x}}_3 \bar{\mathbf{y}}_3 \mathbf{x}_2 \mathbf{y}_2 \bar{\mathbf{x}}_2 \bar{\mathbf{y}}_2} e^{i\mathbf{k}_2\cdot\mathbf{x}_2 - i\bar{\mathbf{k}}_2\cdot\bar{\mathbf{x}}_2 + i\mathbf{q}_2\cdot\mathbf{y}_2 - i(\bar{\mathbf{p}}_2 - \bar{\mathbf{k}}_2)\cdot\bar{\mathbf{y}}_2 - i\mathbf{k}_3\cdot(\mathbf{x}_3 - \bar{\mathbf{x}}_3) - i\mathbf{q}_3\cdot(\mathbf{y}_3 - \bar{\mathbf{y}}_3)} \\ & \times \int_{\mathbf{x}_2}^{\mathbf{x}_3} \mathcal{D}\mathbf{r}_1 \int_{\mathbf{y}_2}^{\mathbf{y}_3} \mathcal{D}\mathbf{r}_2 \int_{\bar{\mathbf{y}}_2}^{\bar{\mathbf{y}}_3} \mathcal{D}\bar{\mathbf{r}}_2 \int_{\bar{\mathbf{x}}_2}^{\bar{\mathbf{x}}_3} \mathcal{D}\bar{\mathbf{r}}_1 e^{i \int_{t_2}^{t_3} ds \left[\frac{zE}{2}(\dot{r}_1^2 - \dot{\bar{r}}_1^2) + \frac{(1-z)E}{2}(\dot{r}_2^2 - \dot{\bar{r}}_2^2) + iC_{Fn}(s)\sigma_{\text{eff}}(s) \right]}. \end{aligned} \quad (\text{B.2})$$

The remaining path integral can be simplified, using a similar method to the one employed in [3]. Start by changing coordinates

$$\begin{aligned} \mathbf{u} &= \mathbf{r}_1 - \mathbf{r}_2 \\ \bar{\mathbf{u}} &= \bar{\mathbf{r}}_1 - \bar{\mathbf{r}}_2 \\ \mathbf{v} &= z(\mathbf{r}_1 - \bar{\mathbf{r}}_1) + (1-z)(\mathbf{r}_2 - \bar{\mathbf{r}}_2) \\ \mathbf{z} &= \frac{1}{2}[z(\mathbf{r}_1 + \bar{\mathbf{r}}_1) + (1-z)(\mathbf{r}_2 + \bar{\mathbf{r}}_2)]. \end{aligned} \quad (\text{B.3})$$

These coordinates are ideal because they eliminate the dependence on \mathbf{z} in both T and σ_{eff} . Then the path integral over \mathbf{z} can be done, which has the effect of forcing \mathbf{v} to be on the classical path. The integrals over \mathbf{z}_3 and \mathbf{z}_2 can then be done, leading to a momentum conserving delta function and a delta function $\delta(\mathbf{v}_3 - \mathbf{v}_2)$. We refer to [3] for more detailed steps. The result is

$$\begin{aligned}
& (\mathbf{k}, \mathbf{q}; \mathbf{k}, \mathbf{q} | S_{\text{non-fac}}^{(4)}(t_\infty, t_2) | \mathbf{k}_2, \mathbf{q}_2; \bar{\mathbf{k}}_2, \bar{\mathbf{p}}_2 - \bar{\mathbf{k}}_2) = (2\pi)^2 \delta(\mathbf{q}_2 + \mathbf{k}_2 - \bar{\mathbf{p}}_2) \\
& \times \int_{t_2}^{\infty} dt_3 \int_{\mathbf{k}_3 \mathbf{q}_3} \mathcal{P}(\mathbf{k} - \mathbf{k}_3 | t_\infty, t_3) \mathcal{P}(\mathbf{q} - \mathbf{q}_3 | t_\infty, t_3) \\
& \times T(t_3) \int_{\mathbf{u}_2 \mathbf{u}_3 \bar{\mathbf{u}}_2 \bar{\mathbf{u}}_3 \mathbf{v}} e^{i\mathbf{v} \cdot (\bar{\mathbf{p}}_2 - \mathbf{q}_3 - \mathbf{k}_3) + i\mathbf{u}_2 \cdot (\mathbf{k}_2 - z\bar{\mathbf{p}}_2) - i\bar{\mathbf{u}}_2 \cdot (\bar{\mathbf{k}}_2 - z\bar{\mathbf{p}}_2) - i(\mathbf{u}_3 - \bar{\mathbf{u}}_3) \cdot ((1-z)\mathbf{k}_3 - z\mathbf{q}_3)} \\
& \times \int_{\mathbf{u}_2}^{\mathbf{u}_3} \mathcal{D}\mathbf{u} \int_{\bar{\mathbf{u}}_2}^{\bar{\mathbf{u}}_3} \mathcal{D}\bar{\mathbf{u}} e^{i \int_{t_2}^{t_3} ds \left[\frac{\omega}{2} (\dot{\mathbf{u}}^2 - \dot{\bar{\mathbf{u}}}^2) + i C_{FN}(s) \sigma_{\text{eff}}(s) \right]}. \tag{B.4}
\end{aligned}$$

We now introduce the same momentum variables as in the factorizable case, namely $\mathbf{p} = (1-z)\mathbf{k} - z\mathbf{q}$, $\mathbf{P} = \mathbf{q} + \mathbf{k}$, $\mathbf{p}_3 = (1-z)\mathbf{k}_3 - z\mathbf{q}_3$ and $\mathbf{P}_3 = \mathbf{q}_3 + \mathbf{k}_3$ and integrate over the total transverse momentum \mathbf{P} . Only the two broadening factors between t and t_∞ depend on \mathbf{P} , and the integral over these is

$$\begin{aligned}
& \int_{\mathbf{P}} \mathcal{P}(z(\mathbf{P} - \mathbf{P}_3) + \mathbf{p} - \mathbf{p}_3 | t_\infty, t_3) \mathcal{P}((1-z)(\mathbf{P} - \mathbf{P}_3) - (\mathbf{p} - \mathbf{p}_3) | t_\infty, t_3) \\
& = \int_{\mathbf{w}} e^{-i(\mathbf{p} - \mathbf{p}_3) \cdot \mathbf{w}} \mathcal{P}(z\mathbf{w} | t_\infty, t_3) \mathcal{P}((1-z)\mathbf{w} | t_\infty, t_3) \tag{B.5}
\end{aligned}$$

The four-point function is then

$$\begin{aligned}
& \int_{\mathbf{P}} (\mathbf{k}, \mathbf{q}; \mathbf{k}, \mathbf{q} | S_{\text{non-fac}}^{(4)}(t_\infty, t_2) | \mathbf{k}_2, \mathbf{q}_2; \bar{\mathbf{k}}_2, \bar{\mathbf{p}}_2 - \bar{\mathbf{k}}_2) = (2\pi)^2 \delta(\mathbf{q}_2 + \mathbf{k}_2 - \bar{\mathbf{p}}_2) \\
& \times \int_{t_2}^{\infty} dt_3 \int_{\mathbf{p}_3 \mathbf{P}_3} \int_{\mathbf{w}} e^{-i(\mathbf{p} - \mathbf{p}_3) \cdot \mathbf{w}} \mathcal{P}(z\mathbf{w} | t_\infty, t_3) \mathcal{P}((1-z)\mathbf{w} | t_\infty, t_3) \\
& \times T(t_3) \int_{\mathbf{u}_2 \mathbf{u}_3 \bar{\mathbf{u}}_2 \bar{\mathbf{u}}_3 \mathbf{v}} e^{i\mathbf{v} \cdot (\bar{\mathbf{p}}_2 - \mathbf{P}_3) + i\mathbf{u}_2 \cdot (\mathbf{k}_2 - z\bar{\mathbf{p}}_2) - i\bar{\mathbf{u}}_2 \cdot (\bar{\mathbf{k}}_2 - z\bar{\mathbf{p}}_2) - i(\mathbf{u}_3 - \bar{\mathbf{u}}_3) \cdot \mathbf{p}_3} \\
& \times \int_{\mathbf{u}_2}^{\mathbf{u}_3} \mathcal{D}\mathbf{u} \int_{\bar{\mathbf{u}}_2}^{\bar{\mathbf{u}}_3} \mathcal{D}\bar{\mathbf{u}} e^{i \int_{t_2}^{t_3} ds \left[\frac{\omega}{2} (\dot{\mathbf{u}}^2 - \dot{\bar{\mathbf{u}}}^2) + i C_{FN}(s) \sigma_{\text{eff}}(s) \right]}. \tag{B.6}
\end{aligned}$$

Now \mathbf{P}_3 and \mathbf{p}_3 are only present in complex phases and can be integrated over.

$$\int_{\mathbf{p}_3 \mathbf{P}_3} e^{i\mathbf{v} \cdot (\bar{\mathbf{p}}_2 - \mathbf{P}_3)} e^{-i(\mathbf{p} - \mathbf{p}_3) \cdot \mathbf{w}} e^{-i(\mathbf{u}_3 - \bar{\mathbf{u}}_3) \cdot \mathbf{p}_3} = \delta(\mathbf{v}) \delta(\mathbf{w} - (\mathbf{u}_3 - \bar{\mathbf{u}}_3)). \tag{B.7}$$

After doing this you end up in Eq. (3.85).

Bibliography

- [1] J. H. Isaksen and K. Tywoniuk, “Wilson line correlators beyond the large- N_c ,” *JHEP*, vol. 21, p. 125, 2020.
- [2] J. H. Isaksen, A. Takacs, and K. Tywoniuk, “A unified picture of medium-induced radiation,” *JHEP*, vol. 02, p. 156, 2023.
- [3] J. H. Isaksen and K. Tywoniuk, “Precise description of medium-induced emissions,” 3 2023.
- [4] M. E. Peskin and D. V. Schroeder, *An Introduction to quantum field theory*. Reading, USA: Addison-Wesley, 1995.
- [5] M. D. Schwartz, *Quantum Field Theory and the Standard Model*. Cambridge University Press, 3 2014.
- [6] J. Adams *et al.*, “Experimental and theoretical challenges in the search for the quark gluon plasma: The STAR Collaboration’s critical assessment of the evidence from RHIC collisions,” *Nucl. Phys. A*, vol. 757, pp. 102–183, 2005.
- [7] K. Adcox *et al.*, “Formation of dense partonic matter in relativistic nucleus-nucleus collisions at RHIC: Experimental evaluation by the PHENIX collaboration,” *Nucl. Phys. A*, vol. 757, pp. 184–283, 2005.
- [8] K. Aamodt *et al.*, “Suppression of Charged Particle Production at Large Transverse Momentum in Central Pb-Pb Collisions at $\sqrt{s_{NN}} = 2.76$ TeV,” *Phys. Lett. B*, vol. 696, pp. 30–39, 2011.
- [9] V. Khachatryan *et al.*, “Charged-particle nuclear modification factors in PbPb and pPb collisions at $\sqrt{s_{NN}} = 5.02$ TeV,” *JHEP*, vol. 04, p. 039, 2017.
- [10] S. Chatrchyan *et al.*, “Observation and studies of jet quenching in PbPb collisions at nucleon-nucleon center-of-mass energy = 2.76 TeV,” *Phys. Rev. C*, vol. 84, p. 024906, 2011.

- [11] G. Aad *et al.*, “Observation of a Centrality-Dependent Dijet Asymmetry in Lead-Lead Collisions at $\sqrt{s_{NN}} = 2.77$ TeV with the ATLAS Detector at the LHC,” *Phys. Rev. Lett.*, vol. 105, p. 252303, 2010.
- [12] B. Abelev *et al.*, “Measurement of charged jet suppression in Pb-Pb collisions at $\sqrt{s_{NN}} = 2.76$ TeV,” *JHEP*, vol. 03, p. 013, 2014.
- [13] T. K. Nayak, “Probing the QCD phase structure using event-by-event fluctuations,” *J. Phys. Conf. Ser.*, vol. 1602, no. 1, p. 012003, 2020.
- [14] A. Bazavov *et al.*, “Chiral crossover in QCD at zero and non-zero chemical potentials,” *Phys. Lett. B*, vol. 795, pp. 15–21, 2019.
- [15] W. Busza, K. Rajagopal, and W. van der Schee, “Heavy Ion Collisions: The Big Picture, and the Big Questions,” *Ann. Rev. Nucl. Part. Sci.*, vol. 68, pp. 339–376, 2018.
- [16] E. Abbas *et al.*, “Centrality dependence of the pseudorapidity density distribution for charged particles in Pb-Pb collisions at $\sqrt{s_{NN}} = 2.76$ TeV,” *Phys. Lett. B*, vol. 726, pp. 610–622, 2013.
- [17] K. Aamodt *et al.*, “Suppression of Charged Particle Production at Large Transverse Momentum in Central Pb-Pb Collisions at $\sqrt{s_{NN}} = 2.76$ TeV,” *Phys. Lett. B*, vol. 696, pp. 30–39, 2011.
- [18] M. L. Miller, K. Reygers, S. J. Sanders, and P. Steinberg, “Glauber modeling in high energy nuclear collisions,” *Ann. Rev. Nucl. Part. Sci.*, vol. 57, pp. 205–243, 2007.
- [19] F. Gelis, E. Iancu, J. Jalilian-Marian, and R. Venugopalan, “The Color Glass Condensate,” *Ann. Rev. Nucl. Part. Sci.*, vol. 60, pp. 463–489, 2010.
- [20] A. Bazavov *et al.*, “Equation of state and QCD transition at finite temperature,” *Phys. Rev. D*, vol. 80, p. 014504, 2009.
- [21] C. Gattringer and K. Langfeld, “Approaches to the sign problem in lattice field theory,” *Int. J. Mod. Phys. A*, vol. 31, no. 22, p. 1643007, 2016.
- [22] W. Florkowski, *Phenomenology of Ultra-Relativistic Heavy-Ion Collisions*. 3 2010.
- [23] C. Adler *et al.*, “Azimuthal anisotropy and correlations in the hard scattering regime at RHIC,” *Phys. Rev. Lett.*, vol. 90, p. 032301, 2003.
- [24] Z. Qiu, C. Shen, and U. Heinz, “Hydrodynamic elliptic and triangular flow in Pb-Pb collisions at $\sqrt{s} = 2.76$ ATeV,” *Phys. Lett. B*, vol. 707, pp. 151–155, 2012.

- [25] P. Kovtun, D. T. Son, and A. O. Starinets, “Viscosity in strongly interacting quantum field theories from black hole physics,” *Phys. Rev. Lett.*, vol. 94, p. 111601, 2005.
- [26] A. Andronic, P. Braun-Munzinger, K. Redlich, and J. Stachel, “Decoding the phase structure of QCD via particle production at high energy,” *Nature*, vol. 561, no. 7723, pp. 321–330, 2018.
- [27] K. Aamodt *et al.*, “Elliptic flow of charged particles in Pb-Pb collisions at 2.76 TeV,” *Phys. Rev. Lett.*, vol. 105, p. 252302, 2010.
- [28] L. Apolinário, Y.-J. Lee, and M. Winn, “Heavy quarks and jets as probes of the QGP,” 3 2022.
- [29] B. Abelev *et al.*, “Transverse momentum distribution and nuclear modification factor of charged particles in p -Pb collisions at $\sqrt{s_{NN}} = 5.02$ TeV,” *Phys. Rev. Lett.*, vol. 110, no. 8, p. 082302, 2013.
- [30] F. Arleo, “Hard pion and prompt photon at RHIC, from single to double inclusive production,” *JHEP*, vol. 09, p. 015, 2006.
- [31] G. Aad *et al.*, “Observation of a Centrality-Dependent Dijet Asymmetry in Lead-Lead Collisions at $\sqrt{s_{NN}} = 2.77$ TeV with the ATLAS Detector at the LHC,” *Phys. Rev. Lett.*, vol. 105, p. 252303, 2010.
- [32] R. Kogler *et al.*, “Jet Substructure at the Large Hadron Collider: Experimental Review,” *Rev. Mod. Phys.*, vol. 91, no. 4, p. 045003, 2019.
- [33] A. J. Larkoski, I. Moult, and B. Nachman, “Jet Substructure at the Large Hadron Collider: A Review of Recent Advances in Theory and Machine Learning,” *Phys. Rept.*, vol. 841, pp. 1–63, 2020.
- [34] G. P. Salam, “Towards Jetography,” *Eur. Phys. J. C*, vol. 67, pp. 637–686, 2010.
- [35] Y. L. Dokshitzer, V. A. Khoze, A. H. Mueller, and S. I. Troian, *Basics of perturbative QCD*. Editions Frontieres, 1991.
- [36] R. K. Ellis, W. J. Stirling, and B. R. Webber, *QCD and collider physics*. Cambridge monographs on particle physics, nuclear physics, and cosmology, Cambridge: Cambridge University Press, 2003. Photography by S. Vascotto.
- [37] V. N. Gribov and L. N. Lipatov, “Deep inelastic $e p$ scattering in perturbation theory,” *Sov. J. Nucl. Phys.*, vol. 15, pp. 438–450, 1972.

- [38] G. Altarelli and G. Parisi, “Asymptotic Freedom in Parton Language,” *Nucl. Phys. B*, vol. 126, pp. 298–318, 1977.
- [39] Y. L. Dokshitzer, “Calculation of the Structure Functions for Deep Inelastic Scattering and e^+e^- Annihilation by Perturbation Theory in Quantum Chromodynamics.,” *Sov. Phys. JETP*, vol. 46, pp. 641–653, 1977.
- [40] G. Marchesini and B. R. Webber, “Monte Carlo Simulation of General Hard Processes with Coherent QCD Radiation,” *Nucl. Phys. B*, vol. 310, pp. 461–526, 1988.
- [41] Y. L. Dokshitzer, V. A. Khoze, S. I. Troyan, and A. H. Mueller, “Qcd coherence in high-energy reactions,” *Rev. Mod. Phys.*, vol. 60, pp. 373–388, Apr 1988.
- [42] J. Casalderrey-Solana and C. A. Salgado, “Introductory lectures on jet quenching in heavy ion collisions,” *Acta Phys. Polon. B*, vol. 38, pp. 3731–3794, 2007.
- [43] K. J. Eskola, V. J. Kolhinen, and C. A. Salgado, “The Scale dependent nuclear effects in parton distributions for practical applications,” *Eur. Phys. J. C*, vol. 9, pp. 61–68, 1999.
- [44] K. Zapp, G. Ingelman, J. Rathsmann, J. Stachel, and U. A. Wiedemann, “A Monte Carlo Model for ‘Jet Quenching’,” *Eur. Phys. J. C*, vol. 60, pp. 617–632, 2009.
- [45] P. Caucal, E. Iancu, A. H. Mueller, and G. Soyez *Phys. Rev. Lett.*, vol. 120, p. 232001, 2018.
- [46] M. Connors, C. Nattrass, R. Reed, and S. Salur, “Jet measurements in heavy ion physics,” *Rev. Mod. Phys.*, vol. 90, p. 025005, 2018.
- [47] L. Cunqueiro and A. M. Sickles, “Studying the QGP with Jets at the LHC and RHIC,” *Prog. Part. Nucl. Phys.*, vol. 124, p. 103940, 2022.
- [48] Y. Mehtar-Tani, J. G. Milhano, and K. Tywoniuk, “Jet physics in heavy-ion collisions,” *Int. J. Mod. Phys. A*, vol. 28, p. 1340013, 2013.
- [49] D. d’Enterria, “Jet quenching,” *Landolt-Bornstein*, vol. 23, p. 471, 2010.
- [50] J. Casalderrey-Solana, H. Liu, D. Mateos, K. Rajagopal, and U. A. Wiedemann, *Gauge/String Duality, Hot QCD and Heavy Ion Collisions*. Cambridge University Press, 2014.
- [51] R. Baier, Y. L. Dokshitzer, A. H. Mueller, S. Peigne, and D. Schiff, “Radiative energy loss of high-energy quarks and gluons in a finite volume quark - gluon plasma,” *Nucl. Phys. B*, vol. 483, pp. 291–320, 1997.

- [52] L. D. McLerran and R. Venugopalan, “Computing quark and gluon distribution functions for very large nuclei,” *Phys. Rev. D*, vol. 49, pp. 2233–2241, 1994.
- [53] L. D. McLerran and R. Venugopalan, “Gluon distribution functions for very large nuclei at small transverse momentum,” *Phys. Rev. D*, vol. 49, pp. 3352–3355, 1994.
- [54] L. D. McLerran and R. Venugopalan, “Green’s functions in the color field of a large nucleus,” *Phys. Rev. D*, vol. 50, pp. 2225–2233, 1994.
- [55] P. Caucal, “Jet evolution in a dense QCD medium,” other thesis, 10 2020.
- [56] F. Gelis and Y. Mehtar-Tani, “Gluon propagation inside a high-energy nucleus,” *Phys. Rev. D*, vol. 73, p. 034019, 2006.
- [57] M. Gyulassy and X.-n. Wang, “Multiple collisions and induced gluon Bremsstrahlung in QCD,” *Nucl. Phys. B*, vol. 420, pp. 583–614, 1994.
- [58] P. Aurenche, F. Gelis, and H. Zaraket, “A Simple sum rule for the thermal gluon spectral function and applications,” *JHEP*, vol. 05, p. 043, 2002.
- [59] J.-P. Blaizot, F. Dominguez, E. Iancu, and Y. Mehtar-Tani, “Medium-induced gluon branching,” *JHEP*, vol. 01, p. 143, 2013.
- [60] Y. Mehtar-Tani and K. Tywoniuk, “Radiative energy loss of neighboring subjects,” *Nucl. Phys. A*, vol. 979, pp. 165–203, 2018.
- [61] L. Apolinário, N. Armesto, J. G. Milhano, and C. A. Salgado, “Medium-induced gluon radiation and colour decoherence beyond the soft approximation,” *JHEP*, vol. 02, p. 119, 2015.
- [62] J.-P. Blaizot, F. Dominguez, E. Iancu, and Y. Mehtar-Tani, “Probabilistic picture for medium-induced jet evolution,” *JHEP*, vol. 06, p. 075, 2014.
- [63] Y. Mehtar-Tani, C. A. Salgado, and K. Tywoniuk, “Jets in QCD Media: From Color Coherence to Decoherence,” *Phys. Lett. B*, vol. 707, pp. 156–159, 2012.
- [64] S. Caron-Huot and C. Gale, “Finite-size effects on the radiative energy loss of a fast parton in hot and dense strongly interacting matter,” *Phys. Rev. C*, vol. 82, p. 064902, 2010.
- [65] X. Feal and R. Vazquez, “Intensity of gluon bremsstrahlung in a finite plasma,” *Phys. Rev. D*, vol. 98, no. 7, p. 074029, 2018.
- [66] C. Andres, L. Apolinário, and F. Dominguez, “Medium-induced gluon radiation with full resummation of multiple scatterings for realistic parton-medium interactions,” *JHEP*, vol. 07, p. 114, 2020.

- [67] M. Gyulassy, P. Levai, and I. Vitev, “Jet quenching in thin quark gluon plasmas. 1. Formalism,” *Nucl. Phys. B*, vol. 571, pp. 197–233, 2000.
- [68] U. A. Wiedemann, “Gluon radiation off hard quarks in a nuclear environment: Opacity expansion,” *Nucl. Phys. B*, vol. 588, pp. 303–344, 2000.
- [69] M. Djordjevic and M. Gyulassy, “Heavy quark radiative energy loss in QCD matter,” *Nucl. Phys. A*, vol. 733, pp. 265–298, 2004.
- [70] M. D. Sievert and I. Vitev, “Quark branching in QCD matter to any order in opacity beyond the soft gluon emission limit,” *Phys. Rev. D*, vol. 98, no. 9, p. 094010, 2018.
- [71] C. Andres, F. Dominguez, and M. Gonzalez Martinez, “From soft to hard radiation: the role of multiple scatterings in medium-induced gluon emissions,” *JHEP*, vol. 03, p. 102, 2021.
- [72] Y. Mehtar-Tani, “Gluon bremsstrahlung in finite media beyond multiple soft scattering approximation,” *JHEP*, vol. 07, p. 057, 2019.
- [73] Y. Mehtar-Tani and K. Tywoniuk, “Improved opacity expansion for medium-induced parton splitting,” *JHEP*, vol. 06, p. 187, 2020.
- [74] J. a. Barata and Y. Mehtar-Tani, “Improved opacity expansion at NNLO for medium induced gluon radiation,” *JHEP*, vol. 10, p. 176, 2020.
- [75] J. a. Barata, Y. Mehtar-Tani, A. Soto-Ontoso, and K. Tywoniuk, “Revisiting transverse momentum broadening in dense QCD media,” *Phys. Rev. D*, vol. 104, no. 5, p. 054047, 2021.
- [76] J. a. Barata, Y. Mehtar-Tani, A. Soto-Ontoso, and K. Tywoniuk, “Medium-induced radiative kernel with the Improved Opacity Expansion,” *JHEP*, vol. 09, p. 153, 2021.
- [77] B. Zakharov, “Fully quantum treatment of the Landau-Pomeranchuk-Migdal effect in QED and QCD,” *JETP Lett.*, vol. 63, pp. 952–957, 1996.
- [78] P. B. Arnold, G. D. Moore, and L. G. Yaffe, “Effective kinetic theory for high temperature gauge theories,” *JHEP*, vol. 01, p. 030, 2003.
- [79] P. Arnold and S. Iqbal, “The LPM effect in sequential bremsstrahlung,” *JHEP*, vol. 04, p. 070, 2015. [Erratum: *JHEP* 09, 072 (2016)].
- [80] P. Arnold, T. Gorda, and S. Iqbal, “The LPM effect in sequential bremsstrahlung: nearly complete results for QCD,” *JHEP*, vol. 11, p. 053, 2020.
- [81] P. Arnold, T. Gorda, and S. Iqbal, “The LPM effect in sequential bremsstrahlung: analytic results for sub-leading (single) logarithms,” *JHEP*, vol. 04, p. 085, 2022.

-
- [82] J.-P. Blaizot, E. Iancu, and Y. Mehtar-Tani, “Medium-induced QCD cascade: democratic branching and wave turbulence,” *Phys. Rev. Lett.*, vol. 111, p. 052001, 2013.
- [83] J.-P. Blaizot and Y. Mehtar-Tani, “Energy flow along the medium-induced parton cascade,” *Annals Phys.*, vol. 368, pp. 148–176, 2016.

Scientific articles

Article I

Wilson line correlators beyond the large- N_c

J. H. Isaksen and K. Tywoniuk

Journal of High Energy Physics, **11**, 125 (2021)

Wilson line correlators beyond the large- N_c

Johannes Hamre Isaksen and Konrad Tywoniuk

*Department of Physics and Technology, University of Bergen,
5007 Bergen, Norway*

E-mail: johannes.isaksen@uib.no, konrad.tywoniuk@uib.no

ABSTRACT: We study hard $1 \rightarrow 2$ final-state parton splittings in the medium, and put special emphasis on calculating the Wilson line correlators that appear in these calculations. As partons go through the medium their color continuously rotates, an effect that is encapsulated in a Wilson line along their trajectory. When calculating observables, one typically has to calculate traces of two or more medium-averaged Wilson lines. These are usually dealt with in the literature by invoking the large- N_c limit, but exact calculations have been lacking in many cases. In our work, we show how correlators of multiple Wilson lines appear, and develop a method to calculate them numerically to all orders in N_c . Initially, we focus on the trace of four Wilson lines, which we develop a differential equation for. We will then generalize this calculation to a product of an arbitrary number of Wilson lines, and show how to do the exact calculation numerically, and even analytically in the large- N_c limit. Color sub-leading corrections, that are suppressed with a factor N_c^{-2} relative to the leading scaling, are calculated explicitly for the four-point correlator and we discuss how to extend this method to the general case. These results are relevant for high- p_T jet processes and initial stage physics at the LHC.

KEYWORDS: Heavy Ion Phenomenology, Jets

ARXIV EPRINT: [2107.02542](https://arxiv.org/abs/2107.02542)

Contents

1	Introduction	1
2	Basic elements and notation	4
3	Emission spectra	7
3.1	Derivation of the splitting functions	9
3.2	Numerical results	12
4	Calculating Wilson line correlators	15
4.1	Four Wilson lines	16
4.2	General method for Wilson line correlators	20
4.3	Wilson line correlators in the large- N_c limit	23
5	Conclusion and outlook	26
A	Calculation of spectrums	27
A.1	Pair production	27
A.2	Quark-gluon splitting	27
A.3	Gluon-gluon splitting	28
B	Six and eight Wilson lines	30
B.1	Six lines	30
B.1.1	Quark-gluon splitting in the large- N_c	31
B.2	Eight Wilson lines	32
C	Derivation of differential equation	32

1 Introduction

One of the primary reasons for colliding heavy ions with ultra-relativistic energies is to probe QCD matter in an extremely hot and dense phase, called the quark-gluon plasma (QGP). There are multiple ways to probe and learn about the properties of QGP, utilizing the properties of bulk particle production and rare probes. In one example of the latter category, the heavy-ion collision involves a hard partonic sub-collision that produces hard partons that propagate through the medium and escape to the detectors as jets. The study of how the properties of these jets change as they go through the medium, colloquially referred to as “jet quenching,” is a versatile tool to study hot QCD matter [1–3].

Experiments at RHIC [4, 5] and the LHC [6–10] colliders have found strong suppression of high- p_T particles in heavy-ion collisions compared to proton-proton collisions, which is

interpreted as a clear sign of the energy loss of jets that suffer final-state interactions with the surrounding QGP. On the theoretical side, this is interpreted in terms of radiative energy loss, where particles in the jet lose energy through medium-induced emission of gluons that end up outside of the reconstructed jet cone, and elastic drag. For large media, as typically encountered in central to semi-central lead-lead collisions, it is the former process that dominates the total lost energy.

The energy loss process for single partons is well understood since many years, see, e.g., [11–17]. However, a jet is a more complicated composite object consisting of several hard partons. A hard parton propagating through the medium will typically undergo several splittings, resulting in a multi-parton state that will interact differently with the medium compared to how the individual partons would. Such splittings can occur as long as the scale of the splittings, for instance the generated relative transverse momentum in the splitting, is bigger than what the medium can supply through multiple scattering. In particular, the modifications of effects of color coherence play an important role in determining which emissions will be resolved by the medium and contribute toward the total energy loss [18–21]. Instead of focusing on single partons, we will study a hard parton splitting into two, and their subsequent propagation through the medium. This is certainly a better approximation of a real jet than a single parton, and has the additional advantage that one can build up jets from several partons by consecutive $1 \rightarrow 2$ splittings.

Previous studies of such processes focused mostly on a hard photon splitting into a quark-antiquark pair [18, 22] and invoked the large- N_c approximation to obtain analytical formulas. In this work, we consider three generic QCD splitting processes that involve up to eight correlated Wilson lines in the fundamental representation, in the case of gluon splitting into two daughter gluons. Our specific improvement concerns a more precise way to calculate correlators of Wilson lines that often appear in these calculations, and it can, in principle, be extended for an arbitrary number of propagating particles through the medium.

To give a general flavor of how our procedure works, recall that a matrix element generally involves several propagators that resum multiple scattering through Wilson lines V , which extend along the trajectories in the medium. Ignoring some factors irrelevant for the present discussion, the matrix element squared will take the following simplified form

$$\langle |\mathcal{M}|^2 \rangle \sim \langle \text{tr}[V^\dagger V \dots V^\dagger V] \dots \text{tr}[V^\dagger V \dots V^\dagger V] \rangle, \quad (1.1)$$

where the angular brackets denote an average over medium configurations. For a generic $1 \rightarrow 2$ process, the amplitude squared can be reduced to a product of two-, three- and four-point correlators [23, 24]. To calculate these processes it is imperative to know the form of the Wilson line correlator appearing on the right hand side of (1.1), which we will denote by the letter C^K for correlator, where the superscript K refers to the number of traces. If you assume that the number of colors N_c is large the calculation of these correlators usually simplifies sufficiently to be possible to calculate. Namely, the leading N_c scaling emerges from simplifying the medium averages to $\langle \text{tr}[V^\dagger V \dots V^\dagger V] \rangle \dots \langle \text{tr}[V^\dagger V \dots V^\dagger V] \rangle$, which scales like N_c^K . However, since $N_c = 3$ is not a very large number it is sensible to ask whether this approximation is sound or not. As we will see, the terms that are discarded by performing the large- N_c approximation will be smaller than the other terms by a factor

$\sim 1/N_c^2 \simeq 10\%$ for typical situations. However, evaluating the correlators at large times, could lead to big discrepancies between the finite and large- N_c calculations.

In this paper we will develop a method for calculating correlators of an arbitrary number of Wilson lines at finite N_c , which casts their evolution and mixing in terms of a coupled evolution equation in time (referring to their trajectories through the medium). This reduces the complexity of the formulation compared to previous calculations of multi-Wilson line correlators, see [25, 26] for a technique based on diagonalization of the evolution matrix and [24, 27] for an iterative procedure. The derivation of the evolution matrix culminates in eq. (4.26). This allows us to evaluate these correlators at an arbitrary time, and can be addressed using numerical techniques. We also consider in detail the large- N_c approximation, which leads to a striking simplification of the dynamics since all higher-order correlators can be calculated using two-point correlators (dipoles) and their convolutions. Furthermore, we have computed the sub-leading correction in color. Considering again the generic correlator C^K from eq. (1.1) above, the generic expansion in N_c takes the following form,

$$C^K = N_c^K \hat{C}_{\text{leading } N_c}^K + N_c^{K-2} \hat{C}_{\text{sub-leading } N_c}^K + \mathcal{O}(N_c^{K-4}), \quad (1.2)$$

where the two first terms can be found analytically (the hat over the correlators imply that we have explicitly extracted their leading N_c behavior). It turns out that, in many cases, $C_{\text{sub-leading } N_c}^K$ is essential to recover the correct long-time behavior of the correlators.

We will explore how big the error is by comparing the exact results to the large- N_c approximation in realistic settings in high-energy jet splittings. We mainly consider hard emissions early in the medium, i.e. at scales much larger than those provided by the medium, and therefore we neglect any broadening of the particles. The daughters are traversing the medium at a fixed angle, or “tilt”, given by the kinematics of the hard splitting (we fix our coordinate system so that the parent particle has zero angle). For splittings where at least one of the daughters becomes very soft or is being emitted at a large angle, one should also allow for additional transverse momentum broadening, as done in [23, 24], albeit only in the large- N_c approximation. We have left this additional complication for future work.

Our calculation is also very pertinent for improving our understanding of color dynamics in the medium, for instance in the context of multi-gluon emissions with overlapping formation times [28] and to understand hadronization after exiting the QGP [29]. In the process of evaluation of the multi-Wilson line correlators, the only assumption made is the exact form of the medium average, see eq. (2.5), which is also employed in other contexts than for a thermal medium, see, e.g., [30] for calculating such correlators on the lattice. Therefore, although we have derived our method of calculating Wilson line correlators in the context of jet quenching, it is a general result that can be applied in more branches of QCD. One concrete example refer to initial state physics, where multi-particle production is considered an important channel to verify saturation effects in the nuclei [25, 31, 32]. Furthermore, sub-leading corrections in color have also been considered in the context of high-energy QCD evolution at next-to-leading order [33]. Finally, the generic color structure of high-energy QCD events is actively studied [27, 34]. It is also interesting to note that sub-leading color corrections have been considered in the context of improving parton showers in the vacuum, see, e.g., [35, 36].

Let us briefly outline the structure of the paper. Section 2 introduces the notation and formalism we will make use of throughout the paper. In section 3 we will consider three examples of splitting processes that lead to Wilson line correlators: a photon producing a quark-antiquark pair, a quark emitting a gluon and a gluon splitting into two gluons. Those processes will provide the motivation for the rest of the calculation in the paper. In section 4.1, we will go into detail about calculating the simplest of the Wilson line structures from section 3, which is a trace of four lines. Here, we also develop a method to compute the color sub-leading corrections, corresponding to the second term on the right hand side in eq. (1.2). Thereafter, in section 4 we will generalize the method used in section 4.1 to correlators of an arbitrary number of Wilson lines, and show how one can always make a system of differential equations to describe these structures. This section contains the main theoretical results of the paper. The formulas developed in section 4 are used to calculate the more complicated Wilson line structures appearing in section 3. We will show how the calculations simplify in the large- N_c approximation, and use numerical evaluation to compare the approximate results to the exact ones.

2 Basic elements and notation

We will assume that the partons propagating through the medium are highly energetic and travelling on the light-cone almost strictly in the positive z direction. In light-cone (LC) coordinates it will have momentum (p^+, p^-, \mathbf{p}) , where $p^+ = (p^0 + p^3)/2$ is identified with the LC energy $E \equiv p^+$, $p^- = p^0 - p^3$ is negligible and \mathbf{p} is the transverse momentum. The parton interacts with the medium, which is modelled by a classical background gauge field $A^{\mu,a}(t, \mathbf{r})$. The interaction of the parton with the classical field leads to transverse momentum broadening and energy loss. The interactions can be resummed using a framework developed by Baier-Dokshitzer-Mueller-Peigné-Schiff [11–14] and Zakharov [15, 16], and is known as the BDMPS-Z formalism. For small media, where interactions are rare, this is equivalent with considering only one interaction, known as the Gyulassy-Levai-Vitev (GLV) [37] approximation.

It is possible to construct Feynman rules from the BDMPS-Z approach, with special in-medium propagators and vertices [18]. In this formulation a highly energetic parton travelling through the medium can be described by the propagator

$$(\mathbf{x}|\mathcal{G}_R(t, t_0)|\mathbf{x}_0) = \Theta(t - t_0) \int_{\mathbf{x}_0}^{\mathbf{x}} \mathcal{D}\mathbf{r} \exp \left[i \frac{E}{2} \int_{t_0}^t ds \dot{\mathbf{r}}^2(s) \right] V_R(t, t_0; \mathbf{r}(t)). \quad (2.1)$$

In this expression V_R is a Wilson line in the representation R , which is given by

$$V_R(t, t_0; \mathbf{r}(t)) = \mathcal{P} \exp \left[ig \int_{t_0}^t ds A^a(s, \mathbf{r}(s)) T_R^a \right], \quad (2.2)$$

where the symbol \mathcal{P} enforces path ordering. A quark transforms in the fundamental representation, so the group generator is $T_F^a \equiv t_{ij}^a$. Similarly, a gluon transforms in the adjoint representation, and its group generator is $T_A^a \equiv (T^a)^{bc} = -if^{abc}$. The final results in this paper will mainly concern fundamental lines, which we will denote by $V \equiv V_F$.

Similarly, we will write the adjoint lines as $U \equiv V_A$. Focusing on fundamental lines is sufficient, since one can always transform adjoint Wilson lines to fundamental ones through the identity

$$U^{ab} = 2 \operatorname{tr} \left[t^a V t^b V^\dagger \right] = U^{\dagger ba}. \quad (2.3)$$

In the absence of interactions, i.e. when the Wilson line is evaluated at $g = 0$, we simply get

$$\langle \mathbf{x} | \mathcal{G}_0(t, t_0) | \mathbf{x}_0 \rangle \equiv \mathcal{G}_0(\mathbf{x} - \mathbf{x}_0, t - t_0) = \Theta(t - t_0) \frac{E}{2\pi i(t - t_0)} e^{i \frac{E}{2} \frac{(\mathbf{x} - \mathbf{x}_0)^2}{(t - t_0)}}, \quad (2.4)$$

which is a representation of the retarded part of the Feynman propagator ($E > 0$).

As mentioned in the introduction, the matrix element describing final-state interactions in the QGP will involve one or more propagators of the form in eq. (2.1). Hence, on the level of the matrix element squared, we have to compute correlators of such lines averaged over all possible medium configurations. The medium average is indicated by $\langle \dots \rangle$, and we assume that the correlator of the medium fields takes the form

$$\langle A^a(t, \mathbf{r}) A^b(t', \mathbf{r}') \rangle = \delta^{ab} n(t) \delta(t - t') \gamma(\mathbf{r} - \mathbf{r}'), \quad (2.5)$$

which corresponds to the Gaussian noise approximation. Here, $n(t)$ is the (time-dependent) density of scattering centers in the medium and

$$\gamma(\mathbf{r}) = \int \frac{d^2 \mathbf{q}}{(2\pi)^2} e^{i \mathbf{q} \cdot \mathbf{r}} \frac{d^2 \sigma_{\text{el}}}{d^2 \mathbf{q}} \sim g^2 \int \frac{d^2 \mathbf{q}}{(2\pi)^2} \frac{e^{i \mathbf{q} \cdot \mathbf{r}}}{\mathbf{q}^4}, \quad (2.6)$$

is the Fourier transform of the in-medium elastic scattering potential, where the infrared behavior of the potential is regulated by an in-medium screening mass. The delta function in time indicates that we have assumed the medium interactions to be instantaneous. In many cases it will be convenient to define

$$\sigma(\mathbf{r}) = g^2 [\gamma(\mathbf{0}) - \gamma(\mathbf{r})]. \quad (2.7)$$

The form of the function σ depends on how the medium is modelled. The two main ways of calculating this is through the Gyulassy-Wang model [38] or through Hard Thermal Loop theory [39]. These models differ mainly in how infrared screening is implemented when $q_\perp \rightarrow 0$. In this paper, we will however work in the harmonic oscillator approximation, which accounts for multiple soft interactions. In this case, the potential $\sigma(\mathbf{r})$ can be cast as

$$C_R n \sigma(\mathbf{r}) \simeq \frac{1}{4} \mathbf{r}^2 \hat{q}_R(t), \quad (2.8)$$

where

$$\hat{q}_R = C_R n g^2 \int^{q_\perp^{\text{max}}} \frac{d^2 \mathbf{q}}{(2\pi)^2} \mathbf{q}^2 \frac{d^2 \sigma_{\text{el}}}{d^2 \mathbf{q}}, \quad (2.9)$$

is the jet quenching coefficient where R denotes the color representation of the Wilson lines. For the fundamental and adjoint representations we have $C_F = \frac{N_c^2 - 1}{2N_c}$ and $C_A = N_c$, respectively. In this paper we will use $\hat{q} = \hat{q}_F$ unless otherwise stated. In eq. (2.9) we have explicitly introduced a UV cut-off to regularize the integral. A more systematic

approach to the regularization of the integral, and the extension beyond the soft scattering approximation, has been pursued in refs. [19, 40, 41].

We stress that the approximation in (2.8) is not necessary in order to solve numerically the system of equations for arbitrary n -point correlators, but it is very useful to employ to compare these exact results to analytical calculations of the leading and sub-leading color correlators.

In the current work, we will focus on hard $1 \rightarrow 2$ splitting processes in the medium, where the initial particle has energy E and the two splitting products carry, respectively, $\omega_1 = (1 - z)E$ and $\omega_2 = zE$. This is formally equivalent to setting the energy of the mother particle, $E \rightarrow \infty$, and considering a finite momentum sharing fraction $0 \ll z \ll 1$. These conditions enforce that both the mother and daughter particles travel on classical paths. Concretely, the trajectory of a particle in the medium between time t_0 and t , given by the propagator $(\mathbf{x}|\mathcal{G}(t, t_0)|\mathbf{x}_0)$, in configuration space, for $E \gg (t - t_0)^{-1}$ gets strongly constrained to the classical path connecting the initial and final transverse positions, see eq. (2.1), and leads to

$$(\mathbf{x}|\mathcal{G}_R(t, t_0)|\mathbf{x}_0) \simeq \mathcal{G}_0(\mathbf{x} - \mathbf{x}_0, t - t_0) V_R(t, t_0; [\mathbf{x}_{cl}(s)]), \quad (2.10)$$

where the classical trajectory is given by $\mathbf{x}_{cl}(s) = \mathbf{x}_0 + \frac{s-t_0}{t-t_0}(\mathbf{x} - \mathbf{x}_0)$. This corresponds to the product of a Wilson line, trailing the direction of the particle, times a vacuum propagator, see eq. (2.4). Corrections to this limit can also be systematically be calculated [42]. In the mixed representation, this leads to,

$$(\mathbf{p}|\mathcal{G}_R(t, t_0)|\mathbf{p}_0) \simeq (2\pi)^2 \delta(\mathbf{p} - \mathbf{p}_0) V_R(t, t_0; [\mathbf{x}_{cl}(s) = \mathbf{n}s]) e^{-i\frac{\mathbf{p}^2}{2E}(t-t_0)}, \quad (2.11)$$

where $\mathbf{n} = \mathbf{p}/E$, see [18, 22]. The last term in this product is simply the Fourier transform of the vacuum propagator.

In detail, the $1 \rightarrow 2$ partonic processes we consider are: 1) $\gamma \rightarrow q + \bar{q}$, 2) $q \rightarrow q + g$, 3) $g \rightarrow g + g$. These will, at most, involve correlators of 4, 6 and 8 Wilson lines (in the fundamental representation). We also write out the relevant correlators for $g \rightarrow q + \bar{q}$, but we do not explicitly evaluate the spectrum in this case. All three processes consist of one (off-shell) particle¹ traversing the medium splitting into two particles. While we derive formulas for a generic medium profile, our numerical calculations apply to a medium with constant density (aka the “brick”), where the splitting can occur either inside the medium or outside.

As mentioned above, the first particle, with LC energy E , is produced at initial time $t_0 = 0$ and is propagating along the light-cone in the positive z direction. It splits at times t_1 in the amplitude and t_2 in the complex conjugate amplitude, see figure 1. The two daughter particles, which now carry LC energies $(1 - z)E$ and zE , respectively, then propagate on the classical paths $\mathbf{r}_1(t)$ ($\mathbf{r}_{\bar{1}}(t)$) and $\mathbf{r}_2(t)$ ($\mathbf{r}_{\bar{2}}(t)$) in the amplitude (complex conjugate amplitude) to the end of the medium at L . In the high-energy, eikonal approximation these

¹We will however only consider physical polarizations/spin states for the initial particle, since other contributions do not propagate.

paths are classical and are given by

$$\begin{aligned}
 \mathbf{r}_1(t) &= \mathbf{n}_1(t - t_1), \\
 \mathbf{r}_2(t) &= \mathbf{n}_2(t - t_1), \\
 \mathbf{r}_{\bar{1}}(t) &= \mathbf{n}_1(t - t_2), \\
 \mathbf{r}_{\bar{2}}(t) &= \mathbf{n}_2(t - t_2),
 \end{aligned}
 \tag{2.12}$$

where $\mathbf{n}_1 \equiv \frac{\mathbf{p}_1}{(1-z)E}$ and $\mathbf{n}_2 \equiv \frac{\mathbf{p}_2}{zE}$ are the transverse velocity vectors. To slightly compress the notation we will usually refer to the coordinates as numbers, meaning that we will write $V(\mathbf{r}_1) \equiv V_1$ and $\gamma(\mathbf{r}_1 - \mathbf{r}_{\bar{2}}) \equiv \gamma_{1\bar{2}}$, etc.

Finally, in the harmonic approximation, we need the square of the differences of the transverse coordinates. Using the eikonal approximation this is

$$\begin{aligned}
 (\mathbf{r}_1 - \mathbf{r}_2)^2 &= (t - t_1)^2 \theta^2, \\
 (\mathbf{r}_{\bar{1}} - \mathbf{r}_{\bar{2}})^2 &= (t - t_2)^2 \theta^2, \\
 (\mathbf{r}_1 - \mathbf{r}_{\bar{1}})^2 &= z^2 (t_2 - t_1)^2 \theta^2, \\
 (\mathbf{r}_2 - \mathbf{r}_{\bar{2}})^2 &= (1 - z)^2 (t_2 - t_1)^2 \theta^2, \\
 (\mathbf{r}_1 - \mathbf{r}_{\bar{2}})^2 &= (t - zt_1 - (1 - z)t_2)^2 \theta^2, \\
 (\mathbf{r}_{\bar{1}} - \mathbf{r}_2)^2 &= (t - (1 - z)t_1 - zt_2)^2 \theta^2,
 \end{aligned}
 \tag{2.13}$$

where we have assumed that the angle θ is small.

3 Emission spectra

In this section we will present the results for the in-medium emission spectra $\frac{dI}{dzd\theta}$ for the in-medium splitting processes. We refer to appendix A for the details of the calculations. All of the Wilson line correlators in this section were calculated using the methods developed in section 4. For more details about the calculation of correlators of six and eight Wilson lines we refer to appendix B.

One can define the vacuum spectrum as

$$\frac{dI^{\text{vac}}}{dz d\theta} = \frac{\alpha P(z)}{\pi \theta}, \tag{3.1}$$

where α can be α_{em} or α_s depending on the process, and $P(z)$ is the relevant Altarelli-Parisi splitting function. Then one can write the full spectrum on the form [22]

$$\begin{aligned}
 \frac{dI^{\text{full}}}{dz d\theta} &= \frac{dI^{\text{vac}}}{dz d\theta} + \frac{dI^{\text{med}}}{dz d\theta} \\
 &= \frac{dI^{\text{vac}}}{dz d\theta} (1 + F_{\text{med}}(z, \theta)).
 \end{aligned}
 \tag{3.2}$$

The term $F_{\text{med}}(z, \theta)$ contains the medium modification to the processes. For a generic medium profile the medium radiation reads

$$\frac{dI^{\text{med}}}{dz d\theta} = \frac{dI^{\text{vac}}}{dz d\theta} 2\text{Re} \int_0^L \frac{dt_1}{t_f} \int_{t_1}^L \frac{dt_2}{t_f} e^{-i\frac{t_2-t_1}{t_f}} \mathcal{C}^{(4)}(L, t_2) \mathcal{C}^{(3)}(t_2, t_1), \tag{3.3}$$

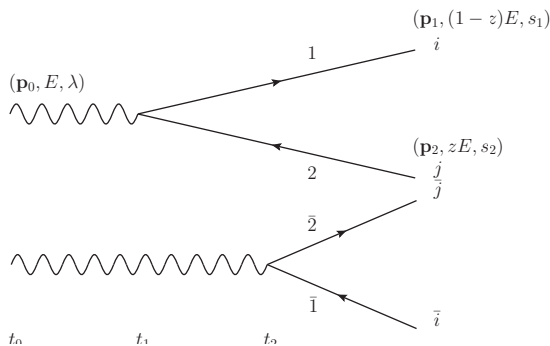


Figure 1. The process of a photon splitting to a quark-antiquark pair. The amplitude is on the top and the complex conjugate amplitude on the bottom. The splitting happens at time t_1 in the amplitude and at a later time t_2 in the complex conjugate amplitude.

where, in the high-energy limit employed in this paper, the medium-induced spectrum is proportional to the vacuum spectrum. This proportionality does not *a priori* hold in all the phase space, in particular whenever the transverse momentum in the splitting $k_{\perp} = z(1-z)E\theta$ is comparable to the transverse momentum accumulated in the medium $Q_s \sim \hat{q}L$ [23]. Finally, the factors $\mathcal{C}^{(n)}(t_b, t_a)$ appearing in (3.3) are n -particle correlators that have support during time $t_a < t < t_b$, and $t_f = \frac{2}{z(1-z)E\theta^2}$ is the formation time of the process. The splitting process is illustrated in figure 1.

For a medium with fixed density and extension L , we have $\hat{q}(t) = \hat{q}\Theta(L-t)$. In this case, the integrals over the emission times t_1 and t_2 in (3.3) can be split, so that

$$\frac{dI^{\text{in-in}}}{dz d\theta} = \frac{dI^{\text{vac}}}{dz d\theta} 2\text{Re} \int_0^L \frac{dt_1}{t_f} \int_{t_1}^L \frac{dt_2}{t_f} e^{-i\frac{t_2-t_1}{t_f}} \mathcal{C}^{(4)}(L, t_2) \mathcal{C}^{(3)}(t_2, t_1), \quad (3.4)$$

$$\frac{dI^{\text{in-out}}}{dz d\theta} = \frac{dI^{\text{vac}}}{dz d\theta} 2\text{Im} \int_0^L \frac{dt_1}{t_f} e^{-i\frac{L-t_1}{t_f}} \mathcal{C}^{(3)}(L, t_1), \quad (3.5)$$

where $dN^{\text{med}}/(dzd\theta) = dN^{\text{in-in}}/(dzd\theta) + dN^{\text{in-out}}/(dzd\theta)$. Taking into account that the Wilson line correlators are real the medium modification term can be written [22]

$$F_{\text{med}} = 2 \int_0^L \frac{dt_1}{t_f} \left[\int_{t_1}^L \frac{dt_2}{t_f} \cos\left(\frac{t_2-t_1}{t_f}\right) \mathcal{C}^{(4)}(L, t_2) \mathcal{C}^{(3)}(t_2, t_1) - \sin\left(\frac{L-t_1}{t_f}\right) \mathcal{C}^{(3)}(L, t_1) \right]. \quad (3.6)$$

We now will discuss three concrete cases that are relevant for jet quenching phenomenology. We will compute the double-differential spectrum for a wide range of LC energy sharing fraction z and angles θ to map the regions where medium-induced corrections appear, as quantified by the factor $F_{\text{med}}(z, \theta)$. Our focus here is to provide a test bed for evaluating precisely the multi-Wilson line correlators appearing in (3.6), and we will therefore not worry about the validity of the eikonal approximation (2.10) of the splitting products. Including non-eikonal corrections on the particle trajectories will be postponed to future work.

3.1 Derivation of the splitting functions

Photon splitting. We will start with the case of a photon splitting into a quark-antiquark pair, i.e. $\gamma \rightarrow q + \bar{q}$. Due to the least number of fundamental Wilson lines, this is the simplest process to analyze. We will therefore treat it in more detail, taking the advantage to discuss the relevant medium and jet scales appearing in the calculation.

In this case, the vacuum emission spectrum is given by (3.1) with the QED coupling constant α_{em} and the Altarelli-Parisi splitting function being $P_{q\gamma}(z) = n_f N_c [z^2 + (1-z)^2]$, where n_f is the number of active flavors. Furthermore, the correlator $\mathcal{C}^{(3)}$ reduces to an effective two-point function because the photon does not carry color charge. We have

$$\mathcal{C}_{q\gamma}^{(4)}(L, t_2) = \frac{1}{N_c} \langle \text{tr}[V_1 V_2^\dagger V_2 V_1^\dagger] \rangle, \quad (3.7)$$

$$\mathcal{C}_{q\gamma}^{(3)}(t_2, t_1) = \frac{1}{N_c} \text{tr} \langle V_1 V_2^\dagger \rangle, \quad (3.8)$$

where the time extension of each of the medium-averaged color correlators on the right hand side is implied by the time argument on left hand side of the equation.

The correlator of two Wilson lines, which in this case corresponds to $\mathcal{C}_{q\gamma}^{(3)}(t, t_1) = \mathcal{S}_{12}(t, t_1)$, is generally referred to as a dipole correlator, and is known to be

$$\mathcal{S}_{12}(t, t_1) \equiv \frac{1}{N_c} \langle \text{tr}[V_1 V_2^\dagger] \rangle = e^{-C_F \int_{t_1}^t ds n(s) \sigma(\mathbf{r})}, \quad (3.9)$$

where $\mathbf{r} = \mathbf{r}_1 - \mathbf{r}_2$ is the difference of transverse positions of the two Wilson lines. For a fixed separation, i.e. $\mathbf{r} = \text{const.}$, in the HO approximation and in a medium with constant density, it simply reads $\mathcal{S}_{12}(t, t_1) = e^{-\frac{1}{4} \hat{q}(t-t_1) r^2}$, where, as a reminder, we have denoted $\hat{q} \equiv \hat{q}_F$. However, for the kinematics we consider, see eq. (2.13), this becomes

$$\mathcal{S}_{12}(t, t_1) = e^{-\frac{1}{12} \hat{q}(t-t_1)^3 \theta^2}. \quad (3.10)$$

Then, assuming that $t = t_2$ and $t_2 - t_1 \sim t_f$, we find

$$\mathcal{S}_{12} \approx e^{-\frac{2}{3} \omega \frac{\hat{q}}{\omega^3 \theta^4}}, \quad (3.11)$$

with $\omega = z(1-z)E$. This implies that medium modifications appear, in this term, whenever $\omega^3 \theta^4 \lesssim \hat{q}$.

The correlator of four Wilson lines $\mathcal{C}^{(4)}(t, t_2)$, referred to as the quadrupole (in the fundamental representation), can only be calculated numerically at finite- N_c . We will later show how this can be achieved through the differential equation eq. (4.10). In the large- N_c limit, however, it can be calculated analytically through the simplified differential equation eq. (4.12). There are only two ways of connecting the Wilson lines at the final time (their connection at initial time is given by the vacuum splitting process). We can therefore define $C_{1\bar{2}}(t, t_2) \equiv \langle \text{tr}[V_1 V_2^\dagger] \text{tr}[V_{\bar{2}} V_{\bar{1}}^\dagger] \rangle$ and $C_{2\bar{1}}(t, t_2) \equiv \langle \text{tr}[V_1 V_2^\dagger V_{\bar{2}} V_{\bar{1}}^\dagger] \rangle$, note the absence of explicit normalization factors at this stage. In the large- N_c approximation, the first of these correlators reads simply,

$$\frac{1}{N_c^2} C_{1\bar{2}}(t, t_2) \simeq e^{-\frac{1}{12} \hat{q} \theta^2 [(t-t_2)^3 + (t-t_1)^3 - \tau^3]}, \quad (3.12)$$

where $\tau \equiv t_2 - t_1$, and the dependence on t_1 appears as a consequence of the fixed trajectories. Here we have used the eikonal (2.12) and harmonic oscillator approximations (2.8). Similarly, at large- N_c , the second correlator is

$$\frac{1}{N_c} C_{21}^r(t, t_2) \simeq e^{-\frac{1}{4} \hat{q} \theta^2 \xi (t-t_2) \tau^2} - \frac{1}{2} \hat{q} \theta^2 z (1-z) \tau^2 \int_{t_2}^t ds e^{-\frac{1}{4} \hat{q} \theta^2 \xi (t-s) \tau^2} e^{-\frac{1}{12} \hat{q} \theta^2 [(s-t_2)^3 + (s-t_1)^3 - \tau^3]}, \quad (3.13)$$

where we defined $\xi \equiv z^2 + (1-z)^2$. Only the latter of these correlators appears in the spectrum, cf. eq. (3.7), but we include both for completeness.² Assuming the dominance of the first term in (3.13), setting $t = L$ and assuming that $L \gg t_f$, we find that

$$\frac{1}{N_c} C_{21}^r \approx e^{-\frac{1}{6} \frac{\hat{q} L}{(\omega \theta)^2}}, \quad (3.14)$$

where we put $\xi \approx 2/3$. The factor in the exponential becomes large whenever $\omega \theta < \sqrt{\hat{q} L}$. This factor is related to momentum broadening of the quark and anti-quark after they have been produced.

Let us compare the two conditions when exponential suppression arise either in the dipole $\mathcal{S}_{12}(t_2, t_1)$ or quadrupole $C_{21}^r(L, t_2)$. For a fixed energy ω , the two conditions are equal at the critical angle

$$\theta_c \sim (\hat{q} L^3)^{-1/2}. \quad (3.15)$$

Let us also define the characteristic energies $\omega_d = (\hat{q}/\theta^4)^{1/3}$ and $\omega_{\text{broad}} = \sqrt{\hat{q} L}/\theta$. At large angles $\theta > \theta_c$, the condition from the dipole starts affecting soft gluon emissions, i.e. $\omega_d < \omega_{\text{broad}}$. This reflects the length-dependence color coherence. On the one hand, the dipole, which has support only during the formation time $t_f \lesssim L$, needs a large angle to resolve the two particles within that time scale. On the other hand, the quadrupole, which extends up to L , will ultimately resolve even narrower configurations.

We also plot the dependence on the latest time of both $C_{q\gamma}^{(3)}(t, t_1)$ and $C_{q\gamma}^{(4)}(t, t_2)$ in figure 2a, keeping $t_1 = 0.3 \text{ fm}$ fixed, in the case of the dipole, and both $t_2 = 1 \text{ fm}$ and $t_1 = 0.3 \text{ fm}$ fixed, in the case of the quadrupole. The other parameters are chosen as $\hat{q} = 1.5 \text{ GeV}^2/\text{fm}$, $\theta = 0.5$ and $z = 0.5$. We notice the fast decay of the dipole, that goes like $\sim e^{-t^3}$ according to (3.10), compared to the exponential decay of the quadrupole, i.e. $\sim e^{-t}$, at large times. Finally, we notice that the large- N_c approximation to the full quadrupole, given in eq. (3.13), is very good up very late times.

Quark-gluon splitting. Next we consider the slightly more complicated problem of a quark-gluon splitting. This was also outlined in [22], but not calculated explicitly. For this process, the vacuum emission spectrum is given by (3.1), with the QCD coupling constant α_s and the Altarelli-Parisi splitting function $P_{gq}(z) = C_F \frac{1+(1-z)^2}{z}$. The four- and

²In [22] C_{21}^r is also calculated in the large- N_c limit. In their eq. (29) they get the same as (3.13), except they lack the factor of 1/2 in front of the second term.

three-point functions read

$$\mathcal{C}_{gq}^{(4)}(L, t_2) = \frac{1}{N_c^2 - 1} \left\langle \text{tr}[V_1^\dagger V_1 V_2^\dagger V_2] \text{tr}[V_2^\dagger V_2] - \frac{1}{N_c} \text{tr}[V_1^\dagger V_1] \right\rangle, \quad (3.16)$$

$$\mathcal{C}_{gq}^{(3)}(t_2, t_1) = \frac{1}{N_c^2 - 1} \left\langle \text{tr}[V_2^\dagger V_1] \text{tr}[V_0^\dagger V_2] - \frac{1}{N_c} \text{tr}[V_0^\dagger V_1] \right\rangle. \quad (3.17)$$

The emission spectrum is composed of correlators of two, four and six Wilson lines. The three-point function can be solved exactly, see (B.7), resulting in

$$\begin{aligned} \mathcal{C}_{gq}^{(3)}(t_2, t_1) &= e^{-\frac{1}{2} \int_{t_1}^{t_2} ds n(s) [N_c(\sigma_{02} + \sigma_{12}) - \frac{1}{N_c} \sigma_{01}]} \\ &= e^{-\frac{1}{12} \hat{q}(t_2 - t_1)^3 \theta^2 \left(1 + z^2 + \frac{2z}{N_c^2 - 1}\right)}. \end{aligned} \quad (3.18)$$

This expression is very similar to the dipole term in eq. (3.10) and the same scale analysis applies.

The four-point correlator involving six and two Wilson lines can only be calculated numerically at finite N_c . In the large- N_c limit, the former can be calculated analytically, and reads

$$\begin{aligned} \frac{1}{N_c^2} \langle \text{tr}[V_1 V_2^\dagger V_2 V_1^\dagger] \text{tr}[V_2 V_2^\dagger] \rangle &\simeq e^{-\frac{1}{4} \hat{q} \theta^2 (t - t_2)(t_2 - t_1)^2 (1 - 2z + 3z^2)} \\ &\times \left(1 - \frac{1}{2} \hat{q} \theta^2 z(1 - z)(t_2 - t_1)^2 \int_{t_2}^t ds e^{-\frac{1}{12} \hat{q} \theta^2 [(s - t_2)^2 (2s - 3t_1 + t_2) + 6z(1 - z)(s - t_2)(t_2 - t_1)^2]} \right). \end{aligned} \quad (3.19)$$

Once again, the first term in the correlator above has a form very similar to the four-point function relevant for photon splitting, see eq. (3.13).

Gluon-gluon splitting. The last process of interest is the case of a gluon splitting into two other gluons. This process was discussed quite extensively in [23]. For this process, the vacuum emission spectrum is given by (3.1) with the QCD coupling constant α_s and the Altarelli-Parisi splitting function $P_{gg}(z) = 2N_c \left[z(1 - z) + \frac{1-z}{z} + \frac{z}{1-z} \right]$. In this case the 4- and 3-point functions read

$$\mathcal{C}_{gg}^{(4)}(L, t_2) = \frac{1}{N_c(N_c^2 - 1)} \left\langle \text{tr}[V_1 V_1^\dagger] \text{tr}[V_2 V_2^\dagger V_1^\dagger V_1] \text{tr}[V_2 V_2^\dagger] - \text{tr}[V_1 V_1^\dagger V_2 V_2^\dagger V_1^\dagger V_1 V_2 V_2^\dagger] \right\rangle, \quad (3.20)$$

$$\mathcal{C}_{gg}^{(3)}(t_2, t_1) = \frac{1}{N_c(N_c^2 - 1)} \left\langle \text{tr}[V_1 V_2^\dagger] \text{tr}[V_0 V_1^\dagger] \text{tr}[V_2 V_0^\dagger] - \text{tr}[V_1 V_2^\dagger V_0 V_1^\dagger V_2 V_0^\dagger] \right\rangle. \quad (3.21)$$

When cast as correlators of Wilson lines in the fundamental representation, the $\mathcal{C}_{gg}^{(4)}$ involves 8-point correlators, which is the largest number we will calculate in detail.

The 3-point function can be solved exactly, either by the differential equation (4.26) or by writing it in terms of adjoint Wilson lines (A.17). In the end, the result reads

$$\begin{aligned} \mathcal{C}_{gg}^{(3)}(t_2, t_1) &= e^{-\frac{N_c}{2} \int_{t_1}^{t_2} dt n(t) [\sigma_{01} + \sigma_{02} + \sigma_{12}]} \\ &= e^{-\frac{1}{12} \hat{q}(t_2 - t_1)^3 \theta^2 \frac{N_c}{C_F} (1 - z + z^2)}. \end{aligned} \quad (3.22)$$

Note the similarity to the previous results, see eqs. (3.10) and (3.18).

The 4-point function consists of two different correlators of eight Wilson lines. They can be calculated through the differential equation in eq. (4.26). Interestingly, the four-point function $C_{gg}^{(4)}$ involves a eight-point correlator, see the second term in (3.20), which cannot be reduced further in the large- N_c approximation. This can nevertheless still be exactly solved in the large- N_c approximation, which we present in the figures below, but the expression is too long to extract any meaningful approximation. Anticipating the numerical results, we can mention that it is for this correlator that the large- N_c approximation gives the biggest deviations with respect to the exact result.

Gluon-quark splitting. We now consider a gluon that splits into a quark-antiquark pair. The Altarelli-Parisi splitting function is $P_{qg}(z) = n_f T_R [z^2 + (1-z)^2]$ and the correlators read

$$C_{qg}^{(4)}(L, t_2) = \frac{1}{N_c} \left\langle \text{tr}[V_1 V_2^\dagger V_2 V_1^\dagger] - \frac{1}{N_c} \text{tr}[V_1 V_1^\dagger] \text{tr}[V_2 V_2^\dagger] \right\rangle, \quad (3.23)$$

$$C_{qg}^{(3)}(t_2, t_1) = \frac{1}{N_c^2 - 1} \left\langle \text{tr}[V_1 V_0^\dagger] \text{tr}[V_0 V_2^\dagger] - \frac{1}{N_c} \text{tr}[V_1 V_2^\dagger] \right\rangle. \quad (3.24)$$

Since these expressions involve only quadrupoles and dipoles, that were previously encountered and analyzed in detail above, we will not present further results for this splitting process.

3.2 Numerical results

Here we present the numerical calculations of the results from the previous section. We focus first on the details of the three- and four-point functions for each of the three splitting processes, and proceed with calculating the double-differential spectrum in the momentum sharing fraction z and angle θ .

In figure 2, we show how $C_{ij}^{(3)}(t, t_1)$, with blue, solid curves, and $C_{ij}^{(4)}(t, t_2)$, with orange, solid curves, for the three processes evolve with time. For the four-point functions, we also plot the large- N_c approximation with orange, dashed curves. We fix both $t_1 = 0.3$ fm and $t_2 = 1$ fm and plot for the latest time $t = L$. For the other parameters we choose $\hat{q} = 1.5$ GeV²/fm, $\theta = 0.5$ and $z = 0.5$.

While this approximation turns out to work extremely well for the photon splitting, see figure 2a, we note that it has a more limited range of applicability for both the quark-gluon, see figure 2b, and gluon-gluon, see figure 2c, splitting processes, respectively. In all of the cases the exact value is slightly higher than the approximate one. As we derived analytically, the $C_{ij}^{(3)}$ terms all decay as $\sim e^{-\hat{q}(t-t_1)^3 \tau^2 \theta^2 f(z)}$, where $f(z)$ is a process dependent regular function. The $C_{ij}^{(4)}$ terms are more complicated, especially at early times where all terms contribute, but at late times the dominant contribution comes from $\sim e^{-\hat{q}(t-t_2)\theta^2}$.

The ratio of double-differential in-medium to vacuum spectrum reveals the medium modification factor $F_{\text{med}}(z, \theta) = dI^{\text{med}}/(dzd\theta)/dI^{\text{vac}}/(dzd\theta)$. We plot this factor, calculated at finite N_c , for the three processes in figure 3. These results have been obtained for the medium parameters $\hat{q} = 1.5$ GeV²/fm and $L = 2$ fm and an energy of the initial particle, before splitting, of $E = 100$ GeV.

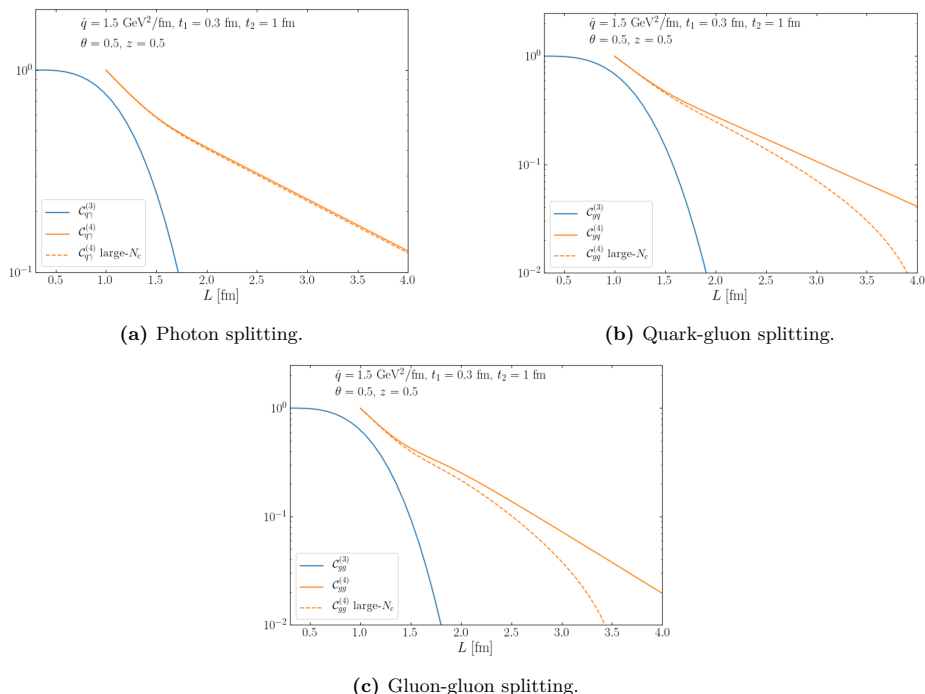


Figure 2. The time evolution of $\mathcal{C}^{(3)}(L, t_1)$ and $\mathcal{C}^{(4)}(L, t_2)$ for the three processes. For $\mathcal{C}^{(4)}(L, t_2)$ both the exact and large- N_c versions are plotted.

As one can see from figure 3, the medium modification factor $F_{\text{med}}(z, \theta)$ has roughly the same characteristic shape for all three processes. The medium modifications appear at large angles $\theta > \theta_c$, in between the characteristic lines $\omega^3 \theta^3 < \hat{q}$ and $\omega^2 \theta^2 < \hat{q}L$ which we have identified for the three- and four-point functions in section 3.1. This corresponds to formation times smaller than the medium length, $t_f < L$. In fact, we can recast these conditions in terms of the formation time of the process, namely $t_f < t_d$ and $t_f < t_{\text{broad}}$, where

$$t_d \sim \left(\frac{1}{\hat{q}\theta^2}\right)^{1/3}, \quad \text{and} \quad t_{\text{broad}} \sim \left(\frac{1}{\hat{q}\theta^2 L}\right)^{1/2}. \quad (3.25)$$

The modifications appear for the range of formation times $t_{\text{broad}} < t_f < t_d$ and $\theta > \theta_c$ [22]. There also seems to be a trend that both the magnitude and the region of the modifications grow with the number of Wilson lines. This can be traced back to the finite terms, $f(z)$, in the exponents that modify the scaling behavior. Naively, we would expect the relevant jet quenching parameter to be roughly a factor $N_c/C_F \approx 2$ larger for gluon splitting than for the photon.

Our main focus in this work is to highlight the differences between the finite- N_c results versus their large- N_c approximated counterparts. To illustrate this we have plotted the ratio of the exact and large- N_c medium modification factors, i.e. $F_{\text{med}}(z, \theta)|_{\text{large-}N_c}/F_{\text{med}}(z, \theta)$ in figure 4. The difference between the exact and approximate result is small in the whole

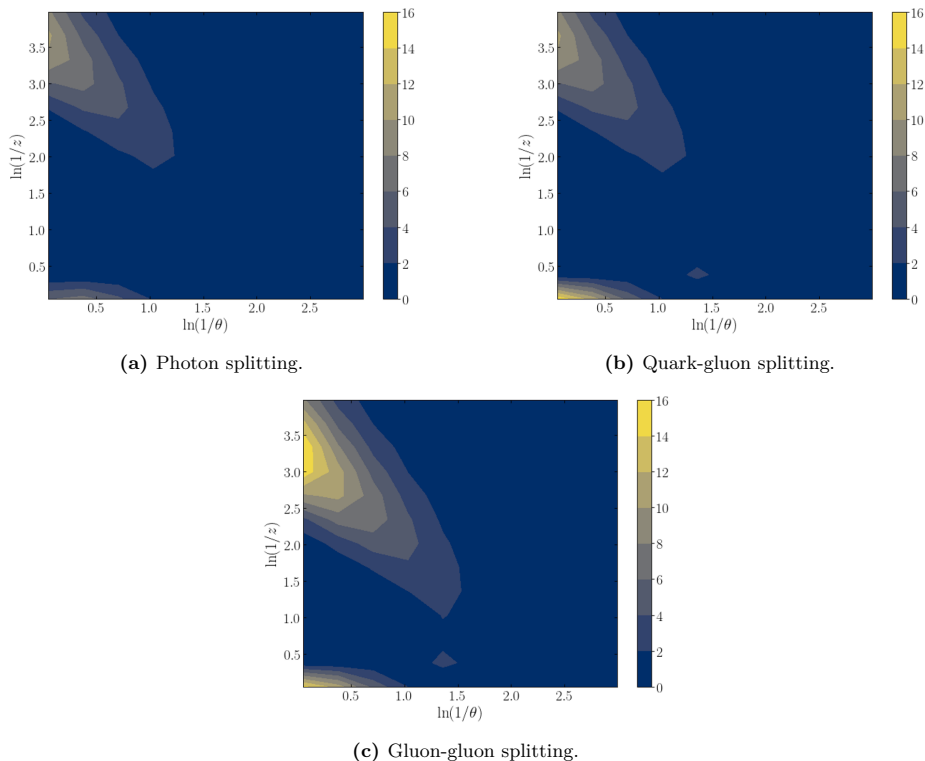


Figure 3. The medium modification factor $F_{\text{med}}(z, \theta)$ for three splitting processes as a function of θ and z with $L = 2$ fm and $E = 100$ GeV at finite N_c .

phase space in the photon splitting case, where there is a correlator of four Wilson lines. However, in the cases of quark-gluon and especially gluon-gluon splitting, which contain correlators of six and eight Wilson lines, the error can be relatively big, maximally of the order of 16% in case of the latter process. This is the reflection of the behavior observed previously in figure 2. From these calculations it seems like the more complicated color structure, the bigger the error is by using the large- N_c approximation. Once again, the error becomes most sizable at relatively large in-medium formation times, i.e. $t_f \sim t_{\text{broad}}$ and $t_f \sim t_d$, but at the same time $t_f < L$. This is most clearly seen in the gluon-gluon splitting, cf. figure 4c. Finally, we note that the finite- N_c corrections come as a modulation along the previously established scaling lines which hints that such corrections could perhaps be absorbed into an *effective* jet quenching parameter.

To summarize, we have calculated the double-differential spectrum $\frac{dI}{dzd\theta}$ for three different splitting processes, and shown that the resulting expressions factorize into three- and four-point functions that contain medium-averaged products of 2, 4, 6 and 8 fundamental Wilson lines. In the coming section 4 we will detail how these are calculated. Strikingly,

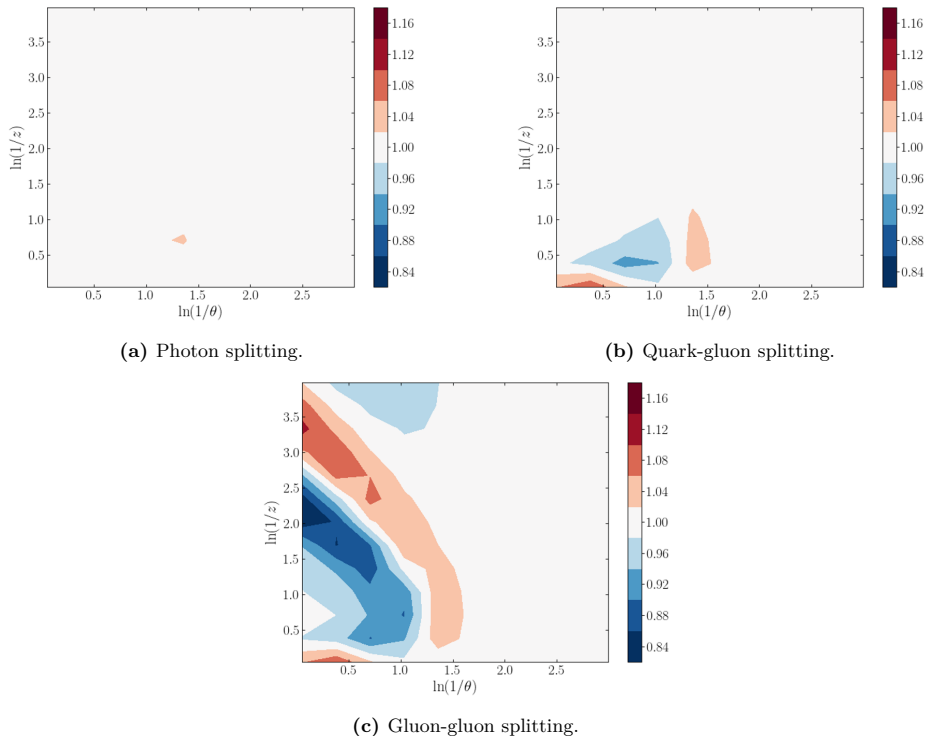


Figure 4. The ratio $F_{\text{med}}(z, \theta)|_{\text{large-}N_c}/F_{\text{med}}(z, \theta)$ for three splitting processes as a function of θ and z with $L = 2$ fm and $E = 100$ GeV.

the three- and four-point functions all take a very similar scaling form as was derived analytically exactly, for the former, and in the large- N_c approximation, for the latter. This corresponds to the identification of two characteristic time-scales in the medium, related to broadening along the length of the medium, t_{broad} , and decoherence during the formation of the splitting, t_{d} . These were identified first in [22] for the photon splitting process, and we have here extended their validity to all other splitting QCD processes. Finally, we have seen that finite- N_c corrections play an increasingly important role the bigger the total color charge involved in the splitting process.

4 Calculating Wilson line correlators

In this section we will present our method for calculating Wilson line correlators. As an illustration we will first show how it is done in the simple case of four Wilson lines in the fundamental representation. Thereafter this process will be generalized to an arbitrary number of Wilson lines.

4.1 Four Wilson lines

The simplest Wilson line correlator comes from the pair production process (3.7), where there is a trace of four Wilson lines $\langle \text{tr}[V_1 V_2^\dagger V_2 V_1^\dagger] \rangle$. In this section, we will show how to derive a system of differential equations to calculate this. Let the Wilson lines have support from t_0 to some arbitrary time $t + \epsilon$. Then, following [25], we expand them between t and $t + \epsilon$ to get

$$\begin{aligned}
 V(t+\epsilon, t_0; \mathbf{r}) &= V(t+\epsilon, t; \mathbf{r})V(t, t_0; \mathbf{r}) \\
 &= \left(1 + ig \int_t^{t+\epsilon} ds A^a(s, \mathbf{r}) t^a - \frac{g^2}{2!} \int_t^{t+\epsilon} ds \int_t^{t+\epsilon} ds' A^a(s, \mathbf{r}) A^b(s', \mathbf{r}') t^a t^b + \mathcal{O}(\epsilon^2) \right) \\
 &\quad \times V(t, t_0; \mathbf{r}), \tag{4.1}
 \end{aligned}$$

where we have kept some of the color indices implicit. All four Wilson lines are expanded in this manner. We end up with having to take the medium average of the integrals over two medium fields, traced over the relevant color indices, which is dealt in the following way

$$\begin{aligned}
 \int_t^{t+\epsilon} ds \int_t^{t+\epsilon} ds' \langle A^a(s, \mathbf{r}) A^b(s', \mathbf{r}') [t^a t^b]_{ij} \rangle &= \int_t^{t+\epsilon} ds n(s) \gamma(\mathbf{r} - \mathbf{r}') t_{ik}^a t_{kj}^a \\
 &\simeq \epsilon C_F n(t) \gamma(\mathbf{r} - \mathbf{r}') \delta_{ij}, \tag{4.2}
 \end{aligned}$$

where in the first step we applied the medium average (2.5). Then, keeping terms up to the first order of ϵ this becomes

$$\begin{aligned}
 \langle \text{tr}[V_1 V_2^\dagger V_2 V_1^\dagger] \rangle_{(t+\epsilon)} &= \left(1 + \epsilon g^2 n(t) C_F [\gamma_{1\bar{1}} + \gamma_{2\bar{2}} - 2\gamma_0] \right) \langle \text{tr}[V_1 V_2^\dagger V_2 V_1^\dagger] \rangle_{(t)} \\
 &\quad - \epsilon g^2 n(t) [\gamma_{1\bar{2}} - \gamma_{12} - \gamma_{\bar{1}\bar{2}} + \gamma_{2\bar{1}}] \langle \text{tr}[t^a V_1 V_2^\dagger t^a V_2 V_1^\dagger] \rangle_{(t)}. \tag{4.3}
 \end{aligned}$$

Using the Fierz identity

$$t_{ij}^a t_{kl}^a = \frac{1}{2} \left(\delta_{il} \delta_{jk} - \frac{1}{N_c} \delta_{ij} \delta_{kl} \right), \tag{4.4}$$

this results in the differential equation

$$\begin{aligned}
 \frac{d}{dt} \langle \text{tr}[V_1 V_2^\dagger V_2 V_1^\dagger] \rangle_{(t)} &= \lim_{\epsilon \rightarrow 0} \frac{\langle \text{tr}[V_1 V_2^\dagger V_2 V_1^\dagger] \rangle_{(t+\epsilon)} - \langle \text{tr}[V_1 V_2^\dagger V_2 V_1^\dagger] \rangle_{(t)}}{\epsilon} \\
 &= g^2 n(t) \left[C_F (\gamma_{1\bar{1}} + \gamma_{2\bar{2}} - 2\gamma_0) + \frac{1}{2N_c} (\gamma_{1\bar{2}} - \gamma_{12} - \gamma_{\bar{1}\bar{2}} + \gamma_{2\bar{1}}) \right] \langle \text{tr}[V_1 V_2^\dagger V_2 V_1^\dagger] \rangle_{(t)} \\
 &\quad - \frac{1}{2} g^2 n(t) (\gamma_{1\bar{2}} - \gamma_{12} - \gamma_{\bar{1}\bar{2}} + \gamma_{2\bar{1}}) \langle \text{tr}[V_1 V_2^\dagger] \text{tr}[V_2 V_1^\dagger] \rangle_{(t)}. \tag{4.5}
 \end{aligned}$$

It is evident that the original term mixes with another four-point correlator, given in the term on the last line. To understand this, let us look closer at the term $\langle \text{tr}[V_1 V_2^\dagger V_2 V_1^\dagger] \rangle$. Since the process is happening in the medium the quarks and antiquarks can at any time exchange gluons, so their color is continuously rotating. In the case of four Wilson lines there are two possible ways of connecting the color at time t to ensure color conservation, namely as shown in figure 5. The second way is exactly the term $\langle \text{tr}[V_1 V_2^\dagger] \text{tr}[V_2 V_1^\dagger] \rangle$ that appeared in equation (4.5). The inclusion of this term in the differential equation (4.5) just represents the possibility for color rotation to happen at each time.

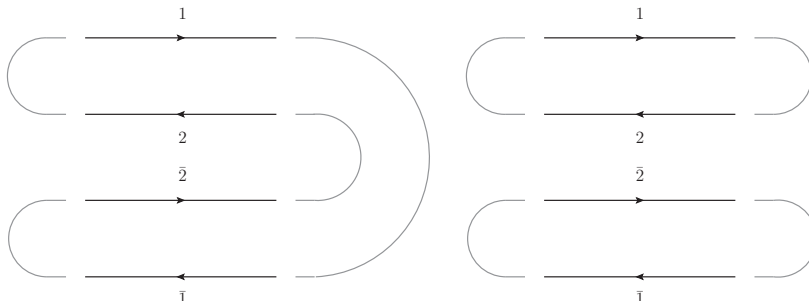


Figure 5. The two possible ways of color connecting the four Wilson lines. On the left is $C_{\bar{2}1} \equiv \langle \text{tr}[V_1 V_2^\dagger V_2 V_1^\dagger] \rangle$, while on the right is $C_{1\bar{2}} \equiv \langle \text{tr}[V_1 V_2^\dagger] \text{tr}[V_2 V_1^\dagger] \rangle$, both going from times t_2 to an arbitrary time t . The grey lines at the beginning and end indicate the colour connections.

To continue one can find a complementary differential equation for $\langle \text{tr}[V_1 V_2^\dagger] \text{tr}[V_2 V_1^\dagger] \rangle$ and see if we can find a solution for the set. Going through the same procedure as above gives

$$\begin{aligned} \frac{d}{dt} \langle \text{tr}[V_1 V_2^\dagger] \text{tr}[V_2 V_1^\dagger] \rangle(t) &= g^2 n(t) \left[C_F (\gamma_{12} + \gamma_{\bar{1}\bar{2}} - 2\gamma_0) + \frac{1}{2N_c} (\gamma_{1\bar{2}} - \gamma_{\bar{1}1} - \gamma_{2\bar{2}} + \gamma_{\bar{1}2}) \right] \langle \text{tr}[V_1 V_2^\dagger] \text{tr}[V_2 V_1^\dagger] \rangle(t) \\ &\quad - \frac{1}{2} g^2 n(t) (\gamma_{1\bar{2}} - \gamma_{\bar{1}1} - \gamma_{2\bar{2}} + \gamma_{\bar{1}2}) \langle \text{tr}[V_1 V_2^\dagger V_2 V_1^\dagger] \rangle(t). \end{aligned} \tag{4.6}$$

We now have a set of two coupled differential equations. To save space the following notation will be used $C_{1\bar{2}}(t) \equiv \langle \text{tr}[V_1 V_2^\dagger] \text{tr}[V_2 V_1^\dagger] \rangle(t)$ and $C_{\bar{2}1}(t) \equiv \langle \text{tr}[V_1 V_2^\dagger V_2 V_1^\dagger] \rangle(t)$. This notation warrants some more explanation. Both of these expressions are composed of the two pairs of Wilson lines, namely $V_1 V_2^\dagger$ and $V_2 V_1^\dagger$. The only difference is how to connect them. The two subscripts in the C 's tell which Wilson line comes immediately after the two pairs. So $C_{\bar{2}1}$ means that $V_1 V_2^\dagger$ is connected to V_2 and $V_2 V_1^\dagger$ connects to V_1 . The result is $\langle \text{tr}[V_1 V_2^\dagger V_2 V_1^\dagger] \rangle$. This notation might seem overly complicated, but it will prove to be useful when considering more than four Wilson lines.

The two differential equations (4.5) and (4.6) can be gathered into the following system,

$$\frac{d}{dt} \begin{bmatrix} C_{1\bar{2}}(t) \\ C_{\bar{2}1}(t) \end{bmatrix} = -\frac{n(t)}{2} \mathbb{M} \begin{bmatrix} C_{1\bar{2}}(t) \\ C_{\bar{2}1}(t) \end{bmatrix}, \tag{4.7}$$

where the evolution matrix takes the following form,

$$\mathbb{M} = \begin{bmatrix} 2C_F(\sigma_{12} + \sigma_{\bar{2}\bar{1}}) + \frac{1}{N_c} \Sigma_1 & -\Sigma_1 \\ -\Sigma_2 & 2C_F(\sigma_{\bar{1}\bar{1}} + \sigma_{22}) + \frac{1}{N_c} \Sigma_2 \end{bmatrix}. \tag{4.8}$$

Here we have used eq. (2.7) to define $\sigma_{12} = \sigma(\mathbf{r}_1 - \mathbf{r}_2)$, and introduced

$$\begin{aligned} \Sigma_1 &\equiv \sigma_{1\bar{2}} + \sigma_{2\bar{1}} - \sigma_{\bar{1}\bar{1}} - \sigma_{22} \\ \Sigma_2 &\equiv \sigma_{1\bar{2}} + \sigma_{\bar{1}2} - \sigma_{12} - \sigma_{\bar{1}\bar{2}}. \end{aligned} \tag{4.9}$$

To proceed, we employ the harmonic approximation (2.8). For the eikonal, straight-line trajectories, given in eqs. (2.12), the evolution matrix becomes

$$-\frac{n(t)}{2} \mathbb{M} = -\frac{\hat{q}\theta^2}{4C_F} \begin{bmatrix} C_F[(t-t_1)^2 + (t-t_2)^2] - \frac{1}{N_c}(t-t_1)(t-t_2) & -(t-t_1)(t-t_2) \\ z(1-z)\tau^2 & C_F\tau^2\xi - \frac{1}{N_c}z(1-z)\tau^2 \end{bmatrix}, \quad (4.10)$$

where we have defined $\tau \equiv t_2 - t_1$, $\xi = z^2 + (1-z)^2$ and assumed that the angle between the two particles θ is small. Unfortunately, since the matrix elements depend on time in our setup, we can only solve this system of differential equations exactly by using numerical methods.

The authors of [22] calculated the four-point function $\langle \text{tr}[V_1 V_2^\dagger V_2 V_1^\dagger] \rangle$ in the large- N_c limit, which is interesting to compare with our results. This example is illustrative of the general structure of the hierarchy between the different correlators, and we will therefore go through it in detail. To take the large- N_c limit you start the system of differential equations (4.7) and count the powers of N_c in each term in the evolution matrix and the vector of correlators, taking into account that $C_{1\bar{2}} \sim N_c^2$ and $C_{\bar{2}1} \sim N_c^1$. In this limit we also have $C_F \sim N_c/2$. The terms on the right-hand side of (4.7) then have the following powers of N_c ,

$$\begin{bmatrix} \mathcal{O}(N_c^0) + \mathcal{O}(N_c^{-2}) & \mathcal{O}(N_c^{-1}) \\ \mathcal{O}(N_c^{-1}) & \mathcal{O}(N_c^0) + \mathcal{O}(N_c^{-2}) \end{bmatrix} \begin{bmatrix} \mathcal{O}(N_c^2) \\ \mathcal{O}(N_c^1) \end{bmatrix} \xrightarrow{\text{large-}N_c} \begin{bmatrix} \mathcal{O}(N_c^0) & 0 \\ \mathcal{O}(N_c^{-1}) & \mathcal{O}(N_c^0) \end{bmatrix} \begin{bmatrix} \mathcal{O}(N_c^2) \\ \mathcal{O}(N_c^1) \end{bmatrix}. \quad (4.11)$$

The large- N_c approximation amounts to dropping all the terms in the matrix that are not scaling with the same power of N_c as the original vector, given by the second term in (4.11). We see that the next-to-leading power of N_c turns out to be a factor N_c^{-2} smaller compared to the leading terms. This scaling has also been corroborated generally for n -line correlators in section 4.2.

Hence, employing the large- N_c approximation leads to the simplified system of equations

$$\frac{d}{dt} \begin{bmatrix} C_{1\bar{2}}(t) \\ C_{\bar{2}1}(t) \end{bmatrix} \simeq -\frac{\hat{q}\theta^2}{4N_c} \begin{bmatrix} N_c[(t-t_1)^2 + (t-t_2)^2] & 0 \\ 2z(1-z)\tau^2 & N_c\tau^2\xi \end{bmatrix} \begin{bmatrix} C_{1\bar{2}}(t) \\ C_{\bar{2}1}(t) \end{bmatrix}. \quad (4.12)$$

Now it is evident that the differential equation for $C_{1\bar{2}}$ is separable and can be solved easily, which means that $C_{\bar{2}1}$ also can be solved. This leads to the equations (3.12) and (3.13). The physical picture of this differential equation is quite transparent. The correlator of the two particles (described by two lines in the amplitude and two lines in the complex conjugate amplitude) can be in either of the states shown in figure 5, and there is a possibility of exchanging a gluon and transferring from one state to the other. This is encoded in the off-diagonal terms in the matrix (4.8), and is associated with a factor of $\sim \sigma$, which scales as N_c^{-1} . Say you start in the state $C_{1\bar{2}}$ shown on the right in figure 5, scaling as N_c^2 . If you exchange a gluon you pick up a factor N_c^{-1} from the σ , and go to the state $C_{\bar{2}1}$, which is a single trace correlator that scales as N_c^1 , so in total this transition is associated with a factor N_c^0 . This is a factor N_c^{-2} smaller compared to the starting point so it can safely be dropped in the large- N_c limit. However, starting with $C_{\bar{2}1}$ and going to $C_{1\bar{2}}$ you go from a state that scales as N_c^1 to one scaling as N_c^2 , but you lose a power of N_c from the σ , so

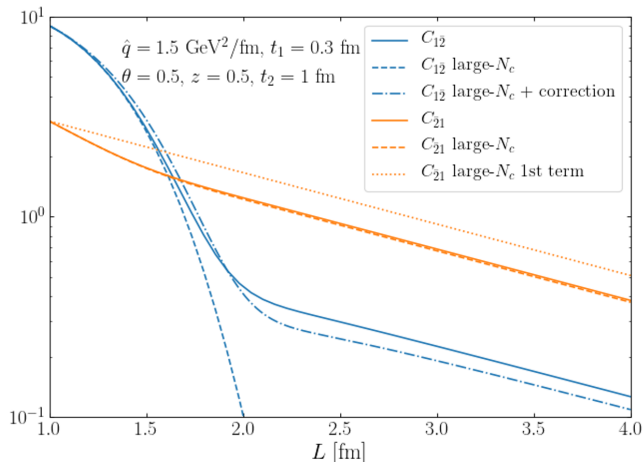


Figure 6. The exact and large- N_c version of $C_{12}(t) = \langle \text{tr}[V_1 V_2^\dagger] \text{tr}[V_2 V_1^\dagger] \rangle$ (blue, solid and blue, dashed lines, respectively) and $C_{21}(t) = \langle \text{tr}[V_1 V_2^\dagger V_2 V_1^\dagger] \rangle$ (orange, solid and orange, dashed lines, respectively). We also plot only the leading, diagonal term of the large- N_c approximation of C_{21} (orange, dotted line) which exhibits the correct large-time asymptotic behavior.

in this case the end result has the same N_c scaling as the starting point. Hence, in the large- N_c limit you can drop the upper right term in the matrix, but must keep the lower left one, see section 4.2 for a general argument for n -point correlators.

The solutions to (4.10) and (4.12) were plotted in figure 6 (solid and dashed lines, respectively). For this particular case, the agreement between the large- N_c approximation and the exact, finite- N_c result is strikingly good for the C_{21} correlator. At late times, we observe an exponential suppression, $\propto e^{-t}$, with a slope that is in good agreement with the first term of eq. (3.13). At early times, there is an interplay between C_{21} and C_{12} that leads to a more rapid decrease initially. This is however well captured by the large- N_c approximation, given by both terms in eq. (3.13).

The C_{12} correlator is described well within the large- N_c approximation at early times. However, at late times it exhibits a long tail that is not captured within this approximation. This can be remedied by including sub-leading corrections in color.

Sub-leading corrections in color can be incorporated to improve on the sometimes crude large- N_c calculation above. To do this write the full correlators as the sum of their large- N_c versions calculated through (4.12) and some smaller correction term,

$$\mathbf{C} = \mathbf{C}^{(0)} + \mathbf{C}^{(1)}, \tag{4.13}$$

where $\mathbf{C} = (C_{12}, C_{21})^\top$ is a vector of the correlators in question, so that $\mathbf{C}^{(1)}$ is a factor $\mathcal{O}(N_c^{-2})$ smaller than $\mathbf{C}^{(0)}$. We can also write the matrix \mathbb{M} in a form that isolates the large- N_c terms from the finite- N_c corrections, i.e.

$$\mathbb{M} = \mathbb{M}^{(0)} + \mathbb{M}^{\text{corr.}}, \tag{4.14}$$

where the first term strictly corresponds to the leading terms in the large- N_c limit. In our example above, we find that

$$-\frac{n(t)}{2} \mathbb{M}^{(0)} = -\frac{\hat{q}\theta^2}{4} \begin{bmatrix} (t-t_1)^2 + (t-t_2)^2 & 0 \\ \frac{2}{N_c} z(1-z)\tau^2 & \tau^2 \xi \end{bmatrix}, \quad (4.15)$$

while

$$-\frac{n(t)}{2} \mathbb{M}^{\text{corr.}} \simeq \frac{\hat{q}\theta^2}{2N_c^2} \begin{bmatrix} (t-t_1)(t-t_2) & N_c(t-t_1)(t-t_2) \\ -\frac{1}{N_c} z(1-z)\tau^2 & z(1-z)\tau^2 \end{bmatrix}, \quad (4.16)$$

where we expanded the correction matrix to find the leading terms in N_c . It can be confirmed that the overall correction to both correlators is of the order N_c^{-2} .

The correlators at leading color, i.e. $\mathbf{C}^{(0)}$, are known. They solve the simplified set of equations $d\mathbf{C}^{(0)}(t)/dt = -\frac{n(t)}{2} \mathbb{M}^{(0)} \mathbf{C}^{(0)}(t)$, and are given explicitly in (3.12) and (3.13). This can now be used to calculate the color sub-leading contributions $\mathbf{C}^{(1)}$. Simply plugging this into the full differential equation (4.7) results in the following differential equation for the first correction

$$\frac{d}{dt} \mathbf{C}^{(1)}(t) \simeq -\frac{n(t)}{2} \mathbb{M}^{(0)} \mathbf{C}^{(1)}(t) - \frac{n(t)}{2} \mathbb{M}^{\text{corr.}} \mathbf{C}^{(0)}(t), \quad (4.17)$$

where we have neglected terms that are even more sub-leading, i.e. resulting from $\mathbb{M}^{\text{corr.}} \mathbf{C}^{(1)}$. This is a nonhomogeneous version of the large- N_c system of differential equations (4.12), and can also be solved exactly. As an example the first correction to $C_{12}^{(1)}(t)$ is

$$C_{12}^{(1)}(t) = \frac{\hat{q}\theta^2}{2N_c^2} \int_{t_2}^t ds (s-t_1)(s-t_2) \left[C_{12}^{(0)}(s) + N_c C_{21}^{(0)}(s) \right] \times e^{\frac{\hat{q}\theta^2}{12} [(t-t_1)^3 - (s-t_1)^3 + (t-t_2)^3 - (s-t_2)^3]}. \quad (4.18)$$

The first correction contains $C_{21}^{(0)}(t)$, given in (3.13) which as can be seen in figure 6 has a linear tail at long times. One would therefore expect that this correction will rectify the difference between the exact calculation and the large- N_c version of $C_{12}(t)$ at long times which can be seen in the same plot. On figure 6, we have plotted this correction, and it is indeed clear that it contains this linear tail. It is also worth noticing that the N_c -scaling of the correction is $C_{12}^{(1)} \sim N_c^0$, since there is an N_c^{-1} in the pre-factor and $C_{21}^{(0)} \sim N_c^1$. As expected the correction is lower by a factor N_c^{-2} compared to the large- N_c result.

It is possible to calculate higher order corrections going as N_c^{-4} , N_c^{-6} etc. compared to the large- N_c expression using the same technique recursively.

4.2 General method for Wilson line correlators

In section 3, we showed that doing similar calculations starting with a quark or a gluon emitting a gluon leads to correlators of six and eight fundamental Wilson lines, respectively. We will now generalize the procedure demonstrated in the preceding section and develop a method of calculating correlators of an arbitrary number of fundamental Wilson lines. To be more precise we get systems of differential equations like in (4.7), and will show how to easily calculate all the matrix elements in the $K! \times K!$ matrices. The system can then be solved numerically or, as we will see, analytically in the large- N_c limit.

The correlators of six and eight Wilson lines that appeared in section 3 are

- $\langle \text{tr}[V_1^\dagger V_1 V_2^\dagger V_2] \text{tr}[V_2^\dagger V_2] \rangle$,
- $\langle \text{tr}[V_1 V_1^\dagger] \text{tr}[V_2 V_2^\dagger V_1 V_1^\dagger] \text{tr}[V_2 V_2^\dagger] \rangle$,
- and $\langle \text{tr}[V_1 V_1^\dagger V_2 V_2^\dagger V_1 V_1^\dagger V_2 V_2^\dagger] \rangle$.

Note that one can divide the correlators of these Wilson lines into pairs on the form $[V_n V_m^\dagger]_{i_n j_m}$ times some Kronecker deltas that connect the indices.

To start, consider the special case of calculating a correlator involving K pairs of a Wilson line in the amplitude times the same Wilson line in the complex conjugate amplitude

$$\langle [V_1 V_1^\dagger]_{i_1 j_1} [V_2 V_2^\dagger]_{i_2 j_2} \dots [V_K V_K^\dagger]_{i_K j_K} \rangle = \langle \prod_{n=1}^K [V_n V_n^\dagger]_{i_n j_n} \rangle. \quad (4.19)$$

This is very useful to consider, even though none of the correlators mentioned above are of this exact form. The reason is that in this form all of the formulas derived in this section become much nicer. In addition, it is easy to generalize this to include all cases simply by changing the labels of the Wilson lines in (4.19) to whatever is needed in the specific problem at hand. For example, choosing $K = 3$ and changing labels $(1, \bar{1}, 2, \bar{2}, 3, \bar{3}) \rightarrow (1, 2, \bar{2}, \bar{1}, 2, \bar{2})$ gives the structure needed in (3.16), while $K = 4$ and changing labels $(1, \bar{1}, 2, \bar{2}, 3, \bar{3}, 4, \bar{4}) \rightarrow (1, \bar{1}, 2, \bar{2}, \bar{1}, 1, \bar{2}, 2)$ reproduces the correlators in (3.20). So even though it seems we are calculating a special case, simply changing the labels in the equations in this section leads to all possible cases.

To compress the notation a bit we will write the k 'th instance of a Wilson line pair as

$$W_{i_k j_k}^k \equiv [V_k V_k^\dagger]_{i_k j_k}. \quad (4.20)$$

It is possible to generalize the method of reaching a system of differential equations showed in the previous section to an arbitrary number K pairs of Wilson lines. The steps are outlined in appendix C. This procedure leads to the differential equation,

$$\begin{aligned} & \frac{2N_c}{g^2} \frac{d}{dt} \left\langle \prod_{n=1}^K W_{i_n j_n}^n \right\rangle \\ &= n(t) \left[\sum_{k=1}^{K-1} \sum_{l>k}^K (\gamma_{kl} + \gamma_{\bar{k}\bar{l}} - \gamma_{k\bar{l}} - \gamma_{\bar{k}l}) - \sum_{k=1}^K \gamma_{k\bar{k}} - K(N_c^2 - 1)\gamma_0 \right] \left\langle \prod_{n=1}^K W_{i_n j_n}^n \right\rangle \\ &+ n(t) \sum_{k=1}^K \left[\gamma_{k\bar{k}} \left\langle \text{tr}(W^k) \delta_{i_k j_k} \left(\prod_{n \neq k}^K W_{i_n j_n}^n \right) \right\rangle \right] \\ &+ n(t) \sum_{k=1}^{K-1} \sum_{l>k}^K \left\langle \left(\gamma_{k\bar{l}} \delta_{i_k j_l} [W^l W^k]_{i_l j_k} + \gamma_{\bar{k}l} \delta_{i_l j_k} [W^k W^l]_{i_k j_l} - \gamma_{kl} W_{i_l j_k}^k W_{i_k j_l}^l - \gamma_{\bar{k}\bar{l}} W_{i_k j_l}^k W_{i_l j_k}^l \right) \right. \\ &\quad \left. \times \prod_{n \neq k, n \neq l}^K W_{i_n j_n}^n \right\rangle. \end{aligned} \quad (4.21)$$

One can see that the term on the first line has the same index structure as the original, while the subsequent lines contain mixing terms. Notice that, in the mixing terms, only at most two W 's change place. The rest stay the same as before.

The above equation is a step in the right direction. It makes it possible to quite easily project out all the different differential equations by contraction with the product of K Kronecker deltas. For example starting with (4.21) and projecting out with $\delta_{j_1 i_1} \delta_{j_2 i_2} \dots \delta_{j_K i_K}$ turns it into a differential equation for $\frac{d}{dt} \langle \text{tr}[W^1] \text{tr}[W^2] \dots \text{tr}[W^K] \rangle$, while $\delta_{j_1 i_2} \delta_{j_2 i_3} \dots \delta_{j_K i_1}$ leads to $\frac{d}{dt} \langle \text{tr}[W^1 W^2 \dots W^K] \rangle$. We will denote these two possibilities by $C_{12\dots K} \equiv \langle \text{tr}[W^1] \text{tr}[W^2] \dots \text{tr}[W^K] \rangle$ and $C_{23\dots K1} \equiv \langle \text{tr}[W^1 W^2 \dots W^K] \rangle$. The general version of this is $C_{m_1 m_2 \dots m_K}$, where $m_1 m_2 \dots m_K$ is one of the $K!$ permutations of the numbers between 1 and K . The idea behind this notation is that W^1 is connected to W^{m_1} , W^2 is connected to W^{m_2} etc.³

Although it is possible to use (4.21) to project out all the necessary differential equations, there are actually $K!$ such projections, which quickly becomes a huge number. It would be much preferable to write this system in matrix form, like in eq. (4.7). Making use of the notation we described above we want to write the system of differential equations for K pairs of Wilson lines as

$$\frac{d}{dt} C_{m_1 m_2 \dots m_K} = -\frac{1}{2} n(t) \sum_{p_1 p_2 \dots p_K} \mathbb{M}_{m_1 m_2 \dots m_K}^{p_1 p_2 \dots p_K} C_{p_1 p_2 \dots p_K}, \quad (4.22)$$

where $p_1 p_2 \dots p_K$ also is one of the $K!$ permutations of $12 \dots K$.

Starting from (4.21), one can deduce the general form of the matrix elements $\mathbb{M}_{m_1 m_2 \dots m_K}^{p_1 p_2 \dots p_K}$. For details on how this is done, we refer to appendix C. Fortunately, most of the matrix elements are zero, and those that are not have quite simple expressions. The $K!$ diagonal entries are

$$\mathbb{M}_{m_1 m_2 \dots m_K}^{m_1 m_2 \dots m_K} = N_c \sum_{k=1}^K \sigma_{\bar{k} m_k} + \frac{1}{N_c} \underbrace{\sum_{k=1}^K \sum_{l>k}^K (\sigma_{kl} + \sigma_{\bar{k}l} - \sigma_{k\bar{l}} - \sigma_{\bar{k}l})}_{A_K} - \frac{1}{N_c} \sum_{k=1}^K \sigma_{k\bar{k}} \quad (4.23)$$

Note here that only the first sum depends on the exact permutation we use. The two latter sums are independent of this, and are common to all the diagonal terms, so we call it A_K . The only other non-zero matrix elements $\mathbb{M}_{m_1 m_2 \dots m_K}^{p_1 p_2 \dots p_K}$ are those where $p_1 p_2 \dots p_K$ is just $m_1 m_2 \dots m_K$, but with exactly two entries swapped places. If our original sequence is $m_1 m_2 \dots m_i \dots m_j \dots m_K$, and its entries in positions i and j have changed places it becomes $m_1 m_2 \dots m_j \dots m_i \dots m_K$. Then we get $K! \frac{K(K-1)}{2}$ entries of the form

$$\mathbb{M}_{m_1 m_2 \dots m_j \dots m_i \dots m_K}^{m_1 m_2 \dots m_i \dots m_j \dots m_K} = \sigma_{\bar{i} m_j} + \sigma_{m_i \bar{j}} - \sigma_{m_i m_j} - \sigma_{\bar{i} \bar{j}}. \quad (4.24)$$

Finally, we have

$$\mathbb{M}_{m_1 m_2 \dots m_K}^{p_1 p_2 \dots p_K} = 0, \quad (4.25)$$

³One final example to clarify the notation can, for instance, be the correlator $C_{213\dots K} \equiv \langle \text{tr}[W^1 W^2] \text{tr}[W^3] \dots \text{tr}[W^K] \rangle$.

for $p_1 p_2 \dots p_K$ being any other permutation of $m_1 m_2 \dots m_K$. This means that out of the $K!$ matrix elements, only $\frac{1}{2}K!(K^2 - K + 2)$ are non-zero. These are given by the relatively simple formulas (4.23) and (4.24). Putting it all together this becomes

$$\begin{aligned} \frac{d}{dt} C_{m_1 m_2 \dots m_i \dots m_j \dots m_K} &= -\frac{1}{2}n(t) \left(N_c \sum_{k=1}^K \sigma_{\bar{k} m_k} + \frac{1}{N_c} A_K \right) C_{m_1 m_2 \dots m_i \dots m_j \dots m_K} \\ &\quad - \frac{1}{2}n(t) \sum_{i=1}^{K-1} \sum_{j>i}^K (\sigma_{\bar{i} m_j} + \sigma_{m_i \bar{j}} - \sigma_{m_i m_j} - \sigma_{\bar{i} \bar{j}}) C_{m_1 m_2 \dots m_j \dots m_i \dots m_K}. \end{aligned} \quad (4.26)$$

Of course, for all differential equations you need to specify some initial conditions. It is clear from the definition of the Wilson line (2.2) that $V_{ij}(t_0, t_0) = \delta_{ij}$. The trace of this is $\text{tr} V(t_0, t_0) = N_c$. This means that the initial condition of a Wilson line correlator is N_c to the power of traces it contains. A few illustrative examples of this are $C_{12\dots K} = \langle \text{tr}[W^1] \text{tr}[W^2] \dots \text{tr}[W^K] \rangle \sim N_c^K$, $C_{213\dots K} = \langle \text{tr}[W^1 W^2] \text{tr}[W^3] \dots \text{tr}[W^K] \rangle \sim N_c^{K-1}$ and $C_{23\dots K1} = \langle \text{tr}[W^1 W^2 \dots W^K] \rangle \sim N_c^1$.

The system of differential equations given by eq. (4.26) is to our knowledge not possible to solve analytically in the case where σ is a function of time, so we have to turn to numerical techniques. We have written a code to solve the differential equation numerically using the SciPy library in Python. For the examples encountered in this paper, this is quite fast (in a matter of seconds on a standard computer), even for a 24×24 system. However, since the size of the system goes as $K!$, we expect that it will become much slower as K increases. If the elements σ are time-independent it should be possible to diagonalize the matrix and find analytic solutions to the differential equation. However, since this is not the case in the problems we consider it is not pursued here.

To better understand what this system of differential equations looks like, it is useful to view it in matrix form. Generally, there will be several correlators that go as the same power of N_c . It is useful to gather these in vectors \mathbf{C}^M , where the superscript M is meant to indicate that this scales as N_c^M . Then, eq. (4.26) can be represented as

$$\frac{d}{dt} \begin{bmatrix} C^K \\ C^{K-1} \\ C^{K-2} \\ \vdots \\ C^2 \\ C^1 \end{bmatrix} \sim \left(\text{diag} \left(N_c \sigma + \frac{1}{N_c} \sigma, \dots, N_c \sigma + \frac{1}{N_c} \sigma \right) + \begin{bmatrix} 0 & \sigma & 0 & \dots & \dots & 0 \\ \sigma & 0 & \sigma & 0 & \dots & 0 \\ 0 & \sigma & 0 & \sigma & 0 & 0 \\ \vdots & \vdots & \vdots & \vdots & \vdots & \vdots \\ 0 & \dots & 0 & \sigma & 0 & \sigma \\ 0 & \dots & \dots & 0 & \sigma & 0 \end{bmatrix} \right) \begin{bmatrix} C^K \\ C^{K-1} \\ C^{K-2} \\ \vdots \\ C^2 \\ C^1 \end{bmatrix}. \quad (4.27)$$

The first matrix contains the diagonal elements, written in detail in (4.23). The second matrix represents the non-diagonal elements, and σ is a block containing non-zero elements, which we get from eq. (4.24).

4.3 Wilson line correlators in the large- N_c limit

The system of differential equations (4.26) can in general only be solved numerically at finite N_c . However, in the large- N_c limit, the system simplifies in a way that makes it

possible to solve it exactly. This can be seen from the matrix representation in eq. (4.27). Since $\sigma \sim N_c^{-1}$, the diagonal matrix elements go as $\sim N_c^0 + N_c^{-2}$, while the non-diagonal ones go as $\sim N_c^{-1}$. Multiplying in the vector on the end and representing every term by its N_c scaling this becomes

$$\frac{d}{dt} \begin{bmatrix} C^K \\ C^{K-1} \\ C^{K-2} \\ \vdots \\ C^2 \\ C^1 \end{bmatrix} \sim \begin{bmatrix} (N_c^0 + N_c^{-2})C^K \\ (N_c^0 + N_c^{-2})C^{K-1} \\ (N_c^0 + N_c^{-2})C^{K-2} \\ \vdots \\ (N_c^0 + N_c^{-2})C^2 \\ (N_c^0 + N_c^{-2})C^1 \end{bmatrix} + \begin{bmatrix} N_c^{-1}C^{K-1} \\ N_c^{-1}(C^K + C^{K-2}) \\ N_c^{-1}(C^{K-1} + C^{K-3}) \\ \vdots \\ N_c^{-1}(C^3 + C^1) \\ N_c^{-1}C^2 \end{bmatrix}. \quad (4.28)$$

Taking the large- N_c limit is equivalent to keeping only the leading order of N_c in each row, and dropping terms going as N_c^{-2} compared to the leading term. Translating this back to the form in eq. (4.27), this becomes

$$\frac{d}{dt} \begin{bmatrix} C^K \\ C^{K-1} \\ C^{K-2} \\ \vdots \\ C^2 \\ C^1 \end{bmatrix} \sim \left(\text{diag}(N_c\sigma, \dots, N_c\sigma) + \begin{bmatrix} 0 & 0 & 0 & \dots & \dots & 0 \\ \sigma & 0 & 0 & 0 & \dots & 0 \\ 0 & \sigma & 0 & 0 & 0 & 0 \\ \vdots & \vdots & \vdots & \vdots & \vdots & \vdots \\ 0 & \dots & 0 & \sigma & 0 & 0 \\ 0 & \dots & \dots & 0 & \sigma & 0 \end{bmatrix} \right) \begin{bmatrix} C^K \\ C^{K-1} \\ C^{K-2} \\ \vdots \\ C^2 \\ C^1 \end{bmatrix}. \quad (4.29)$$

Hence, in the large- N_c limit, all of the terms above the diagonal go to zero, and the system simplifies drastically. To get some more intuition into why this is true physically it is useful to imagine being in some color configuration that scales as $\sim N_c^M$. At any point it is possible to exchange one gluon, after which the possible resulting color configurations of the system will change its N_c power by exactly one, and go as $\sim N_c^{M+1}$ or $\sim N_c^{M-1}$. The gluon exchange comes with a factor $\sigma \sim N_c^{-1}$, so in total the overall N_c power of going to these systems are N_c^M and N_c^{M-2} . In the large- N_c approximation the latter possibility is discarded, which is equivalent to dropping all the terms above the diagonal in the matrix (4.29).

It is clear from this discussion that the system of differential equations (4.26) simplifies, in the large- N_c limit, to

$$\begin{aligned} \frac{d}{dt} C_{m_1 m_2 \dots m_i \dots m_j \dots m_K}^M &\simeq -\frac{1}{2} n(t) N_c \sum_{k=1}^K \sigma_{\bar{k} m_k} C_{m_1 m_2 \dots m_i \dots m_j \dots m_K}^M \\ &\quad - \frac{1}{2} n(t) \sum_{i=1}^{K-1} \sum_{j>i}^K (\sigma_{\bar{i} m_j} + \sigma_{m_i \bar{j}} - \sigma_{m_i m_j} - \sigma_{\bar{i} \bar{j}}) C_{m_1 m_2 \dots m_j \dots m_i \dots m_K}^{M+1}. \end{aligned} \quad (4.30)$$

Here we have included superscripts to show the N_c -scaling. In the second line, we have indicated that only the correlators scaling as N_c^{M+1} should be included in the sum. This means that in the large- N_c limit the correlators with M traces only depend on the correlators

with $M + 1$ traces. Similarly, the correlators with $M + 1$ traces depend on the correlators with $M + 2$ traces and so on. This continues all the way up to the correlators with $K - 1$ traces, which depend on the correlators with K traces. Using (4.30) the differential equation for the correlator scaling as N_c^K is

$$\frac{d}{dt} C_{12\dots K} \simeq -\frac{1}{2} n(t) N_c \sum_{k=1}^K \sigma_{\bar{k}k} C_{12\dots K}. \quad (4.31)$$

Since this is exactly solvable,

$$C_{12\dots K}(t) = N_c^K e^{-\frac{1}{2} N_c \int_{t_2}^t ds n(s) \sum_{k=1}^K \sigma_{\bar{k}k}(s)}, \quad (4.32)$$

this provides a “bootstrap” for the whole system of equations. The above argument shows that in principle all the correlators can be solved exactly in the large- N_c limit.

As a side note, we can also understand the large- N_c approximation as a simplification of the operation of performing medium averages on multiple traced correlators. Given that a dipole in the large- N_c is given by

$$\mathcal{S}_{1\bar{1}}(t, t_2) \equiv \frac{1}{N_c} \langle \text{tr}[V_1 V_1^\dagger] \rangle = e^{-\frac{1}{2} N_c \int_{t_2}^t ds n(s) \sigma_{1\bar{1}}}, \quad (4.33)$$

the answer for $C_{1\dots K}(t)$ is just given by the product of K dipoles, i.e. $C_{1\dots K} \simeq N_c^K \mathcal{S}_{1\bar{1}} \dots \mathcal{S}_{K\bar{K}}$. On the level of the full correlator, this corresponds to the simplification

$$\langle \text{tr}[W^1] \text{tr}[W^2] \dots \text{tr}[W^K] \rangle \approx \langle \text{tr}[W^1] \rangle \langle \text{tr}[W^2] \rangle \dots \langle \text{tr}[W^K] \rangle. \quad (4.34)$$

This argument can also be extended to any of the other correlators discussed above, e.g. $\langle \text{tr}[W^1] \text{tr}[W^2 \dots W^K] \rangle \approx \langle \text{tr}[W^1] \rangle \langle \text{tr}[W^2 \dots W^K] \rangle$.

The simplified differential equation, eq. (4.30), can also be solved directly to get the recursive formula

$$\begin{aligned} C_{m_1 m_2 \dots m_i \dots m_j \dots m_K}^M &= N_c^M e^{-\frac{1}{2} N_c \int_{t_2}^t ds n(s) \sum_{k=1}^K \sigma_{\bar{k}m_k}} \\ &\quad - \frac{1}{2} \int_{t_2}^t ds n(s) \sum_{i=1}^{K-1} \sum_{j>i}^K \left((\sigma_{\bar{i}m_j} + \sigma_{m_i \bar{j}} - \sigma_{m_i m_j} - \sigma_{\bar{i} \bar{j}}) C_{m_1 m_2 \dots m_j \dots m_i \dots m_K}^{M+1} \right) \\ &\quad \times e^{-\frac{1}{2} N_c \int_s^t ds' n(s') \sum_{k=1}^K \sigma_{\bar{k}m_k}. \end{aligned} \quad (4.35)$$

This can also be written in terms of dipoles, namely

$$\begin{aligned} C_{m_1 m_2 \dots m_i \dots m_j \dots m_K}^M &= N_c^M \prod_{k=1}^K \mathcal{S}_{m_k \bar{k}}(t, t_2) \\ &\quad - \frac{1}{2} \int_{t_2}^t ds n(s) \sum_{i=1}^{K-1} \sum_{j>i}^K \left((\sigma_{\bar{i}m_j} + \sigma_{m_i \bar{j}} - \sigma_{m_i m_j} - \sigma_{\bar{i} \bar{j}}) C_{m_1 m_2 \dots m_j \dots m_i \dots m_K}^{M+1} \right) \prod_{k=1}^K \mathcal{S}_{m_k \bar{k}}(t, s). \end{aligned} \quad (4.36)$$

From this equation it is clear that all of the Wilson line correlators can be written in terms of dipoles in the large- N_c limit. That is because eq. (4.36) is a recursive relation

(“bootstrap”) that stops when you reach the term with K traces, which is given in terms of dipoles in (4.34). Since the only Wilson line structure that appears in both (4.34) and (4.36) is dipoles, it means all the correlator can be written in terms of dipoles. In ref. [34] it was pointed out that all higher-order correlators can be reduced to dipoles and quadrupoles at large- N_c . This is true, but it is interesting to note that eq. (4.36) with $K = 2$ shows that quadrupoles also can be written in terms of dipoles, albeit in a convoluted form. The result in this section directly confirms the results of [34], but goes one step further and shows that really only dipoles are needed at large- N_c .

We could, in principle, also devise a scheme to compute sub-leading color corrections, that scale like N_c^{-2} relative to the leading terms, following the steps in eqs. (4.13) and (4.14), and below. We have nevertheless not pursued this program further in this work.

5 Conclusion and outlook

In this paper we have developed a general method for calculating correlators involving an arbitrary number of Wilson lines in the fundamental representation. This culminated in the system of differential equations in eq. (4.26). This system can be solved numerically. We showed that in the large- N_c limit the resulting simplified system of differential equations, eq. (4.30), can be solved exactly. We also provided a general way to compute color sub-leading corrections, suppressed by N_c^{-2} relative to the leading terms. This was done in detail for the four-point correlator, in eqs. (4.13) and (4.14), but can easily be extended to any higher-order correlator. All the results can then be written in terms of dipoles and their convolutions.

This technique was applied on three different cases of $1 \rightarrow 2$ parton splittings in the medium, which were shown to involve correlators containing up to eight (fundamental) Wilson lines. We used our method to calculate these both at finite and large N_c . Comparisons of the results are shown in figure 4. From these plots it is clear that in this exact case the large- N_c approximations works quite well for small θ , but the differences become bigger as θ grows. In certain areas of the phase space the error in using the large- N_c limit might be as high as 16%. This is expected given that the corrections we find generically scale as N_c^{-2} .

Since our method deals with a generic set of correlated Wilson lines, representing particles moving on eikonal trajectories through a background field, it could easily be extended to many other physical situations. For future work it would be interesting to apply our results in initial state physics, where similar correlators of Wilson lines also appear, and for soft contributions to event or jet observables in electron-positron or proton-proton collisions. Finally, we plan on extending the formulation to account for non-eikonal corrections to the particle trajectories.

Acknowledgments

We would like to thank A. Takacs for useful discussions. This work is supported by a Starting Grant from Trond Mohn Foundation (BFS2018REK01) and the University of Bergen.

A Calculation of spectrums

Here we will show the calculations leading up to the for the emission spectra $\frac{dI}{dzd\theta}$. The Feynman rules from [18] have been used to calculate the matrix elements.

A.1 Pair production

We start with the process of a photon producing a quark-antiquark pair. This process has been calculated in [22] but we will restate some of the results. The amplitude is

$$\begin{aligned} \mathcal{M}_{s_1, s_2}^{ij} &= \int_{\mathbf{p}_0, \mathbf{p}'_1, \mathbf{p}'_2} \int_{t_0}^L dt_1 (2\pi)^2 \delta(\mathbf{p}_0 - \mathbf{p}'_1 - \mathbf{p}'_2) \left[(\mathbf{p}_1 | \mathcal{G}_F(L, t_1) | \mathbf{p}'_1) (\mathbf{p}'_2 | \bar{\mathcal{G}}_F(L, t_1) | \mathbf{p}_2) \right]^{ij} \\ &\times A_{\lambda, s_1, s_2}(\mathbf{p}'_2 - z\mathbf{p}_0, z) \frac{1}{2E} e^{-i\frac{\mathbf{p}_0^2}{2E}(t_1 - t_0)} \mathcal{M}_{0\lambda}(\mathbf{p}_0), \end{aligned} \quad (\text{A.1})$$

where the photon-quark vertex is given by

$$A_{\lambda, s_1, s_2}(\mathbf{q}, z) = \frac{2ie}{\sqrt{z(1-z)}} \delta_{-s_2 s_1} (z\delta_{\lambda s_1} - (1-z)\delta_{\lambda s_2}) \mathbf{q} \cdot \epsilon_\lambda. \quad (\text{A.2})$$

The initial hard process is represented by the amplitude \mathcal{M}_0 . After using the eikonal approximation (2.11) this becomes (up to some phase that cancels when we take the square)

$$\begin{aligned} \mathcal{M}_{s_1, s_2}^{ij} &= \frac{1}{2E} \int_{t_0}^L dt_1 e^{i\frac{1}{2z(1-z)E}((1-z)\mathbf{p}_2 - z\mathbf{p}_1)^2 t_1} \left[V_1(L, t_1) V_2^\dagger(t_1, L) \right]^{ij} \\ &\times A_{\lambda, s_1, s_2}((1-z)\mathbf{p}_2 - z\mathbf{p}_1, z) \mathcal{M}_{0\lambda}(\mathbf{p}_1 + \mathbf{p}_2). \end{aligned} \quad (\text{A.3})$$

We have used the more compact notation to write $V_F(\mathbf{r}_1) \equiv V_1$, $V_F(\mathbf{r}_2) \equiv V_2$. The goal is to calculate

$$\frac{dI}{dz d\theta} = \frac{z(1-z)E^2\theta}{8\pi^2} \frac{\langle |\mathcal{M}|^2 \rangle}{\langle |\mathcal{M}_0|^2 \rangle}. \quad (\text{A.4})$$

The Wilson lines can be split using $V(L, t_1) = V(L, t_2)V(t_2, t_1)$. Then we only need to deal with the two time intervals (L, t_2) and (t_2, t_1) . After squaring the amplitude, averaging over initial polarization, summing the final spins, flavor and colors and taking the medium average this becomes (3.3) with (3.7) and (3.8).

A.2 Quark-gluon splitting

The amplitude was calculated in [18] and is

$$\begin{aligned} \mathcal{M}_{\lambda, s}^{ai} &= \int_{\mathbf{p}_0, \mathbf{p}'_0, \mathbf{k}', \mathbf{p}'} \int_{t_0}^L dt_1 (2\pi)^2 \delta(\mathbf{p}'_0 - \mathbf{k}' - \mathbf{p}') (\mathbf{k}' | \mathcal{G}_A^{ab}(L, t_1) | \mathbf{k}') \\ &\times \left[(\mathbf{p}' | \mathcal{G}_F(L, t_1) | \mathbf{p}') A_{\lambda, s, s'}^b(\mathbf{k}' - z\mathbf{p}'_0, z) \frac{1}{2E} (\mathbf{p}'_0 | \mathcal{G}_F(t_1, t_0) | \mathbf{p}_0) \right]^{ij} \mathcal{M}_{0s'}^j(\mathbf{p}_0), \end{aligned} \quad (\text{A.5})$$

where the quark-gluon vertex is

$$A_{\lambda, s, s'}^{aj}(\mathbf{q}, z) = -\frac{2igt_{ij}^a}{z\sqrt{1-z}} \delta_{s's} [\delta_{\lambda s} + (1-z)\delta_{\lambda -s}] \mathbf{q} \cdot \epsilon_\lambda^*. \quad (\text{A.6})$$

Again this simplifies in the eikonal limit (2.11)

$$\mathcal{M}_{\lambda,s}^{ai} = \frac{1}{2E} \int_{t_0}^L dt_1 e^{i\frac{1}{2z(1-z)E}((1-z)\mathbf{k}-z\mathbf{p})^2 t_1} U_2^{ab}(L, t_1) [V_1(L, t_1) A_{\lambda,s,s'}^b V_0(t_1, t_0)]^{ij} \mathcal{M}_{0s'}^j(\mathbf{k} + \mathbf{p}). \quad (\text{A.7})$$

We have denoted the adjoint Wilson line as $V_A(\mathbf{r}_2) \equiv U_2$. Squaring the amplitude, summing/averaging over spins and colors and taking the medium average gives

$$\begin{aligned} \frac{dI}{dz d\theta} &= \frac{\alpha_s}{\pi} \frac{P_{gq}(z)}{\theta} \frac{2}{N_c^2 - 1} 2 \operatorname{Re} \int_{t_0}^L \frac{dt_1}{t_f} \int_{t_1}^L \frac{dt_2}{t_f} e^{-i\frac{t_2-t_1}{t_f}} \\ &\times \langle [U^\dagger(t_2, L) U(L, t_1)]^{\bar{b}b} \operatorname{tr} [V_0^\dagger(0, t_2) t^{\bar{b}} V_1^\dagger(t_2, L) V_1(L, t_1) t^b V_0(t_1, 0)] \rangle, \end{aligned} \quad (\text{A.8})$$

where the relevant Altarelli-Parisi splitting function is

$$P_{gq}(z) = C_F \frac{1 + (1-z)^2}{z}. \quad (\text{A.9})$$

To continue we transform the adjoint Wilson lines into fundamental ones using the identity (2.3). The resulting expression will contain many group generators t^a , and can be simplified by using the Fierz identity (4.4). Finally, completely in the fundamental representation the Wilson line structure becomes

$$\begin{aligned} &\langle [U^\dagger(t_2, L) U(L, t_1)]^{\bar{b}b} \operatorname{tr} [V_0^\dagger(0, t_2) t^{\bar{b}} V_1^\dagger(t_2, L) V_1(L, t_1) t^b V_0(t_1, 0)] \rangle \\ &= \frac{1}{2} \langle \left([V_2^\dagger V_2 V_1^\dagger V_1]_{kj} [V_2^\dagger V_2]_{il} - \frac{1}{N_c} [V_1^\dagger V_1]_{ij} \delta_{kl} \right)_{(L, t_2)} \\ &\quad \times \left([V_1 V_2^\dagger]_{jk} [V_2 V_0^\dagger]_{li} - \frac{1}{N_c} [V_1 V_0^\dagger]_{ji} \delta_{lk} \right)_{(t_2, t_1)} \rangle. \end{aligned} \quad (\text{A.10})$$

Conservation of color then makes it possible to connect i, l and j, k so when we include the proper normalization factor the whole expression turns into (3.3) with (3.16) and (3.17).

A.3 Gluon-gluon splitting

The calculation of the emission spectrum for gluon-gluon splittings was done in [23]. For completeness we will also include the main results here. The matrix element of the process is

$$\begin{aligned} \mathcal{M}_{\lambda_1, \lambda_2}^{a_1 a_2} &= \int_{\mathbf{k}_0, \mathbf{k}'_0, \mathbf{k}'_1, \mathbf{k}'_2} \int_{t_0}^L dt_1 (2\pi)^2 \delta(\mathbf{k}'_0 - \mathbf{k}'_1 - \mathbf{k}'_2) \\ &\times (\mathbf{k}_1 | \mathcal{G}_A^{a_1 b_1}(L, t_1) | \mathbf{k}'_1) (\mathbf{k}_2 | \mathcal{G}_A^{a_2 b_2}(L, t_1) | \mathbf{k}'_2) A_{\lambda_0, \lambda_1, \lambda_2}^{b_0 b_1 b_2}(\mathbf{k}'_2 - z\mathbf{k}'_0, z) \frac{1}{2E} (\mathbf{k}'_0 | \mathcal{G}_A^{b_0 c}(t_1, t_0) | \mathbf{k}_0) \\ &\times \mathcal{M}_{0\lambda_0}^c(\mathbf{k}_0), \end{aligned} \quad (\text{A.11})$$

where the gluon-gluon vertex is

$$A_{\lambda_0, \lambda_1, \lambda_2}^{b_0 b_1 b_2}(\mathbf{q}, z) = -2ig(T^{b_0})^{b_1 b_2} \left[\frac{1}{z} (\mathbf{q} \cdot \boldsymbol{\epsilon}_{\lambda_2}^*) \delta_{\lambda_0 \lambda_1} + \frac{1}{1-z} (\mathbf{q} \cdot \boldsymbol{\epsilon}_{\lambda_1}^*) \delta_{\lambda_0 \lambda_2} - (\mathbf{q} \cdot \boldsymbol{\epsilon}_{\lambda_0}) \delta_{\lambda_1 \lambda_2} \right]. \quad (\text{A.12})$$

In the eikonal approximation (2.11) the amplitude is

$$\begin{aligned} \mathcal{M}_{\lambda_1, \lambda_2}^{a_1 a_2} &= \frac{1}{2E} \int_{t_0}^L dt_1 e^{i \frac{1}{2z(1-z)E} ((1-z)\mathbf{k}_2 - z\mathbf{k}_1)^2 t_1} U_1^{a_1 b_1}(L, t_1) U_2^{a_2 b_2}(L, t_1) A_{\lambda_0, \lambda_1, \lambda_2}^{b_0 b_1 b_2} U_0^{b_0 c}(t_1, t_0) \\ &\times \mathcal{M}_{0s'}^c(\mathbf{k}_1 + \mathbf{k}_2). \end{aligned} \quad (\text{A.13})$$

After taking the square of the amplitude, summing/averaging over spins and colors and taking the medium average this becomes

$$\begin{aligned} \frac{dI}{dz d\theta} &= \frac{\alpha_s}{\pi} \frac{P_{gg}(z)}{\theta} \frac{2}{N_c(N_c^2 - 1)} 2\text{Re} \int_{t_0}^L \frac{dt_1}{t_f} \int_{t_1}^L \frac{dt_2}{t_f} e^{-i \frac{t_2 - t_1}{t_f}} \\ &\times f^{b_0 b_1 b_2} f^{\bar{b}_0 \bar{b}_1 \bar{b}_2} \langle [U_1^{a_1 d_1} U_2^{a_2 d_2} U_1^{\dagger \bar{b}_1 a_1} U_2^{\dagger \bar{b}_2 a_2}]_{(L, t_2)} [U_1^{d_1 b_1} U_2^{d_2 b_2} U_0^{\dagger b_0 \bar{b}_0}]_{(t_2, t_1)} \rangle, \end{aligned} \quad (\text{A.14})$$

where the relevant Altarelli-Parisi splitting function is

$$P_{gg}(z) = N_c \left[z(1-z) + \frac{1-z}{z} + \frac{z}{1-z} \right]. \quad (\text{A.15})$$

Conservation of color lets us decouple the Wilson lines in the two time intervals (L, t_2) and (t_2, t_1)

$$f^{b_0 b_1 b_2} U_1^{d_1 b_1} U_2^{d_2 b_2} U_0^{\dagger b_0 \bar{b}_0} = \frac{1}{N_c(N_c^2 - 1)} f^{d_1 d_2 \bar{b}_0} f^{d'_1 d'_2 \bar{b}'_0} f^{b_0 b_1 b_2} U_1^{d'_1 b_1} U_2^{d'_2 b_2} U_0^{\dagger b_0 \bar{b}'_0}. \quad (\text{A.16})$$

The part in the time interval (t_2, t_1) can be calculated explicitly because of its simple color structure

$$\frac{1}{N_c(N_c^2 - 1)} f^{d'_1 d'_2 \bar{b}'_0} f^{b_0 b_1 b_2} U_1^{d'_1 b_1} U_2^{d'_2 b_2} U_0^{\dagger b_0 \bar{b}'_0} = e^{-\frac{N_c}{2} \int_{t_1}^{t_2} dt n(t) [\sigma_{01} + \sigma_{02} + \sigma_{12}]}. \quad (\text{A.17})$$

What remains are the Wilson lines in time interval (L, t_2)

$$f^{d_1 d_2 \bar{b}_0} f^{\bar{b}_0 \bar{b}_1 \bar{b}_2} \langle [U_1^{a_1 d_1} U_2^{a_2 d_2} U_1^{\dagger \bar{b}_1 a_1} U_2^{\dagger \bar{b}_2 a_2}]_{(L, t_2)} \rangle. \quad (\text{A.18})$$

However, these are not that easy to calculate. The procedure for calculating Wilson line products detailed in section 4 only involve fundamental Wilson lines, so (2.3) is used to turn all the adjoint Wilson lines into fundamental ones. Then one can use the definition of the structure constants $[t^a, t^b] = i f^{abc} t^c$ and the identity (4.4) to get rid of all the group generators. This was done in [23], and we quote the result

$$\begin{aligned} &f^{d_1 d_2 \bar{b}_0} f^{\bar{b}_0 \bar{b}_1 \bar{b}_2} \langle [U_1^{a_1 d_1} U_2^{a_2 d_2} U_1^{\dagger \bar{b}_1 a_1} U_2^{\dagger \bar{b}_2 a_2}]_{(L, t_2)} \rangle \\ &= \frac{1}{2} \langle \text{tr}[V_1 V_1^\dagger] \text{tr}[V_2 V_2^\dagger V_1 V_1^\dagger] \text{tr}[V_2 V_2^\dagger] - \text{tr}[V_1 V_1^\dagger V_2 V_2^\dagger V_1 V_1^\dagger V_2 V_2^\dagger] + \text{h.c.} \rangle_{(L, t_2)} \\ &= \langle \text{tr}[V_1 V_1^\dagger] \text{tr}[V_2 V_2^\dagger V_1 V_1^\dagger] \text{tr}[V_2 V_2^\dagger] - \text{tr}[V_1 V_1^\dagger V_2 V_2^\dagger V_1 V_1^\dagger V_2 V_2^\dagger] \rangle_{(L, t_2)}. \end{aligned} \quad (\text{A.19})$$

The last step is true because the medium averaged products of Wilson lines are real. This means that in the gluon-gluon case we end up with medium averaged products of up to eight Wilson lines. Putting it all together we get the formula (3.3) with (3.20) and (3.21).

B Six and eight Wilson lines

B.1 Six lines

In section 4 we developed the tools to calculate the correlators of six and eight Wilson lines, which appeared in (3.16) and (3.20). To start we will look at the case of six lines, which follows from (4.26) with $K = 3$. The relevant expression is $\frac{d}{dt} \langle [V_1 V_1^\dagger]_{i_1 j_1} [V_2 V_2^\dagger]_{i_2 j_2} [V_3 V_3^\dagger]_{i_3 j_3} \rangle$. If this is contracted with $\delta_{j_1 i_2} \delta_{j_2 i_1} \delta_{j_3 i_3}$ it becomes

$$\delta_{j_1 i_2} \delta_{j_2 i_1} \delta_{j_3 i_3} \frac{d}{dt} \langle [V_1 V_1^\dagger]_{i_1 j_1} [V_2 V_2^\dagger]_{i_2 j_2} [V_3 V_3^\dagger]_{i_3 j_3} \rangle = \langle \text{tr}[V_1 V_1^\dagger V_2 V_2^\dagger] \text{tr}[V_3 V_3^\dagger] \rangle, \quad (\text{B.1})$$

which is the structure encountered in (3.16). To get exactly the same as in that equation we need only change the labels $(1, \bar{1}, 2, \bar{2}, 3, \bar{3}) \rightarrow (1, 2, \bar{2}, \bar{1}, 2, \bar{2})$, which also simplifies the system somewhat. The six different projections are gathered into a vector

$$\begin{aligned} \mathbf{C}^\top &= (C_{1\bar{2}2}, C_{\bar{2}12}, C_{2\bar{2}1}, C_{12\bar{2}}, C_{21\bar{2}}, C_{\bar{2}21}) \\ &= \left(\langle \text{tr}[V_1 V_2^\dagger] \text{tr}[V_2 V_1^\dagger] \text{tr}[V_2 V_2^\dagger] \rangle, \langle \text{tr}[V_1 V_2^\dagger V_2 V_1^\dagger] \text{tr}[V_2 V_2^\dagger] \rangle, \langle \text{tr}[V_1 V_2^\dagger] \text{tr}[V_2 V_1^\dagger] \rangle, \right. \\ &\quad \left. \langle \text{tr}[V_1 V_2^\dagger] \text{tr}[V_1^\dagger V_2] \rangle, \langle \text{tr}[V_1 V_1^\dagger] \rangle, \langle \text{tr}[V_1 V_2^\dagger V_2 V_1^\dagger V_2 V_2^\dagger] \rangle \right). \end{aligned} \quad (\text{B.2})$$

We can write the system of differential equations as

$$\frac{d}{dt} \mathbf{C} = -\frac{1}{2} n(t) \underline{\mathbb{M}} \mathbf{C}. \quad (\text{B.3})$$

One can get the elements of the 6×6 matrix $\underline{\mathbb{M}}$ from (4.23) and (4.24). The 6 diagonal entries are simply

$$\mathbb{M}_{m_1 m_2 m_3}^{m_1 m_2 m_3} = N_c (\sigma_{2m_1} + \sigma_{\bar{1}m_2} + \sigma_{\bar{2}m_3}) - \frac{1}{N_c} \sigma_{1\bar{1}}, \quad (\text{B.4})$$

where (m_1, m_2, m_3) now is some permutation of $(1, \bar{2}, 2)$. The non-zero non-diagonal entries are given by

$$\begin{aligned} \mathbb{M}_{m_1 m_2 m_3}^{m_2 m_1 m_3} &= \sigma_{2m_2} + \sigma_{\bar{1}m_1} - \sigma_{m_2 m_1} - \sigma_{2\bar{1}} \\ \mathbb{M}_{m_1 m_2 m_3}^{m_3 m_2 m_1} &= \sigma_{2m_3} + \sigma_{\bar{2}m_1} - \sigma_{m_3 m_1} - \sigma_{2\bar{2}} \\ \mathbb{M}_{m_1 m_2 m_3}^{m_1 m_3 m_2} &= \sigma_{\bar{1}m_3} + \sigma_{\bar{2}m_2} - \sigma_{m_3 m_2} - \sigma_{\bar{1}\bar{2}}. \end{aligned} \quad (\text{B.5})$$

This leads to six differential equations which can be solved numerically for the six functions in \mathbf{C} . Interestingly this 6×6 system is reducible into two 3×3 systems. The first of these systems leads to three differential equations that actually can be solved exactly:

$$\begin{aligned} \frac{d}{dt} \langle \text{tr}[V_1 V_1^\dagger] \rangle &= -C_{Fn}(t) \sigma_{1\bar{1}} \langle \text{tr}[V_1 V_1^\dagger] \rangle \\ \frac{d}{dt} \langle \text{tr}[V_1 V_2^\dagger] \text{tr}[V_2 V_1^\dagger] \rangle &= -\frac{1}{2} n(t) [N_c (\sigma_{\bar{1}\bar{2}} + \sigma_{1\bar{2}}) - \frac{1}{N_c} \sigma_{1\bar{1}}] \langle \text{tr}[V_1 V_2^\dagger] \text{tr}[V_2 V_1^\dagger] \rangle \\ &\quad - \frac{1}{2} n(t) (\sigma_{1\bar{1}} - \sigma_{\bar{1}\bar{2}} - \sigma_{\bar{1}\bar{2}}) \langle \text{tr}[V_1 V_1^\dagger] \rangle \\ \frac{d}{dt} \langle \text{tr}[V_1 V_2^\dagger] \text{tr}[V_2 V_1^\dagger] \rangle &= -\frac{1}{2} n(t) [N_c (\sigma_{\bar{1}\bar{2}} + \sigma_{1\bar{2}}) - \frac{1}{N_c} \sigma_{1\bar{1}}] \langle \text{tr}[V_1 V_2^\dagger] \text{tr}[V_2 V_1^\dagger] \rangle \\ &\quad - \frac{1}{2} n(t) (\sigma_{1\bar{1}} - \sigma_{1\bar{2}} - \sigma_{\bar{1}\bar{2}}) \langle \text{tr}[V_1 V_1^\dagger] \rangle \end{aligned} \quad (\text{B.6})$$

This is a nice consistency check, as taking the system for four Wilson lines (4.7) and letting $2 \rightarrow \bar{2}$ reproduces the first and second of these equations. Similarly, (4.7) with $\bar{2} \rightarrow 2$ reproduces the first and third. Solving the first two gives

$$\begin{aligned} \langle \text{tr}[V_1 V_1^\dagger] \rangle &= N_c e^{-C_F \int_{t_2}^t ds n(s) \sigma_{1\bar{1}}(s)} \\ \langle \text{tr}[V_1 V_2^\dagger] \text{tr}[V_2 V_1^\dagger] \rangle &= (N_c^2 - 1) e^{-\frac{1}{2} \int_{t_2}^t ds n(s) (N_c(\sigma_{1\bar{2}} + \sigma_{12}) - \frac{1}{N_c} \sigma_{1\bar{1}})} + e^{-C_F \int_{t_2}^t ds n(s) \sigma_{1\bar{1}}(s)}. \end{aligned} \quad (\text{B.7})$$

One can easily get $\langle \text{tr}[V_1 V_2^\dagger] \text{tr}[V_2 V_1^\dagger] \rangle$ from the second of these equations by changing $\bar{2} \rightarrow 2$. The first equation in (B.7) is a well known result, so it is nice that we reproduce that.

However, this is nothing new, merely a check that the system of six Wilson lines is consistent with the previous calculations. The remaining 3×3 system contains the correlator we actually want to solve, but is also a more complicated nonhomogeneous system. It is useful to define two vectors with the 3 unknown and 3 known functions

$$\begin{aligned} \mathbf{C}_1^\top &= \left(\langle \text{tr}[V_1 V_2^\dagger] \text{tr}[V_2 V_1^\dagger] \text{tr}[V_2 V_2^\dagger] \rangle, \langle \text{tr}[V_1 V_2^\dagger V_2 V_1^\dagger] \text{tr}[V_2 V_2^\dagger] \rangle, \langle \text{tr}[V_1 V_2^\dagger V_2 V_1^\dagger V_2 V_2^\dagger] \rangle \right) \\ \mathbf{C}_2^\top &= \left(\langle \text{tr}[V_1 V_2^\dagger] \text{tr}[V_2 V_1^\dagger] \rangle, \langle \text{tr}[V_1 V_2^\dagger] \text{tr}[V_1^\dagger V_2] \rangle, \langle \text{tr}[V_1 V_1^\dagger] \rangle \right). \end{aligned} \quad (\text{B.8})$$

Then we can write the remaining system of differential equations as

$$\frac{d}{dt} \mathbf{C}_1 = -\frac{1}{2} n(t) (\underline{\mathbb{M}}_1 \mathbf{C}_1 + \underline{\mathbb{M}}_2 \mathbf{C}_2). \quad (\text{B.9})$$

The 3×3 matrices $\underline{\mathbb{M}}_1$ and $\underline{\mathbb{M}}_2$ are subsets of the 6×6 matrix $\underline{\mathbb{M}}$ and have the form

$$\underline{\mathbb{M}}_1 = \begin{bmatrix} N_c(\sigma_{12} + \sigma_{1\bar{2}} + \sigma_{2\bar{2}}) - \frac{1}{N_c} \sigma_{1\bar{1}} & \sigma_{1\bar{1}} + \sigma_{2\bar{2}} - \sigma_{1\bar{2}} - \sigma_{12} & 0 \\ \sigma_{12} + \sigma_{1\bar{2}} - \sigma_{1\bar{2}} - \sigma_{12} & 2(C_F \sigma_{1\bar{1}} + N_c \sigma_{2\bar{2}}) & \sigma_{1\bar{2}} + \sigma_{12} - \sigma_{12} - \sigma_{1\bar{2}} \\ 0 & \sigma_{1\bar{1}} + \sigma_{2\bar{2}} - \sigma_{12} - \sigma_{1\bar{2}} & N_c(\sigma_{2\bar{2}} + \sigma_{1\bar{2}} + \sigma_{12}) - \frac{1}{N_c} \sigma_{1\bar{1}} \end{bmatrix}. \quad (\text{B.10})$$

$$\underline{\mathbb{M}}_2 = \begin{bmatrix} \sigma_{1\bar{2}} - \sigma_{12} - \sigma_{2\bar{2}} & \sigma_{1\bar{2}} - \sigma_{2\bar{2}} - \sigma_{1\bar{2}} & 0 \\ 0 & 0 & -2\sigma_{2\bar{2}} \\ \sigma_{1\bar{2}} - \sigma_{2\bar{2}} - \sigma_{12} & \sigma_{12} - \sigma_{1\bar{2}} - \sigma_{2\bar{2}} & 0 \end{bmatrix}. \quad (\text{B.11})$$

This can be solved numerically for the three functions in \mathbf{C}_1 , and the result can be seen in figure 7.

B.1.1 Quark-gluon splitting in the large- N_c

As showed in section 4.3 all the functions in \mathbf{C} can be solved exactly in the large- N_c limit. The two terms with highest powers of N_c , $\langle [\text{tr}[V_1 V_2^\dagger] \text{tr}[V_2 V_1^\dagger] \text{tr}[V_2 V_2^\dagger]] \rangle$ and $\langle \text{tr}[V_1 V_2^\dagger V_2 V_1^\dagger] \text{tr}[V_2 V_2^\dagger] \rangle$ can be gotten directly from (4.31) and (4.36) respectively. Alternatively one can count the N_c powers in (B.7) and realize that $\underline{\mathbb{M}}_1$ and $\underline{\mathbb{M}}_2$ simplify to

$$\underline{\mathbb{M}}_1 \simeq \begin{bmatrix} N_c(\sigma_{12} + \sigma_{1\bar{2}} + \sigma_{2\bar{2}}) & 0 & 0 \\ \sigma_{12} + \sigma_{1\bar{2}} - \sigma_{1\bar{2}} - \sigma_{12} & N_c(\sigma_{1\bar{1}} + 2\sigma_{2\bar{2}}) & 0 \\ 0 & \sigma_{1\bar{1}} + \sigma_{2\bar{2}} - \sigma_{12} - \sigma_{1\bar{2}} & N_c(\sigma_{2\bar{2}} + \sigma_{1\bar{2}} + \sigma_{12}) \end{bmatrix}. \quad (\text{B.12})$$

$$\underline{\mathbb{M}}_2 \simeq \begin{bmatrix} 0 & 0 & 0 \\ 0 & 0 & 0 \\ \sigma_{1\bar{2}} - \sigma_{2\bar{2}} - \sigma_{12} & \sigma_{12} - \sigma_{1\bar{2}} - \sigma_{2\bar{2}} & 0 \end{bmatrix}. \quad (\text{B.13})$$

The solutions to the simplified differential equation leads to (3.19).

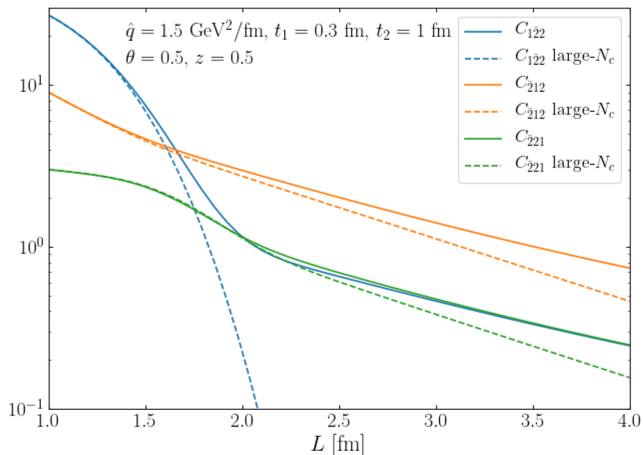


Figure 7. The exact and large- N_c solutions to the system of differential equations (B.9).

B.2 Eight Wilson lines

For more than six Wilson lines the matrix in (4.26) becomes so big that it is impractical to analyze it by hand.

For eight lines it involves the $4! = 24$ projections of $\langle [V_1 V_1^\dagger]_{i_1 j_1} [V_2 V_2^\dagger]_{i_2 j_2} [V_3 V_3^\dagger]_{i_3 j_3} [V_4 V_4^\dagger]_{i_4 j_4} \rangle$, and the matrix \mathbb{M} has 24^2 elements. The power of our result in section 4 is here evident, as simply solving the differential equation (4.26) for $K = 4$ numerically immediately gives the result for eight lines Wilson lines. To get the Wilson line correlators we want from (3.20) the four last labels must be changed $(\bar{3}, \bar{3}, \bar{4}, \bar{4}) \rightarrow (\bar{1}, \bar{1}, \bar{2}, \bar{2})$ so that $\langle [V_1 V_1^\dagger]_{i_1 j_1} [V_2 V_2^\dagger]_{i_2 j_2} [V_3 V_3^\dagger]_{i_3 j_3} [V_4 V_4^\dagger]_{i_4 j_4} \rangle \rightarrow \langle [V_1 V_1^\dagger]_{i_1 j_1} [V_2 V_2^\dagger]_{i_2 j_2} [V_1 V_1^\dagger]_{i_3 j_3} [V_2 V_2^\dagger]_{i_4 j_4} \rangle$. The two relevant solutions are shown in figure 8.

One thing to notice in figure 8 is that for the case of eight Wilson lines correlators, keeping only the first term in the large- N_c limit does not work well.

C Derivation of differential equation

In this appendix we will show in more detail how the differential equation (4.26) was derived.

We start with the derivation of (4.21). To illustrate we will first show the calculation for $K = 2$, that is calculating $\langle [V_1 V_1^\dagger]_{i_1 j_1} [V_2 V_2^\dagger]_{i_2 j_2} \rangle$. This generalizes rather easily to the arbitrary K case (4.19). Expanding the first of these pairs like in (4.1) up to first order of ϵ and defining $\mathbf{A} \equiv A^a t^a$ it becomes

$$\begin{aligned}
 [V_1 V_1^\dagger]_{i_1 j_1}(t+\epsilon, t_0) &= \left[V_1 V_1^\dagger + ig \int_t^{t+\epsilon} ds (\mathbf{A}_1(s) V_1 V_1^\dagger - V_1 V_1^\dagger \mathbf{A}_1(s)) \right. \\
 &\quad \left. + \frac{1}{2} g^2 \int_t^{t+\epsilon} ds \int_t^{t+\epsilon} ds' (2\mathbf{A}_1(s) V_1 V_1^\dagger \mathbf{A}_1(s') - \mathbf{A}_1(s) \mathbf{A}_1(s') V_1 V_1^\dagger - V_1 V_1^\dagger \mathbf{A}_1(s) \mathbf{A}_1(s')) \right]_{i_1 j_1}.
 \end{aligned} \tag{C.1}$$

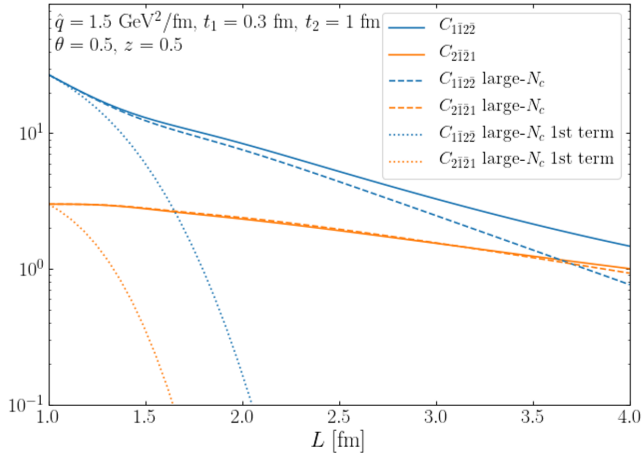


Figure 8. The exact and large- N_c version of $C_{1\bar{1}2\bar{2}} = \langle \text{tr}[V_1 V_1^\dagger] \text{tr}[V_2 V_2^\dagger V_1 V_1^\dagger] \text{tr}[V_2 V_2^\dagger] \rangle$ and $C_{2\bar{1}2\bar{2}} = \langle \text{tr}[V_1 V_1^\dagger V_2 V_2^\dagger V_1 V_1^\dagger V_2 V_2^\dagger] \rangle$.

Here all the Wilson lines on the right hand side go from t_0 to t . After taking the medium average (2.5) and using the Fierz identity (4.4) the last term becomes

$$\begin{aligned} & \frac{1}{2} g^2 \int_t^{t+\epsilon} ds \int_t^{t+\epsilon} ds' \langle [2\mathbf{A}_1(s) V_1 V_1^\dagger \mathbf{A}_1(s') - \mathbf{A}_1(s) \mathbf{A}_1(s') V_1 V_1^\dagger - V_1 V_1^\dagger \mathbf{A}_1(s) \mathbf{A}_1(s')]_{i_1 j_1} \rangle \\ & = \frac{1}{2} g^2 n(t) \epsilon \left[\gamma_{1\bar{1}} \langle \text{tr}(V_1 V_1^\dagger) \rangle \delta_{i_1 j_1} - \left(2C_F \gamma_0 + \frac{1}{N_c} \gamma_{1\bar{1}} \right) \langle V_1 V_1^\dagger \rangle_{i_1 j_1} \right]. \end{aligned} \quad (\text{C.2})$$

Now adding the second pair of Wilson lines and taking the medium average, while disregarding higher orders of ϵ , it takes the form

$$\begin{aligned} & \langle [V_1 V_1^\dagger]_{i_1 j_1} [V_2 V_2^\dagger]_{i_2 j_2} \rangle(t + \epsilon, t_0) = \langle [V_1 V_1^\dagger]_{i_1 j_1} [V_2 V_2^\dagger]_{i_2 j_2} \rangle(t, t_0) \\ & + \frac{1}{2} g^2 \epsilon n(t) \left\langle \left[\gamma_{1\bar{1}} \text{tr}(V_1 V_1^\dagger) \delta_{i_1 j_1} - \left(2C_F \gamma_0 + \frac{1}{N_c} \gamma_{1\bar{1}} \right) [V_1 V_1^\dagger]_{i_1 j_1} \right] [V_2 V_2^\dagger]_{i_2 j_2} \right. \\ & + [V_1 V_1^\dagger]_{i_1 j_1} \left[\gamma_{2\bar{2}} \text{tr}(V_2 V_2^\dagger) \delta_{i_2 j_2} - \left(2C_F \gamma_0 + \frac{1}{N_c} \gamma_{2\bar{2}} \right) [V_2 V_2^\dagger]_{i_2 j_2} \right] \Big\rangle \\ & - g^2 \int_t^{t+\epsilon} ds \int_t^{t+\epsilon} ds' \langle [\mathbf{A}_1(s) V_1 V_1^\dagger - V_1 V_1^\dagger \mathbf{A}_1(s)]_{i_1 j_1} [\mathbf{A}_2(s') V_2 V_2^\dagger - V_2 V_2^\dagger \mathbf{A}_2(s')]_{i_2 j_2} \rangle. \end{aligned} \quad (\text{C.3})$$

The last term simplifies to

$$\begin{aligned} & g^2 \int_t^{t+\epsilon} ds \int_t^{t+\epsilon} ds' \langle [\mathbf{A}_1(s) V_1 V_1^\dagger - V_1 V_1^\dagger \mathbf{A}_1(s)]_{i_1 j_1} [\mathbf{A}_2(s') V_2 V_2^\dagger - V_2 V_2^\dagger \mathbf{A}_2(s')]_{i_2 j_2} \rangle \\ & = \frac{1}{2} g^2 n(t) \epsilon \left(\gamma_{12} [V_1 V_1^\dagger]_{i_2 j_1} [V_2 V_2^\dagger]_{i_1 j_2} + \gamma_{\bar{1}\bar{2}} [V_1 V_1^\dagger]_{i_1 j_2} [V_2 V_2^\dagger]_{i_2 j_1} \right. \\ & \quad - \gamma_{1\bar{2}} \delta_{i_1 j_2} [V_2 V_2^\dagger V_1 V_1^\dagger]_{i_2 j_1} - \gamma_{\bar{1}2} \delta_{i_2 j_1} [V_1 V_1^\dagger V_2 V_2^\dagger]_{i_1 j_2} \\ & \quad \left. + \frac{1}{N_c} (\gamma_{1\bar{2}} + \gamma_{\bar{1}2} - \gamma_{12} - \gamma_{\bar{1}\bar{2}}) [V_1 V_1^\dagger]_{i_1 j_1} [V_2 V_2^\dagger]_{i_2 j_2} \right). \end{aligned} \quad (\text{C.4})$$

Letting ϵ go to zero this turns into a differential equation

$$\begin{aligned}
 & \frac{d}{dt} \langle [V_1 V_1^\dagger]_{i_1 j_1} [V_2 V_2^\dagger]_{i_2 j_2} \rangle \\
 &= \frac{1}{2} g^2 n(t) \left\langle \left[\frac{1}{N_c} (\gamma_{12} + \gamma_{\bar{1}\bar{2}} - \gamma_{1\bar{2}} - \gamma_{\bar{1}2} - \gamma_{1\bar{1}} - \gamma_{2\bar{2}} - 2(N_c^2 - 1)\gamma_0) \right] [V_1 V_1^\dagger]_{i_1 j_1} [V_2 V_2^\dagger]_{i_2 j_2} \right. \\
 & \quad + \gamma_{1\bar{1}} \text{tr}(V_1 V_1^\dagger) \delta_{i_1 j_1} [V_2 V_2^\dagger]_{i_2 j_2} + \gamma_{2\bar{2}} \text{tr}(V_2 V_2^\dagger) [V_1 V_1^\dagger]_{i_1 j_1} \delta_{i_2 j_2} \\
 & \quad - \gamma_{12} [V_1 V_1^\dagger]_{i_2 j_1} [V_2 V_2^\dagger]_{i_1 j_2} - \gamma_{\bar{1}\bar{2}} [V_1 V_1^\dagger]_{i_1 j_2} [V_2 V_2^\dagger]_{i_2 j_1} \\
 & \quad \left. + \gamma_{1\bar{2}} \delta_{i_1 j_2} [V_2 V_2^\dagger V_1 V_1^\dagger]_{i_2 j_1} + \gamma_{\bar{1}2} \delta_{i_2 j_1} [V_1 V_1^\dagger V_2 V_2^\dagger]_{i_1 j_2} \right\rangle. \tag{C.5}
 \end{aligned}$$

Now we only have to project out the two possible ways to connect the Wilson lines. Contracting with $\delta_{j_2 i_1} \delta_{j_1 i_2}$ and $\delta_{j_1 i_1} \delta_{j_2 i_2}$ gives $\frac{d}{dt} \langle \text{tr}[V_1 V_1^\dagger V_2 V_2^\dagger] \rangle$ and $\frac{d}{dt} \langle \text{tr}[V_1 V_1^\dagger] \text{tr}[V_2 V_2^\dagger] \rangle$ respectively. In section 3 we wanted to calculate $\langle \text{tr}[V_1 V_2^\dagger V_2 V_1^\dagger] \rangle$, which is similar to the above, but not exactly the same. Fortunately, our choice of labels is just a convention, and completely arbitrary. Simply making the three changes $\bar{1} \rightarrow 2$, $2 \rightarrow \bar{2}$ and $\bar{2} \rightarrow \bar{1}$ turns (C.5) into the system of differential equations in (4.7). The difference in this approach compared to what we did in section 4.1 is that (C.5) contains both of (4.5) and (4.6). This compact form is highly convenient when considering more than four Wilson lines. Generalizing the steps from equation (C.1) to (C.5) to an arbitrary number K pairs of Wilson lines produces the differential equation (4.21).

The next step is to show how to get from eq. (4.21) to the matrix elements (4.23) and (4.24). Any pair of Wilson lines has two free indices. Take for example the second Wilson line pair in (4.21) which is $W_{i_2 j_2}^2$. Start by projecting out these two indices in all the ways possible, and at the same time making as few assumptions as possible about the rest of the Wilson lines. It turns out that projecting out with two Kronecker deltas gives all the information we need. There are also only two possibilities that need to be considered: either W^2 can connect to other Wilson lines, or it connects to itself and becomes a trace. These two possibilities are given by projecting with $\delta_{j_1 i_2} \delta_{j_2 i_3}$ and $\delta_{j_1 i_3} \delta_{j_2 i_2}$, respectively. To use Wilson lines 1, 2 and 3 is arbitrary. These labels can be changed to anything else without changing the result, so the calculation is completely general.

Using (4.21) and projecting out by the two deltas $\delta_{j_1 i_2} \delta_{j_2 i_3}$ gives a differential equation for $\langle [W^1 W^2 W^3]_{i_1 j_3} W_{i_4 j_4}^4 \dots W_{i_K j_K}^K \rangle$.

$$\begin{aligned}
 & \frac{d}{dt} \langle [W^1 W^2 W^3]_{i_1 j_3} W_{i_4 j_4}^4 \dots W_{i_K j_K}^K \rangle \\
 &= -\frac{1}{2} g^2 n(t) \left(N_c (\sigma_{\bar{1}2} + \sigma_{\bar{2}3}) + \frac{1}{N_c} A_K \right) \langle [W^1 W^2 W^3]_{i_1 j_3} W_{i_4 j_4}^4 \dots W_{i_K j_K}^K \rangle \\
 & \quad - \frac{1}{2} g^2 n(t) (\sigma_{13} + \sigma_{2\bar{2}} - \sigma_{23} - \sigma_{\bar{1}2}) \langle \text{tr} W^2 [W^1 W^3]_{i_1 j_3} W_{i_4 j_4}^4 \dots W_{i_K j_K}^K \rangle \\
 & \quad + (\dots). \tag{C.6}
 \end{aligned}$$

The (...) in the end are terms that are not completely determined by the projection that was made.

Next up is the case where we project out with $\delta_{j_1 i_3} \delta_{j_2 i_2}$, making a differential equation for $\langle \text{tr } W^2 [W^1 W^3]_{i_1 j_3} W_{i_4 j_4}^4 \dots W_{i_K j_K}^K \rangle$.

$$\begin{aligned} \frac{d}{dt} \langle \text{tr } W^2 [W^1 W^3]_{i_1 j_3} W_{i_4 j_4}^4 \dots W_{i_K j_K}^K \rangle &= -\frac{1}{2} g^2 n(t) \left(N_c (\sigma_{\bar{1}3} + \sigma_{\bar{2}2}) + \frac{1}{N_c} A_K \right) \langle \text{tr } W^2 [W^1 W^3]_{i_1 j_3} W_{i_4 j_4}^4 \dots W_{i_K j_K}^K \rangle \\ &\quad - \frac{1}{2} g^2 n(t) (\sigma_{\bar{2}3} + \sigma_{2\bar{1}} - \sigma_{23} - \sigma_{\bar{1}\bar{2}}) \langle [W^1 W^2 W^3]_{i_1 j_3} W_{i_4 j_4}^4 \dots W_{i_K j_K}^K \rangle \\ &\quad + (\dots). \end{aligned} \tag{C.7}$$

In the notation from section 4 these equations become

$$\begin{aligned} \frac{d}{dt} C_{23m_3\dots m_N} &= -\frac{1}{2} g^2 n(t) \left(N_c (\sigma_{\bar{1}2} + \sigma_{\bar{2}3}) + \frac{1}{N_c} A_K \right) C_{23m_3\dots m_N} \\ &\quad - \frac{1}{2} g^2 n(t) (\sigma_{\bar{1}3} + \sigma_{2\bar{2}} - \sigma_{23} - \sigma_{\bar{1}\bar{2}}) C_{32m_3\dots m_N} \\ &\quad + (\dots), \end{aligned} \tag{C.8}$$

$$\begin{aligned} \frac{d}{dt} C_{32m_3\dots m_N} &= -\frac{1}{2} g^2 n(t) \left(N_c (\sigma_{\bar{1}3} + \sigma_{\bar{2}2}) + \frac{1}{N_c} A_K \right) C_{32m_3\dots m_N} \\ &\quad - \frac{1}{2} g^2 n(t) (\sigma_{\bar{2}3} + \sigma_{2\bar{1}} - \sigma_{23} - \sigma_{\bar{1}\bar{2}}) C_{23m_3\dots m_N} \\ &\quad + (\dots). \end{aligned} \tag{C.9}$$

Both of these equations are consistent with the matrix elements (4.23) and (4.24). The point is that when all the indices are projected out all the Wilson lines will connect in one of these two ways. Either they will connect to other Wilson lines or they will only connect to themselves. And since we have shown that in either way the resulting expression is given by (4.23) and (4.24) it means that these two equations are correct for all the possible combinations.

Open Access. This article is distributed under the terms of the Creative Commons Attribution License ([CC-BY 4.0](https://creativecommons.org/licenses/by/4.0/)), which permits any use, distribution and reproduction in any medium, provided the original author(s) and source are credited.

References

- [1] D. d’Enterria, *Jet quenching*, *Landolt-Bornstein* **23** (2010) 471 [[arXiv:0902.2011](https://arxiv.org/abs/0902.2011)] [[INSPIRE](https://inspirehep.net/literature/800000)].
- [2] A. Majumder and M. Van Leeuwen, *The Theory and Phenomenology of Perturbative QCD Based Jet Quenching*, *Prog. Part. Nucl. Phys.* **66** (2011) 41 [[arXiv:1002.2206](https://arxiv.org/abs/1002.2206)] [[INSPIRE](https://inspirehep.net/literature/850000)].
- [3] Y. Mehtar-Tani, J.G. Milhano and K. Tywoniuk, *Jet physics in heavy-ion collisions*, *Int. J. Mod. Phys. A* **28** (2013) 1340013 [[arXiv:1302.2579](https://arxiv.org/abs/1302.2579)] [[INSPIRE](https://inspirehep.net/literature/1100000)].
- [4] STAR collaboration, *Experimental and theoretical challenges in the search for the quark gluon plasma: The STAR Collaboration’s critical assessment of the evidence from RHIC collisions*, *Nucl. Phys. A* **757** (2005) 102 [[nuc1-ex/0501009](https://arxiv.org/abs/nuc1-ex/0501009)] [[INSPIRE](https://inspirehep.net/literature/430000)].

- [5] PHENIX collaboration, *Formation of dense partonic matter in relativistic nucleus-nucleus collisions at RHIC: Experimental evaluation by the PHENIX collaboration*, *Nucl. Phys. A* **757** (2005) 184 [[nucl-ex/0410003](#)] [[INSPIRE](#)].
- [6] ALICE collaboration, *Suppression of Charged Particle Production at Large Transverse Momentum in Central Pb-Pb Collisions at $\sqrt{s_{NN}} = 2.76$ TeV*, *Phys. Lett. B* **696** (2011) 30 [[arXiv:1012.1004](#)] [[INSPIRE](#)].
- [7] CMS collaboration, *Charged-particle nuclear modification factors in PbPb and pPb collisions at $\sqrt{s_{NN}} = 5.02$ TeV*, *JHEP* **04** (2017) 039 [[arXiv:1611.01664](#)] [[INSPIRE](#)].
- [8] CMS collaboration, *Observation and studies of jet quenching in PbPb collisions at $\sqrt{s_{NN}} = 2.76$ TeV*, *Phys. Rev. C* **84** (2011) 024906 [[arXiv:1102.1957](#)] [[INSPIRE](#)].
- [9] ATLAS collaboration, *Observation of a Centrality-Dependent Dijet Asymmetry in Lead-Lead Collisions at $\sqrt{s_{NN}} = 2.77$ TeV with the ATLAS Detector at the LHC*, *Phys. Rev. Lett.* **105** (2010) 252303 [[arXiv:1011.6182](#)] [[INSPIRE](#)].
- [10] ALICE collaboration, *Measurement of charged jet suppression in Pb-Pb collisions at $\sqrt{s_{NN}} = 2.76$ TeV*, *JHEP* **03** (2014) 013 [[arXiv:1311.0633](#)] [[INSPIRE](#)].
- [11] R. Baier, Y.L. Dokshitzer, S. Peigne and D. Schiff, *Induced gluon radiation in a QCD medium*, *Phys. Lett. B* **345** (1995) 277 [[hep-ph/9411409](#)] [[INSPIRE](#)].
- [12] R. Baier, Y.L. Dokshitzer, A.H. Mueller, S. Peigne and D. Schiff, *Radiative energy loss and p_T broadening of high-energy partons in nuclei*, *Nucl. Phys. B* **484** (1997) 265 [[hep-ph/9608322](#)] [[INSPIRE](#)].
- [13] R. Baier, Y.L. Dokshitzer, A.H. Mueller, S. Peigne and D. Schiff, *Radiative energy loss of high-energy quarks and gluons in a finite volume quark-gluon plasma*, *Nucl. Phys. B* **483** (1997) 291 [[hep-ph/9607355](#)] [[INSPIRE](#)].
- [14] R. Baier, Y.L. Dokshitzer, A.H. Mueller and D. Schiff, *Radiative energy loss of high-energy partons traversing an expanding QCD plasma*, *Phys. Rev. C* **58** (1998) 1706 [[hep-ph/9803473](#)] [[INSPIRE](#)].
- [15] B.G. Zakharov, *Fully quantum treatment of the Landau-Pomeranchuk-Migdal effect in QED and QCD*, *JETP Lett.* **63** (1996) 952 [[hep-ph/9607440](#)] [[INSPIRE](#)].
- [16] B.G. Zakharov, *Radiative energy loss of high-energy quarks in finite size nuclear matter and quark-gluon plasma*, *JETP Lett.* **65** (1997) 615 [[hep-ph/9704255](#)] [[INSPIRE](#)].
- [17] U.A. Wiedemann, *Gluon radiation off hard quarks in a nuclear environment: Opacity expansion*, *Nucl. Phys. B* **588** (2000) 303 [[hep-ph/0005129](#)] [[INSPIRE](#)].
- [18] Y. Mehtar-Tani and K. Tywoniuk, *Radiative energy loss of neighboring subjects*, *Nucl. Phys. A* **979** (2018) 165 [[arXiv:1706.06047](#)] [[INSPIRE](#)].
- [19] Y. Mehtar-Tani, *Gluon bremsstrahlung in finite media beyond multiple soft scattering approximation*, *JHEP* **07** (2019) 057 [[arXiv:1903.00506](#)] [[INSPIRE](#)].
- [20] P. Caucal, E. Iancu, A.H. Mueller and G. Soyez, *Vacuum-like jet fragmentation in a dense QCD medium*, *Phys. Rev. Lett.* **120** (2018) 232001 [[arXiv:1801.09703](#)] [[INSPIRE](#)].
- [21] P. Caucal, E. Iancu, A.H. Mueller and G. Soyez, *Nuclear modification factors for jet fragmentation*, *JHEP* **10** (2020) 204 [[arXiv:2005.05852](#)] [[INSPIRE](#)].
- [22] F. Dominguez, J.G. Milhano, C.A. Salgado, K. Tywoniuk and V. Vila, *Mapping collinear in-medium parton splittings*, *Eur. Phys. J. C* **80** (2020) 11 [[arXiv:1907.03653](#)] [[INSPIRE](#)].
- [23] J.-P. Blaizot, F. Dominguez, E. Iancu and Y. Mehtar-Tani, *Medium-induced gluon branching*, *JHEP* **01** (2013) 143 [[arXiv:1209.4585](#)] [[INSPIRE](#)].

- [24] L. Apolinário, N. Armesto, J.G. Milhano and C.A. Salgado, *Medium-induced gluon radiation and colour decoherence beyond the soft approximation*, *JHEP* **02** (2015) 119 [[arXiv:1407.0599](#)] [[INSPIRE](#)].
- [25] A. Kovner and U.A. Wiedemann, *Eikonal evolution and gluon radiation*, *Phys. Rev. D* **64** (2001) 114002 [[hep-ph/0106240](#)] [[INSPIRE](#)].
- [26] K. Dusling, M. Mace and R. Venugopalan, *Parton model description of multiparticle azimuthal correlations in pA collisions*, *Phys. Rev. D* **97** (2018) 016014 [[arXiv:1706.06260](#)] [[INSPIRE](#)].
- [27] F. Dominguez, C. Marquet, B.-W. Xiao and F. Yuan, *Universality of Unintegrated Gluon Distributions at small x* , *Phys. Rev. D* **83** (2011) 105005 [[arXiv:1101.0715](#)] [[INSPIRE](#)].
- [28] P. Arnold, *Landau-Pomeranchuk-Migdal effect in sequential bremsstrahlung: From large- N QCD to $N = 3$ via the $SU(N)$ analog of Wigner 6- j symbols*, *Phys. Rev. D* **100** (2019) 034030 [[arXiv:1904.04264](#)] [[INSPIRE](#)].
- [29] B.G. Zakharov, *Color randomization of fast gluon-gluon pairs in the quark-gluon plasma*, *J. Exp. Theor. Phys.* **128** (2019) 243 [[arXiv:1806.04723](#)] [[INSPIRE](#)].
- [30] Y. Hatta and T. Ueda, *Non-global logarithms in hadron collisions at $N_c = 3$* , *Nucl. Phys. B* **962** (2021) 115273 [[arXiv:2011.04154](#)] [[INSPIRE](#)].
- [31] J. Jalilian-Marian and Y.V. Kovchegov, *Inclusive two-gluon and valence quark-gluon production in DIS and pA* , *Phys. Rev. D* **70** (2004) 114017 [Erratum *ibid.* **71** (2005) 079901] [[hep-ph/0405266](#)] [[INSPIRE](#)].
- [32] E. Iancu and D.N. Triantafyllopoulos, *Higher-point correlations from the JIMWLK evolution*, *JHEP* **11** (2011) 105 [[arXiv:1109.0302](#)] [[INSPIRE](#)].
- [33] T. Lappi, H. Mäntysaari and A. Ramnath, *Next-to-leading order Balitsky-Kovchegov equation beyond large N_c* , *Phys. Rev. D* **102** (2020) 074027 [[arXiv:2007.00751](#)] [[INSPIRE](#)].
- [34] F. Dominguez, C. Marquet, A.M. Stasto and B.-W. Xiao, *Universality of multiparticle production in QCD at high energies*, *Phys. Rev. D* **87** (2013) 034007 [[arXiv:1210.1141](#)] [[INSPIRE](#)].
- [35] Z. Nagy and D.E. Soper, *Parton shower evolution with subleading color*, *JHEP* **06** (2012) 044 [[arXiv:1202.4496](#)] [[INSPIRE](#)].
- [36] K. Hamilton, R. Medves, G.P. Salam, L. Scyboz and G. Soyez, *Colour and logarithmic accuracy in final-state parton showers*, *JHEP* **03** (2021) 041 [[arXiv:2011.10054](#)] [[INSPIRE](#)].
- [37] M. Gyulassy, P. Levai and I. Vitev, *Reaction operator approach to nonAbelian energy loss*, *Nucl. Phys. B* **594** (2001) 371 [[nucl-th/0006010](#)] [[INSPIRE](#)].
- [38] X.-N. Wang and M. Gyulassy, *Gluon shadowing and jet quenching in $A + A$ collisions at $\sqrt{s} = 200$ GeV*, *Phys. Rev. Lett.* **68** (1992) 1480 [[INSPIRE](#)].
- [39] P. Aurenche, F. Gelis and H. Zaraket, *A Simple sum rule for the thermal gluon spectral function and applications*, *JHEP* **05** (2002) 043 [[hep-ph/0204146](#)] [[INSPIRE](#)].
- [40] Y. Mehtar-Tani and K. Tywoniuk, *Improved opacity expansion for medium-induced parton splitting*, *JHEP* **06** (2020) 187 [[arXiv:1910.02032](#)] [[INSPIRE](#)].
- [41] J. Barata, Y. Mehtar-Tani, A. Soto-Ontoso and K. Tywoniuk, *Revisiting transverse momentum broadening in dense QCD media*, *Phys. Rev. D* **104** (2021) 054047 [[arXiv:2009.13667](#)] [[INSPIRE](#)].
- [42] T. Altinoluk, N. Armesto, G. Beuf, M. Martínez and C.A. Salgado, *Next-to-eikonal corrections in the CGC: gluon production and spin asymmetries in pA collisions*, *JHEP* **07** (2014) 068 [[arXiv:1404.2219](#)] [[INSPIRE](#)].

Article II

A unified picture of medium-induced radiation

J. H. Isaksen, A. Takacs, and K. Tywoniuk

Journal of High Energy Physics, **2**, 156 (2023)

A unified picture of medium-induced radiation

Johannes Hamre Isaksen, Adam Takacs and Konrad Tywoniuk

*Department of Physics and Technology, University of Bergen,
Allegaten 55, 5007 Bergen, Norway*

E-mail: johannes.isaksen@uib.no, adam.takacs@uib.no,
konrad.tywoniuk@uib.no

ABSTRACT: We revisit the picture of jets propagating in the quark-gluon plasma. In addition to vacuum radiation, partons scatter on the medium constituents resulting in induced emissions. Analytical approaches to including these interactions have traditionally dealt separately with multiple, soft, or rare, hard scatterings. A full description has so far only been available using numerical methods. We achieve full analytical control of the relevant scales and map out the dominant physical processes in the full phase space. To this aim, we extend existing expansion schemes for the medium-induced spectrum to the Bethe-Heitler regime. This covers the whole phase space from early to late times, and from hard splittings to emissions below the thermal scale. Based on the separation of scales, a space-time picture naturally emerges: at early times, induced emissions start to build from rare scatterings with the medium. At a later stage, induced emissions due to multiple soft scatterings result in a turbulent cascade that rapidly degrades energy down to, and including, the Bethe-Heitler regime. We quantify the impact of such an improved picture, compared to the current state-of-the-art factorization that includes only soft scatterings, by both analytical and numerical methods for the medium-induced energy distribution function. Our work serves to improve our understanding of jet quenching from small to large systems and for future upgrades of Monte Carlo generators.

KEYWORDS: Jets and Jet Substructure, Quark-Gluon Plasma

ARXIV EPRINT: [2206.02811](https://arxiv.org/abs/2206.02811)

Contents

1	Introduction	1
2	Heuristic discussion of the medium-induced spectrum	4
3	Spectrum of medium-induced emissions	9
3.1	General formalism	9
3.2	Opacity expansion (OE)	12
3.3	Resummed opacity expansion (ROE)	14
3.4	Improved opacity expansion (IOE)	18
3.5	Summary of the regimes and the induced emission spectrum	23
4	Resumming multiple emissions in the medium	25
4.1	The necessity of multiple emissions	25
4.2	Resummation of multiple emissions	26
4.3	Analytic solutions of the evolution equation	29
5	Numerical evaluation of the medium cascade	33
6	Conclusions and outlook	37
A	All order formulas for medium-induced spectrum in the soft limit	38
A.1	Opacity expansion	38
A.2	Resummed opacity expansion	39
A.3	Improved opacity expansion	41
B	General formulas for the emission rate in the soft limit	43
C	Medium-induced spectrum and rate with finite-z corrections	43
C.1	Opacity expansion	45
C.2	Resummed opacity expansion	46
C.3	Improved opacity expansion	47
D	Numerical implementation of the evolution equation	50
E	HTL potential	51

1 Introduction

Short-lived droplets of hot and dense nuclear matter, called the quark-gluon plasma (QGP), are produced in relativistic heavy-ion collisions at RHIC and LHC. Embedded in the same high-energy collisions, hard QCD processes are also present, resulting in the production of collimated sprays of energetic particles that are commonly referred to as jets [1, 2]. Jets are well-understood, perturbative objects within perturbative QCD and they are described

up to high precision in proton-proton collisions [3–5]. During their propagation, however, jet particles can interact with the surrounding nuclear matter. The modification of jet features, therefore, reflects the properties of the QGP created in heavy-ion collisions [6–11]. Currently, a vigorous experimental program dedicated to quantifying jet modifications is ongoing at both RHIC and LHC, focusing on a broad set of observables which includes measurements of the modification of the jet spectrum, jet substructure observables, and jet correlations [12–16] (for a selection of predictions see refs. [17–27]).

High-energy jets are particularly suitable probes of the QGP because their energy scale Q_{jet} is much larger than the typical momentum scale of the medium Q_{med} . If this is the case, the impact of medium modifications should therefore not affect the internal structure of the jet, which would still rely on perturbative QCD [28–30]. A key ingredient when considering jet modifications is the radiation induced by scatterings with the deconfined medium constituents. Such emissions typically appear at scales comparable to Q_{med} . Emission at scales much higher than Q_{med} , on the other hand, are unaffected by the medium, resulting in a factorized picture between vacuum and medium processes [29, 31]. Medium-induced emissions redistribute the original jet parton energy to multiple, soft particles over large angles, including out of the jet cone. This leads to a net jet energy loss which, in turn, is manifested as a suppression of the jet spectrum (for an updated discussion of jet quenching see refs. [25, 26], and for applications to substructure see refs. [18, 20, 24]). Consequently, medium-induced emissions are a crucial component of jet energy loss and thus of phenomenological studies of jet observables in heavy-ion collisions.

The medium-induced emission spectrum was formulated a long time ago [32–34]. Previous solutions were limited to either (i) expanding in the number of scatterings (referred to as the opacity expansion) [35–38], or (ii) considering multiple soft scatterings (called the harmonic oscillator approximation) [32, 33, 39, 40]. Meanwhile, several works focused on the underlying scales that separate the limiting cases [32, 41–46]. The full problem has also been tackled by numerical techniques [47, 48] (or more recently in refs. [49–52]). Not long ago, analytical techniques were developed that provided a unified description of the multiple, soft and rare, hard scatterings in a dense medium [53–57], which better match the full numerical solutions. The main challenge, common to both the numeric and analytic approaches, resides in dealing with multiple interactions with the underlying medium.

In this paper, we revisit the different analytic approaches to resumming multiple interactions for calculating the medium-induced emission spectrum. These include the opacity expansion (OE) and the improved opacity expansion (IOE), which includes harmonic oscillator approximation as the leading term. Moreover, we rigorously derive the resummed opacity expansion (ROE) for the first time, which extends the description of the spectrum to low energy emissions in the Bethe-Heitler regime. We provide a novel unified picture of these resummation schemes by identifying their relevant emergent scales and demonstrating their respective regions of validity. For example, we show that the single scattering approximation, contained in the leading order of OE, is valid even for a big medium, where one would expect more than one scattering if the emitted energy is high enough. We show that the full phase space of medium-induced emissions, spanning from the maximal jet energy to the thermal scale, is covered by a union of these expansions, see also ref. [46]. Each of the

expansions is also associated with the corresponding physical scattering processes, and thus we reinterpret the frequently used terms such as GLV emissions, coherent scatterings, and Bethe-Heitler region in a unified framework. Our framework goes beyond previous attempts to describe all regimes of medium-induced bremsstrahlung by presenting a resummation framework that can be systematically improved and that is valid both in the dilute and dense regimes.

As a next step, we identify the regimes where not only multiple interactions are important, but also multiple emissions [58, 59]. These conditions are met for sufficiently soft emissions in a large medium. The previously established hierarchy of emergent scales plays a crucial role in mapping out early, rare, and relatively hard emissions and a successive cascade of soft splittings. In this context, hard medium-induced splittings can be thought of as extra sources, in addition to the parent parton, for the full cascade. This description is realized analytically in a novel scheme that combines a fixed order expansion of rare emissions with an all-order resummation of soft splittings. The resulting energy distribution links the asymptotic early and late time behaviors for which analytical solutions exist. Finally, we resum multiple induced emissions numerically, using the previously obtained precise determination of the in-medium splitting rates, to calculate the energy distribution function. We highlight the interplay of rare hard scatterings, coherent soft splittings, and Bethe-Heitler emissions in a finite medium, providing a state-of-the-art resummation.

Our reorganized picture helps not only with the physical understanding of induced emissions, but provides a fast and efficient way to calculate the medium-induced spectrum, which is a key ingredient for estimating jet energy loss. It also serves to inform Monte Carlo algorithms simulating full jet evolution inside the medium about how to implement multiple medium-induced emissions and how to combine them with vacuum-like emissions, e.g. see in ref. [29].

The paper is structured as follows. In section 2, as an introduction, we discuss the structure of the induced spectrum in the various regimes using heuristic arguments, and we show how the radiation in the different regimes is related to single soft, multiple soft and single hard scatterings with the medium, see figure 3. The spectrum is calculated in detail in section 3. We revisit the opacity expansion and the improved opacity expansion schemes, and put on a firm footing a novel resummation scheme, dubbed resummed opacity expansion, which is valid for emissions below the Bethe-Heitler scale. Improving on previous discussions, we provide formulas for the spectrum at arbitrary order and calculate it exactly up to second order in all the expansions, allowing us for the first time to establish regions where they converge. Finally, in section 4 we consider the problem of multiple emissions. We analyze induced particles coming from the full phase space and confirm the importance of considering multiple emissions, especially in the soft sector. In order to facilitate an improved analytical understanding of the problem, we finally suggest a resummation scheme of multiple emissions by iterating in rare, hard emissions and including an arbitrary number of soft splittings. This is compared to the full numerical results. We conclude with an outlook in section 6. The appendix contains lots of useful formulas, including the rate of emissions and finite- z corrections that are important for phenomenology. The code we have developed to calculate the kernels and solve for the energy distribution is provided at <https://github.com/adam-takacs/kernels.git>.

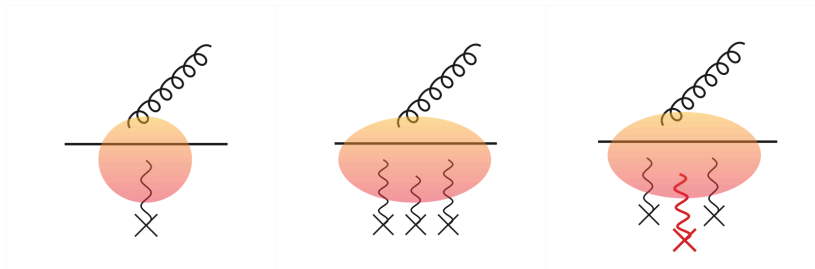


Figure 1. Three regimes of the radiative spectrum in dense media, $L \gg \lambda$: the Bethe-Heitler regime $\omega < \omega_{\text{BH}}$ (leftmost), the BDMPS-Z regime $\omega_{\text{BH}} < \omega < \omega_c$ (middle), and the hard GLV regime $\omega_c < \omega$ (rightmost figure). The size of the blob represents the typical formation time of the emission, which is $t_f < \lambda$ in the leftmost panel and $t_f > \lambda$ in the center and rightmost panels. Black, wavy lines represent soft interactions with the medium, where the momentum transfer is of the order of the medium scale $|\mathbf{q}| \lesssim \mu$, while the red, wavy line represents a hard scattering event, with $|\mathbf{q}| \gg \mu$.

2 Heuristic discussion of the medium-induced spectrum

The spectrum of gluon emissions induced by scatterings on a deconfined medium plays a central role in the phenomenology of jet quenching. However, a full understanding of all regimes have so far been lacking analytically and was previously only achievable through numerical methods. Here, we present a unified view of all relevant medium scales and their related regimes. Similar heuristic discussions have previously been presented in, e.g., [8, 32, 46, 53]. In section 3 we will provide rigorous derivations of the findings argued for here.

We formulate the spectrum of induced emissions by focusing on the relevant length scales:

- The **size** of the medium L (or the length of propagation $t < L$).
- The **mean free path** of the medium $\lambda \sim \frac{1}{n\sigma_{\text{tot}}}$, which combines the density n and the scattering strength $\sigma_{\text{tot}} \sim \int d\sigma$, and it describes the distance between typical scatterings.
- The **formation time** of an emission $t_f = \frac{2\omega}{\mathbf{k}^2}$, where ω is the energy and \mathbf{k} is the transverse momentum of the emission.

In addition, the relation between the in-medium screening scale μ and the range of available transverse momenta $|\mathbf{k}|$ is also important.

The *opacity* $\chi \equiv L/\lambda$ characterizes the denseness of the medium. If the opacity is small ($L \ll \lambda$), the medium is “dilute”, or weakly interacting, while it is “dense”, or strongly interacting if $L \gg \lambda$.¹ The dilute medium barely consists of scattering centers, however, in the dense medium one should account for an arbitrary number of interactions.

¹From this perspective, we have “fixed” L and vary λ . Naturally, we could also have identified these two regimes as a “large” and “small” media, where we “fix” the mean free path and vary L instead.

A big part of this paper will be about calculating the spectrum of medium-induced emissions. For reference, the vacuum spectrum reads,

$$\omega \frac{dI}{d\omega} \sim \alpha_s \int \frac{d\mathbf{k}^2}{\mathbf{k}^2}, \quad (2.1)$$

where currently we did not specify the limits of the transverse momentum integral. This contains the well-known soft ($\omega \rightarrow 0$) and collinear ($\mathbf{k}^2 \rightarrow 0$) divergences. In contrast, the collinear divergence in the medium spectrum is removed by the need to exchange transverse momentum with the medium.

Motivated by this, we introduce a heuristic model that captures some of the features of the medium-induced spectrum, given by

$$\omega \frac{dI}{d\omega} \sim \alpha_s L \int d^2\mathbf{k} \sigma(\mathbf{k}) \sim \alpha_s^3 n L \int \frac{d\mathbf{k}^2}{(\mathbf{k}^2 + \mu^2)^2}, \quad (2.2)$$

where n is the medium density and μ a screening mass. The behavior at high- \mathbf{k} , $\sigma \sim \mathbf{k}^{-4}$, reproduces the expected Coulomb tail. The factor L arises since the emission can take place anywhere along the medium length. For a more accurate description of medium-induced emissions, we refer the reader to section 3.

In our effective description, we focus on the hierarchy among the introduced scales and show the separation of different scattering regions. Firstly, in the $t_f \gg L$ limit, the formation of the emission extends beyond the medium, where one naturally should expect vacuum physics to dominate.² We will hence not consider this possibility here. The remaining cases are listed below:

Dilute media ($t_f \leq L \ll \lambda$). In case of a low medium opacity, we expect that roughly one scattering occurs. This process will typically transfer a momentum of order of the Debye mass to the emitted gluon, or $\langle \mathbf{k}^2 \rangle \sim \mu^2$, leading to $t_f = 2\omega/\mu^2$. The formation of the gluon has to take place inside the medium, giving rise to the characteristic energy scale in the dilute regime, namely

$$\bar{\omega}_c = \frac{1}{2} \mu^2 L. \quad (2.3)$$

This separates two regimes of emissions that are sourced via different scattering processes: on the one side soft gluons with $\omega < \bar{\omega}_c$, generated via a soft scattering with the medium $\langle \mathbf{k}^2 \rangle \lesssim \mu^2$. Hard gluons with $\omega > \bar{\omega}_c$ can also be generated, however those demand a large momentum exchange with the medium, $\langle \mathbf{k}^2 \rangle > \mu^2$, which is comparatively rare. Let us now consider how the spectrum behaves in these two distinct regimes.

According to our discussion above, the soft production should be dominated by soft transverse momentum exchanges with the medium. Hence, we expect that the spectrum of emitted gluons goes as

$$\omega \frac{dI}{d\omega} \Big|_{\omega < \bar{\omega}_c} \sim \alpha_s L \int_0^\infty d\mathbf{k}^2 \frac{\alpha_s^2 n}{(\mathbf{k}^2 + \mu^2)^2} \sim \alpha_s \frac{L}{\lambda}, \quad (2.4)$$

²For such soft emissions, medium effects can influence the color coherence properties leading to a modification of the phase space [60, 61].

where the integral is dominated by $\mathbf{k}^2 \lesssim \mu^2$. This integral gives the proportionality with the inverse mean free path i.e. $n/\mu^2 \sim 1/\lambda$, resulting in an overall factor of medium opacity L/λ . This parametric estimate misses an important logarithmic factor $\sim \ln \bar{\omega}_c/\omega$, see a further discussion in section 3.2, which signals that the simplifications pertaining to the “soft” regime break down at $\omega \approx \bar{\omega}_c$.

For hard emissions, $\omega > \bar{\omega}_c$, we instead get that

$$\omega \frac{dI}{d\omega} \Big|_{\omega > \bar{\omega}_c} \sim \alpha_s^3 n L \int_{\omega/L}^{\infty} \frac{d\mathbf{k}^2}{\mathbf{k}^4} \sim \alpha_s \frac{L \bar{\omega}_c}{\lambda \omega}, \quad (2.5)$$

where we used $t_f = 2\omega/\mathbf{k}^2 < L$, and neglected the screening mass μ^2 in this parametric regime, since $\langle \mathbf{k}^2 \rangle \gg \mu^2$. Compared to the soft regime from eq. (2.4) it is suppressed by an additional power of $\bar{\omega}_c/\omega \ll 1$. The complete spectrum in the dilute regime is sketched in figure 2 (left).

Dense media with long formation time ($\lambda \ll t_f \ll L$). In a dense medium we should expect that typically many scatterings occur during the emission process, which is illustrated in the middle of figure 1. This demands a more sophisticated model than what we suggested in eq. (2.2). Nevertheless, we can approximate the total transferred transverse momentum by $\langle \mathbf{k}^2 \rangle \sim \hat{q}t$, which resembles a random walk for t time in two dimensions, with \hat{q} playing the role of a diffusion constant.³ This constant determines the typical transverse momentum accumulated per unit length, or $\hat{q} \sim n \sim \mu^2/\lambda$. In this case the formation time becomes

$$t_f = \sqrt{\frac{2\omega}{\hat{q}}}. \quad (2.6)$$

This is often called the coherence length, since during the formation time, interference effects between multiple scattering with the medium are active and the gluon feels only one effective scattering center. The accumulated transverse momentum during the splitting process is in this case $\langle \mathbf{k}^2 \rangle = \sqrt{2\omega\hat{q}}$, which is the celebrated Landau-Pomeranchuk-Migdal (LPM) effect.

Again, comparing the formation time to the medium length, leads to the characteristic energy scale in the dense regime, namely

$$\omega_c = \frac{1}{2} \hat{q} L^2, \quad (2.7)$$

and thus $\omega < \omega_c$ for multiple soft scatterings. The maximal possible momentum accumulated via multiple soft scatterings is denoted $\langle \mathbf{k}^2 \rangle \sim Q_s^2 = \hat{q}L$. The other limiting scale of the multiple scattering regime arises when considering the minimal formation time in this hierarchy, i.e. $t_f > \lambda$, giving rise the scale $\omega > \omega_{\text{BH}}$, (see later in eq. (2.10)). In this case, the accumulated transverse momentum squared reduces to a single soft scattering $\langle \mathbf{k}^2 \rangle \sim \hat{q}\lambda \sim \mu^2$.

³Arbitrary dense medium, would result in overlapping scatterings that description if beyond the scope of this paper. Multiple independent scatterings require well separated scattering centers ($1/\mu \ll \lambda$) see in ref. [32].

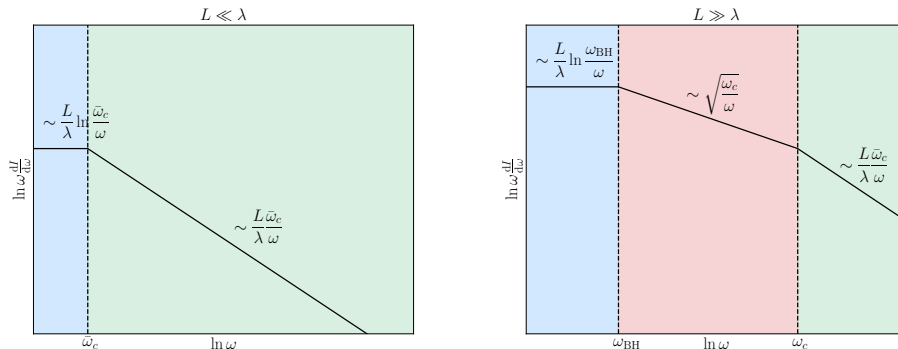


Figure 2. A sketch of the spectrum of medium-induced gluons in a dilute medium $L \ll \lambda$ (left) and in a dense medium $L \gg \lambda$ (right).

In the multiple soft scattering regime, characterized by $\omega_{\text{BH}} \ll \omega \ll \omega_c$, the mean free path has to be replaced by the formation time in eq. (2.4), leading to

$$\omega \frac{dI}{d\omega} \Big|_{\omega_{\text{BH}} \ll \omega \ll \omega_c} \sim \alpha_s \frac{L}{t_f} \sim \alpha_s \sqrt{\frac{\hat{q} L^2}{\omega}}. \quad (2.8)$$

This is also often referred to as the BDMPS-Z spectrum in the soft limit.

For hard gluon emissions, $\omega \gg \omega_c$, we also have to demand that $\langle k^2 \rangle \gg Q_s$. In other words, only a hard scattering can provide sufficient transverse momentum to fulfill all the conditions. The relevant contribution is therefore captured by eq. (2.5) and, remarkably, the spectrum in this limit is identical to the hard tail in the dilute regime, namely

$$\omega \frac{dI}{d\omega} \Big|_{\omega \gg \omega_c} \sim \alpha_s \frac{L \bar{\omega}_c}{\lambda \omega}. \quad (2.9)$$

This demonstrates that, even in a dense medium, hard emissions mostly are driven by single, rare hard scattering events. An illustration of this can be seen on the right in figure 1.

Dense media with short formation time ($t_f \ll \lambda \ll L$). The picture we just described should hold as long as there indeed is time for multiple scatterings during the emission process, namely that $t_f > \lambda$. However, when the formation time is short the parton will only have time to scatter once before it splits. This is illustrated on the left in figure 1. The transverse scale is typically soft ($\langle k^2 \rangle \sim \mu^2$), and thus $t_f = \frac{2\omega}{\mu^2}$. This regime is characterized by $t_f \ll \lambda$, or equivalently as a condition on the energy $\omega \ll \omega_{\text{BH}}$, where we have defined the scale

$$\omega_{\text{BH}} = \frac{1}{2} \mu^2 \lambda. \quad (2.10)$$

Note that $\bar{\omega}_c(\lambda) \equiv \omega_{\text{BH}}$. In this case the spectrum becomes

$$\omega \frac{dI}{d\omega} \Big|_{\omega < \omega_{\text{BH}}} \sim \alpha_s \frac{L}{\lambda}, \quad (2.11)$$

which is similar to the result in eq. (2.4) and it is sometimes referred to as Bethe-Heitler region because of the QED analogue. The $t_f \ll \lambda$ condition is satisfactory but not necessary

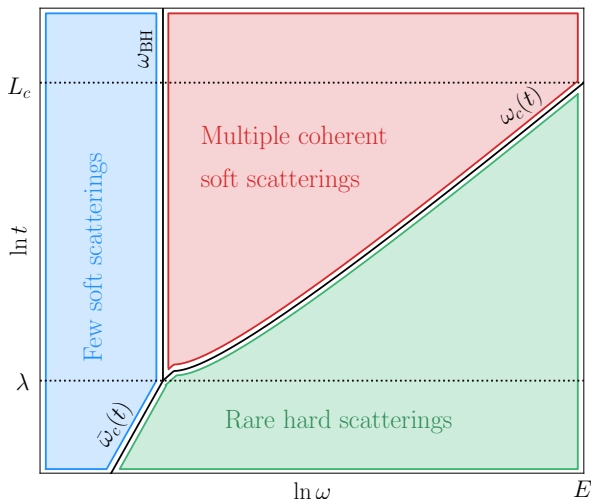


Figure 3. The phase space for medium-induced emissions designated to the leading scattering processes. The main length scales of the problem are λ and the critical length L_c , corresponding to the characteristic energies ω_{BH} and E , see text for further details.

for BH emissions. There are BH emissions with $t_f > \lambda$ but only with one real scattering. We show this more rigorously later in section 3. Our heuristic analysis fails to capture the additional logarithmic term which in this case comes with $\ln \omega_{\text{BH}}/\omega$, see section 3.3. A sketch of the spectrum in a dense medium can be found in figure 2 (right).

Summary. Bringing together the heuristic arguments of this section, we show a sketch of the emission spectrum for dilute and dense media in figure 2. The full emission phase space is divided by three lines corresponding to the emergent scales: $\bar{\omega}_c(t) = \frac{1}{2}\mu^2 t$ in the dilute regime ($L < \lambda$), and $\omega_{\text{BH}} = \frac{1}{2}\mu^2 \lambda$ and $\omega_c(t) = \frac{1}{2}\hat{q}t^2$ in the dense regime ($L > \lambda$) and they are shown in figure 3. The $\omega_c(t)$ line is not completely straight because \hat{q} in general is ω dependent (see in section 3.4). When the medium size is of the order of the mean free path they all collapse to the same value, i.e. $\bar{\omega}_c(\lambda) = \omega_c(\lambda) = \omega_{\text{BH}}$. Typically, we adopt a notation where the scales written without the t -argument denote their respective values at L , e.g. $\omega_c \equiv \omega_c(L)$.

These scales delineate three distinct regimes of scattering processes and thus induced emissions that were discussed in the preceding paragraphs. The areas between these scales are governed by few soft, multiple soft and rare hard interactions with the medium, as depicted with colors in figure 3 and discussed above. We also show two length scales: the mean free path λ and the critical medium length L_c . The mean free path marks the time where multiple scatterings appear. The critical medium length indicates where rare, hard scatterings will no longer have an effect, that is where $\omega_c(t) = E$, leading to $L_c = \sqrt{2E/\hat{q}}$.⁴

⁴When considering a finite splitting fraction z the exact definition turns out to be $L_c = \sqrt{E/(2\hat{q})}$.

As the parton moves through the medium, at each instant t the emission rate $\omega dI/(d\omega dt)$ is different since the phase space for available emissions changes. The emission spectrum $\omega dI/d\omega$, evaluated at a given t (typically $t = L$), includes the accumulated range of processes that occurred up to that time. The main goal of this work is to consider multiple medium-induced emissions in this system of dynamically evolving scales presented in figure 3. In the next section, section 3, we will formally derive the results we only have argued for in this section. Finally, in section 4 we will tackle the issue of multiple emissions in this scheme.

3 Spectrum of medium-induced emissions

In this section, we derive the all order emission spectrum induced by elastic scatterings on a deconfined medium. Of the three expansions we present here, the opacity expansion and the improved opacity expansion have been discussed in depth in previous works, see refs. [35, 36] and [53–57] respectively. The resummed opacity expansion has been argued for before, see [36, 46, 62], but is here derived rigorously for the first time. This paper strives to be a comprehensive reference for all of the expansions, and hence they are all presented in detail. Furthermore, we extend previous calculations to all orders and present results to order $N = 2$ for the opacity expansion and $N_r = 2$ for the resummed opacity expansion, and extract the relevant limits analytically. This provides valuable insight into the underlying structure of the expansions in different regimes.

3.1 General formalism

Currently, we consider the emission of a gluon with energy ω from a parent parton with energy E in the soft limit, i.e. $\omega \ll E$. The soft limit is used in this section because it is much more clear and readable. For a description beyond the strictly soft limit we refer to appendix C, which includes novel results.

Our starting point is the definition of the spectrum of medium-induced gluons [32–34, 36],

$$\omega \frac{dI}{d\omega} = \frac{2\alpha_s C_R}{\omega^2} \text{Re} \int_0^\infty dt_2 \int_0^{t_2} dt_1 \partial_{\mathbf{x}} \cdot \partial_{\mathbf{y}} [\mathcal{K}(\mathbf{x}, t_2; \mathbf{y}, t_1) - \mathcal{K}_0(\mathbf{x}, t_2; \mathbf{y}, t_1)]_{\mathbf{x}=\mathbf{y}=0}, \quad (3.1)$$

where C_R is the Casimir color factor of the emitting particle ($C_R = C_F$ for a quark and $C_R = N_c$ for a gluon).⁵ The three-point correlator \mathcal{K} solves the Schrödinger equation

$$\left[i\partial_t + \frac{\partial_{\mathbf{x}}^2}{2\omega} + iv(\mathbf{x}, t) \right] \mathcal{K}(\mathbf{x}, t; \mathbf{y}, t_0) = i\delta(t - t_0)\delta(\mathbf{x} - \mathbf{y}), \quad (3.2)$$

where the potential $v(\mathbf{x}, t)$ describes scatterings in a thermal or quasi-particle like background,⁶

$$v(\mathbf{x}, t) = \int_{\mathbf{q}} \sigma(\mathbf{q}, t) \left(1 - e^{i\mathbf{q} \cdot \mathbf{x}} \right). \quad (3.3)$$

⁵This expression can be derived directly from the fully z dependent spectrum in eq. (C.1), see the discussion in appendix C.

⁶Throughout, we adopt a shorthand notation, so that $\int_p = \int \frac{d^4 p}{(2\pi)^4}$, $\int_{\mathbf{p}} = \int \frac{d^2 \mathbf{p}}{(2\pi)^2}$, and $\int_{\mathbf{x}} = \int d^2 \mathbf{x}$.

Here $\sigma(\mathbf{q}, t) = N_c n(t) d^2\sigma_{\text{el}}/d^2\mathbf{q}$ is proportional to the in-medium elastic scattering cross section, where $n(t) \sim T^3$ is the density of scattering centers.⁷ The color factor N_c appears because, in this limit, only the emitted gluon picks up transverse momentum in the medium. The potential can be extracted from an effective theory that accounts for both large and small momentum exchanges with the medium [63]. In the main part of this paper, we will use the Gyulassy-Wang potential [64] that both contains a hard Coulomb-tail and implements screening in the infrared $\mu^2 \gg \mathbf{q}^2$,

$$\frac{d^2\sigma_{\text{el}}}{d^2\mathbf{q}} = \frac{g^4}{(\mathbf{q}^2 + \mu^2)^2}, \tag{3.4}$$

where μ is a screening mass of the order of the Debye mass of a thermal medium. We also provide the spectrum in appendix E with the LO hard thermal loop (HTL) potential [65]. Also, in eq. (3.2) we neglect quark and gluon thermal masses, which corresponds to taking the high-energy limit ($E \gg m_{q,g}^4/\hat{q} \sim \omega_{\text{BH}}$), see e.g. refs. [41, 62] for further discussion.

When the medium is not present, $v = 0$, one recovers the propagation of a single parton in vacuum, $\mathcal{K}(\mathbf{x}, t_2; \mathbf{y}, t_1) \equiv \mathcal{K}_0(\mathbf{x} - \mathbf{y}, t_2 - t_1)$ with $\mathcal{K}_0(\mathbf{x}, t) = \frac{\omega}{2\pi i t} \exp[i\omega \mathbf{x}^2/(2t)]$. To only capture medium effects, the vacuum term is explicitly subtracted in eq. (3.1).

The emission spectrum in eq. (3.1) is the result of a path integral formalism in which arbitrarily many soft and hard scatterings are included. It does, however, not account for longitudinal momentum (\sim energy) exchange with the medium. Having written the expression as a spectrum we also implicitly assume that the creation of the initial parton is factorized from the induced process (for example it was created in a highly virtual vacuum process). Finally, the medium averages leading to the simple form of the three-point correlator, as in eq. (3.2), assumes independent scatterings on the medium. This parametrically holds if the size of the potential is much smaller than the mean free path, i.e. $\mu^{-1} \ll \lambda$, where the typical exchanged momentum is $|\delta\mathbf{q}| \sim \mu$ [32].

We should also note that eq. (3.1) emerges as the result of a momentum integral of the differential spectrum $dI/(d\omega d^2\mathbf{k})$ in the soft limit [39, 57], with no kinematical constraint on the transverse momentum (\mathbf{k}) integral similarly to refs. [34, 58]. A more careful treatment of the kinematics would be important especially if one is interested in emissions inside or out of a given cone [26, 39, 51].

Let us now cast the equation for the spectrum in an equivalent form. On many occasions it is more practical to work in transverse momentum space,

$$\mathcal{K}(\mathbf{p}, t_2; \mathbf{p}_0, t_1) = \int_{\mathbf{x}, \mathbf{y}} e^{-i\mathbf{p}\cdot\mathbf{x} + i\mathbf{p}_0\cdot\mathbf{y}} \mathcal{K}(\mathbf{x}, t_2; \mathbf{y}, t_1). \tag{3.5}$$

The vacuum propagator \mathcal{K}_0 then becomes a plane wave, i.e. $\mathcal{K}_0(\mathbf{p}, t) = \exp[-i\mathbf{p}^2 t/(2\omega)]$. In this representation, the solution to the Schrödinger equation (3.2) can be written as the

⁷We include the number density of the scattering centers $n(t)$ into $v(\mathbf{x}, t)$ and $\sigma(\mathbf{q}, t)$ similarly to the previous works in refs. [53, 54, 57].

recursive equation

$$\begin{aligned} \mathcal{K}(\mathbf{p}, t_2; \mathbf{p}_0, t_1) &= (2\pi)^2 \delta(\mathbf{p} - \mathbf{p}_0) \mathcal{K}_0(\mathbf{p}; t_2 - t_1) \\ &\quad - \int_{t_1}^{t_2} ds \int_{\mathbf{q}} \mathcal{K}_0(\mathbf{p}; t_2 - s) v(\mathbf{q}, s) \mathcal{K}(\mathbf{p} - \mathbf{q}, s; \mathbf{p}_0, t_1), \end{aligned} \quad (3.6)$$

where now

$$v(\mathbf{q}, s) = (2\pi)^2 \delta(\mathbf{q}) \Sigma(s) - \sigma(\mathbf{q}, s), \quad (3.7)$$

ensures probability conservation. Here, $\Sigma(s) \equiv \int_{\mathbf{q}} \sigma(\mathbf{q}, s)$ can be interpreted as the inverse of the (local) mean free path λ along a trajectory of a propagating parton, or

$$\lambda(s) = \frac{1}{\Sigma(s)}. \quad (3.8)$$

In these expressions, we have assumed that the integral over the elastic scattering cross section exists. In many cases, e.g. for the HTL potential [65], one needs to introduce an IR regulator. However, $v(\mathbf{q}, s)$ in eq. (3.7) is not sensitive to this IR regulation and therefore the expansion in eq. (3.6) is well-defined. We have provided a further discussion of the HTL potential in appendix E.

The medium-induced spectrum now reads

$$\omega \frac{dI}{d\omega} = \frac{2\alpha_s C_R}{\omega^2} \text{Re} \int_0^\infty dt_2 \int_0^{t_2} dt_1 \int_{\mathbf{p}, \mathbf{q}} \mathbf{p} \cdot \mathbf{q} [\mathcal{K}(\mathbf{p}, t_2; \mathbf{q}, t_1) - (2\pi)^2 \delta(\mathbf{p} - \mathbf{q}) \mathcal{K}_0(\mathbf{p}, t_2 - t_1)]. \quad (3.9)$$

The vacuum contribution can then be removed by inserting eq. (3.6) into eq. (3.9), yielding

$$\omega \frac{dI}{d\omega} = \frac{4\alpha_s C_R}{\omega} \text{Re} i \int_0^L dt_2 \int_0^{t_2} dt_1 \int_{\mathbf{p}, \mathbf{p}_0, \mathbf{q}} \frac{\mathbf{p} \cdot \mathbf{p}_0}{\mathbf{p}^2} v(\mathbf{q}, t_2) \mathcal{K}(\mathbf{p} - \mathbf{q}, t_2; \mathbf{p}_0, t_1), \quad (3.10)$$

where we regulated the integral over the latter time coordinate using an adiabatic turn-off at infinity (see also ref. [46]). The other time integrals are limited by the extent of the medium L . Noticing, that

$$\int_{\mathbf{p}} \frac{p^i}{\mathbf{p}^2} v(\mathbf{p} - \mathbf{k}, s) = \frac{k^i}{\mathbf{k}^2} \Sigma(\mathbf{k}^2, s), \quad (3.11)$$

where $\Sigma(\mathbf{k}^2, s) = \int_{\mathbf{q}} \sigma(\mathbf{q}, s) \Theta(\mathbf{q}^2 - \mathbf{k}^2)$,⁸ we obtain

$$\omega \frac{dI}{d\omega} = \frac{4\alpha_s C_R}{\omega} \text{Re} i \int_0^L dt_2 \int_0^{t_2} dt_1 \int_{\mathbf{p}, \mathbf{p}_0} \Sigma(\mathbf{p}^2, t_2) \frac{\mathbf{p} \cdot \mathbf{p}_0}{\mathbf{p}^2} \mathcal{K}(\mathbf{p}, t_2; \mathbf{p}_0, t_1). \quad (3.12)$$

While the above results are valid for any medium potential, in this work we will focus on the GW scattering potential, defined in eq. (3.4). In this case, we find that

$$\Sigma(\mathbf{k}^2, s) = \frac{\hat{q}_0(s)}{\mathbf{k}^2 + \mu^2}, \quad (3.13)$$

where $\hat{q}_0(s) = 4\pi\alpha_s^2 N_c n(s)$ is a measure of the scattering density. Currently, we consider a medium of constant density, $n(s) = n_0$.

⁸Also $\Sigma(0, s) = \Sigma(s)$, consistent with the definition in eq. (3.7).

The spectrum, given by eq. (3.1) or eq. (3.12), can be evaluated using numerical techniques [47–52] or by employing analytical approximations. As we will see the approximate approaches rely on expanding the problem as a series, which will give the true answer at infinite order. The different series have different radii of convergence, and none of them will alone converge for all L and ω , meaning more than one have to be employed. In most cases, however, the first order expansion is sufficient to provide an accurate approximation of the all order result. In the following we discuss three well-defined approaches that together provide an accurate description of the true problem for all L and ω , called: the opacity expansion, the resummed opacity expansion, and the improved opacity expansion. We will derive these, discuss their limits and their regions of validity.

We also point out that the medium parameters for the numerical evaluations in figures 4–6 (right) are chosen to maximally separate the relevant scales and to illustrate the main features of the spectrum. They are also similar to the ones used in phenomenological studies [24, 26, 57]. It is worth pointing out that, although this particular choice violates the assumption of non-overlapping scattering centers and should be treated with care, changing the values of the parameters would not alter the qualitative picture of separating different regimes in the (ω, t) plane.

3.2 Opacity expansion (OE)

The opacity expansion of the spectrum arises when inserting eq. (3.6) directly into eq. (3.12), and was developed in refs. [36, 66].⁹ The truncation of this series at a given order n in the medium scattering potential gives the $N = n$ term, which is by definition proportional to $(L/\lambda)^n$ (see eq. (A.2)). Physically this means, at $N = n$ one counts n number of scatterings (both with and without momentum exchange) on the full elastic potential. The relevant energy scales that arise are $\bar{\omega}_c = \frac{1}{2}\mu^2 L$, and $\frac{L}{\lambda}\bar{\omega}_c = \frac{1}{2}\hat{q}_0 L^2$ as discussed in section 2. A general formula for the spectrum at any order is derived in appendix A, and with finite- z corrections in appendix C. These results are used in the following calculations, and we will refer to the appendices for more details.

First order ($N = 1$). The spectrum at first order of opacity is well known [35, 36]. Since eq. (3.12) already includes at least one scattering, we obtain the $N = 1$ term by replacing the full propagator \mathcal{K} by the vacuum one. We then find,

$$\omega \frac{dI^{N=1}}{d\omega} = 8\pi\bar{\alpha} \frac{L}{\lambda} \frac{\bar{\omega}_c}{\omega} \int_p \tilde{\Sigma}(\mathbf{p}^2) \operatorname{Re} i \int_0^1 dt_1 \int_0^{t_1} dt_0 e^{-i\mathbf{p}^2(t_1-t_0)}, \quad (3.14)$$

where we have switched to dimensionless integration variables by defining $\mathbf{p}^2 \rightarrow \mathbf{p}^2 L / (2\omega)$ and $t \rightarrow t/L$, and where $\tilde{\Sigma}(\mathbf{p}^2) = (\mathbf{p}^2 + \bar{\omega}_c/\omega)^{-1}$. This expression can also be obtained from the general $N = n$ result in eq. (A.2). After simplifications, the spectrum becomes

$$\omega \frac{dI^{N=1}}{d\omega} = 2\bar{\alpha} \frac{L}{\lambda} \frac{\bar{\omega}_c}{\omega} \int_0^\infty dp \frac{1}{p + \frac{\bar{\omega}_c}{\omega}} \frac{p - \sin p}{p^2}, \quad (3.15)$$

⁹To be precise, expanding our formulas order by order in opacity reproduces the expansion defined in ref. [36], which reproduces ref. [66] in the “incoherent” limit.

where $\bar{\alpha} = \alpha_s C_R / \pi$ and $\lambda = \mu^2 / \hat{q}_0$. It also agrees with eq. (6.7) in ref. [36] (see also in ref. [39]). We recognize the dependence on the medium opacity L/λ and the ratio $\bar{\omega}_c/\omega$. The remaining integral can be done analytically, but the resulting expression is not very illuminating. However, the limiting behavior can readily be extracted,

$$\omega \frac{dI^{N=1}}{d\omega} \simeq \begin{cases} 2\bar{\alpha} \frac{L}{\lambda} (\ln \frac{\bar{\omega}_c}{\omega} - 1 + \gamma_E), & \text{for } \omega \ll \bar{\omega}_c, \\ \frac{\pi}{2} \bar{\alpha} \frac{L}{\lambda} \frac{\bar{\omega}_c}{\omega}, & \text{for } \omega \gg \bar{\omega}_c. \end{cases} \quad (3.16)$$

This agrees well with the heuristic discussion in section 2. In particular, we identify a logarithmic behavior $\sim \ln \frac{\bar{\omega}_c}{\omega}$ in the infrared. Notice the different expansion structures in the soft $\sim \bar{\alpha} \frac{L}{\lambda}$ and in the hard $\sim \bar{\alpha} \frac{L}{\lambda} \frac{\bar{\omega}_c}{\omega}$ limits, which we will come back to.

Second order ($N = 2$). The calculation for $N = 2$ follows in a similar way, leading to

$$\begin{aligned} \omega \frac{dI^{N=2}}{d\omega} &= -8\pi\bar{\alpha} \left(\frac{L}{\lambda}\right)^2 \frac{\bar{\omega}_c}{\omega} \int_{\mathbf{p}_2, \mathbf{p}_1} \tilde{\Sigma}(\mathbf{p}_2^2) \frac{\mathbf{p}_2 \cdot \mathbf{p}_1}{p_2^2} \tilde{v}(\mathbf{p}_2 - \mathbf{p}_1) \\ &\quad \times \text{Re } i \int_0^1 dt_2 \int_0^{t_2} dt_1 \int_0^{t_1} dt_0 e^{-ip_2^2(t_2-t_1)} e^{-ip_1^2(t_1-t_0)}, \end{aligned} \quad (3.17)$$

with dimensionless integration variables, and where $\tilde{v}(\mathbf{p}) = (2\pi)^2 \delta(\mathbf{p}) - \frac{\bar{\omega}_c}{\omega} \tilde{\sigma}(\mathbf{p})$. In the GW model, $\tilde{\sigma}(\mathbf{p}) = 4\pi/(\mathbf{p}^2 + \frac{\bar{\omega}_c}{\omega})^2$. After inserting \tilde{v} , doing the time integrals and simplifying this can be written as

$$\omega \frac{dI^{N=2}}{d\omega} = -4\bar{\alpha} \left(\frac{L}{\lambda}\right)^2 \frac{\bar{\omega}_c}{\omega} \left[\mathcal{I}_1 \left(\frac{\bar{\omega}_c}{\omega}\right) - \frac{\bar{\omega}_c}{\omega} \mathcal{I}_2 \left(\frac{\bar{\omega}_c}{\omega}\right) \right], \quad (3.18)$$

where we have defined the integrals

$$\mathcal{I}_1 \left(\frac{\bar{\omega}_c}{\omega}\right) = \int_0^\infty dp \frac{1}{p + \frac{\bar{\omega}_c}{\omega}} \frac{1 - \cos p - \frac{p}{2} \sin p}{p^3}, \quad (3.19)$$

$$\begin{aligned} \mathcal{I}_2 \left(\frac{\bar{\omega}_c}{\omega}\right) &= \int_0^\infty dp_2 \int_0^\infty dp_1 \frac{p_1}{p_2 + \frac{\bar{\omega}_c}{\omega}} \frac{1}{\left[(p_2 + p_1 + \frac{\bar{\omega}_c}{\omega})^2 - 4p_2 p_1 \right]^{3/2}} \\ &\quad \times \frac{1}{p_2 - p_1} \left[\frac{1}{p_1^2} (1 - \cos p_1) - \frac{1}{p_2^2} (1 - \cos p_2) \right]. \end{aligned} \quad (3.20)$$

The \mathcal{I}_1 integral can be done analytically, but \mathcal{I}_2 is more complicated. It can be shown that it is much smaller than \mathcal{I}_1 in the soft limit. In the hard limit, \mathcal{I}_1 and \mathcal{I}_2 cancel at the order of $\mathcal{O}(\frac{\bar{\omega}_c}{\omega})$, leaving a positive contribution going as $\mathcal{O}(\frac{\bar{\omega}_c}{\omega})^2$. In summary,

$$\omega \frac{dI^{N=2}}{d\omega} \simeq \begin{cases} -\bar{\alpha} \left(\frac{L}{\lambda}\right)^2, & \text{for } \omega \ll \bar{\omega}_c, \\ \sim \bar{\alpha} \left(\frac{L}{\lambda}\right)^2 \left(\frac{\bar{\omega}_c}{\omega}\right)^2, & \text{for } \omega \gg \bar{\omega}_c. \end{cases} \quad (3.21)$$

We notice that the $N = 2$ is proportional to $\bar{\alpha} \left(\frac{L}{\lambda}\right)^2$ in the soft limit, and goes like $\bar{\alpha} \left(\frac{L}{\lambda}\right)^2 \left(\frac{\bar{\omega}_c}{\omega}\right)^2$ in the hard limit. This immediately implies that $N = 2$ is always subleading to $N = 1$ if the medium is dilute $L \ll \lambda$ or if the emission is hard $\omega \gg \frac{L}{\lambda} \bar{\omega}_c$. Given the structure of the expansion, we expect the previous statement to hold at arbitrary $N = n$ order. This is in agreement with the earlier, heuristic observation in refs. [41, 67].

Based on the limits for $N = 1$ and $N = 2$, given by eqs. (3.16) and (3.21), in the regimes where the expansion holds the all order OE spectrum is expected to take the form

$$\omega \frac{dI}{d\omega} = \begin{cases} \bar{\alpha} \sum_{n=1}^{\infty} \left(\frac{L}{\lambda}\right)^n h_n\left(\frac{\omega}{\bar{\omega}_c}\right), & \omega \ll \bar{\omega}_c, \\ \bar{\alpha} \sum_{n=1}^{\infty} \left(\frac{L\bar{\omega}_c}{\lambda\omega}\right)^n \tilde{h}_n\left(\frac{\bar{\omega}_c}{\omega}\right), & \omega \gg \bar{\omega}_c, \end{cases} \quad (3.22)$$

where the OE coefficients h_n, \tilde{h}_n are finite and can be calculated order by order. Note that we have not strictly proven this for all orders, although our $N = 1$ and $N = 2$ results strongly indicate this structure. In the soft limit $\omega \ll \bar{\omega}_c$, the OE expansion converges rapidly, defining the expected “naive” radius of convergence $L/\lambda < 1$. However, in the hard limit $\omega \gg \bar{\omega}_c$ there is convergence even if the medium is big, provided $\frac{L\bar{\omega}_c}{\lambda\omega} < 1$. The full region of convergence is shown in green in the left panel of figure 4. Outside of this region we expect higher orders to grow uncontrollably and hence the OE is not valid when truncated at any finite order.

The resulting spectrum from eqs. (3.15) and (3.18) is shown in the right panel of figure 4 for different propagation lengths (labeled with t). For short lengths $t < \lambda$ the OE is valid for all ω . For $t > \lambda$, the OE is only valid if $\frac{t\bar{\omega}_c}{\lambda\omega} < 1$ (see also the green region on the left panel). We note that the $N = 2$ correction becomes important at $t > \lambda$ and $\omega \approx \frac{t}{\lambda}\bar{\omega}_c$ (the latter constraint shown as bullets in the figure). For larger media, the grey bullets, representing the minimal energy for achieving convergence, moves to higher values, and the truncated OE series at ω smaller than this becomes ill-defined. This can be seen, for instance, in the upper line in figure 4 (right) for a medium length of $t = 4$ fm. We have also compared to a full numerical evaluation of the spectrum from refs. [51, 68]. The figure shows that this indeed is well approximated by the OE in its region of validity, as we have argued. Our curves are not expected to hold in the limit $\omega \ll 1$ GeV, where several important effects were not taken into account such as thermal masses, realistic 2–2 elastic scatterings, and other non-perturbative effects. We still plot the curves down to very small ω to compare the different expansion schemes.

3.3 Resummed opacity expansion (ROE)

Next, we turn to dense media, $L \gg \lambda$, where multiple scattering have to be accounted for. However, as depicted to the left in figure 1 and discussed in section 2, for soft emissions with short formation times, a single scattering still gives the leading contribution to the spectrum. This defines the so-called Bethe-Heitler regime named after the QED analogue of this process. A qualitative argument of this regime was first given in ref. [36] and later developed in ref. [46], see also in ref. [62] which coined the name “resummed opacity expansion” (ROE).¹⁰

¹⁰In ref. [32], authors derive the opacity expansion from the all-order formula eq. (3.1) in a similar way as we did by expanding \mathcal{K} . Accidentally, in one of their intermediate steps in section 4, they kept the virtual interactions resummed, which corresponds to our ROE. Back then, however, they did not realize the importance of that formula and they expanded it to reproduce the OE.

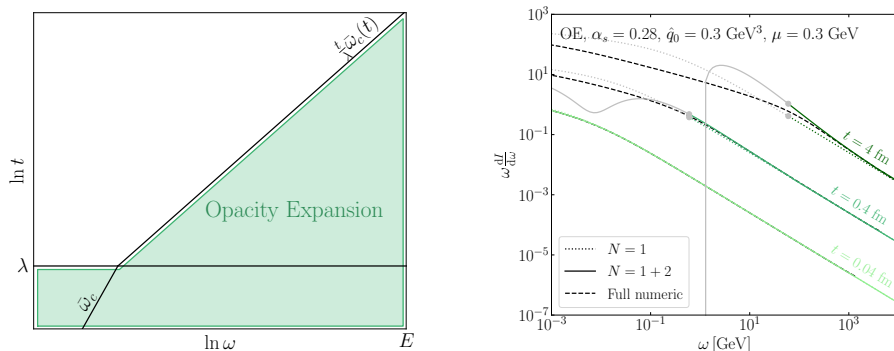


Figure 4. *Left:* the sketch of the region of validity (and convergence) of the opacity expansion for different propagation length t and emission energy ω . *Right:* the induced emission spectrum for gluons in the opacity expansion. The gray part of the curves denotes regions, where the expansion is not valid. Using the parameters presented, $\lambda = 0.06$ fm. The full numeric solution is also presented with dashed lines.

Here, we provide for the first time a consistent framework for dealing with an expansion of the *real* scatterings with the medium, whereby real we mean interactions with a finite transverse momentum exchange. At the same time, an all-order resummation of the corresponding *virtual* interactions, with zero transverse momentum exchange, is performed.

Dividing eq. (3.6) by the vacuum propagator leaves us with

$$\frac{\mathcal{K}(\mathbf{p}, t; \mathbf{p}_0, t_0)}{\mathcal{K}_0(\mathbf{p}; t - t_0)} = (2\pi)^2 \delta(\mathbf{p} - \mathbf{p}_0) - \int_{t_0}^t ds \int_{\mathbf{q}} v(\mathbf{q}, s) \frac{\mathcal{K}(\mathbf{p} - \mathbf{q}, s; \mathbf{p}_0, t_0)}{\mathcal{K}_0(\mathbf{p}; s - t_0)}. \quad (3.23)$$

Next, taking a derivative with respect to the latest time results in

$$\frac{\partial}{\partial t} \frac{\mathcal{K}(\mathbf{p}, t; \mathbf{p}_0, t_0)}{\mathcal{K}_0(\mathbf{p}; t - t_0)} + \Sigma(t) \frac{\mathcal{K}(\mathbf{p}, t; \mathbf{p}_0, t_0)}{\mathcal{K}_0(\mathbf{p}; t - t_0)} = \int_{\mathbf{q}} \sigma(\mathbf{q}) \frac{\mathcal{K}(\mathbf{p} - \mathbf{q}, t; \mathbf{p}_0, t_0)}{\mathcal{K}_0(\mathbf{p}; t - t_0)}, \quad (3.24)$$

where $\Sigma(t) = \int_{\mathbf{q}} \sigma(\mathbf{q}, t)$, as before. This motivates defining the elastic Sudakov factor,

$$\Delta(t, t_0) \equiv e^{-\int_{t_0}^t ds \Sigma(s)} = e^{-(t-t_0)\Sigma}, \quad (3.25)$$

where the last equality holds for media with constant density.¹¹ This represents the probability of no elastic scattering occurring between times t_0 and t . Integrating out the time, we arrive at a slightly modified iterative equation

$$\begin{aligned} \mathcal{K}(\mathbf{p}, t; \mathbf{p}_0, t_0) &= (2\pi)^2 \delta(\mathbf{p} - \mathbf{p}_0) \Delta(t, t_0) \mathcal{K}_0(\mathbf{p}; t - t_0) \\ &+ \int_{t_0}^t ds \frac{\Delta(t, t_0)}{\Delta(s, t_0)} \int_{\mathbf{q}} \mathcal{K}_0(\mathbf{p}; t - s) \sigma(\mathbf{q}, s) \mathcal{K}(\mathbf{p} - \mathbf{q}, s; \mathbf{p}_0, t_0). \end{aligned} \quad (3.26)$$

¹¹For medium potentials with unscreened soft divergences, such as the HTL potential, one has to modify this prescription to include an IR regulator. We refer to appendix E for a further discussion.

Compared to the standard opacity expansion in eq. (3.6), this looks very similar. However, the expansion is not in the potential $v(\mathbf{q}, s)$, which contains both a “real” and a “virtual” part, but in the potential scattering $\sigma(\mathbf{q}, s)$ which comes from the term that provides a finite momentum transfer in the process. The virtual contributions, where no net momentum was exchanged, are accounted for to all orders in the Sudakov factor. This is why this expansion referred as a *resummed* opacity expansion.

The relevant scale that appears at high opacity is $\omega_{\text{BH}} = \frac{1}{2}\mu^2\lambda$, as we discussed in section 2. Interestingly, at low opacity $L \ll \lambda$, the scale changes to $\bar{\omega}_c = \frac{1}{2}\mu^2L$, which we recognize from the opacity expansion. In this regime the ROE is actually equivalent to the OE if one gathers all the terms up to the same order in $(\frac{L}{\lambda})^n$. However, as we will see, the terms are reshuffled in the ROE compared to the OE.

It is possible to reach a general formula for the resummed opacity expansion at arbitrary order. This was done in appendix A.2, and we refer to that section for detailed calculations.

First order ($N_r = 1$). The first order can be obtained from eq. (A.9) with $n = 1$, and reads

$$\omega \frac{dI^{N_r=1}}{d\omega} = -8\pi\bar{\alpha} \frac{L\bar{\omega}_c}{\lambda\omega} \int_{\mathbf{p}} \tilde{\Sigma}(\mathbf{p}^2) \text{Im} T\left(\mathbf{p}^2 - i\frac{L}{\lambda}\right), \quad (3.27)$$

in re-scaled, dimensionless variables. Equation (3.27) corresponds to the formula (eq. (4.6)) in ref. [46], but is here derived more rigorously. Here, we have defined the function

$$T(x) = \int_0^1 dt_1 \int_0^{t_1} dt_0 e^{-ix(t_1-t_0)} = \frac{1 - ix - e^{-ix}}{x^2}. \quad (3.28)$$

The real and imaginary parts of $T(\mathbf{p}^2 - i\chi)$ are given in eq. (A.10). After doing the angular integral this becomes

$$\omega \frac{dI^{N_r=1}}{d\omega} = -2\bar{\alpha} \frac{L\bar{\omega}_c}{\lambda\omega} \int_0^\infty dp \frac{1}{p + \frac{\bar{\omega}_c}{\omega}} \text{Im} T\left(p - i\frac{L}{\lambda}\right). \quad (3.29)$$

At low opacity $L \ll \lambda$, the function $T(p - iL/\lambda)$ becomes

$$-\text{Im} T(p)|_{L \ll \lambda} = \frac{p - \sin(p)}{p^2}, \quad (3.30)$$

making it equivalent to the OE result in eq. (3.15). The limiting behavior in the relevant limits of eq. (3.29) can be extracted, leading to

$$\omega \frac{dI^{N_r=1}}{d\omega} \simeq \begin{cases} 2\bar{\alpha} \frac{L}{\lambda} \left(\ln\left(\frac{\bar{\omega}_c}{\omega}\right) - 1 + \gamma_E \right) - \bar{\alpha} \left(\frac{L}{\lambda}\right)^2 \left(1 - \pi \frac{\omega}{\bar{\omega}_c}\right), & \text{for } \omega \ll \bar{\omega}_c, \\ \frac{\pi\bar{\alpha}}{2} \frac{L\bar{\omega}_c}{\lambda\omega} - \frac{\pi}{6}\bar{\alpha} \left(\frac{L}{\lambda}\right)^2 \frac{\bar{\omega}_c}{\omega}, & \text{for } \omega \gg \bar{\omega}_c. \end{cases} \quad (3.31)$$

At leading order in $\mathcal{O}(\frac{L}{\lambda})$ this is the same as the $N = 1$ opacity expansion, presented in eq. (3.16). However, in contrast to the OE, subleading “ $N = 2$ ”-like terms $\sim (\frac{L}{\lambda})^2$ appear, which only will be relevant when compared to higher-order contributions at $N_r = 2$.

In the high opacity limit $L \gg \lambda$, we have to extract the relevant limit of $T(p - i\chi)$ in a careful way, yielding

$$-\text{Im} T(p - i\chi)|_{L \gg \lambda} \simeq \frac{p}{(L/\lambda)^2 + p^2}. \quad (3.32)$$

Changing the integration variable to $q = p\lambda/L$, we observe that ω_{BH} replaces $\bar{\omega}_c$ as the relevant scale, and eq. (3.29) becomes

$$\omega \frac{dI^{N_r=1}}{d\omega} \simeq 2\bar{\alpha} \frac{L}{\lambda} \frac{\omega_{\text{BH}}}{\omega} \int_0^\infty dq \frac{1}{q + \frac{\omega_{\text{BH}}}{\omega}} \frac{q}{1 + q^2} = 2\bar{\alpha} \frac{L}{\lambda} \frac{\omega_{\text{BH}}}{\omega} \frac{\frac{\pi}{2} + \frac{\omega_{\text{BH}}}{\omega} \ln\left(\frac{\omega_{\text{BH}}}{\omega}\right)}{1 + \left(\frac{\omega_{\text{BH}}}{\omega}\right)^2}. \quad (3.33)$$

Finally, one can extract the soft and hard limits of this expression, which are given by

$$\omega \frac{dI^{N_r=1}}{d\omega} \simeq \begin{cases} 2\bar{\alpha} \frac{L}{\lambda} \left(\ln\left(\frac{\omega_{\text{BH}}}{\omega}\right) + \frac{\pi}{2} \frac{\omega}{\omega_{\text{BH}}} \right), & \text{for } \omega \ll \omega_{\text{BH}}, \\ \pi \bar{\alpha} \frac{L}{\lambda} \frac{\omega_{\text{BH}}}{\omega}, & \text{for } \omega \gg \omega_{\text{BH}}. \end{cases} \quad (3.34)$$

The soft limit agrees with the heuristic discussion in section 2. Strikingly, we see that the behavior in the soft and hard limit takes exactly the same form as for $N = 1$ except that $\bar{\omega}_c$ has been replaced by ω_{BH} (note that $\bar{\omega}_c(L = \lambda) = \omega_{\text{BH}}$).

Second order ($N_r = 2$). The second order is found from eq. (A.9) with $n = 2$, and reads

$$\begin{aligned} \omega \frac{dI^{N_r=2}}{d\omega} &= 8\pi\bar{\alpha} \left(\frac{L}{\lambda}\right)^2 \left(\frac{\bar{\omega}_c}{\omega}\right)^2 \int_{\mathbf{p}_2, \mathbf{p}_1} \tilde{\Sigma}(\mathbf{p}_2^2) \frac{\mathbf{p}_2 \cdot \mathbf{p}_1}{\mathbf{p}_2^2} \tilde{\sigma}(\mathbf{p}_2 - \mathbf{p}_1) \\ &\quad \times \frac{1}{\mathbf{p}_2^2 - \mathbf{p}_1^2} \left(\text{Re} T(\mathbf{p}_1^2 - i\chi) - \text{Re} T(\mathbf{p}_2^2 - i\chi) \right). \end{aligned} \quad (3.35)$$

After going to polar coordinates and doing the angular integrals, this becomes

$$\begin{aligned} \omega \frac{dI^{N_r=2}}{d\omega} &= 4\bar{\alpha} \left(\frac{L}{\lambda}\right)^2 \left(\frac{\bar{\omega}_c}{\omega}\right)^2 \int_0^\infty dp_2 \int_0^\infty dp_1 \frac{1}{p_2 + \frac{\bar{\omega}_c}{\omega}} \frac{p_1}{\left[(p_1 + p_2 + \frac{\bar{\omega}_c}{\omega})^2 - 4p_1 p_2 \right]^{3/2}} \\ &\quad \times \frac{1}{p_2 - p_1} \left(\text{Re} T(p_1 - i\chi) - \text{Re} T(p_2 - i\chi) \right). \end{aligned} \quad (3.36)$$

We study this expression separately in the low- and high-opacity limits.

In the low opacity limit $L \ll \lambda$, the spectrum becomes

$$\begin{aligned} \omega \frac{dI^{N_r=2}}{d\omega} &\simeq 4\bar{\alpha} \left(\frac{L}{\lambda}\right)^2 \left(\frac{\bar{\omega}_c}{\omega}\right)^2 \int_0^\infty dp_2 \int_0^\infty dp_1 \frac{1}{p_2 + \frac{\bar{\omega}_c}{\omega}} \frac{p_1}{\left[(p_1 + p_2 + \frac{\bar{\omega}_c}{\omega})^2 - 4p_1 p_2 \right]^{3/2}} \\ &\quad \times \frac{1}{p_2 - p_1} \left(\frac{1 - \cos p_1}{p_1^2} - \frac{1 - \cos p_2}{p_2^2} \right), \end{aligned} \quad (3.37)$$

where again the only relevant energy scale is $\bar{\omega}_c$, as it is in the OE. The double momentum integral can be recognized as \mathcal{I}_2 from $N = 2$ of the opacity expansion. The soft and hard limits are

$$\omega \frac{dI^{N_r=2}}{d\omega} \simeq \begin{cases} \pi \bar{\alpha} \left(\frac{L}{\lambda}\right)^2 \frac{\omega}{\bar{\omega}_c}, & \text{for } \omega \ll \bar{\omega}_c, \\ \frac{\pi}{6} \bar{\alpha} \left(\frac{L}{\lambda}\right)^2 \frac{\bar{\omega}_c}{\omega}, & \text{for } \omega \gg \bar{\omega}_c. \end{cases} \quad (3.38)$$

Summing up the two first orders of the ROE and OE we see that $N_r = 1 + 2$ agrees with $N = 1 + 2$, but only when keeping the subleading $\sim (L/\lambda)^2$ terms at order $N_r = 1$. As mentioned before, the opacity expansion is arranged so that the order $N = n$ only contains terms where the opacity scales as $\sim \chi^n$, where $\chi = L/\lambda$. The resummed opacity expansion also includes all of the same terms, but they are spread out over different orders of the expansion due to the resummation contained in the Sudakov factor. The orders $N_r < n$ do contain terms going as χ^n . To get the right term at order χ^n in the ROE one therefore has to keep the subleading corrections going as χ^n at all previous orders of the expansion. For this reason the opacity expansion is more convenient to use in the low opacity limit, as it does not mix orders of opacity.

In the high opacity limit $L \gg \lambda$, we get

$$\omega \frac{dI^{N_r=2}}{d\omega} \simeq 4\bar{\alpha} \frac{L}{\lambda} \left(\frac{\omega_{\text{BH}}}{\omega} \right)^2 \int_0^\infty dp_2 \int_0^\infty dp_1 \frac{1}{p_2 + \frac{\bar{\omega}_c}{\omega}} \frac{p_1}{\left[(p_1 + p_2 + \frac{\bar{\omega}_c}{\omega})^2 - 4p_1 p_2 \right]^{3/2}} \times \frac{p_2 + p_1}{(1 + p_2^2)(1 + p_1^2)}. \quad (3.39)$$

The soft and hard limits of this expression are given by

$$\omega \frac{dI^{N_r=2}}{d\omega} \simeq \begin{cases} \pi\bar{\alpha} \frac{L}{\lambda} \frac{\omega}{\omega_{\text{BH}}}, & \text{for } \omega \ll \omega_{\text{BH}}, \\ \pi\bar{\alpha} \frac{L}{\lambda} \frac{\omega_{\text{BH}}}{\omega}, & \text{for } \omega \gg \omega_{\text{BH}}, \end{cases} \quad (3.40)$$

where similarly to $N_r = 1$, the relevant scale is now ω_{BH} . Both $N_r = 1$ and 2 goes as $\sim \bar{\alpha} \frac{L}{\lambda}$, however, in the soft limit $N_r = 1$ dominates, while in the hard limit $dI^{N_r=2} \sim dI^{N_r=1}$. This shows that ROE is quickly convergent if $\omega \ll \omega_{\text{BH}}$, while the expansion appears to break down for harder emissions. We expect this structure to appear to all orders in $N_r = n$. The resulting validity of the expansion is shown in the left of figure 5 in blue. Based on our findings, the expansion scheme for the ROE at high opacity $L \gg \lambda$ is

$$\omega \frac{dI}{d\omega} = \bar{\alpha} \frac{L}{\lambda} \sum_{n=0}^\infty f_n \left(\frac{\omega}{\omega_{\text{BH}}} \right), \quad (3.41)$$

where f_n is a finite function that can be obtained order by order for $\omega \ll \omega_{\text{BH}}$.

The resulting spectrum is shown in the right of figure 5 for different propagation lengths. For short times ($t < \lambda$), the ROE is valid for all ω and it gives the same spectrum as the OE (compare to the right panel of figure 4). For longer propagation the ROE is only valid if $\omega < \omega_{\text{BH}}$, which is denoted with bullets in the figure. Outside of the valid region, the curves turn to gray (see also the left panel). Based on the figure, $N_r = 2$ has negligible contribution to the spectrum until $t \approx \lambda$ or $\omega \approx \omega_{\text{BH}}$. Again, the dashed line represents the full numerical evaluation of the spectrum from refs. [51, 68] which is well approximated by the ROE in its region of validity.

3.4 Improved opacity expansion (IOE)

The final expansion scheme we consider is the improved opacity expansion, introduced in refs. [53–57]. We saw that the ROE at high opacity does not work for energies much higher than ω_{BH} . This makes sense since at higher energies the formation time t_f of the

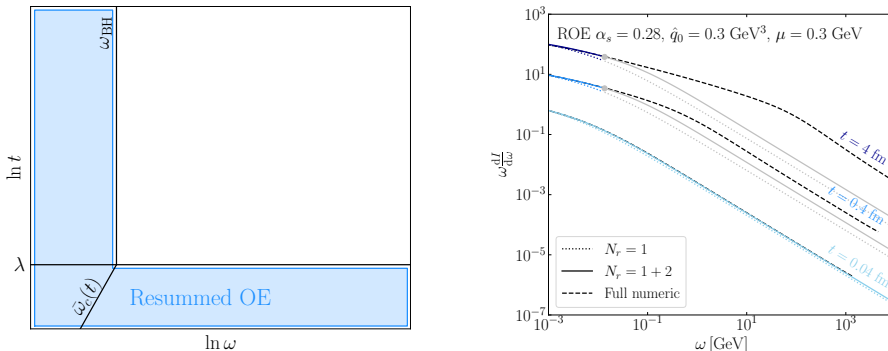


Figure 5. *Left:* the sketch of region of validity (and convergence) of the resummed opacity expansion for different propagation length t and emission energy ω . *Right:* the induced emission spectrum for gluons in the resummed opacity expansion. The gray part of the curves denotes regions, where the expansion is not valid. With the parameters presented, $\lambda = 0.06$ fm. The full numeric solution is also presented with dashed lines.

emission becomes bigger than the mean free path, implying that the parton will scatter many times on the medium. The main motivation for the improved opacity expansion is to resum multiple soft scatterings, while account perturbatively for rare, hard scatterings. This is achieved by introducing a scale Q^2 that separates soft and hard scatterings in the scattering potential,

$$v(\mathbf{x}, t) \approx v_{\text{HO}}(\mathbf{x}, t) + \delta v(\mathbf{x}, t), \quad (3.42)$$

where $v_{\text{HO}}(\mathbf{x}, t) = \frac{\hat{q}(t)}{4} \mathbf{x}^2$ and $\delta v(\mathbf{x}, t) = \frac{\hat{q}_0(t)}{4} \mathbf{x}^2 \ln \frac{1}{Q^2 \mathbf{x}^2}$. Equation (3.42) is the $\mu|\mathbf{x}| \ll 1$ expansion of eq. (3.3) with the GW potential. The first term is referred to as the harmonic oscillator approximation (HO), where the jet quenching parameter is

$$\hat{q}(t) = \hat{q}_0(t) \ln \frac{Q^2}{\mu_*^2}, \quad (3.43)$$

where $\mu_*^2 = \frac{\mu^2}{4} e^{-1+2\gamma_E}$ for the GW potential. The logarithm in \hat{q} comes from the fact that the typical exchanged momentum $\langle \mathbf{k}^2 \rangle = L \int_q \mathbf{q}^2 \sigma(\mathbf{q})$ is divergent and thus it has to be regulated resulting in the leading logarithmic form in eq. (3.43) (see in ref. [42]). As long as $Q^2/\mu_*^2 \gg 1/(Q^2 \mathbf{x}^2)$, the HO term dominates over δv , and the latter can be treated as a perturbation. This provides a big advantage, since the multiple scattering in the HO approximation can be resummed analytically.

The separation scale Q^2 has to be fixed in a meaningful way to not to interfere with the expansion [55]. A natural choice that achieves this is evaluating Q^2 at the typical transverse momentum of the emission $\mathbf{k}^2 \sim \hat{q}_t$, that yields

$$Q_r^2(\omega) = \sqrt{\omega \hat{q}(\omega)}, \quad (3.44)$$

which constitutes an implicit equation for $Q_r^2(\omega)$, and for $\hat{q}(\omega) \equiv \hat{q}(Q_r(\omega))$, see eq. (3.43).¹²

¹²Equation (3.44) has a solution only if $\omega > 2e \frac{\mu_*^4}{q_0} \simeq 0.925 \omega_{\text{BH}}$. When this is satisfied, and $L > \lambda$, then $Q_r^2 > \mu_*^2$ by default. This is the necessary condition for the convergence of the IOE. The IOE therefore breaks down for $\omega \lesssim \omega_{\text{BH}}$.

The IOE corresponds to expanding the full medium solution for $\mathcal{K}(\mathbf{x}; \mathbf{y})$ around the harmonic oscillator, in contrast to the conventional opacity expansion where one expands around the vacuum solution. It can be cast in the iterative equation

$$\begin{aligned} \mathcal{K}(\mathbf{x}, t_2; \mathbf{y}, t_1) &= \mathcal{K}_{\text{HO}}(\mathbf{x}, t_2; \mathbf{y}, t_1) \\ &\quad - \int_{t_1}^{t_2} ds \int_{\mathbf{z}} \mathcal{K}_{\text{HO}}(\mathbf{x}, t_2; \mathbf{z}, s) \delta v(\mathbf{z}, s) \mathcal{K}(\mathbf{z}, s; \mathbf{y}, t_1). \end{aligned} \quad (3.45)$$

Here, $\mathcal{K}_{\text{HO}}(\mathbf{x}; \mathbf{y})$ is itself the solution to an iterative equation, namely

$$\begin{aligned} \mathcal{K}_{\text{HO}}(\mathbf{x}, t_2; \mathbf{y}, t_1) &= \mathcal{K}_0(\mathbf{x} - \mathbf{y}, t_2 - t_1) \\ &\quad - \int_{t_1}^{t_2} ds \int_{\mathbf{z}} \mathcal{K}_0(\mathbf{x} - \mathbf{z}, t_2 - s) v_{\text{HO}}(\mathbf{z}, s) \mathcal{K}_{\text{HO}}(\mathbf{z}, s; \mathbf{y}, t_1). \end{aligned} \quad (3.46)$$

The formal solution for $\mathcal{K}_{\text{HO}}(\mathbf{x}, t_2; \mathbf{y}, t_1)$ can also be cast as a path integral, namely

$$\mathcal{K}_{\text{HO}}(\mathbf{x}, t_2; \mathbf{y}, t_1) = \int_{r(t_1)=\mathbf{y}}^{r(t_2)=\mathbf{x}} \mathcal{D}\mathbf{r} e^{i \int_{t_1}^{t_2} ds \left[\frac{\omega}{2} \dot{r}^2 + i v_{\text{HO}}(r, s) \right]}, \quad (3.47)$$

which has a well-known analytical solution in a static medium,

$$\mathcal{K}_{\text{HO}}(\mathbf{x}, t_2; \mathbf{y}, t_1) = \frac{\omega \Omega}{2\pi i \sin(\Omega \Delta t)} e^{\frac{i\omega\Omega}{2\sin(\Omega\Delta t)} [\cos(\Omega\Delta t) (\mathbf{x}^2 + \mathbf{y}^2) - 2\mathbf{x}\cdot\mathbf{y}]}, \quad (3.48)$$

where $\Delta t \equiv t_2 - t_1$ and $\Omega = \frac{1-i}{2} \sqrt{\hat{q}(\omega)/\omega}$ is the characteristic oscillator frequency.

Inserting this expansion into the equation for the medium-induced spectrum eq. (3.1) separates it into two parts,

$$\omega \frac{dI^{\text{HO}}}{d\omega} = \frac{2\alpha_s C_R}{\omega^2} \text{Re} \int_0^\infty dt_2 \int_0^{t_2} dt_1 \partial_{\mathbf{x}} \cdot \partial_{\mathbf{y}} [\mathcal{K}_{\text{HO}}(\mathbf{x}, t_2; \mathbf{y}, t_1) - \mathcal{K}_0(\mathbf{x}, t_2; \mathbf{y}, t_1)]_{\mathbf{x}=\mathbf{y}=0}, \quad (3.49)$$

$$\begin{aligned} \omega \frac{dI^{\text{IOE}}}{d\omega} &= -\frac{2\alpha_s C_R}{\omega^2} \text{Re} \int_0^\infty dt_2 \int_0^{t_2} ds \int_0^s dt_1 \int_{\mathbf{z}} \\ &\quad \times \partial_{\mathbf{x}} \cdot \partial_{\mathbf{y}} [\mathcal{K}_{\text{HO}}(\mathbf{x}, t_2; \mathbf{z}, s) \delta v(\mathbf{z}, s) \mathcal{K}(\mathbf{z}, s; \mathbf{y}, t_1)]_{\mathbf{x}=\mathbf{y}=0}. \end{aligned} \quad (3.50)$$

The first term gives rise to the well-known HO spectrum, while the second constitutes an expansion in hard splittings around the harmonic oscillator. The IOE spectrum can be simplified further, giving

$$\omega \frac{dI^{\text{IOE}}}{d\omega} = \frac{2\bar{\alpha}}{\omega} \text{Re} i \int_0^L dt_2 \int_0^{t_2} dt_1 \int_{\mathbf{x}} e^{-i\frac{\omega\Omega}{2} \tan(\Omega(L-t_2)) \mathbf{x}^2} \delta v(\mathbf{x}) \frac{\mathbf{x}}{\mathbf{x}^2} \cdot \partial_{\mathbf{y}} \mathcal{K}(\mathbf{x}, t_2; \mathbf{y}, t_1)|_{\mathbf{y}=0}, \quad (3.51)$$

where $\mathcal{K}(\mathbf{x}; \mathbf{y})$ should be iterated using eq. (3.45) in order to generate higher orders of the expansion. A general formula for the improved opacity expansion at arbitrary order can also be derived, which was done in section A.3, see also in ref. [55].

Harmonic oscillator (HO). The harmonic oscillator approximation resums all coherent soft scatterings during the formation of the emission. The relevant scale is

$$\omega_c \equiv \frac{1}{2} \hat{q}(\omega_c) L^2, \quad (3.52)$$

where the scale in the jet quenching parameter is set to ω_c . This scale was already identified in section 2. The HO approximation is expected to be valid for $\omega_{\text{BH}} \ll \omega \ll \omega_c$.

We derive here the familiar harmonic oscillator spectrum in a new way. The vacuum contribution can easily be subtracted by inserting eq. (3.45) into eq. (3.1), which gives

$$\begin{aligned} \omega \frac{dI^{\text{HO}}}{d\omega} &= -\frac{2\alpha_s C_R}{\omega^2} \text{Re} \int_0^\infty dt_2 \int_0^{t_2} ds \int_0^s dt_1 \int_{\mathbf{z}} \\ &\quad \times \partial_{\mathbf{x}} \cdot \partial_{\mathbf{y}} [\mathcal{K}_0(\mathbf{x}, t_2; \mathbf{z}, s) v_{\text{HO}}(\mathbf{z}, s) \mathcal{K}_{\text{HO}}(\mathbf{z}, s; \mathbf{y}, t_1)]|_{\mathbf{x}=\mathbf{y}=0}. \end{aligned} \quad (3.53)$$

Using the fact that $\int_s^\infty dt_2 \partial_{\mathbf{x}} \mathcal{K}_0(\mathbf{x}, t_2; \mathbf{z}, s)|_{\mathbf{x}=0} = -i \frac{\omega}{\pi} \frac{\mathbf{z}}{z^2}$, the spectrum becomes

$$\omega \frac{dI^{\text{HO}}}{d\omega} = \frac{\bar{\alpha} \hat{q}(\omega)}{2\omega} \text{Re} i \int_0^L dt_2 \int_0^{t_2} dt_1 \int_{\mathbf{z}} \mathbf{z} \cdot \partial_{\mathbf{y}} \mathcal{K}_{\text{HO}}(\mathbf{z}, t_2; \mathbf{y}, t_1)|_{\mathbf{y}=0}. \quad (3.54)$$

This can be further simplified by using that

$$\begin{aligned} \int_{\mathbf{z}} \mathbf{z} \cdot \partial_{\mathbf{y}} \mathcal{K}_{\text{HO}}(\mathbf{z}, t_2; \mathbf{y}, t_1)|_{\mathbf{y}=0} &= -\frac{(\omega\Omega)^2}{2\pi \sin^2(\Omega(t_2 - t_1))} \int_{\mathbf{z}} \mathbf{z}^2 e^{i \frac{\omega\Omega}{2} z^2 \cot(\Omega(t_2 - t_1))}, \\ &= \frac{2}{\cos^2(\Omega(t_2 - t_1))}. \end{aligned} \quad (3.55)$$

The time integration can be now be dealt with straightforwardly, yielding

$$\int_0^L dt_2 \int_0^{t_2} dt_1 \frac{1}{\cos^2(\Omega(t_2 - t_1))} = -\frac{\ln \cos \Omega L}{\Omega^2}, \quad (3.56)$$

and thus the spectrum becomes

$$\omega \frac{dI^{\text{HO}}}{d\omega} = 2\bar{\alpha} \ln |\cos \Omega L|, \quad (3.57)$$

which is the familiar BDMPS-Z spectrum [32, 69]. The limits of this are

$$\omega \frac{dI^{\text{HO}}}{d\omega} \simeq \begin{cases} \bar{\alpha} \sqrt{\frac{2\omega_c}{\omega}}, & \text{for } \omega \ll \omega_c, \\ \frac{\bar{\alpha}}{6} \left(\frac{\omega_c}{\omega}\right)^2, & \text{for } \omega \gg \omega_c. \end{cases} \quad (3.58)$$

The soft limit agrees with the discussion in section 2, while the hard limit is subleading compared to the OE $N = 1$ in eq. (3.16). Defining \hat{q} with a logarithm extends the region of validity, which was also found in ref. [42], leading to the curved $\omega_c(t)$ line in figure 3.

Next-to-harmonic oscillator (NHO). Using the definition in eq. (3.51) and the results of section A.3, the first order of the improved opacity expansion can be written as

$$\omega \frac{dI^{\text{NHO}}}{d\omega} = \frac{2\bar{\alpha} L \bar{\omega}_c}{\pi \lambda \omega} \text{Re} \int_0^1 ds \int_{\mathbf{u}} \frac{1}{2} \ln \left(\frac{\omega}{\bar{\omega}_c} \frac{\mu^2}{2Q^2} \frac{1}{\mathbf{u}^2} \right) e^{\frac{i}{2} f(s) \mathbf{u}^2}, \quad (3.59)$$

where we have defined the function $f(s) = \sigma\sqrt{\omega_c/\omega}[\cot(\sigma s\sqrt{\omega_c/\omega}) - \tan(\sigma(1-s)\sqrt{\omega_c/\omega})]$, and $\sigma = \frac{1-i}{\sqrt{2}}$. After doing the \mathbf{u} integral this becomes

$$\omega \frac{dI^{\text{NHO}}}{d\omega} = 2\bar{\alpha} \frac{L \bar{\omega}_c}{\lambda \omega} \text{Re} i \int_0^1 ds \frac{1}{f(s)} \left[1 - \gamma_E + \ln \left(-i \frac{\omega}{\bar{\omega}_c} \frac{\mu_*^2}{Q^2} f(s) \right) \right]. \quad (3.60)$$

The limits of this expression can readily be extracted. In the soft limit, $\omega \ll \omega_c$, we have $f(s) \rightarrow 2i\sigma\sqrt{\omega_c/\omega}$ while in the hard limit, $\omega \gg \omega_c$, it becomes $f(s) \rightarrow 1/s$. These simplifications make it possible to do the last time integration. Hence, the extracted limiting behavior is,

$$\omega \frac{dI^{\text{NHO}}}{d\omega} \simeq \begin{cases} \bar{\alpha} \sqrt{\frac{2\omega_c}{\omega}} \frac{1}{2 \ln Q^2/\mu_*^2} \left(\frac{\pi}{4} + \gamma_E + \ln \left(\frac{\sqrt{q}\omega}{\sqrt{2}Q^2} \right) \right), & \text{for } \omega \ll \omega_c, \\ \frac{\pi \bar{\alpha}}{2} \frac{L \bar{\omega}_c}{\lambda \omega}, & \text{for } \omega \gg \omega_c. \end{cases} \quad (3.61)$$

In the soft limit $\omega \ll \omega_c$, NⁿHO terms will take the form of the HO by using Q_r , and thus

$$\omega \frac{dI}{d\omega} = \bar{\alpha} \sqrt{\frac{\hat{q}(\omega)L^2}{\omega}} \left(1 + \frac{1}{2} \frac{a_0}{\ln Q_r^2/\mu_*^2} + \mathcal{O} \left(\frac{1}{\ln Q_r^2/\mu_*^2} \right)^2 \right), \quad (3.62)$$

where we added the HO term, and used eq. (3.44). The choice of $Q = Q_r(\omega)$ is effective, when the medium is big enough $L \gg \lambda$. It is clear that the expansion parameter of the IOE is $\ln^{-1}(Q_r^2/\mu_*^2) \ll 1$ in the soft limit. Therefore, NⁿHO terms can be absorbed into an effective jet transport parameter,

$$\hat{q}_{\text{eff}}(Q^2) = \hat{q}_0 \ln \left(\frac{Q_r^2}{\mu_*^2} \right) \left[1 + \frac{a_0}{\ln Q_r^2/\mu_*^2} + \frac{a_1}{\ln^2 Q_r^2/\mu_*^2} + \dots \right]. \quad (3.63)$$

The coefficients $a_0 = 1.016$ and $a_1 = 0.316$ of the expansion and higher-order terms up to N²HO were found in ref. [55].

In the hard limit of eq. (3.61), one can see that the IOE reproduces the hard limit of $N = 1$ in the OE from eq. (3.16). Furthermore, it is bigger than the HO contribution in eq. (3.57) and thus NHO dominates for $\omega \gg \omega_c$.

As mentioned above, the HO is meaningful if $L > \lambda$ and $\omega > \omega_{\text{BH}}$. Furthermore, the IOE is expected to converge if $v_{\text{HO}} > \delta v$ or equivalently $\omega > \omega_{\text{BH}}$. However, as the hard limits of the first order of the IOE and the OE are equal, and the OE is valid down to $\bar{\omega}_c$, it is reasonable to assume that also the IOE is valid down to $\bar{\omega}_c$. Therefore, the region of validity will be extended to all L and $\omega > \min(\omega_{\text{BH}}, \bar{\omega}_c)$, as shown in the left of figure 6 in red.

The spectra obtained with the IOE from eq. (3.57) and eq. (3.61) are shown in the right panel of figure 6 for different propagation lengths. At early times $t < \lambda$, the HO approximation is highly suppressed, due to the absence of multiple scattering. However, the contribution from the NHO makes the total agree with the hard limit of $N = 1$ OE and $N_r = 1$ ROE (cf. figures 4 and 5). The deviation close to $\omega \approx \bar{\omega}_c$ (gray bullet) arises since Q_r was chosen to reproduce the HO spectrum which is strictly valid for $L \gg \lambda$. For later times $t > \lambda$, both the HO and NHO will give sizable contributions, where the HO dominates if $\omega < \omega_c$ (red bullets) and NHO dominates if $\omega > \omega_c$. The HO approximation breaks down if $\omega < \omega_{\text{BH}}$ (gray bullets). The dashed line is the full numerical solution from refs. [51, 68] and the IOE well captures it in its region of validity.

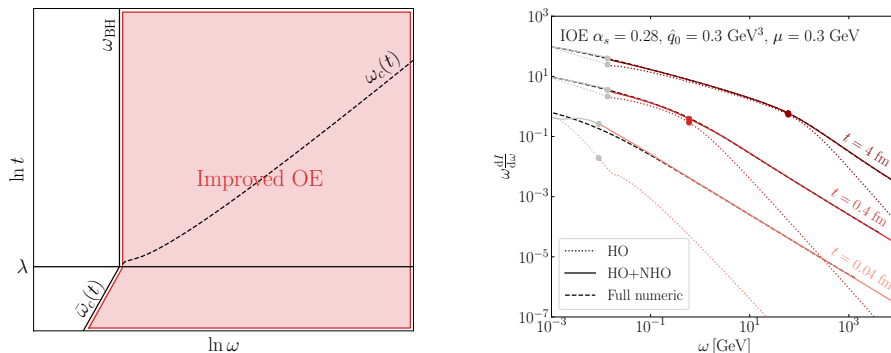


Figure 6. *Left:* the sketch of region of validity (and convergence) of the improved opacity expansion for different propagation length t and emission energy ω . *Right:* the induced emission spectrum for gluons in the improved opacity expansion. The gray part of the curves denotes regions where the expansion is not valid. Using the parameters presented, $\lambda = 0.06$ fm. The full numeric solution is also presented with dashed lines.

3.5 Summary of the regimes and the induced emission spectrum

In this section, we have presented three distinct perturbative expansions (OE, ROE, and IOE) that provide different ways of calculating the induced emission spectrum $\omega \frac{dI}{d\omega}$ in their respective regimes of convergence. The OE and IOE are expansion schemes that were first developed in previous works, while the ROE is rigorously derived in this section for the first time. Their regions of validity are sketched previously in figures 4–6, and at least one of the expansions is valid at every point in the phase space (ω, t) . Here ω is the emitted energy and t is the propagated length (L is the maximal length of the medium and E is the energy of the emitting particle). As a consequence, our description of the spectrum is complete in the full phase space, as one can always use one of the expansions to reach an approximation of the true spectrum, and one can reach better accuracy by including higher orders. Note that the expansions are overlapping: for $L < \lambda$ both OE and ROE are valid, and for $\omega > \omega_c$ both IOE the OE can be used.

The results presented obtained so far within the unified resummation framework are valid in both dilute and dense regimes and can be systematically improved to arbitrary high order in the expansions. For practical purposes, however, a handy and efficient interpolation formula such suffice to capture the relevant features to high precision. This would be very useful for other applications, such as resumming multiple emissions in sections 4 and 5. To describe the spectrum in the whole phase space, we use (to first order)

$$\frac{dI^{\text{Full}}}{d\omega} = \begin{cases} \frac{dI^{\text{ROE}}}{d\omega}, & \omega < \min(\omega_{\text{BH}}, \bar{\omega}_c(t)), \\ \frac{dI^{\text{IOE}}}{d\omega}, & \text{otherwise.} \end{cases} \quad (3.64)$$

Based on figures 4–6 (and the all order expansion formulas), the first-order terms already capture the most important effects. We stress that this is arguable the most straightforward

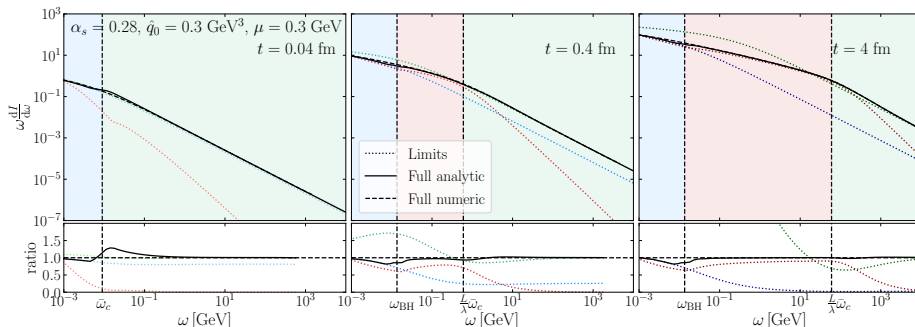


Figure 7. Summary of the induced emission spectrum for gluons, combined from the three expansion schemes at different propagation length (different panels). The black lines are our final forms from eq. (3.64) that uses $N_r = 1$ and HO+NHO. The shaded areas denote the leading scattering process and the corresponding dotted lines are the limiting $N = 1$, HO and $N_r = 1$ contributions. The dashed lines are the numerical solution of eq. (3.1) from ref. [51].

interpolation scheme. However, it turns out that it gives a good description in almost the whole phase space, deviating maximally 30% from the exact numerical results around the Bethe-Heitler energy in the dilute regime, see figure 7 (left, lower panel).¹³

To summarize, the limiting behaviour of the spectrum in different regions of the phase space is

$$\omega \frac{dI}{d\omega} \Big|_{L \ll \lambda} = \begin{cases} 2\bar{\alpha} \frac{L}{\lambda} (\ln \frac{\bar{\omega}_c}{\omega} - 1 + \gamma_E), & \text{for } \omega \ll \bar{\omega}_c, \\ \frac{\pi}{2} \bar{\alpha} \frac{L}{\lambda} \frac{\bar{\omega}_c}{\omega}, & \text{for } \bar{\omega}_c \ll \omega, \end{cases} \quad (3.65)$$

for $L \ll \lambda$, and

$$\omega \frac{dI}{d\omega} \Big|_{L \gg \lambda} = \begin{cases} 2\bar{\alpha} \frac{L}{\lambda} \ln \left(\frac{\omega_{\text{BH}}}{\omega} \right), & \text{for } \omega \ll \omega_{\text{BH}}, \\ \bar{\alpha} \sqrt{\frac{2\omega_c}{\omega}}, & \text{for } \omega_{\text{BH}} \ll \omega \ll \omega_c, \\ \frac{\pi}{2} \bar{\alpha} \frac{L}{\lambda} \frac{\bar{\omega}_c}{\omega}, & \text{for } \omega_c \ll \omega, \end{cases} \quad (3.66)$$

for $L \gg \lambda$. This agrees with the formulas from the heuristic discussion in section 2. In figure 7, we evaluated eq. (3.64) (black curve) up to $N_r = 1$ and HO+NHO for different times. The dotted curves are the limits of $N_r = 1$, HO and $N = 1$, shown in blue, red and green respectively. The regions are shaded with the same colors as in figure 3, visualizing the regions of the distinct scattering processes. At the transition point $\min(\omega_{\text{BH}}, \bar{\omega}_c(t))$, the spectrum is not completely smooth, and the difference is expected to vanish as one goes to higher orders in the perturbative expansion. We defined a switching function that makes the transition smoother, which is described in appendix D.

In figure 7, we have also plotted the full numerical spectra from refs. [51, 68] with dashed lines. The excellent agreement with our curves corroborates the validity of our formula in

¹³The interpolation can be further inspected in figure 11, where we plot the spectrum on a semilog scale. The exact details of matching the ROE regime with the IOE involves a smooth interpolation function, that avoids blowing up the logarithmic dependence of \hat{q} . This is described in detail in appendix D.

eq. (3.64), where we used $N_r = 1$ and HO+NHO in the plot. In the ratio panel, one can see, how the different regions are adding up to give an overall very accurate description of the full spectrum. Moreover, as we saw in figures 4–6, by including higher orders e.g. $N_r = 2$, the description becomes more accurate, smoothing the transition around ω_{BH} . We leave the study of these higher-order corrections and the corresponding uncertainties for future studies.

4 Resumming multiple emissions in the medium

Section 3 presents a theoretical framework consisting of different perturbative expansions (namely the opacity expansion (OE), the resummed OE (ROE), and the improved OE (IOE)) to describe the full phase space (ω, t) of the medium-induced gluon emission spectrum. The emitted energy ω is limited by the energy of the emitter $\omega \ll E$, and the propagation time (length) t is in turn limited by the medium length $t < L$. Our effective formalism accounts for arbitrarily many scatterings that can be arbitrarily hard or soft. Finally, eq. (3.64) describes the emission spectrum up to arbitrary precision and recovers the full solution of eq. (3.1) that has only been achieved numerically before [48, 49, 51].

It is now time to explore what consequences the full induced spectrum instills on a parton propagating through the medium. In this section, we will present analytical solutions of the evolution equation of the medium-induced cascade. We present the inclusive gluon energy distribution for different medium lengths, and we will focus on gluons for transparency. The numerical solutions are presented in section 5. Vacuum emissions belong outside of the scope of the current work.

4.1 The necessity of multiple emissions

Multiple emissions have to be taken into account whenever the multiplicity of gluons is large. We define the multiplicity of gluons above the energy ω in terms of the spectrum $dI/d\omega$, as

$$N(\omega) = \int_{\omega}^{\infty} d\omega' \frac{dI}{d\omega'}. \quad (4.1)$$

The upper limit of the integral is taken to infinity because we will currently assume that the energy of the emitter E is much larger than the largest available medium energy scale. Also, for our current purposes, it suffices to consider the leading behavior of the spectrum in the various scattering regimes presented in figure 3.

At low opacity $L \ll \lambda$ and starting from $\omega < \omega_{\text{BH}}$, we find

$$N(\omega) \simeq \bar{\alpha} \frac{L}{\lambda} \ln^2 \frac{\bar{\omega}_c}{\omega} + \frac{\pi \bar{\alpha}}{2} \frac{L}{\lambda}, \quad (4.2)$$

where $\bar{\omega}_c = \frac{1}{2} \mu^2 L$ and we have only kept the leading terms. The maximal multiplicity in the hard regime, see the second term, is always small for perturbative splittings with $\bar{\alpha} \ll 1$. Furthermore, the multiplicity in the soft (Bethe-Heitler) regime, given by the first term, becomes large only at very small energies, i.e. $\omega < e^{\sqrt{1/(\bar{\alpha}L/\lambda)}} \bar{\omega}_c$. We can therefore safely neglect multiple emissions at low opacities.

For dense media, $L \gg \lambda$, we discuss the three pertinent cases. As usual, we will denote $\omega_c = \frac{1}{2}\hat{q}L^2$. Then, for $\omega \gg \omega_c$ (rare hard scattering regime), we find

$$N(\omega) \simeq \bar{\alpha} \frac{L \bar{\omega}_c}{\lambda \omega}, \tag{4.3}$$

where we again neglected subleading terms. Hence hard emissions, described by the OE expansion, can safely be considered to be rare.

Next, for $\omega_{\text{BH}} \ll \omega \ll \omega_c$ we get

$$N(\omega) \simeq 2^{\frac{3}{2}} \bar{\alpha} \sqrt{\frac{\omega_c}{\omega}}, \tag{4.4}$$

where we introduced the leading behavior of the spectrum and neglected the multiplicity from hard emissions, following the discussion above. The multiplicity becomes large $N(\omega) \gg 1$ at energies $\omega \ll \bar{\alpha}^2 \omega_c$ and thus multiple emission becomes dominant. For large enough medium length $L \gg \lambda$, there is a significant phase space allowing for multiple emission ($\bar{\alpha}_s^2 \omega_c(t) > \omega_{\text{BH}}$), resulting in the power enhancement.

Finally, for soft gluon energies $\omega < \omega_{\text{BH}} \ll \omega_c$, the multiplicity is

$$N(\omega) \simeq \bar{\alpha} \frac{L}{\lambda} \ln^2 \frac{\omega_{\text{BH}}}{\omega} + 2^{\frac{3}{2}} \bar{\alpha} \sqrt{\frac{\omega_c}{\omega_{\text{BH}}}}, \tag{4.5}$$

where, again, only the leading terms from each regime were kept. The second term in eq. (4.5) scales as $\sim (L/\lambda) \sqrt{\hat{q}/\hat{q}_0}$. Based on the discussion above, this term is already large and the multiplicity continues to grow only logarithmically for small ω , and therefore multiple emissions are going to happen.

4.2 Resummation of multiple emissions

Considering multiple emissions in a medium poses a tremendous theoretical challenge. The situation is quite analogous to the description of multiple gluon emissions in vacuum. Similar to QCD jets, the main challenge when considering medium effects lies in dealing with intricate interference effects between subsequent emissions, see e.g. refs. [70–72]. However, when considering multiple soft emissions, that occur quasi-instantaneously, these effects can safely be neglected [58, 59].¹⁴

In order to clarify the framework that we work in, let us briefly recall the main arguments for neglecting interference effects for a set of multiple induced emissions. For the time being, we stick to emissions in the HO region which dominate the multiplicity. The typical time it takes an emission to form, often referred to as a *formation time* (or in some works branching time), of a soft gluon is $t_f \sim \sqrt{\omega/\hat{q}}$. This time is much smaller than the extent of the medium $t_f \ll L$ as long as $\omega \ll \omega_c$.

Another relevant quantity is the time between two subsequent emissions. This is related to the no emission probability (or Sudakov factor). For a leading particle with energy E , the first emission is produced at time t_{f1} , with energy ω_1 . A second, strongly ordered

¹⁴We can also extend this logic for the semi-hard emissions which are included in our formalism, since they are rare occurrences and therefore the resummation has no effect, see section 4.3.

emission ($\omega_2 \ll \omega_1$) of the original parton forms much quicker $t_{f2} \ll t_{f1}$. The time between the two emissions t_{split} can be estimated with $\int_{t_{f1}}^{t_{\text{split}}} dt \int_{\omega_2}^{\omega_1} d\omega \frac{dI}{d\omega dt} \sim 1$, that is basically the probability of not having emissions between $\omega_2 < \omega < \omega_1$, resulting in

$$t_{\text{split}} \sim t_{f1} + \frac{1}{\bar{\alpha}} t_{f2}. \tag{4.6}$$

Hence, our rough estimate implies that typically $t_{\text{split}} \gg t_{f2}$ (for $\bar{\alpha} \ll 1$). Therefore, the formation of emissions is short compared to the time that separates emissions and thus emissions form independently. This motivates the resummation of multiple independent emissions in terms of a rate equation.

Similar analysis can be done for hard emissions $\omega \gg \omega_c$, for which t_{split} is very long due to the unlikelihood of hard scatterings, and therefore the emissions are formed independently.

For soft emissions $\omega \ll \omega_{\text{BH}}$, $t_{\text{split}} \sim t_{f1} + \frac{1}{\bar{\alpha}} \ln^{-2} \frac{\lambda}{t_{f2}}$ and thus emissions form independently. Close to the boundary in cases where $t_{\text{split}} \approx t_{f1} + t_{f2}$, a more complicated structure appears in terms of resummation, as emissions might overlap. In this case, interference effects between the two emissions have to be included. A similar thing happens in vacuum for wide angle soft emissions, which result in angular ordering and in non-global effects for which the resummation has been understood just recently [73]. We will use the rate equation to account for emissions with any ω . However, it will not necessarily account correctly for interference among them and further study is needed in the future.

One question still remains open, namely the choice of the time scale used in the rate equation. In case of two emissions, the second emission experiences a shorter medium, of the scale $\sim L - t_{f1} - t_{\text{split}}$. We know, however, that in the soft limit $\omega \ll \omega_c$, the formation time is $t_f \ll L$, and therefore, the length degradation should not matter for a large medium [58, 59]. For small media, or for emissions with comparable formation times, these corrections can become significant. It is an unresolved question how to incorporate these corrections into a rate equation see e.g. ref. [71].¹⁵ However, as argued above, the corrections to the rate coming from finite-size effects can be treated in a perturbative fashion. While these issues merit further studies, perhaps within a Monte Carlo approach, we consider them to go beyond our present scope and we assume that all emissions experience the same length L . This matches the approximation in most of the current energy-loss models.

In this section, we will focus on the single-inclusive energy distribution of partons carrying energy xE after traveling length t in the medium, where E is the initial energy. It is defined as

$$D(x, t) \equiv x \frac{dN}{dx}. \tag{4.7}$$

The formalism can easily be extended to account for parton flavors, see e.g. [75], but for now, we restrict our attention to a pure gluon cascade.

In section 3 we focused on emissions of soft gluons with energies $\omega \ll E$. Now we will consider generic splitting processes where a parton with flavor index $a = q, g$ and initial energy E shares its energy with two daughter partons, with energies zE and $(1 - z)E$ and flavor indices b and c , respectively, for $0 < z < 1$. The spectrum of such splittings dI_{ba}/dz

¹⁵See also section 4 in ref. [74], where modifications of the rate due to finite formation time were studied.

is given by eq. (C.1). The general features of figure 3 remain the same with the substitution $\omega \rightarrow z(1-z)E$.¹⁶ For further details, see the discussion in appendix C.

As was shown in refs. [43, 59], for sufficiently soft emissions, with formation times much smaller than the medium length, interference effects are suppressed and one can consider multiple emissions as occurring independently. The evolution equation for the energy distribution, that accounts for an arbitrary number of induced emissions, is given by

$$\frac{\partial}{\partial t} D(x, t) = \int_x^1 dz \mathcal{K}\left(z, \frac{x}{z}E, t\right) D\left(\frac{x}{z}, t\right) - \int_0^1 dz z \mathcal{K}(z, xE, t) D(x, t). \quad (4.8)$$

The initial condition is a single gluon carrying energy E , hence $D(x, 0) = \delta(1-x)$. The splitting kernel $\mathcal{K}(z, E, t)$ is the rate of emissions off a particle with energy E ,

$$\mathcal{K}(z, E, t) = 2 \left. \frac{dI_{gg}}{dz dt} \right|_E, \quad (4.9)$$

and the rate with full z -dependence for the $g \rightarrow gg$ splitting can be found in eq. (C.1).¹⁷ The first term in eq. (4.8) is a real emission describing an emitted gluon with energy fraction x (gain term), while the second is a virtual emission that does not change the energy of the emitter (loss term). Both terms contribute to cancelling out the apparent divergence at $z \rightarrow 1$. The evolution equation conserves the total energy contained in the spectrum,

$$\int_0^1 dx D(x, t) = 1, \quad (4.10)$$

which can be confirmed directly from (4.8).

The leading parametric behavior of the splitting kernels can be derived by taking appropriate limits and is presented in section 3, cf. eqs. (3.16), (3.34), and (3.58). This results in,

$$\mathcal{K}(z, E, t)|_{t \ll \lambda} = \begin{cases} \frac{2\tilde{\alpha}}{z(1-z)} \frac{1}{\lambda} \ln\left(\frac{\bar{\omega}_c(t)}{z(1-z)E}\right) & \text{for } z(1-z)E \ll \bar{\omega}_c(t), \\ \frac{\tilde{\alpha}\pi}{2} \frac{\hat{q}_0 t}{[z(1-z)]^2 E} & \text{for } \bar{\omega}_c(t) \ll z(1-z)E, \end{cases} \quad (4.11)$$

for $t \ll \lambda$, and

$$\mathcal{K}(z, E, t)|_{t \gg \lambda} = \begin{cases} \frac{2\tilde{\alpha}}{z(1-z)} \frac{1}{\lambda} \ln\left(\frac{\omega_{\text{BH}}}{z(1-z)E}\right) & \text{for } z(1-z)E \ll \omega_{\text{BH}}, \\ \tilde{\alpha} \sqrt{\frac{\hat{q}}{[z(1-z)]^3 E}} & \text{for } \omega_{\text{BH}} \ll z(1-z)E \ll \omega_c(t), \\ \frac{\tilde{\alpha}\pi}{2} \frac{\hat{q}_0 t}{[z(1-z)]^2 E} & \text{for } \omega_c(t) \ll z(1-z)E, \end{cases} \quad (4.12)$$

for $t \gg \lambda$, where $\bar{\omega}_c(t) = \frac{1}{2}\mu^2 t$ and $\omega_c = \frac{1}{2}\hat{q}t^2$. For the analytical estimates in this section we neglect the running of \hat{q} , but this will be included in the numerics presented in section 5.

¹⁶Hence the upper limit of ω in figure 3 should now be $E/4$.

¹⁷In the soft limit, the kernel is closely related to the spectrum discussed in the previous section or, more precisely, the rate $dI/(d\omega dt)$, calculated in appendix B. Importantly, for the gluon splitting kernel, the divergences in $z \rightarrow 0$ and $z \rightarrow 1$ are folded together in the limit $\omega \rightarrow 0$, hence the additional symmetry factor in eq. (4.9).

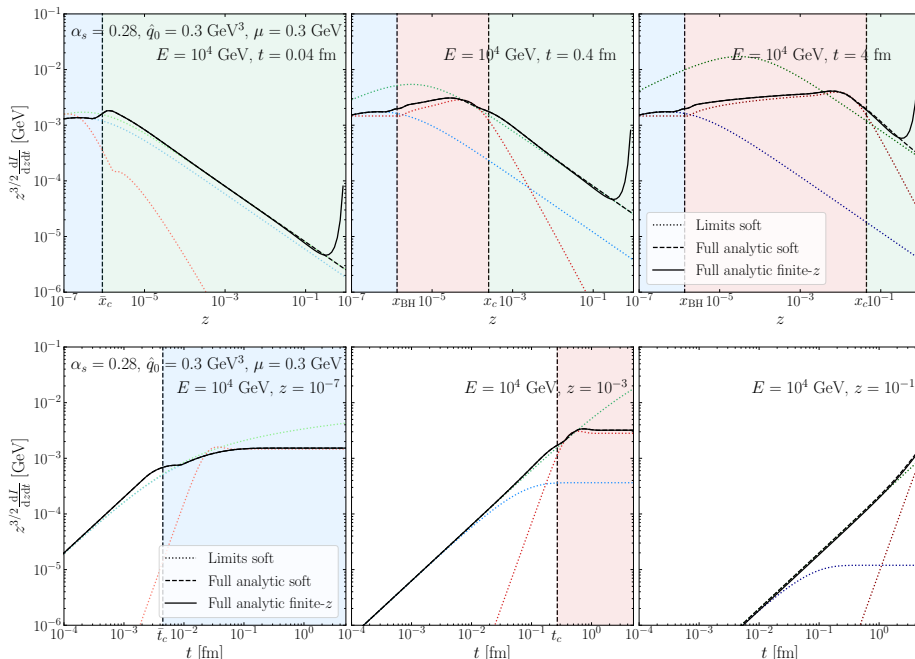


Figure 8. The medium-induced rate from eqs. (4.9), and (3.64) for gluons for different emitted energy and propagation time (black dashed lines). The black solid lines include finite- z corrections. The dotted lines are the $N_r = 1$, HO and $N = 1$ lines according to figure 7. The color shading corresponds to figure 3*i.e.* denoting the dominant scattering processes. The parameters correspond to $\lambda = 0.06$ fm.

The rate $dI/(dzdt)$ is plotted in figure 8, in a similar manner to the spectrum in figure 7, and rescaled by a factor $z^{3/2}$ to highlight the behavior at small z . The panels in the upper part show the z -dependence for three different t (early, mid-, and late times), and has a very similar structure to that of the spectrum. The color shading corresponds to figure 3, *i.e.* the dominant scattering processes. The dotted lines are the $N_r = 1$, HO and $N = 1$ lines from section 3 as in figure 7, where $\omega \rightarrow zE$ was used. Similarly, the dashed line is the full solution in the soft limit with $\omega \rightarrow zE$. The solid black lines are from eq. (5.3) and they contain finite- z corrections from appendix C. The finite- z corrections change the rate for hard emissions around $z \sim 1$. The panels in the lower part show the time dependence of the rate for a fixed emitted energy.

4.3 Analytic solutions of the evolution equation

The evolution equation (4.8) is readily solved by numerical evaluation, which will be discussed in section 5. Here we will discuss limiting cases where analytical solutions can be found. We can find such solutions at early times (considering only one emission) and at late times (considering many soft emissions). These are by now well-known limiting

cases. Finally, we also consider the novel case of the evolution equation at intermediate times, where both rare, hard emissions and multiple, soft emissions can occur in sequence according to their respective allowed phase space of emissions, given in figure 3.

To simplify our discussion, in this section we will neglect the Bethe-Heitler regime. We will nevertheless include it in the full numerical solutions presented in section 5.

Early time evolution. At an early stage of medium propagation, the leading parton has little time to interact with the medium which also translates into a small probability of splitting. Given our previous discussion, the natural medium scale to compare with is the mean free path λ . Hence, at $t \lesssim \lambda$ we consider a single splitting, leading to

$$\begin{aligned}
 D(x, t) &\simeq \delta(1-x) \left[1 - \int_0^t ds \int_0^1 dz z \mathcal{K}(z, xE, s) \right] + \int_0^t ds \int_x^1 dz \mathcal{K}\left(z, \frac{x}{z}E, s\right) \delta\left(1 - \frac{x}{z}\right) \\
 &= \int_0^t ds x \mathcal{K}(x, E, s),
 \end{aligned}
 \tag{4.13}$$

where we dropped the term proportional to $\delta(1-x)$, which is only important for energy conservation, cf. eq. (4.10). Using the results in eq. (4.11), we find that

$$D(x, t) \simeq \begin{cases} 2\bar{\alpha} \frac{t}{\lambda} \frac{1}{1-x} \ln\left(\frac{\bar{\omega}_c(t)}{x(1-x)E}\right) & \text{for } x \ll \bar{x}_c, \\ \frac{\pi\bar{\alpha}}{4} \frac{\hat{q}_0}{E} \frac{t^2}{x(1-x)^2} & \text{for } \bar{x}_c \ll x \ll 1 - \bar{x}_c, \end{cases}
 \tag{4.14}$$

where we have defined $\bar{x}_c = \bar{\omega}_c(t)/E$. For $x \ll \bar{x}_c$, corresponding to the single soft or Bethe-Heitler scattering regime, a characteristic $D \sim \ln 1/x$ structure appears that is similar to the DGLAP energy distribution in vacuum. On the contrary, for $x \gg \bar{x}_c$, corresponding to the single hard scattering regime, $D \sim 1/x$, and the two regimes are separated by \bar{x}_c . The limiting case of eq. (4.14) is shown in figure 9 with dashed lines for different times (different panels). Since we, as we move onward, will largely neglect the description of the infrared regime, we only used the single hard scattering (green) contribution that is valid $x > \bar{x}_c$.

Formally, the early-time expansion breaks down when $t > \lambda$ which is also the characteristic time when multiple interactions with the medium become important. Finally, we do not expect the early time solution to hold for $x < \bar{\alpha}^2 \omega_c/E$ where multiple emissions play an important role.

Late time evolution. The evolution equation can be solved exactly if one assumes coherent scatterings dominate for all momentum fractions x and all times t . This approximation is most sound when $t \gg L_c$, as seen in figure 3. The analytical solution neglects the Bethe-Heitler, which will make the solution less reliable for very small $x < \omega_{\text{BH}}/E$. We will call this solution D_0 as it serves as a baseline for subsequent calculations. It is the solution to the evolution equation

$$\frac{\partial}{\partial t} D_0(x, t) = \int_x^1 dz \mathcal{K}_{\text{coh}}\left(z, \frac{x}{z}E, t\right) D_0\left(\frac{x}{z}, t\right) - \int_0^1 dz z \mathcal{K}_{\text{coh}}(z, xE, t) D_0(x, t)
 \tag{4.15}$$

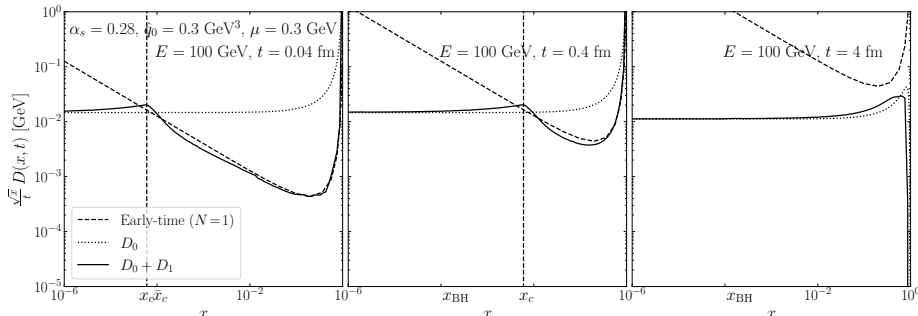


Figure 9. Analytic solutions of the energy distribution in different approximations (eqs. (4.13), (4.16) and (4.26)). With these parameters $\lambda = 0.06$ fm, and thus the different panels are $t < \lambda$, $\lambda < t < L_c$, and $t \lesssim L_c$.

where \mathcal{K}_{coh} is the soft limit of the harmonic oscillator regime, see the middle term in eq. (4.12). The solution from ref. [76] is

$$D_0(x, \tau) = \frac{\tau}{\sqrt{x(1-x)^{3/2}} e^{-\pi \frac{\tau^2}{1-x}}}, \quad (4.16)$$

where we dropped the $\delta(x)$ zero mode term, which is only important for energy conservation. We have also defined the re-scaled evolution variable which absorbs the energy scale,

$$\tau = \bar{\alpha} \sqrt{\frac{\hat{q}_0}{E}} t. \quad (4.17)$$

The solution has the $D_0 \sim \tau/\sqrt{x}$ shape characteristic of the turbulent cascade. Equation (4.16) is shown in figure 9 with dotted lines for different times.

Intermediate time evolution. To reach an approximate solution for intermediate times it is useful to cast the evolution in different variables. Following ref. [77], and defining $\xi = x/z$ in the gain term and $\xi = xz$ in the loss term the evolution can be rewritten as

$$\frac{\partial}{\partial \tau} D(x, \tau) = \int_x^1 d\xi P(x, \xi, \tau) D(\xi, \tau) - D(x, \tau) \int_0^x d\xi P(\xi, x, \tau), \quad (4.18)$$

where $P(x, \xi, \tau) = \frac{1}{\bar{\alpha}} \sqrt{\frac{E}{\hat{q}_0}} \frac{x}{\xi^2} \mathcal{K}(\frac{x}{\xi}, \xi E, t)$ and τ is defined in (4.17). This form of the evolution equation clearly shows the cancellation of divergences between the gain and loss terms at $\xi \rightarrow x$.

At early times, $t < \lambda$, the emissions are governed by single interactions with the medium. In the regime $\lambda < t < L_c$ you also have to take into account that coherent emissions play a role in the soft regime $\omega < \omega_c(t)$ (neglecting Bethe-Heitler emissions). However, the region above $\omega_c(t)$ will contain emissions from single hard scatterings, see eq. (4.12) (third line). In that case the kernel will be modified to include both a soft and a hard component, divided by the $\omega_c(t)$ separation line, as follows

$$P(x, \xi, \tau) = \theta_c(x, \xi, \tau) P_{\text{coh}}(x, \xi, \tau) + \theta_h(x, \xi, \tau) P_{\text{hard}}(x, \xi, \tau), \quad (4.19)$$

where the coherent and hard emission kernels were defined in eq. (4.12). After changing variables they become

$$\begin{aligned}
 P_{\text{coh}}(x, \xi, \tau) &= \sqrt{\frac{\xi}{x}} \frac{1}{(\xi - x)^{3/2}} && \text{for } x \ll x_c \quad \text{or} \quad \xi - x_c \ll x, \\
 P_{\text{hard}}(x, \xi, \tau) &= \frac{\pi}{2\bar{\alpha}} \frac{\xi}{x} \frac{1}{(\xi - x)^2} \tau && \text{for } x_c \ll x \ll \xi - x_c,
 \end{aligned}
 \tag{4.20}$$

where $x_c \equiv \omega_c(t)/E = \tau^2/(2\bar{\alpha}^2)$ and we have assumed that $x_c \ll 1$ in the limits. These conditions can be encoded in a set of Heaviside theta-functions to make sure that each kernel is used solely in its regime of validity, namely¹⁸

$$\begin{aligned}
 \theta_c(x, \xi, \tau) &= \Theta(x_c - x) + \Theta(x_c + x - \xi) - \Theta(x_c - x)\Theta(x_c + x - \xi), \\
 \theta_h(x, \xi, \tau) &= \Theta(x - x_c)\Theta(\xi - x_c - x).
 \end{aligned}
 \tag{4.21}$$

The now τ -dependent separation line $x_c(\tau)$ distinguishes the different regimes.

The full solution can be written as

$$D(x, \tau) = D_0(x, \tau) + \delta D(x, \tau),
 \tag{4.22}$$

where $D_0(x, \tau)$ is a solution to the coherent, soft kernel defined in eq. (4.16), and $\delta D(x, \tau)$ is a correcting factor.

Inserting this into the evolution equation (4.18), we get

$$\begin{aligned}
 \frac{\partial}{\partial \tau} D(x, \tau) &= \int_x^1 d\xi P(x, \xi, \tau) D_0(\xi, \tau) - D_0(x, \tau) \int_0^x d\xi P(\xi, x, \tau) \\
 &\quad + \int_x^1 d\xi P(x, \xi, \tau) \delta D(\xi, \tau) - \delta D(x, \tau) \int_0^x d\xi P(\xi, x, \tau).
 \end{aligned}
 \tag{4.23}$$

Taking into account that $\theta_c + \theta_h = 1$, one can rewrite the kernel as

$$P(x, \xi, \tau) = P_{\text{coh}}(x, \xi, \tau) + \delta P(x, \xi, \tau),
 \tag{4.24}$$

where $\delta P \equiv (P_{\text{hard}} - P_{\text{coh}})\theta_h$. Inserting the new kernel into eq. (4.23), the term $\partial D_0/\partial \tau$ cancels, and we are left with an iterative formula for δD ,

$$\begin{aligned}
 \delta D(x, \tau) &= D_1(x, \tau) \\
 &\quad + \int_0^\tau d\sigma \int_x^1 d\xi P(x, \xi, \sigma) \delta D(\xi, \sigma) - \int_0^\tau d\sigma \delta D(x, \sigma) \int_0^x d\xi P(\xi, x, \sigma).
 \end{aligned}
 \tag{4.25}$$

Here we have defined the leading term in the correction as

$$D_1(x, \tau) = \int_0^\tau d\sigma \int_x^1 d\xi \delta P(x, \xi, \sigma) D_0(\xi, \sigma) - \int_0^\tau d\sigma D_0(x, \sigma) \int_0^x d\xi \delta P(\xi, x, \sigma),
 \tag{4.26}$$

¹⁸In the case where x_c is not small the conditions are slightly more complicated, and the hard regime is encoded in $\theta_h(x, \xi, \tau) = \Theta\left(x - \frac{\xi}{2} \left(1 - \sqrt{1 - \frac{4x_c}{\xi}}\right)\right) \Theta\left(\frac{\xi}{2} \left(1 + \sqrt{1 - \frac{4x_c}{\xi}}\right) - x\right)$, and $\theta_c = 1 - \theta_h$.

which is given entirely in terms of known functions. To capture the main modifications with respect to the purely coherent solution $D_0(x, \tau)$, it is sufficient to keep only $D_1(x, \tau)$. This is sound because $D_0(x, t = 0) = \delta(1 - x)$, implying that $\delta D(x, t = 0) = 0$. Therefore, all terms going as $\sim \delta D$ start out small. At later times, single hard emissions are rare, and thus δD becomes less and less important.

Based on this discussion it is reasonable to assume that one can approximate the intermediate time solution by the sum of the two leading terms $D_0 + D_1$. For this to be true it must be checked that it reproduces the correct behavior at early and late times. The early times expansion is

$$\begin{aligned} \lim_{\tau \rightarrow 0} (D_0(x, \tau) + D_1(x, \tau)) &\simeq \int_0^\tau d\sigma \int_x^1 d\xi P_{\text{coh}}(x, \xi, \sigma) \delta(1 - \xi) \\ &\quad + \int_0^\tau d\sigma \int_x^1 d\xi [P_{\text{hard}}(x, \xi, \tau) - P_{\text{coh}}(x, \xi, \tau)] \delta(1 - \xi) \\ &= \frac{\pi}{4\bar{\alpha}} \frac{\tau^2}{x(1-x)^2}, \end{aligned} \tag{4.27}$$

where we kept the leading term and ignored virtual terms containing $\delta(1 - x)$. Therefore, the sum $D_0 + D_1$ reproduces the hard part of the early time expansion given in eq. (4.14). Moreover, at late times ($t > L_c$), the phase space for hard ($\omega > \omega_c$) emissions vanishes, and thus $D_1 \rightarrow 0$. Hence, at late times the intermediate time solution simply goes to the late time solution D_0 . Consequently, we expect that the sum of the two first terms $D_0 + D_1$ to provide a decent approximation of the true solution at all times. One can systematically calculate corrections to this solution by iterating eq. (4.25).

The the early time solution eq. (4.13) (dashed), the soft limit of the HO approximation (4.16) (dotted), and the first correction $D_0 + D_1$ are shown in figure 9 with full lines for different times. For short lengths (left panel), $D_0 + D_1$ closely resembles the early time solution, as expected. For late times $D_0 + D_1$ reduces to D_0 , as there is not any phase space for hard emissions left. The D_0 presents the small x tail $D_0 \sim \sqrt{x}$ characteristic for turbulence [76]. At intermediate times we see that $D_0 + D_1$ goes to D_0 at low x , while at high x there is a suppression due to the lack of coherent scatterings at early times. Qualitatively, figure 9 resembles the full numerical solution shown in figure 10. In order to compare the two figures, we have marked the value of $x_{\text{BH}} \equiv \omega_{\text{BH}}/E$ in figure 9. We have also not included the color coding in this figure since it does not include the physics from all the relevant regimes represented in figure 3.

5 Numerical evaluation of the medium cascade

In section 3 we presented an effective framework that describes medium-induced emissions up to arbitrary precision. By using this framework we showed in section 4 how different scattering processes contribute to multiple induced emissions. Based on the properties of the medium (e.g. length, mean free path), not all induced emissions are necessary to resum (or to consider many of them). For example, induced emissions from hard scatterings are not as important to resum as emissions from multiple soft scatterings. We developed a simple analytic model to include a single hard emission correction to the resummation of

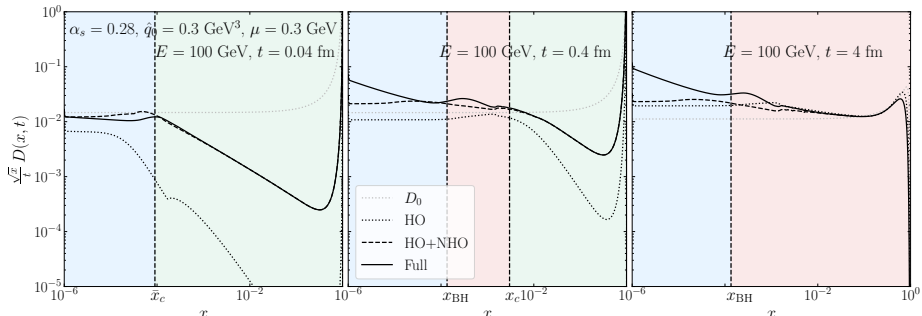


Figure 10. The energy distribution solution of the medium-induced emission evolution eq. (4.8) at different times (different panels) and using different scattering mechanisms to calculate the emission rate in eq. (4.9) (different line styles). The vertical dashed lines and the shaded areas separate different scattering regions, where on the first panel $t < \lambda$ and on the last panel $t > L_c$.

the multiple soft ones. In section 4, we made several simplifications e.g. we simplified the emission kernel \mathcal{K} , and neglected Bethe-Heitler emissions. It is important to understand how the energy distribution behaves also without using these simplifications and to understand the error introduced by employing them. That is the subject of this section.

In this section, we evaluate eq. (4.8) numerically using the kernel in our new framework. For more details about the numerical implementation, see appendix D and the complementary code [78]. The resulting energy distribution is presented in figure 10, where the different lines stem from using emission kernels $\mathcal{K}(z, E, t)$ at varying levels of approximation. The three panels correspond to three different time stages in the evolution: $t < \lambda$, $\lambda < t < L_c$, and $t > L_c$. As a reminder, there are no rare hard splittings for $t > L_c$, which is evident on the rightmost panel of figure 10.

The evolution starts at $t = 0$, with a single gluon of energy distribution $D(x, 0) = \delta(1-x)$ with $E = 100$ GeV energy. We solely use gluons during the evolution for simplicity, however our formalism is valid for other flavors too. The kernels we use include finite- z corrections, see appendix C.3 for more details. The vertical dashed lines in figure 10 separate the regions where different scattering processes dominate, which are the same regions as in figure 3. The phase space for emissions is determined by comparing $z(1-z)E$ with $\bar{\omega}_c(t)$, ω_{BH} , and $\omega_c(t)$ in the relevant regions, as it is described in appendix C. The turbulent cascade solution $D_0(x, t)$ from eq. (4.16) is also shown as a baseline, and was discussed in more detail in section 4.3.

It is important to note that vacuum emissions are not included in the current study, and thus many important effects (e.g. vacuum fragmentation, medium resolution, color coherence), which are essential if one wishes to compare to measurements, will not be discussed in this work. We refer the interested readers to refs. [29, 44, 45, 61, 74] for further details.

Harmonic oscillator. A simple and much studied method of solving the evolution equation eq. (4.8) is by using the harmonic oscillator (HO) approximation of the emission

rate (see for example in refs. [20, 23, 29, 76, 77, 79–81]). The kernel is then simply given by

$$\mathcal{K}(z, E, t) \approx 2 \left. \frac{d^2 I^{\text{HO}}}{dz dt} \right|_E, \quad (5.1)$$

where the HO approximation was discussed in section 3.4 and in the numerics we used eq. (C.27). In this approximation, the induced emissions originate from multiple soft elastic scatterings with the medium, and we expect this process to dominate for $t \gg \lambda$ and $x_{\text{BH}} \ll x \ll x_c(t)$ (red region in figure 3).

The energy distribution obtained by using the HO approximation is shown in figure 10 with black dotted lines. The HO spectrum exhibits the well know turbulent cascade behavior [76, 77], resulting in a characteristic tail $D(x \ll 1, t) \sim t/\sqrt{x}$, which can be seen on the plot as horizontal lines at small x . This is also a feature of the simplified analytic solution D_0 . The turbulent cascade involves a constant flux of energy propagating in time to $x \rightarrow 0$. The turbulence appears below $x < x_c(t)$, and the energy increases with time due to the time dependent emission phase space (see also $\omega_c(t)$ in figure 3).

Above $x > x_c(t)$ the HO kernel switches from $\mathcal{K} \sim 1/z^{3/2}$ to $1/z^3$ and thus the energy distribution starts going as $D(x, t) \sim 1/x^2$. This is especially visible in the middle panel of figure 10.

It is interesting to note that due to the running of \hat{q} (see eq. (3.43)), deviations from the pure $D \sim 1/\sqrt{x}$ are expected in the HO solution. A consequence of this can be seen as a small kink on the dotted curves (most visible in the left panel at $x \approx 10^{-4}$). Below the kink, $\hat{q}(\omega) \rightarrow \hat{q}_0$ is used.

Improved opacity expansion. The IOE from section 3.4 makes it possible to extend the HO description to include rare hard scatterings, covering both red and green regions in figure 3. Here, the evolution equation is solved using the IOE kernel, which is

$$\mathcal{K}(z, E, t) \approx 2 \left. \frac{d^2 I^{\text{IOE}}}{dz dt} \right|_E. \quad (5.2)$$

This is valid from early to late times, for energies above the Bethe-Heitler regime $x \gg x_{\text{BH}}$.

The energy distribution obtained using the IOE (HO+NHO is used in the numerical implementation from eqs. (C.27)–(C.34)) is shown in figure 10 with black dashed lines. In the $x \ll x_c(t)$ region the HO dominates and $D(x, t)$ qualitatively does not change by including hard emissions. The turbulent tail $D \sim 1/\sqrt{x}$ is still present. The offset between the HO and HO+NHO results originates from the effective contribution of the NHO term to $\hat{q} \approx \hat{q}_0 \ln \frac{Q_x^2}{\mu_*^2} (1 + 1.016 \ln^{-1} \frac{Q_x^2}{\mu_*^2})$.

In the region $x > x_c(t)$, the distribution function changes from the purely HO result, due to the inclusion of the NHO corrections. The splitting function here behaves as $\mathcal{K} \sim 1/z^2$, resulting in the distribution going as $D(x) \sim 1/x$, which is visible in the green region. Our analytic result from section 4.3, given by $D_0 + D_1$, includes a single hard emission in addition to the HO cascade. Comparing the analytic results in figure 9 with the numerical ones in figure 10 it is evident that the analytical result succeeds in capturing qualitatively the behavior induced by using the IOE kernel.

Several models are based mainly on the $N = 1$ term, see refs. [82–84], and also refs. [85, 86]. However, these models miss the soft scatterings that are present in a large medium with $L > \lambda$. Soft scatterings are crucial to include to achieve an accurate description of the energy distribution for $x < x_c(t)$. We would like to also emphasize that by numerically solving eq. (4.8), we also resum hard emissions and thus we consider the possibility of emitting arbitrarily many of them.

Full solution. Finally, we present the energy distribution using our new picture. It is given by solving the evolution equation (4.8) using the full kernel

$$\mathcal{K}(z, E, t) = 2 \frac{d^2 I^{\text{Full}}}{dz dt} = 2 \begin{cases} \frac{d^2 I^{\text{ROE}}}{dz dt}, & \text{if } z(1-z)E < \min(\bar{\omega}_c(t), \omega_{\text{BH}}), \\ \frac{d^2 I^{\text{IOE}}}{dz dt}, & \text{otherwise.} \end{cases} \quad (5.3)$$

This covers the full emission phase space in (z, t, E) and was derived in detail in section 3. In practice we used $N_r = 1$ and HO+NHO terms, derived from eqs. (3.31), (3.34), (3.58) and (3.61). This provides an excellent approximation to the true result, as can be seen when comparing to the numerical evaluation of the kernel in figure 7.

The resulting energy distribution is shown as full black lines in figure 10. One can see that the results obtained by solely using the IOE (dashed lines) agrees very well with the full kernel for $x \gg x_{\text{BH}}$, but they start to differ when $x \lesssim x_{\text{BH}}$. It is clear that all the difference between these two curves comes from Bethe-Heitler emissions. An increasing tail appears at low x , which becomes more and more important for later times, due to the logarithmic soft limit of the ROE kernel. In this region the ROE kernel is $\mathcal{K} \sim \ln(z)/z$, resulting in the energy distribution going as $D \sim \ln \frac{1}{x}$, which is similar to the DGLAP evolution in vacuum.

A new, interesting bump also appears in the full solution close to x_{BH} , which warrants an explanation. First, the energy flux that brings quanta from $x = 1$ to $x = 0$ is not the same on the two sides of x_{BH} . If the energy transport is more efficient from the right (red region), that will result in a slowing of the flux when going from higher to lower x . The bump can then be understood as a sediment of energy building up around x_{BH} . Secondly, the emission kernel defined in eq. (5.3) is not smooth around the transition point $\min(\bar{\omega}_c(t), \omega_{\text{BH}})$. This discontinuity introduces additional uncertainties in the true behavior of the energy distribution around x_{BH} . This transition would smoothen by including more orders of the expansion, which should be studied in the future. This uncertainty could also be connected with the observed bump. In our numerical implementation we introduced a smoothing function to minimize this uncertainty, but it is still present. In addition, other effects like $2 \rightarrow 2$ scattering process and thermal masses are also important here [52], which we do not presently discuss. A thorough study of this region is needed where all these effects are included, which motivates future work.

Bethe-Heitler emissions have a soft divergence and thus an IR regulator ω_{min} has to be introduced. A similar regulator was introduced in the numerical differential equation solver. For more details, see appendix D.

6 Conclusions and outlook

In this paper, we studied emissions induced by elastic scatterings on the quark gluon plasma. We considered the interplay of the relevant length scales of the problem, which are the propagation length, the mean free path between scatterings, and the formation time. From these considerations, we derived the emergent energy scales that separate the induced emission spectrum into regimes governed by different scattering processes. The emerging hierarchy of scales and related processes is illustrated in figure 3.

We presented a new theoretical framework consisting of different perturbative expansions, namely the opacity expansion (OE), the improved OE (IOE), and the resummed OE (ROE), which we derived rigorously. Together these are suitable to describe the induced emission spectrum in different regimes. We showed that at least one of the expansions is valid in every phase space (ω, t) point, where ω is the energy of the emitted gluon and t is the propagation time (length) in the medium.¹⁹ While these expansions are formally simply reorganizations of the multiple scattering series, it is also important to note that none of the expansions *when truncated at any fixed order* is valid everywhere. Relying on the multiple approaches to obtain the spectrum, our composite framework can account for an arbitrary number of medium interactions that can be soft or hard. Most importantly, it is systematically improvable and can, in principle, describe the emission spectrum (and rate) up to arbitrary precision, which has only been achieved numerically before [48, 49, 51].

In the current work, we have elucidated the convergence properties up to second order in the studied resummations. Identifying the expansion structure in the different regimes opens for the possibility of studying the accuracy of resummations in the medium. Finally, our new description provides a quick and efficient way to evaluate the induced emission spectrum (and rate), which is an essential ingredient of medium-induced cascades and jet quenching study. Our implementation is available in an online repository [78].

In order to tackle multiple emissions, we also studied the in-medium energy distribution $D(x, t)$ within our new formalism. This is an essential ingredient of jet quenching phenomenology as it describes how the energy of a leading particle gets distributed within a cascade. Having first identified the conditions to generate multiple emissions in the medium, we demonstrated the separation between early, rare emissions — generated mainly by a single momentum exchange with the medium — and a following cascade of soft splittings. We also showed that emissions are formed independently up to suppressed terms, justifying a posteriori the formulation of the cascade via a rate equation. We developed new analytic tools to combine the resummation of multiple soft with rare hard emissions, and thus we showed how different scattering processes appear on the level of the energy distribution. Finally, using numerical evaluation based on the previously derived full splitting kernels, we showed more rigorously the transition effects between different scattering regions. We identified the importance of the time dependent phase space separation, multiple Bethe-Heitler emissions, and the running of \hat{q} , to mention some.

Even though this work can immediately be applied to jet quenching phenomenology one should also tackle other challenges, such as vacuum emissions and coherence effects, which

¹⁹For the general case valid beyond the strictly soft limit ω refers to the reduced energy of the three-body evolution $\omega = z(1-z)E$, where E is the initial energy of the emitter and z is the momentum sharing fraction.

we have neglected here and left for future studies. We also acknowledge the importance of soft emissions for which one should study thermal masses, energy changing $2 \rightarrow 2$ scatterings, and thermalization [52, 87] to correctly describe the very infrared regime close to the thermal scale and below. Moreover, other non-perturbative effects such as expanding, inhomogeneous medium are also important, in which direction our framework is extendable [23, 28, 88, 89].

Acknowledgments

We thank Paul Caucal, Alexandre Falcão, Aleksas Mazeliauskas, and Sören Schlichting for helpful discussions. We also thank Carlota Andres, Liliana Apolinário, Fabio Dominguez, and Marcos Gonzalez Martinez for providing us with the numerical results for the spectrum computed in ref. [51]. The work is supported by a Starting Grant from Trond Mohn Foundation (BFS2018REK01) and the University of Bergen.

A All order formulas for medium-induced spectrum in the soft limit

Here we present some general formulas for the different expansions, that aided us in calculating the spectrum in section 3. In all cases the full spectrum is given as the sum of all the terms $\omega \frac{dI}{d\omega} = \sum_n \omega \frac{dI^{N=n}}{d\omega}$. The expansion therefore only converges if the terms decrease sufficiently fast order by order $\omega \frac{dI^{N=n+1}}{d\omega} < \omega \frac{dI^{N=n}}{d\omega}$.

A.1 Opacity expansion

Combining the formulas for the opacity expansion eq. (3.6) and the spectrum eq. (3.12) one can write the formula for the n^{th} term of the opacity expansion as²⁰

$$\begin{aligned} \omega \frac{dI^{N=n}}{d\omega} &= (-1)^{n-1} \frac{4\alpha_s C_R}{\omega} \int_{\mathbf{p}_n, \dots, \mathbf{p}_1} \Sigma(\mathbf{p}_n^2) \frac{\mathbf{p}_n \cdot \mathbf{p}_1}{\mathbf{p}_n^2} v(\mathbf{p}_n - \mathbf{p}_{n-1}) \dots v(\mathbf{p}_2 - \mathbf{p}_1) \\ &\times \text{Re} i \int_0^L dt_n \int_0^{t_n} dt_0 \int_0^{t_n} dt_{n-1} \int_{t_0}^{t_{n-1}} dt_{n-2} \dots \int_{t_0}^{t_2} dt_1 e^{-i\frac{\mathbf{p}_n^2}{2\omega}(t_n - t_{n-1})} \dots e^{-i\frac{\mathbf{p}_1^2}{2\omega}(t_1 - t_0)}, \end{aligned} \quad (\text{A.1})$$

where $v(\mathbf{p}, s)$ is given in eq. (3.7) and $\Sigma(\mathbf{p}^2)$ in given in eq. (3.13) in the GW model. It is useful to go to unitless integration variables, by defining $\sqrt{L/2\omega} \mathbf{p}_k \rightarrow \mathbf{p}_k$ and $\frac{t_k}{L} \rightarrow t_k$,

$$\begin{aligned} \omega \frac{dI^{N=n}}{d\omega} &= (-1)^{n-1} 8\pi\bar{\alpha} \left(\frac{L}{\lambda}\right)^n \frac{\bar{\omega}_c}{\omega} \int_{\mathbf{p}_n, \dots, \mathbf{p}_1} \tilde{\Sigma}(\mathbf{p}_n^2) \frac{\mathbf{p}_n \cdot \mathbf{p}_1}{\mathbf{p}_n^2} \tilde{v}(\mathbf{p}_n - \mathbf{p}_{n-1}) \dots \tilde{v}(\mathbf{p}_2 - \mathbf{p}_1) \\ &\times \text{Re} i \int_0^1 dt_n \int_0^{t_n} dt_0 \int_0^{t_n} dt_{n-1} \int_{t_0}^{t_{n-1}} dt_{n-2} \dots \int_{t_0}^{t_2} dt_1 e^{-i\mathbf{p}_n^2(t_n - t_{n-1})} \dots e^{-i\mathbf{p}_1^2(t_1 - t_0)}. \end{aligned} \quad (\text{A.2})$$

Here we have used the unitless function $\tilde{v}(\mathbf{p}) = (2\pi)^2 \delta(\mathbf{p}) - \frac{\bar{\omega}_c}{\omega} \tilde{\sigma}(\mathbf{p})$, where in the GW model

$$\begin{aligned} \tilde{\sigma}(\mathbf{p}) &= \frac{4\pi}{(\mathbf{p}^2 + \frac{\bar{\omega}_c}{\omega})^2}, \\ \tilde{\Sigma}(\mathbf{p}^2) &= \frac{1}{\mathbf{p}^2 + \frac{\bar{\omega}_c}{\omega}}. \end{aligned} \quad (\text{A.3})$$

²⁰The gluon color factors appearing in v are not trivial at n^{th} order and thus we refer the reader to appendix C for further discussion.

The momentum and time integrals only depend on the unitless combination $\bar{\omega}_c/\omega$. This means that the spectrum will take the form $\omega \frac{dI^{N=n}}{d\omega} = \bar{\alpha} \left(\frac{L}{\lambda}\right)^n h_n\left(\frac{\omega}{\bar{\omega}_c}\right)$, for some function h_n . This would naively imply convergence for $L/\lambda < 1$, but the exact form of the function h_n must also be taken into account. In section 3.2 we showed for $N = 1, 2$ at low energy $\omega \ll \bar{\omega}_c$ that $h_n\left(\frac{\omega}{\bar{\omega}_c}\right)$ is a finite function, meaning the series converges when $L/\lambda < 1$. However, at high energy $\omega \gg \bar{\omega}_c$ the function takes the form $h_n\left(\frac{\omega}{\bar{\omega}_c}\right) \sim \left(\frac{\bar{\omega}_c}{\omega}\right)^n \tilde{h}_n\left(\frac{\bar{\omega}_c}{\omega}\right)$, where \tilde{h}_n is finite, implying convergence when $\frac{L}{\lambda} \frac{\bar{\omega}_c}{\omega} < 1$. Proving this is true to all orders is deferred to future work.

One can also derive a corresponding formula for the rate $\omega \frac{dI^{N=n}}{d\omega dL}$, by taking the length derivative of eq. (A.2)

$$\begin{aligned} & \omega \frac{dI^{N=n}}{d\omega dL} \\ &= (-1)^{n-1} 8\pi\bar{\alpha} \frac{1}{L} \left(\frac{L}{\lambda}\right)^n \frac{\bar{\omega}_c}{\omega} \int_{\mathbf{p}_n, \dots, \mathbf{p}_1} \tilde{\Sigma}(\mathbf{p}_n^2) \frac{\mathbf{p}_n \cdot \mathbf{p}_1}{\mathbf{p}_n^2} \tilde{v}(\mathbf{p}_n - \mathbf{p}_{n-1}) \dots \tilde{v}(\mathbf{p}_2 - \mathbf{p}_1) \\ & \quad \times \text{Re} i \int_0^1 dt_0 \int_{t_0}^1 dt_{n-1} \int_{t_0}^{t_{n-1}} dt_{n-2} \dots \int_{t_0}^{t_2} dt_1 e^{-i\mathbf{p}_n^2(1-t_{n-1})} e^{-i\mathbf{p}_{n-1}^2(t_{n-1}-t_{n-2})} \dots e^{-i\mathbf{p}_1^2(t_1-t_0)}. \end{aligned} \quad (\text{A.4})$$

A.2 Resummed opacity expansion

One can also derive all order formulas for the resummed opacity expansion, by starting with eq. (3.26) and following the same procedure,

$$\begin{aligned} & \omega \frac{dI^{N_r=n}}{d\omega} \\ &= \frac{4\alpha_s C_R}{\omega} \int_{\mathbf{p}_n, \dots, \mathbf{p}_1} \Sigma(\mathbf{p}_n^2) \frac{\mathbf{p}_n \cdot \mathbf{p}_1}{\mathbf{p}_n^2} \sigma(\mathbf{p}_n - \mathbf{p}_{n-1}) \dots \sigma(\mathbf{p}_2 - \mathbf{p}_1) \\ & \quad \times \text{Re} i \int_0^L dt_n \int_0^{t_n} dt_0 \int_{t_0}^{t_n} dt_{n-1} \int_{t_0}^{t_{n-1}} dt_{n-2} \dots \int_{t_0}^{t_2} dt_1 \Delta(t_n, t_0) e^{-i\frac{\mathbf{p}_n^2}{2\omega}(t_n-t_{n-1})} \dots e^{-i\frac{\mathbf{p}_1^2}{2\omega}(t_1-t_0)}. \end{aligned} \quad (\text{A.5})$$

The ROE and OE expansions are equivalent at infinite order at low opacity $L/\lambda \ll 1$, but at finite order the terms are mixed up. The terms containing a delta function in the potential v in the OE are included in the Sudakov factor Δ in the ROE. One can see this by taking $\Delta \rightarrow 1$ and $v \rightarrow -\sigma$ in eq. (A.5) and eq. (A.1) respectively, in which case the expansions become exactly the same. This is however not a good approximation at any order.

After changing to unitless variables we arrive at

$$\begin{aligned} & \omega \frac{dI^{N_r=n}}{d\omega} \\ &= 8\pi\bar{\alpha} \left(\frac{L}{\lambda}\right)^n \left(\frac{\bar{\omega}_c}{\omega}\right)^n \int_{\mathbf{p}_n, \dots, \mathbf{p}_1} \tilde{\Sigma}(\mathbf{p}_n^2) \frac{\mathbf{p}_n \cdot \mathbf{p}_1}{\mathbf{p}_n^2} \tilde{\sigma}(\mathbf{p}_n - \mathbf{p}_{n-1}) \dots \tilde{\sigma}(\mathbf{p}_2 - \mathbf{p}_1) \\ & \quad \times \text{Re} i \int_0^1 dt_n \int_0^{t_n} dt_0 \int_{t_0}^{t_n} dt_{n-1} \int_{t_0}^{t_{n-1}} dt_{n-2} \dots \int_{t_0}^{t_2} dt_1 e^{-\frac{\mathbf{p}_n^2}{\lambda}(t_n-t_0)} e^{-i\mathbf{p}_n^2(t_n-t_{n-1})} \dots e^{-i\mathbf{p}_1^2(t_1-t_0)}, \end{aligned} \quad (\text{A.6})$$

where we have used that in the static medium $\Delta(t_n, t_0) = \exp\left(-\frac{t_n-t_0}{\lambda}\right)$. Again we use the unitless functions $\tilde{\Sigma}(\mathbf{p}^2)$ and $\tilde{\sigma}(\mathbf{p})$ defined in eq. (A.3) for the GW model. In this case the

time integrals can be done analytically

$$\begin{aligned}
 & i \int_0^1 dt_n \int_0^{t_n} dt_0 \int_{t_0}^{t_n} dt_{n-1} \int_{t_0}^{t_{n-1}} dt_{n-2} \cdots \int_{t_0}^{t_2} dt_1 e^{-\frac{L}{\lambda}(t_n-t_0)} e^{-i\mathbf{p}_n^2(t_n-t_{n-1})} \dots e^{-i\mathbf{p}_1^2(t_1-t_0)} \\
 & = i^n \int_0^1 dt_n \int_0^{t_n} dt_0 \sum_{k=1}^n \frac{e^{-i(\mathbf{p}_k^2 - i\frac{L}{\lambda})(t_n-t_0)}}{\prod_{l \neq k} (\mathbf{p}_k^2 - \mathbf{p}_l^2)} = \left(\cos \frac{n\pi}{2} + i \sin \frac{n\pi}{2} \right) \sum_{k=1}^n \frac{T\left(\mathbf{p}_k^2 - i\frac{L}{\lambda}\right)}{\prod_{l \neq k} (\mathbf{p}_k^2 - \mathbf{p}_l^2)}, \tag{A.7}
 \end{aligned}$$

where we have defined the function

$$T(x) = \int_0^1 dt_n \int_0^{t_n} dt_0 e^{-ix(t_n-t_0)} = \frac{1-ix-e^{-x}}{x^2}. \tag{A.8}$$

The reason this simplification was not possible in the OE is that the formula for the time integrals is only valid if $\mathbf{p}_k \neq \mathbf{p}_l$, while the OE has terms containing $\delta(\mathbf{p}_k - \mathbf{p}_{k-1})$. However, in the ROE there are no such deltas, so the formula is valid. In the end the spectrum is

$$\begin{aligned}
 \omega \frac{dI^{N_r=n}}{d\omega} & = 8\pi\bar{\alpha} \left(\frac{L}{\lambda}\right)^n \left(\frac{\bar{\omega}_c}{\omega}\right)^n \int_{\mathbf{p}_n, \dots, \mathbf{p}_1} \tilde{\Sigma}(\mathbf{p}_n^2) \frac{\mathbf{p}_n \cdot \mathbf{p}_1}{\mathbf{p}_n^2} \tilde{\sigma}(\mathbf{p}_n - \mathbf{p}_{n-1}) \dots \tilde{\sigma}(\mathbf{p}_2 - \mathbf{p}_1) \\
 & \times \sum_{k=1}^n \frac{\cos \frac{n\pi}{2} \operatorname{Re} T(\mathbf{p}_k^2 - i\chi) - \sin \frac{n\pi}{2} \operatorname{Im} T(\mathbf{p}_k^2 - i\chi)}{\prod_{l \neq k} (\mathbf{p}_k^2 - \mathbf{p}_l^2)}. \tag{A.9}
 \end{aligned}$$

The remaining momentum integrals will in the end be some function of $\bar{\omega}_c/\omega$ and opacity $\chi = L/\lambda$. As a reference, the real and imaginary parts of $T(\mathbf{p}^2 - i\chi)$ are

$$\begin{aligned}
 \operatorname{Re} T(\mathbf{p}^2 - i\chi) & = \frac{\chi(\mathbf{p}^4 + \chi^2) + \mathbf{p}^4 - \chi^2 - e^{-\chi} ((\mathbf{p}^4 - \chi^2) \cos \mathbf{p}^2 + 2\chi \mathbf{p}^2 \sin \mathbf{p}^2)}{(\mathbf{p}^4 + \chi^2)^2} \\
 -\operatorname{Im} T(\mathbf{p}^2 - i\chi) & = \frac{\mathbf{p}^2(\mathbf{p}^4 + \chi^2) - 2\chi \mathbf{p}^2 - e^{-\chi} ((\mathbf{p}^4 - \chi^2) \sin \mathbf{p}^2 - 2\chi \mathbf{p}^2 \cos \mathbf{p}^2)}{(\mathbf{p}^4 + \chi^2)^2}. \tag{A.10}
 \end{aligned}$$

It is also possible to look at the limits of this function when the opacity χ is low or high. In the low opacity case $\chi \ll 1$ we have

$$\begin{aligned}
 \omega \frac{dI^{N_r=n}}{d\omega} & \simeq 8\pi\bar{\alpha} \left(\frac{L}{\lambda}\right)^n \left(\frac{\bar{\omega}_c}{\omega}\right)^n \int_{\mathbf{p}_n, \dots, \mathbf{p}_1} \tilde{\Sigma}(\mathbf{p}_n^2) \frac{\mathbf{p}_n \cdot \mathbf{p}_1}{\mathbf{p}_n^2} \tilde{\sigma}(\mathbf{p}_n - \mathbf{p}_{n-1}) \dots \tilde{\sigma}(\mathbf{p}_2 - \mathbf{p}_1) \\
 & \times \sum_{k=1}^n \frac{\cos \frac{n\pi}{2} (1 - \cos \mathbf{p}_k^2) + \sin \frac{n\pi}{2} (\mathbf{p}_k^2 - \sin \mathbf{p}_k^2)}{\mathbf{p}_k^4 \prod_{l \neq k} (\mathbf{p}_k^2 - \mathbf{p}_l^2)}. \tag{A.11}
 \end{aligned}$$

In this case the momentum integrals will give a function of $\bar{\omega}_c/\omega$. As mentioned in section 3.3 is it preferable to use the OE (A.2) at low opacity, as the order of opacity is mixed up in the ROE.

In the high opacity case $\chi \gg 1$ you get

$$\begin{aligned}
 \omega \frac{dI^{N_r=n}}{d\omega} & \simeq 8\pi\bar{\alpha} \frac{L}{\lambda} \left(\frac{\omega_{\text{BH}}}{\omega}\right)^n \int_{\mathbf{p}_n, \dots, \mathbf{p}_1} \tilde{\Sigma}(\mathbf{p}_n^2, \omega_{\text{BH}}) \frac{\mathbf{p}_n \cdot \mathbf{p}_1}{\mathbf{p}_n^2} \tilde{\sigma}(\mathbf{p}_n - \mathbf{p}_{n-1}, \omega_{\text{BH}}) \dots \tilde{\sigma}(\mathbf{p}_2 - \mathbf{p}_1, \omega_{\text{BH}}) \\
 & \times \sum_{k=1}^n \frac{\cos \frac{n\pi}{2} + \sin \frac{n\pi}{2} \mathbf{p}_k^2}{(1 + \mathbf{p}_k^4) \prod_{l \neq k} (\mathbf{p}_k^2 - \mathbf{p}_l^2)}. \tag{A.12}
 \end{aligned}$$

Here we see the emergence of the scale $\omega_{\text{BH}} = \frac{1}{2}\mu^2\lambda$, which takes the place of $\bar{\omega}_c$ in the functions $\tilde{\Sigma}$ and $\tilde{\sigma}$, as emphasized in the above formula. The momentum integrals then only become some function of $\omega_{\text{BH}}/\omega$. Notice that this scales as $\sim L/\lambda$ at every order, meaning it can converge also when $L/\lambda > 1$.

In section 3.4 we calculated the high opacity limit to orders $N = 1, 2$. There it was clear that for low $\omega \ll \omega_{\text{BH}}$ the $N = 2$ limit is subleading compared to the $N = 1$ limit, while at high $\omega \gg \omega_{\text{BH}}$ the $N = 2$ and $N = 1$ limits are of the same order. This seems to imply that the expansion converges at low ω , while it breaks down at high ω . Again, proving this for all orders is deferred to future work.

Again the calculation for the rate $\omega \frac{dI^{N_r=n}}{d\omega dL}$ is similar

$$\begin{aligned} & \omega \frac{dI^{N_r=n}}{d\omega dL} \\ &= 8\pi\bar{\alpha} \frac{1}{L} \left(\frac{L}{\lambda}\right)^n \left(\frac{\bar{\omega}_c}{\omega}\right)^n \int_{\mathbf{p}_n, \dots, \mathbf{p}_1} \tilde{\Sigma}(\mathbf{p}_n^2) \frac{\mathbf{p}_n \cdot \mathbf{p}_1}{\mathbf{p}_n^2} \tilde{\sigma}(\mathbf{p}_n - \mathbf{p}_{n-1}) \dots \tilde{\sigma}(\mathbf{p}_2 - \mathbf{p}_1) \\ & \times \sum_{k=1}^n \frac{\cos \frac{n\pi}{2} [\chi - e^{-\chi} (\chi \cos \mathbf{p}_k^2 - \mathbf{p}_k^2 \sin \mathbf{p}_k^2)] + \sin \frac{n\pi}{2} [\mathbf{p}_k^2 - e^{-\chi} (\mathbf{p}_k^2 \cos \mathbf{p}_k^2 + \chi \sin \mathbf{p}_k^2)]}{(\mathbf{p}_k^4 + \chi^2) \prod_{l \neq k}^n (\mathbf{p}_k^2 - \mathbf{p}_l^2)}. \end{aligned} \quad (\text{A.13})$$

A.3 Improved opacity expansion

The spectrum for the improved opacity expansion can be written as the iterative equation

$$\begin{aligned} \omega \frac{dI^{\text{IOE}}}{d\omega} &= -\frac{2\alpha_s C_R}{\omega^2} \text{Re} \int_0^\infty dt_2 \int_0^{t_2} dt_1 \int_{t_1}^{t_2} ds \int d^2\mathbf{z} \\ & \times \partial_{\mathbf{x}} \cdot \partial_{\mathbf{y}} [\mathcal{K}_{\text{HO}}(\mathbf{x}, t_2; \mathbf{z}, s) \delta v(\mathbf{z}, s) \mathcal{K}(\mathbf{z}, s; \mathbf{y}, t_1)]_{\mathbf{x}=\mathbf{y}=0}, \end{aligned} \quad (\text{A.14})$$

where the zeroth order solution is the HO from eq. (3.57) has to be added. In the following we will make use of results from refs. [53, 54]. The harmonic oscillator propagator is

$$\mathcal{K}_{\text{HO}}(\mathbf{x}, t_2; \mathbf{y}, t_1) = \frac{\omega}{2\pi i S(t_2, t_1)} \exp\left(\frac{i\omega}{2S(t_2, t_1)} [C(t_1, t_2) \mathbf{x}^2 + C(t_2, t_1) \mathbf{y}^2 - 2\mathbf{x} \cdot \mathbf{y}]\right). \quad (\text{A.15})$$

The functions S and C are given implicitly by

$$\begin{aligned} \left[\frac{d^2}{dt^2} + \Omega^2(t)\right] S(t, t_0) &= 0, & S(t_0, t_0) &= 0, & \partial_t S(t, t_0)|_{t=t_0} &= 1 \\ \left[\frac{d^2}{dt^2} + \Omega^2(t)\right] C(t, t_0) &= 0, & C(t_0, t_0) &= 1, & \partial_t C(t, t_0)|_{t=t_0} &= 0, \end{aligned} \quad (\text{A.16})$$

where the frequency $\Omega(t)$ is given by

$$\Omega(t) = \frac{1-i}{2} \sqrt{\frac{\hat{q}(t)}{\omega}} \quad (\text{A.17})$$

To continue it is useful to apply the formulas

$$\begin{aligned} \int_s^\infty dt_2 \partial_{\mathbf{x}} \mathcal{K}_{\text{HO}}(\mathbf{x}, t_2; \mathbf{z}, s)|_{\mathbf{x}=0} &= \frac{-i\omega}{\pi} \frac{\mathbf{z}}{z^2} e^{i\frac{\omega}{2}\Omega(s)^2 \frac{S(s,L)}{C(s,L)} z^2} \\ \int_0^s dt_1 \partial_{\mathbf{y}} \mathcal{K}_{\text{HO}}(\mathbf{z}, s; \mathbf{y}, t_1)|_{\mathbf{y}=0} &= \frac{-i\omega}{\pi} \frac{\mathbf{z}}{z^2} e^{-i\frac{\omega}{2} \frac{C(0,s)}{S(0,s)} z^2}. \end{aligned} \quad (\text{A.18})$$

Then the spectrum takes the following form

$$\omega \frac{dI^{\text{IOE}}}{d\omega} = \frac{2\bar{\alpha}}{\omega} \text{Re} i \int_0^L dt_2 \int_0^{t_2} dt_1 \int d^2\mathbf{x} e^{-i\frac{\omega}{2} \tan(\Omega(L-t_2))\mathbf{x}^2} \delta v(\mathbf{x}) \frac{\mathbf{x}}{\mathbf{x}^2} \cdot \partial_{\mathbf{y}} \mathcal{K}(\mathbf{x}, t_2; \mathbf{y}, t_1)|_{\mathbf{y}=0}, \quad (\text{A.19})$$

where we have used that for the brick medium $\hat{q}(t) = \Theta(L-t)\hat{q}$, the functions S and C are simply

$$S(t_2, t_1) = \frac{1}{\Omega} \sin \Omega(t_2 - t_1), \quad \text{and} \quad C(t_2, t_1) = \cos \Omega(t_2 - t_1). \quad (\text{A.20})$$

One can derive a formula for the IOE at arbitrary order, which was also explored in ref. [55].

$$\begin{aligned} \omega \frac{dI^{N_I=n}}{d\omega} &= (-1)^{n-1} \frac{2\bar{\alpha}}{\pi} \int d^2\mathbf{x}_n \dots d^2\mathbf{x}_1 \frac{\mathbf{x}_n \cdot \mathbf{x}_1}{\mathbf{x}_n^2 \mathbf{x}_1^2} \delta v(\mathbf{x}_n) \dots \delta v(\mathbf{x}_1) \\ &\times \text{Re} \int_0^L dt_n \int_0^{t_n} dt_{n-1} \dots \int_0^{t_2} dt_1 e^{i\frac{\omega}{2} [\cot(\Omega t_1) \mathbf{x}_1^2 - \tan(\Omega(L-t_n)) \mathbf{x}_n^2]} \\ &\times \mathcal{K}_{\text{HO}}(\mathbf{x}_n, t_n; \mathbf{x}_{n-1}, t_{n-1}) \dots \mathcal{K}_{\text{HO}}(\mathbf{x}_2, t_2; \mathbf{x}_1, t_1). \end{aligned} \quad (\text{A.21})$$

After changing to unitless variables by defining $\mathbf{u}_k = \sqrt{\mu^2 \omega / (2\bar{\omega}_c)} \mathbf{x}_k$ and $s_k = \frac{t_k}{L}$,

$$\begin{aligned} \omega \frac{dI^{N_I=n}}{d\omega} &= (-1)^{n-1} \frac{2\bar{\alpha}}{\pi} \left(\frac{L}{\lambda}\right)^n \left(\frac{\bar{\omega}_c}{\omega}\right)^n \int d^2\mathbf{u}_n \dots d^2\mathbf{u}_1 \frac{\mathbf{u}_n \cdot \mathbf{u}_1}{\mathbf{u}_n^2 \mathbf{u}_1^2} \delta \tilde{v}(\mathbf{u}_n) \dots \delta \tilde{v}(\mathbf{u}_1) \\ &\times \text{Re} \int_0^1 ds_n \int_0^{s_n} ds_{n-1} \dots \int_0^{s_2} ds_1 e^{i\frac{\sigma}{2} \sqrt{\frac{\bar{\omega}_c}{\omega}} [\cot(\sigma \sqrt{\frac{\bar{\omega}_c}{\omega}} s_1) \mathbf{u}_1^2 - \tan(\sigma \sqrt{\frac{\bar{\omega}_c}{\omega}} (1-s_n)) \mathbf{u}_n^2]} \\ &\times \tilde{\mathcal{K}}_{\text{HO}}(\mathbf{u}_n, s_n; \mathbf{u}_{n-1}, s_{n-1}) \dots \tilde{\mathcal{K}}_{\text{HO}}(\mathbf{u}_2, s_2; \mathbf{u}_1, s_1). \end{aligned} \quad (\text{A.22})$$

Here we have defined $\sigma = \frac{1-i}{\sqrt{2}}$ and the unitless functions

$$\begin{aligned} \delta \tilde{v}(\mathbf{u}) &= \frac{1}{2} \mathbf{u}^2 \ln \left(\frac{\omega}{\bar{\omega}_c} \frac{\mu^2}{2Q^2} \frac{1}{\mathbf{u}^2} \right), \\ \tilde{\mathcal{K}}_{\text{HO}}(\mathbf{u}_2, s_2; \mathbf{u}_1, s_1) &= \frac{\sigma \sqrt{\frac{\bar{\omega}_c}{\omega}}}{2\pi i \sin \left(\sigma \sqrt{\frac{\bar{\omega}_c}{\omega}} (s_2 - s_1) \right)} \\ &\times e^{\frac{i\sigma \sqrt{\frac{\bar{\omega}_c}{\omega}}}{2 \sin \left(\sigma \sqrt{\frac{\bar{\omega}_c}{\omega}} (s_2 - s_1) \right)} [\cos(\sigma \sqrt{\frac{\bar{\omega}_c}{\omega}} (s_2 - s_1)) (\mathbf{u}_2^2 + \mathbf{u}_1^2) - 2\mathbf{u}_2 \cdot \mathbf{u}_1]}. \end{aligned} \quad (\text{A.23})$$

As the integrals only depend on $\sqrt{\frac{\bar{\omega}_c}{\omega}}$ and $\frac{\omega}{\bar{\omega}_c} \frac{\mu^2}{2Q^2}$ the IOE spectrum can be written as $\omega \frac{dI^{N_I=n}}{d\omega} = \frac{2\bar{\alpha}}{\pi} \left(\frac{L}{\lambda}\right)^n \left(\frac{\bar{\omega}_c}{\omega}\right)^n f_n \left(\sqrt{\frac{\bar{\omega}_c}{\omega}}, \frac{\omega}{\bar{\omega}_c} \frac{\mu^2}{2Q^2}\right)$ where the function f_n is given by the integrals. The soft limit $\omega \ll \omega_c$ of the IOE expansion was discussed in detail in [55], and also in section 3.4.

In the hard limit $\omega \gg \omega_c$, the spectrum becomes

$$\begin{aligned} \omega \frac{dI^{N_I=n}}{d\omega} &\simeq (-1)^{n-1} \frac{2\bar{\alpha}}{\pi} \left(\frac{L}{\lambda}\right)^n \left(\frac{\bar{\omega}_c}{\omega}\right)^n \int d^2\mathbf{u}_n \dots d^2\mathbf{u}_1 \frac{\mathbf{u}_n \cdot \mathbf{u}_1}{\mathbf{u}_n^2 \mathbf{u}_1^2} \delta \tilde{v}(\mathbf{u}_n) \dots \delta \tilde{v}(\mathbf{u}_1) \\ &\times \text{Re} \int_0^1 ds_n \int_0^{s_n} ds_{n-1} \dots \int_0^{s_2} ds_1 e^{i\frac{\mathbf{u}_1^2}{2s_1}} \\ &\times \tilde{\mathcal{K}}_0(\mathbf{u}_n, s_n; \mathbf{u}_{n-1}, s_{n-1}) \dots \tilde{\mathcal{K}}_0(\mathbf{u}_2, s_2; \mathbf{u}_1, s_1), \end{aligned} \quad (\text{A.24})$$

where the BDMPS propagator has gone to the vacuum propagator

$$\tilde{\mathcal{K}}_0(\mathbf{u}_2, s_2; \mathbf{u}_1, s_1) = \frac{1}{2\pi i(s_2 - s_1)} e^{i\frac{(\mathbf{u}_2 - \mathbf{u}_1)^2}{2(s_2 - s_1)}}. \quad (\text{A.25})$$

Notice that there is no remaining dependence on the BDMPS scale ω_c . In section 3.4 we calculated the hard limit to first order, and the resulting expression (3.61) is the same as the OE limit (3.16) for high ω . Whether this correspondence is also true at higher orders is an interesting question that will be explored in future work.

B General formulas for the emission rate in the soft limit

In this appendix, we gather the formulas relevant for computing the emission rate in the soft limit. The rate can be written as

$$\omega \frac{dI}{d\omega dt} = \frac{4\bar{\alpha}\pi}{\omega} \text{Re} i \int_0^t dt_1 \int_{\mathbf{p}, \mathbf{p}_0} \Sigma(\mathbf{p}^2, t) \frac{\mathbf{p} \cdot \mathbf{p}_0}{p^2} \mathcal{K}(\mathbf{p}, t; \mathbf{p}_0, t_1), \quad (\text{B.1})$$

in momentum-space representation of the three-point function, and

$$\omega \frac{dI}{d\omega dt} = \frac{2\bar{\alpha}}{\omega} \text{Re} i \int_0^t dt_1 \int_{\mathbf{z}} v(\mathbf{z}, t) \frac{\mathbf{z}}{z^2} \cdot \partial_{\mathbf{y}} \mathcal{K}(\mathbf{z}, t; \mathbf{y}, t_1)|_{\mathbf{y}=0}, \quad (\text{B.2})$$

in coordinate-space representation. Equation (B.1) can be employed directly to derive expressions for the rate in the OE and ROE, by simply inserting the expansions (3.6) and (3.26). We will not attempt at deriving higher-order corrections to these rates here, since they can be also be found for a medium with constant density by taking the appropriate derivative with respect to length on the expression for the spectrum.

For the IOE, the harmonic oscillator spectrum is directly calculable, following the decomposition in eqs. (3.49) and (3.50). For the IOE rates, we find

$$\omega \frac{dI^{\text{HO}}}{d\omega dt} = \frac{\bar{\alpha}}{2\omega} \text{Re} i \int_0^t dt_1 \int_{\mathbf{z}} \hat{q}(t) \mathbf{z} \cdot \partial_{\mathbf{y}} \mathcal{K}_{\text{HO}}(\mathbf{z}, t; \mathbf{y}, t_1)|_{\mathbf{y}=0}, \quad (\text{B.3})$$

$$\omega \frac{dI^{\text{IOE}}}{d\omega dt} = \frac{2\bar{\alpha}}{\omega} \text{Re} i \int_0^t dt_1 \int_{\mathbf{z}} \delta v(\mathbf{z}, t) \frac{\mathbf{z}}{z^2} \cdot \partial_{\mathbf{y}} \mathcal{K}(\mathbf{z}, t; \mathbf{y}, t_1)|_{\mathbf{y}=0}, \quad (\text{B.4})$$

where the three-point correlator $\mathcal{K}(\mathbf{z}; \mathbf{y})$ is found from iterating (3.45). As a cross-check, for a medium with constant density we obtain

$$\omega \frac{dI^{\text{HO}}}{d\omega dt} = \bar{\alpha} x \text{Re} (i - 1) \tan \left[\frac{1 - i}{2} xt \right] = \bar{\alpha} x \frac{\sinh(xt) - \sin(xt)}{\cosh(xt) + \cos(xt)}, \quad (\text{B.5})$$

where $x \equiv \sqrt{\hat{q}/\omega}$, for the harmonic oscillator term.

C Medium-induced spectrum and rate with finite- z corrections

The process we study is a parton of energy E splitting into two partons with energy zE and $(1 - z)E$. In the main text, we refer to the emitted energy zE as ω . However, we stress that this definition is only true in the soft limit. In the more general case we refer to ω as the

reduced energy of the three-body evolution, that is $\omega = z(1-z)E$. This quantity is only equal to the emitted energy when $z \rightarrow 0$, in which case it reduces to $\omega \simeq zE$. This appendix accounts for how our framework generalizes when considering all the finite- z contributions, which means we strictly use the full definition $\omega = z(1-z)E$.

Reference [57] already has an implementation of the OE ($N = 1$) and IOE (HO+NHO) medium-induced emission spectrum in the strictly soft limit ($\omega \ll E$) for a homogeneous brick. We improve on this by keeping finite- z terms, including the rates, and by including the OE and ROE expansions. The resulting code is available online [78].

The starting equation for keeping finite- z corrections can be found in ref. [54],

$$\frac{dI_{ba}^{\text{med}}}{dz} = \frac{\alpha_s}{\omega^2} P_{ba}(z) \text{Re} \int_0^\infty dt_2 \int_0^{t_2} dt_1 \partial_{\mathbf{x}} \cdot \partial_{\mathbf{y}} [\mathcal{K}_{ba}(\mathbf{x}, t_2; \mathbf{y}, t_1) - \mathcal{K}_0(\mathbf{x}, t_2; \mathbf{y}, t_1)]_{\mathbf{x}=\mathbf{y}=0}, \quad (\text{C.1})$$

where the parent parton a carrying energy E splits into partons b and c , carrying energy zE and $(1-z)E$, respectively. It is the finite- z analog of eq. (3.1). The Altarelli-Parisi splitting functions are

$$\begin{aligned} P_{qq}(z) &= C_F \frac{1 + (1-z)^2}{z}, & P_{qg}(z) &= P_{gq}(1-z), \\ P_{gg}(z) &= C_A \frac{[1 + z(1-z)]^2}{z(1-z)}, & P_{gg}(z) &= N_f T_F [z^2 + (1-z)^2], \end{aligned} \quad (\text{C.2})$$

which are valid for $0 < z < 1$. In the soft limit $z \ll 1$, for quarks the splitting function reduces to $P_q(z) \approx \frac{2C_F}{z}$, while for gluons (where $1-z \ll 1$ also has to be included) $P_g(z) \approx \frac{C_A}{z(1-z)} \approx \frac{2C_A}{z}$, where in the last step the $1-z$ contribution has been folded to z with the additional factor of 2. The three-point correlator $\mathcal{K}(\mathbf{x}; \mathbf{y})$ satisfies the following Schrödinger-like equation

$$\left[i \frac{\partial}{\partial t} + \frac{\partial_{\mathbf{x}}^2}{2\omega} + i v_{ba}(\mathbf{x}, t) \right] \mathcal{K}_{ba}(\mathbf{x}, t; \mathbf{y}, t_0) = i \delta(t - t_0) \delta(\mathbf{x} - \mathbf{y}), \quad (\text{C.3})$$

where the potential v_{ba} describes the splitting induced by partons scattering with the medium,

$$v_{ba}(\mathbf{x}, t) = \frac{C_{cba}}{2N_c} v(\mathbf{x}, t) + \frac{C_{acb}}{2N_c} v(z\mathbf{x}, t) + \frac{C_{bac}}{2N_c} v((1-z)\mathbf{x}, t), \quad (\text{C.4})$$

where $C_{ijk} \equiv C_i + C_j - C_k$ and C_i is the Casimir operator squared for particle i and $v(\mathbf{x}, t)$ is defined in eq. (3.3). In the soft limit, $v_g(\mathbf{x}, t) \approx v_q(\mathbf{x}, t) \approx \frac{C_{b,c}}{N_c} v(\mathbf{x}, t)$, where the soft emission is always a gluon (C_b or $C_c = N_c$). Surprisingly, this shows that the potential is sensitive to the emitted gluon's and not the emitter's color in the soft limit because v is proportional with N_c by definition. This was observed previously in the opacity expansion and was explained heuristically in [36]. For quarks in the $z \rightarrow 1$ limit, the potential goes to $v_q(\mathbf{x}, t) \approx \frac{C_E}{N_c} v(\mathbf{x}, t)$, where the color factor compensates the N_c in v .

In momentum space, we find

$$v_{ba}(\mathbf{q}, t) = \frac{C_{cba}}{2N_c} v(\mathbf{q}, t) + \frac{C_{acb}}{2N_c} \frac{1}{z^2} v\left(\frac{\mathbf{q}}{z}, t\right) + \frac{C_{bac}}{2N_c} \frac{1}{(1-z)^2} v\left(\frac{\mathbf{q}}{1-z}, t\right), \quad (\text{C.5})$$

where $v(\mathbf{q}, t) = (2\pi)^2 \delta(\mathbf{q}) \Sigma(t) - \sigma(\mathbf{q}, t)$, and $\Sigma(t) = \Sigma(0, t) = \int_{\mathbf{q}} \sigma(\mathbf{q}, t)$. In the soft limit, $v_g(\mathbf{q}, t) \approx v_q(\mathbf{q}, t) \approx v(\mathbf{q}, t)$, which only becomes apparent once the explicit form of $\sigma(\mathbf{q})$ is used in $v(\frac{\mathbf{q}}{z})$. It is at this point worth extending the definition of the interaction potential to also include an argument defining the screening mass, i.e.

$$\sigma(\mathbf{q}, t, \mu) \equiv \frac{4\pi \hat{q}_0(t)}{(\mathbf{q}^2 + \mu^2)^2}, \quad (\text{C.6})$$

for the GW model (see eq. (3.4)), and similarly for the inverse mean free path $\Sigma(\mathbf{p}^2, t) \rightarrow \Sigma(\mathbf{p}^2, t, \mu)$, where $\Sigma(\mathbf{p}^2, t, \mu) = \int_{\mathbf{q}} \sigma(\mathbf{q}, t, \mu) \Theta(\mathbf{q}^2 - \mathbf{p}^2)$. Then, $\frac{1}{z^2} \sigma(\frac{\mathbf{p}}{z}, t, \mu) = z^2 \sigma(\mathbf{p}, t, z\mu)$.

Further simplifications can be made following the discussion in section 3.1. For the spectrum in momentum space representation, generalizing eq. (3.12) to finite- z , we arrive at

$$\frac{dI_{ba}}{dz} = \frac{2\alpha_s}{\omega} P_{ba}(z) \text{Re} i \int_0^L dt_2 \int_0^{t_2} dt_1 \int_{\mathbf{p}, \mathbf{p}_0} \Sigma_{ba}(\mathbf{p}^2, t_2) \frac{\mathbf{p} \cdot \mathbf{p}_0}{\mathbf{p}^2} \mathcal{K}_{ba}(\mathbf{p}, t_2; \mathbf{p}_0, t_1), \quad (\text{C.7})$$

where

$$\Sigma_{ba}(\mathbf{q}^2, t) = \frac{C_{cba}}{2N_c} \Sigma(\mathbf{q}^2, t, \mu) + \frac{C_{acb}}{2N_c} z^2 \Sigma(\mathbf{q}^2, t, z\mu) + \frac{C_{bac}}{2N_c} (1-z)^2 \Sigma(\mathbf{q}^2, t, (1-z)\mu), \quad (\text{C.8})$$

and the three-point function in momentum-space representation is found through the implicit equation

$$\begin{aligned} \mathcal{K}_{ba}(\mathbf{p}, t; \mathbf{p}_0, t_0) &= (2\pi)^2 \delta(\mathbf{p} - \mathbf{p}_0) \mathcal{K}_0(\mathbf{p}; t - t_0) \\ &\quad - \int_{t_0}^t ds \int_{\mathbf{q}} \mathcal{K}_0(\mathbf{p}; t - s) v_{ba}(\mathbf{q}, s) \mathcal{K}_{ba}(\mathbf{p} - \mathbf{q}, s; \mathbf{p}_0, t_0). \end{aligned} \quad (\text{C.9})$$

Then, analogously to the derivations in appendix B, the rate at finite- z reads

$$\frac{dI_{ba}}{dz dt} = \frac{2\alpha_s}{\omega} P_{ba}(z) \text{Re} i \int_0^t dt_1 \int_{\mathbf{p}, \mathbf{p}_0} \Sigma_{ba}(\mathbf{p}^2, t) \frac{\mathbf{p} \cdot \mathbf{p}_0}{\mathbf{p}^2} \mathcal{K}_{ba}(\mathbf{p}, t; \mathbf{p}_0, t_1). \quad (\text{C.10})$$

Similar manipulations in coordinate-space representation will be done directly in the IOE section below.

To simplify the expressions below we also introduce the shorthand that accounts for the recurring combinations of color and z factors, see e.g. in eq. (C.8). Hence, we have

$$\sum_{p=1}^3 \mathcal{C}_p z_p^2 f(z_p^2 x) = \frac{C_{cba}}{2N_c} f(x) + \frac{C_{acb}}{2N_c} z^2 f(z^2 x) + \frac{C_{bac}}{2N_c} (1-z)^2 f((1-z)^2 x), \quad (\text{C.11})$$

that runs over the three cyclic permutations of $\{a, b, c\}$. Here $\mathcal{C}_p = \left[\frac{C_{cba}}{2N_c}, \frac{C_{acb}}{2N_c}, \frac{C_{bac}}{2N_c} \right]$ and $z_p = [1, z, (1-z)]$, with p running from 1 to 3. In the soft limit this expression simply becomes $\sum_p \mathcal{C}_p z_p^2 f(z_p^2 x) \rightarrow f(x)$.

C.1 Opacity expansion

From eq. (C.7), and following section 3.2, we find the $N = 1$ contribution of the OE at finite- z to be,

$$\frac{dI_{ba}^{N=1}}{dz} = \frac{2\alpha_s}{\pi} \frac{P_{ba}(z)}{z(1-z)} \frac{L}{\lambda} \frac{\mu^2 L}{2E} \sum_p \mathcal{C}_p z_p^2 \mathcal{I}_{N=1}(z_p^2 y), \quad (\text{C.12})$$

where $\lambda = \mu^2/\hat{q}_0$ is the mean free path, $y = \frac{\bar{\omega}_c}{\omega} = \frac{\mu^2 L}{2z(1-z)E}$, and the relevant integral is²¹

$$\mathcal{I}_{N=1}(y) = \int_0^\infty \frac{du}{u^2} \frac{u - \sin u}{u + y} = \begin{cases} \frac{\pi}{4}, & \text{for } y \ll 1, \\ \frac{1}{y}(\gamma_E + \ln y), & \text{for } y \gg 1. \end{cases} \quad (\text{C.13})$$

We have also extracted the asymptotic behaviors for future convenience. The soft limit of a hard emission ($\bar{\omega}_c \ll zE \ll E$) reduces to $\frac{dI}{dz} = \bar{\alpha} \frac{\pi}{2} \frac{L}{\lambda} \frac{\bar{\omega}_c}{z^2 E}$, which is in agreement with eq. (3.16), with $\omega \rightarrow zE$. One could also use $P_g(z) \approx \frac{C_A}{z(1-z)}$ and keep $z(1-z)$, and then an extra 1/2 factor will appear to not double count both contributions $z, 1-z \ll 1$. The rate can be found directly from eq. (C.10) and is given by

$$\frac{dI_{ba}^{N=1}}{dz dt} = \frac{2\alpha_s}{\pi} \frac{P_{ba}(z)}{z(1-z)} \frac{1}{\lambda} \frac{\mu^2 t}{2E} \sum_p C_p z_p^2 \tilde{\mathcal{I}}_{N=1}(z_p^2 y), \quad (\text{C.14})$$

where

$$\tilde{\mathcal{I}}_{N=1}(y) = \int_0^\infty \frac{du}{u} \frac{1 - \cos u}{u + y} = \begin{cases} \frac{\pi}{2}, & \text{for } y \ll 1, \\ \frac{1}{y}(1 + \gamma_E + \ln y), & \text{for } y \gg 1. \end{cases} \quad (\text{C.15})$$

C.2 Resummed opacity expansion

The finite- z potential in eq. (C.4) introduces an additional complication for the ROE. In section 3.3, we separated and resummed the zero momentum exchange mode, while expanding in real scatterings. In eq. (C.4), however, this separation is more complicated because additional zero modes appear in the real terms in the $z, 1-z \rightarrow 0$ limits. Therefore, we make sure to explicitly subtract the zero mode terms in real scatterings

$$v_{ba}(\mathbf{p}, t) = (2\pi)^2 \sum_p C_p \left[(1 - f(z_p)) \delta(\mathbf{p}) \Sigma(t) - \int_{\mathbf{q}} (\delta(\mathbf{p} - z_p \mathbf{q}) - f(z_p) \delta(\mathbf{p})) \sigma(\mathbf{q}) \right]. \quad (\text{C.16})$$

We introduced $f(z)$ arbitrary function, that goes to 1 in the soft limit $z \rightarrow 0$ (and $1-z \rightarrow 0$). In this paper, we make the choice $f(z) = 1 - z^2$. The resummed opacity expansion involves the Sudakov factor of the no elastic scattering probability,

$$\Delta_{ba}(t_2, t_1) = \exp \left[- \int_{t_1}^{t_2} ds \hat{\Sigma}(s, z) \right], \quad (\text{C.17})$$

here $\hat{\Sigma}(s, z) = [\frac{C_{cba}}{2N_c} + z^2 \frac{C_{acb}}{2N_c} + (1-z)^2 \frac{C_{bac}}{2N_c}] \Sigma(s)$. In the soft limit $\hat{\Sigma} \rightarrow \Sigma$, and thus the Sudakov goes to eq. (3.25). The expansion reads

$$\begin{aligned} \mathcal{K}_{ba}(\mathbf{p}, t; \mathbf{p}_0, t_0) &= (2\pi)^2 \delta(\mathbf{p} - \mathbf{p}_0) \Delta_{ba}(t_2, t_1) \mathcal{K}_0(\mathbf{p}; t_2 - t_1) \\ &\quad - \int_{t_1}^{t_2} ds \int_{\mathbf{q}} \Delta_{ba}(t_2, s) \mathcal{K}_0(\mathbf{p}; t_2 - s) \hat{\sigma}_{ba}(\mathbf{q}, s) \mathcal{K}_{ba}(\mathbf{p} - \mathbf{q}, s; \mathbf{p}_0, t_0), \end{aligned} \quad (\text{C.18})$$

where $\hat{\sigma}_{ba}(\mathbf{q}, s) = \sum_p C_p \frac{1}{z_p^2} \sigma(\frac{\mathbf{q}}{z_p}, t) - \sum_p C_p f(z_p) \Sigma(s)$.

²¹The integrals are available with trigonometric integral functions

$$\begin{aligned} \int_0^\infty \frac{du}{u^2} \frac{u - \sin u}{u + y} &= \frac{1}{y^2} \left[y(\gamma_E - 1 + \ln y) + \pi \sin^2 \frac{y}{2} - \text{Ci}(y) \sin y + \text{Si}(y) \cos y \right], \\ \int_0^\infty \frac{du}{u} \frac{1 - \cos u}{u + y} &= \frac{1}{2y} [2(\gamma_E + \ln(y)) - 2 \cos(y) \text{Ci}(y) + \sin(y)(\pi - 2\text{Si}(y))], \end{aligned}$$

where Euler Gamma γ_E , $\text{Ci}(z) = - \int_z^\infty dt/t \cos t$, and $\text{Si}(z) = \int_0^z dt/t \sin t$.

The first order ($N_r = 1$) can be read directly off from eq. (C.7), and reads

$$\begin{aligned} \frac{dI_{ba}^{N_r=1}}{dz} &= \frac{2\alpha_s}{\omega} P_{ba}(z) \operatorname{Re} i \int_0^L dt_2 \int_0^{t_2} dt_1 \int_{\mathbf{p}} \Sigma_{ba}(\mathbf{p}^2, t_2) \mathcal{K}_0(\mathbf{p}; t_2 - t_1) \Delta_{ba}(t_2, t_1), \\ &= \frac{2\alpha_s}{\pi} \frac{P_{ba}(z)}{z(1-z)} \frac{L}{\lambda} \frac{\mu^2 L}{2E} \sum_p \mathcal{C}_p z_p^2 \mathcal{I}_{N_r=1}(z_p^2 y), \end{aligned} \quad (\text{C.19})$$

where $y = \frac{\mu^2 L}{2\omega}$ and, defining $\hat{\chi} \equiv \hat{\Sigma} L$,

$$\mathcal{I}_{N_r=1}(y) = - \int_0^\infty \frac{du}{u+y} \operatorname{Im} T(u - i\hat{\chi}), \quad (\text{C.20})$$

and $T(u) = (1 - iu - e^{-iu})/u^2$. The imaginary part can also be written explicitly, as

$$- \operatorname{Im} T(u - i\hat{\chi}) = \frac{u[u^2 + \hat{\chi}(\hat{\chi} - 2)] + [2u\hat{\chi} \cos u - (u^2 - \hat{\chi}^2) \sin u] e^{-\hat{\chi}}}{[u^2 + \hat{\chi}^2]^2}. \quad (\text{C.21})$$

In the big medium limit ($\hat{\chi} \gg 1$), our formula reproduces eq. (3.34), $\frac{dI}{dz} = \frac{\bar{\alpha}}{z} \frac{L}{\lambda} \ln \frac{\mu^2 \lambda}{2zE}$.

The rate follows directly from eq. (C.10), and reads

$$\frac{dI_{ba}^{N_r=1}}{dz dt} = \frac{2\alpha_s}{\pi} \frac{P_{ba}(z)}{z(1-z)} \frac{1}{\lambda} \frac{\mu^2 t}{2E} \sum_p \mathcal{C}_p z_p^2 \tilde{\mathcal{I}}_{N_r=1}(z_p^2 y), \quad (\text{C.22})$$

with the relevant integral being,²²

$$\tilde{\mathcal{I}}_{N_r=1}(y) = - \int_0^\infty \frac{du}{u+y} \operatorname{Im} \tilde{T}(u - i\hat{\chi}), \quad (\text{C.23})$$

with $\tilde{T}(y) = (-i + ie^{-iu})/u$. The imaginary part of this function is

$$- \operatorname{Im} \tilde{T}(u - i\hat{\chi}) = \frac{u - e^{-\hat{\chi}}(u \cos u + \hat{\chi} \sin u)}{u^2 + \hat{\chi}^2}. \quad (\text{C.24})$$

C.3 Improved opacity expansion

The IOE is similar to that we used in section 3.4, one takes a perturbative expansion in $\mu|x| \ll 1$ of eq. (3.3) in eq. (C.4). By including the color and z -dependence of the splitting,

²²The integral is analytical using $\operatorname{Ei}(x) = - \int_{-x}^\infty dt e^{-t}/t$,

$$\begin{aligned} \int_0^\infty du \frac{u(e^x - \cos u) - \chi \sin u}{(u+y)(u^2 + \chi^2)} &= \frac{e^{-x}}{2(\chi^2 + y^2)} \left[\pi x e^x - \pi \chi (\cos y - \sin y) - 2y (\cos(y) \operatorname{Ci}(y) + \sin(y) \operatorname{Si}(y)) \right. \\ &\quad \left. + 2\chi (\cos(y) \operatorname{Si}(y) - \sin(y) \operatorname{Ci}(y)) + 2y e^x \left(\ln \frac{y}{\chi} + \operatorname{Ei}(-x) \right) \right]. \end{aligned}$$

an effective jet quenching parameter can be defined as²³

$$\begin{aligned} \hat{q}_{ba}(z, t) &\equiv \hat{q}_0(t) \left[\frac{C_{cba}}{2C_A} \ln \frac{Q^2}{\mu_*^2} + \frac{C_{acb}}{2C_A} z^2 \ln \frac{Q^2}{z^2 \mu_*^2} + \frac{C_{bac}}{2C_A} (1-z)^2 \ln \frac{Q^2}{(1-z)^2 \mu_*^2} \right], \\ &= \hat{q}_0(t) \sum_p C_p z_p^2 \ln \frac{Q^2}{z_p^2 \mu_*^2}. \end{aligned} \quad (\text{C.25})$$

The harmonic oscillator potential is then $v_{ba}^{\text{HO}}(\mathbf{x}, t) = \frac{1}{4} \hat{q}_{ba}(z, t) \mathbf{x}^2$, which in the soft limit recovers the expression below eq. (3.42), $\hat{q}_{ba} \rightarrow \hat{q}$.

Harmonic oscillator. The harmonic oscillator spectrum is given by

$$\frac{dI_{ba}^{\text{HO}}}{dz} = \frac{\alpha_s}{\pi} P_{ba}(z) \ln \left[\frac{1}{2} \left(\cos \left(\sqrt{\frac{2\omega_c}{\omega}} \right) + \cosh \left(\sqrt{\frac{2\omega_c}{\omega}} \right) \right) \right], \quad (\text{C.26})$$

where $\omega_c = \frac{1}{2} \hat{q}_{ba}(z) L^2$. In the soft limit, $z \frac{dI}{dz} \approx 2\bar{\alpha} \sqrt{\hat{q}/(2z^3)}$, that reproduces the formula from eq. (3.58). The time-differential rate that appears in the evolution equation is

$$\frac{dI_{ba}^{\text{(HO)}}}{dz dL} = \frac{\alpha_s}{\pi} P_{ba}(z) \frac{1}{L} \sqrt{\frac{2\omega_c}{\omega}} \frac{\sinh \left(\sqrt{\frac{2\omega_c}{\omega}} \right) - \sin \left(\sqrt{\frac{2\omega_c}{\omega}} \right)}{\cos \left(\sqrt{\frac{2\omega_c}{\omega}} \right) + \cosh \left(\sqrt{\frac{2\omega_c}{\omega}} \right)}. \quad (\text{C.27})$$

Next-to harmonic oscillator. The NHO spectrum is given by

$$\begin{aligned} \frac{dI_{ba}^{\text{NHO}}}{dz} &= \frac{\alpha_s}{\omega^2} P_{ba}(z) \text{Re} \int_0^\infty dt_2 \int_0^{t_2} dt_1 \int_z^L ds \partial_x \partial_y \mathcal{K}_{ba}^{\text{HO}}(\mathbf{x}, t_2; \mathbf{z}, s) \delta v_{ba}(z, s) \\ &\quad \times \mathcal{K}_{ba}^{\text{HO}}(\mathbf{z}, s; \mathbf{y}, t_1) |_{\mathbf{x}=\mathbf{y}=0} \end{aligned} \quad (\text{C.28})$$

$$= \frac{\alpha_s}{\pi^2} P_{ba}(z) \text{Re} \int_0^L ds \int_{\mathbf{u}} \frac{1}{\mathbf{u}^2} \delta v_{ba}(\mathbf{u}, s) e^{-k^2(s) \mathbf{u}^2}, \quad (\text{C.29})$$

where we have defined

$$k^2(s) = i \frac{\omega \Omega}{2} [\cot(\Omega s) - \tan(\Omega(L-s))], \quad (\text{C.30})$$

$$\delta v_{ba}(\mathbf{x}, t) = \frac{\hat{q}_0}{4} \mathbf{x}^2 C_{ba}(z) \ln \frac{1}{\mathbf{x}^2 Q^2}, \quad (\text{C.31})$$

and we have used $\Omega = \sqrt{\hat{q}_{ba}/(2i\omega)}$, $C_{ba}(z) = \frac{C_{cba}}{2C_A} + \frac{C_{acb}}{2C_A} z^2 + \frac{C_{bac}}{2C_A} (1-z)^2$ and some sub-leading terms have already been included in \hat{q}_{ba} . The integral over the transverse position can be done

$$\int_{\mathbf{u}} \frac{1}{\mathbf{u}^2} \delta v(\mathbf{u}, s) e^{-k^2(s) \mathbf{u}^2} = \frac{\pi}{4} \hat{q}_0 \frac{1}{-k^2(s)} \left(\gamma_E + \ln \frac{-k^2(s)}{Q^2} \right). \quad (\text{C.32})$$

²³Our definition includes sub-leading $\sim z^2 \ln z^2$ terms to the HO term and thus these terms get resummed. This should make the IOE expansion converge faster. The leading form without these terms would look like

$$\hat{q}_{ba}(z, t) = \hat{q}_0(t) \left[\frac{C_{cba}}{2C_A} + \frac{C_{acb}}{2C_A} z^2 + \frac{C_{bac}}{2C_A} (1-z)^2 \right] \ln \frac{Q^2}{\mu_*^2}.$$

Collecting all terms, we get

$$\begin{aligned} \frac{dI_{ba}^{\text{NHO}}}{dz} &= \frac{\alpha_s}{2\pi} P_{ba}(z) \hat{q}_0 C_{ba}(z) \text{Re} \int_0^L \frac{ds}{-k^2(s)} \left(\gamma_E + \ln \frac{-k^2(s)}{Q^2} \right) \\ &\approx \begin{cases} \frac{\alpha_s}{\pi} P_{ba}(z) C_{ba}(z) \frac{\hat{q}_0}{\hat{q}_{ba}} \sqrt{\frac{\omega_c}{2\omega}} \left\{ \sqrt{\frac{\omega}{2\omega_c}} \left(\frac{\pi^2}{12} \tanh \left(\sqrt{\frac{\omega_c}{2\omega}} \right) - 2 \ln 2 \right) \right. \\ \left. + 1 + \tanh \left(\sqrt{\frac{\omega_c}{2\omega}} \right) \left[\gamma_E - 1 + \frac{\pi}{4} + \ln \left(\frac{\sqrt{\omega} \hat{q}_{ba}}{\sqrt{2} Q^2} \right) \right] \right\}, & \text{for } \omega \ll \omega_c, \\ \frac{\alpha_s}{2} P_{ba}(z) C_{ba}(z) \frac{\hat{q}_0 L^2}{2\omega} \left[1 + \frac{2}{3\pi} \frac{\hat{q}_{ba} L^2}{2\omega} \left(2\gamma_E - \frac{7}{12} + \ln \frac{\omega}{2LQ^2} \right) \right], & \text{for } \omega \gg \omega_c. \end{cases} \end{aligned} \quad (\text{C.33})$$

The rate can be given explicitly in the soft and hard limit

$$\begin{aligned} \frac{dI_{ba}^{\text{NHO}}}{dzdL} &= \frac{\partial}{\partial L} \frac{dI_{ba}^{\text{NHO}}}{dz} \\ &\approx \begin{cases} \frac{\alpha_s}{\pi} P_{ba}(z) C_{ba}(z) \frac{\hat{q}_0}{\hat{q}_{ba}} \frac{1}{2L} \sqrt{\frac{\omega_c}{2\omega}} \text{sech}^2 \left(\sqrt{\frac{\omega_c}{2\omega}} \right) \left\{ 1 + \frac{\pi^2}{12} + \cosh \left(\sqrt{\frac{2\omega_c}{\omega}} \right) \right. \\ \left. + \left(\sqrt{\frac{2\omega_c}{\omega}} + \sinh \left(\sqrt{\frac{2\omega_c}{\omega}} \right) \right) \left(\gamma_E - 1 + \frac{\pi}{4} + \ln \left(\frac{\sqrt{\omega} \hat{q}_{ba}}{\sqrt{2} Q^2} \right) \right) \right\}, & \text{for } \omega \ll \omega_c, \\ \frac{\alpha_s}{2} P_{ba}(z) C_{ba}(z) \frac{\hat{q}_0 L}{\omega} \left[1 + \frac{2}{3\pi} \frac{\hat{q}_{ba} L^2}{2\omega} \left(4\gamma_E - \frac{5}{3} + 2 \ln \left(\frac{\omega}{2LQ^2} \right) \right) \right], & \text{for } \omega \gg \omega_c. \end{cases} \end{aligned} \quad (\text{C.34})$$

The approximated formulas capture the exact formulas up to a few percent deviances and are therefore suitable for numeric implementation, as they do not contain any integrals.

Matching scale. We already introduced the ω dependence of $Q^2(\omega)$, that relied on the soft limit ($\omega \ll \omega_c$) of the spectrum (where the finite- z correction disappears), and thus we use the same definition as in eq. (3.44). In the numerical implementation, we set $\hat{q} = \max(\hat{q}_0, \hat{q}(z))$ and $Q^2 = \max(\sqrt{\epsilon} \mu_*^2, Q^2(z))$. This will only become relevant if $L < \lambda$ and $\bar{\omega}_c < \omega < \omega_{\text{BH}}$ which is a small corner of the phase space, where instead of the IOE one should use the OE. We showed numerically that using the IOE with the frozen matching scale or using the OE for $L < \lambda$ does not matter, however, the latter would need the introduction of a new smoothing between OE and IOE at $L = \lambda$ that complicates the implementation (see also appendix D).

To summarize this section, the full emission phase space is covered by using a similar formula that was presented in section 3.5

$$\frac{dI}{dz} = \begin{cases} \frac{dI^{\text{ROE}}}{dz}, & \omega < \omega_{\text{tr}}, \\ \frac{dI^{\text{IOE}}}{dz}, & \omega > \omega_{\text{tr}}, \end{cases} \quad (\text{C.35})$$

where $\omega_{\text{tr}} = \min(\omega_{\text{BH}}, \bar{\omega}_c)$ and $\omega = z(1-z)E$. The condition on ω comes from the limits calculated in this section. Importantly, the conditions are the same as the ones derived in section 3.

We would like emphasize the $z, 1-z$ symmetry presented in the ω condition. The gluon spectrum is trivially symmetric in $z, 1-z$ as the emitted particles' kinematics is equivalent. The quark spectrum, on the other hand, is strongly asymmetric in z . One can still use the symmetric condition on ω as we saw in the limiting formulas in this section.

D Numerical implementation of the evolution equation

The evolution equation is given in eq. (4.8) and can be rewritten by introducing the variable $\xi = \frac{x}{z}$ ($\xi = xz$) in the gain (loss) term

$$\partial_t D(x, t) = \int_x^1 d\xi f(x, \xi, t) D(\xi, t) - D(x, t) \int_0^1 d\xi f(\xi, x, t), \quad (D.1)$$

$$f(x, \xi, t) = \frac{x}{\xi^2} \frac{d^2 I}{dz dt} \Big|_{E \rightarrow \xi E} \left(z \mapsto \frac{x}{\xi} \right). \quad (D.2)$$

We implemented eq. (C.14) (as $N = 1$), eq. (C.22) (as $N_r = 1$), and eqs. (C.27) and (C.34) (HO+NHO) in f as

$$\frac{d^2 I^{\text{med}}}{dz dt} \Big|_E = (1 - S) \frac{d^2 I^{N_r=1}}{dz dt} \Big|_E + S \frac{d^2 I^{\text{IOE}}}{dz dt} \Big|_E, \quad (D.3)$$

where $\omega_{\text{tr}} = \min(\omega_{\text{BH}}, \bar{\omega}_c)$ and $\omega = z(1-z)E$. The upper formula is not smooth for any finite order of truncation in the transition between the IOE or ROE, and therefore in some cases, we used the switching function $S = \cos\left[\frac{\pi}{2}(1-\alpha)\right]$, with $\alpha = \frac{2\omega - \omega_{\text{tr}}}{3\omega_{\text{tr}}}$ if $\frac{1}{2}\omega_{\text{tr}} < \omega < 2\omega_{\text{tr}}$ to smoothing the transition. The uncertainty introduced by this procedure is smaller than the next higher-order contribution. One can study the matching uncertainty around the BH region by varying ω_{tr} with a factor of 2. To study the matching condition of the IOE, Q can also be varied by a factor of 2 in eq. (3.44) as it was done in ref. [57]. In figure 11 we show the deviation from the numeric solution including both of these variations. Other than the band, figure 11 is equivalent to figure 7, we only use the soft limit ($z \ll 1$). There is a further uncertainty coming from going to one higher order ($N_r = 1 \mapsto 2$ and NHO \mapsto NNHO), that we leave for future studies. We expect this uncertainty, however, to extend the error band in figure 11 up to the numeric solution.

The integrals can then be divided into

$$\text{Gain} = G_{\xi \rightarrow x} + G_{\text{reg}} + G_{>} = \left[\int_x^{x+\epsilon} + \int_{x+\epsilon}^{1-\delta} + \int_{1-\delta}^1 \right] d\xi f(x, \xi, t) D(\xi, t), \quad (D.4)$$

$$\text{Loss} = L_{<} + L_{\text{reg}} + L_{\xi \rightarrow x} = - \left[\int_0^\delta + \int_\delta^{x-\epsilon} + \int_{x-\epsilon}^x \right] d\xi f(\xi, x, t) D(x, t). \quad (D.5)$$

All divergences are present in the $\xi \rightarrow x$ terms, which cancel exactly and thus the trapezoid rule is used

$$G_{\xi \rightarrow x} + L_{\xi \rightarrow x} \approx \frac{\epsilon}{2} [f(x, x + \epsilon) D(x + \epsilon, \tau) - f(x - \epsilon, x) D(x, \tau)], \quad (D.6)$$

which contributes to the regular part of the integrals. In our implementation $\epsilon = 10^{-6}$, and thus we have $x > \epsilon$. Similarly to vacuum physics, the ϵ cut was necessary to introduce because the soft divergence in the Bethe-Heitler region has to be regulated. The $G_{\text{reg}}, L_{<}, L_{\text{reg}}$ are simple integrals and can be done numerically on a grid. So can $G_{>}$, however, we neglect this latter contribution by using the fact $\lim_{x \rightarrow 1} D \rightarrow 0$ (the kernel is soft divergent and thus it moves quanta towards $x < 1$).

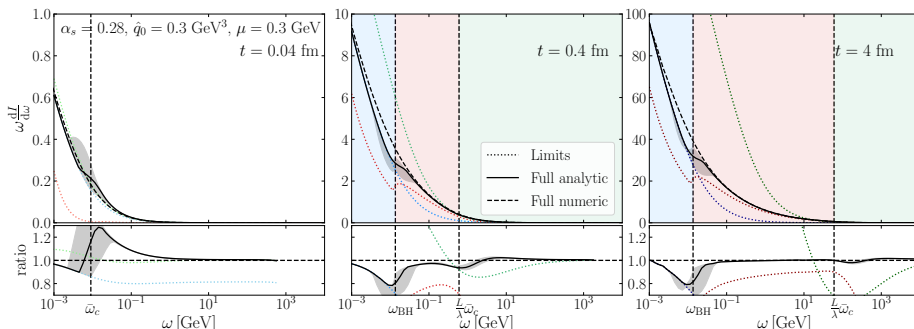


Figure 11. Same as figure 7, on a semilog scale.

E HTL potential

In this appendix, we investigate what happens if employ the HTL potential in the multiple-scattering series. The potential now reads

$$\sigma(\mathbf{q}) = N_c n(t) \frac{d^2 \sigma_{el}}{d^2 \mathbf{q}} = \frac{4\pi \hat{q}_0}{\mathbf{q}^2 (\mathbf{q}^2 + m_D^2)}, \quad (\text{E.1})$$

where m_D is the Debye screening mass in a thermal medium with temperature T and $\hat{q}_0 = 4\pi\alpha_s m_D^2 T$ [65]. In this case, we find that

$$\Sigma(\mathbf{p}^2) = \frac{\hat{q}_0}{m_D^2} \ln \left(\frac{\mathbf{p}^2 + m_D^2}{\mathbf{p}^2} \right), \quad (\text{E.2})$$

where we have a logarithmic divergence as $\mathbf{p}^2 \rightarrow 0$. This implies that the mean free path has to be regulated by an IR cut-off so that $\lambda \sim \Sigma^{-1}(p_{\min}^2)$.

In this case, the OE remains unmodified because the divergence at $p_{\min}^2 \rightarrow 0$ cancels order by order between the real and virtual contributions. The ROE, however, has to be treated with care when truncated at a finite order since we have to introduce an explicit IR cut-off in order to define the elastic Sudakov factor. Hence, the modified Sudakov reads

$$\Delta(t, t_0) = e^{-\Sigma_{\text{reg}}(t-t_0)}, \quad (\text{E.3})$$

in a static medium, where $\Sigma_{\text{reg}} \equiv \Sigma(p_{\min}^2)$ with p_{\min}^2 and unknown IR regulator. Clearly, an all-order resummation of the ROE series would remove the spurious IR dependence.

The role of the medium potential in the IOE was clearly elucidated in [55], where the information about the scattering potential is fully contained in the definition of μ_*^2 . We refer the reader to this paper for an exhaustive discussion.

In order to clarify what modifications arise in the OE and ROE, we compute the respective first-order terms of the expansions, i.e. $N = 1$ and $N_r = 1$, explicitly here. In the OE, we find

$$\omega \frac{dI^{N=1}}{d\omega} = 2\bar{\alpha} \frac{\hat{q}_0 L}{m_D^2} \int_0^\infty du \ln \left(\frac{u+y}{u} \right) [-\text{Im} T(u)], \quad (\text{E.4})$$

where now we defined $y = \bar{\omega}_c/\omega$ with $\bar{\omega}_c = m_D^2 L/2$. The prefactor contains \hat{q}_0/m_D^2 , which is similar to the inverse mean free path (in fact, in the GW model it would be exactly equal to λ^{-1}), with a missing logarithmic factor. Using (3.30), we can immediately extract the limiting behaviors, which yield

$$\omega \frac{dI^{N=1}}{d\omega} = 2\bar{\alpha} \frac{\hat{q}_0 L}{m_D^2} \begin{cases} \ln\left(\frac{\bar{\omega}_c}{\omega}\right) [-1 + \gamma_E + \ln\left(\frac{\bar{\omega}_c}{\omega}\right)] & \text{for } \omega \ll \bar{\omega}_c \\ \frac{\pi}{4} \frac{\bar{\omega}_c}{\omega} & \text{for } \omega \gg \bar{\omega}_c. \end{cases} \quad (\text{E.5})$$

As expected, in this limit there is no sensitivity to the mean free path *per se*. However, compared to the $N = 1$ result in (3.16), there is an additional logarithmic enhancement $\sim \ln \bar{\omega}_c/\omega$ in the soft limit. Comparing to eq. (E.2), we see that this logarithm can be absorbed into the prefactor $\sim \hat{q}_0/m_D^2$ to recreate an effective, regularized mean free path in the HTL theory, i.e.

$$\lambda_{\text{reg}}^{-1} \Big|_{L \ll \lambda} = \frac{\hat{q}_0}{m_D^2} \ln\left(\frac{\bar{\omega}_c}{\omega}\right). \quad (\text{E.6})$$

This regularization follows also from the discussion in refs. [36, 46]. With this modification, the soft limit for low medium opacity is equivalent in the GW and HTL theory.

In the hard limit, $\omega \gg \bar{\omega}_c$, there is no additional logarithmic enhancement in the HTL compared to the GW theory, see (3.16), and the mean free path is simply $\lambda_0^{-1} = \hat{q}_0/m_D^2$. Apart from this subtlety, the expressions are again equivalent.

Let us now turn to the ROE resummation which is valid in dilute (small) media or in the soft limit for dense or large media. At first order $N_r = 1$, we find now

$$\omega \frac{dI^{N_r=1}}{d\omega} = 2\bar{\alpha} \frac{\hat{q}_0 L}{m_D^2} \int_0^\infty du \ln\left(\frac{u+y}{u}\right) [-\text{Im} T(u - i\chi_{\text{reg}})], \quad (\text{E.7})$$

where the opacity is $\chi_{\text{reg}} = \Sigma_{\text{reg}} L$ and $\Sigma_{\text{reg}} = \int_{\mathbf{q}} \sigma(\mathbf{q}) \Theta(\mathbf{q}^2 - q_{\text{min}}^2)$ is the regularized inverse mean free path.²⁴ As discussed at length in section 3.3, at small opacities the ROE is equivalent order by order to the OE. This was discussed in the paragraphs above. For large opacities, $\chi_{\text{reg}} \gg 1$, we use (3.32) to solve the integral analytically. As discussed below eq. (3.32), the expressions permits a transmutation of the relevant scale from $\bar{\omega}_c$ to ω_{BH} , where now $\omega_{\text{BH}} = m_D^2/(2\Sigma_{\text{reg}})$. It is then straightforward to extract the following limiting behavior,

$$\omega \frac{dI^{N_r=1}}{d\omega} = 2\bar{\alpha} \frac{\hat{q}_0 L}{m_D^2} \begin{cases} \frac{1}{24} [5\pi^2 + 12 \ln^2\left(\frac{\omega_{\text{BH}}}{\omega}\right)] & \text{for } \omega \ll \omega_{\text{BH}} \\ \frac{\pi}{2} \frac{\omega_{\text{BH}}}{\omega} & \text{for } \omega \gg \omega_{\text{BH}}. \end{cases} \quad (\text{E.8})$$

The soft and hard limits have again subtly different characteristics. In the former case, we again observe a double-logarithmic enhancement, similar to the soft limit in dilute media (E.5) and stronger than the single-logarithmic behavior in the GW model, see eq. (3.34). We could again absorb one of these factors in an effective mean free path, by defining

$$\lambda_{\text{reg}}^{-1} \Big|_{L \gg \lambda} = \frac{\hat{q}_0}{m_D^2} \ln\left(\frac{\omega_{\text{BH}}}{\omega}\right), \quad (\text{E.9})$$

²⁴For consistency, compared to the “regularized expansion in eq. (3.26), one should also include an IR regulator $\sim q_{\text{min}}^2$ in the lower limit of the integral. We will neglect this subtlety for now.

which demonstrates once more the transmutation of relevant scales. Note that the spurious IR regulator q_{\min}^2 appears now on the level of $\sim \ln \ln(q_{\min}^2)$. In the hard limit, the result is again equivalent to the GW model, see (3.34), by identifying the “bare” mean free path and rescaling the Bethe-Heitler energy ω_{BH} . We recall that in this limit, the ROE opacity breaks down and should be replaced by the IOE resummation.

Open Access. This article is distributed under the terms of the Creative Commons Attribution License ([CC-BY 4.0](https://creativecommons.org/licenses/by/4.0/)), which permits any use, distribution and reproduction in any medium, provided the original author(s) and source are credited. SCOAP³ supports the goals of the International Year of Basic Sciences for Sustainable Development.

References

- [1] R.K. Ellis, W.J. Stirling and B.R. Webber, *QCD and collider physics*, Cambridge monographs on particle physics, nuclear physics, and cosmology **8**, Cambridge University Press (2011) [[DOI](#)] [[INSPIRE](#)].
- [2] Y.L. Dokshitzer, V.A. Khoze, A.H. Mueller and S.I. Troian, *Basics of perturbative QCD*, Editions Frontieres (1991) [[INSPIRE](#)].
- [3] A.J. Larkoski, I. Moult and B. Nachman, *Jet Substructure at the Large Hadron Collider: A Review of Recent Advances in Theory and Machine Learning*, *Phys. Rept.* **841** (2020) 1 [[arXiv:1709.04464](#)] [[INSPIRE](#)].
- [4] S. Marzani, G. Soyez and M. Spannowsky, *Looking inside jets: an introduction to jet substructure and boosted-object phenomenology*, Lecture Notes in Physics **958**, Springer (2019) [[DOI](#)] [[arXiv:1901.10342](#)] [[INSPIRE](#)].
- [5] M. Dasgupta, F.A. Dreyer, K. Hamilton, P.F. Monni, G.P. Salam and G. Soyez, *Parton showers beyond leading logarithmic accuracy*, *Phys. Rev. Lett.* **125** (2020) 052002 [[arXiv:2002.11114](#)] [[INSPIRE](#)].
- [6] M. Gyulassy and M. Plumer, *Jet Quenching in Dense Matter*, *Phys. Lett. B* **243** (1990) 432 [[INSPIRE](#)].
- [7] M. Gyulassy, I. Vitev, X.-N. Wang and B.-W. Zhang, *Jet quenching and radiative energy loss in dense nuclear matter*, [nucl-th/0302077](#) [[INSPIRE](#)].
- [8] S. Peigne and A.V. Smilga, *Energy losses in a hot plasma revisited*, *Phys. Usp.* **52** (2009) 659 [[arXiv:0810.5702](#)] [[INSPIRE](#)].
- [9] Y. Mehtar-Tani, J.G. Milhano and K. Tywoniuk, *Jet physics in heavy-ion collisions*, *Int. J. Mod. Phys. A* **28** (2013) 1340013 [[arXiv:1302.2579](#)] [[INSPIRE](#)].
- [10] J. Ghiglieri and D. Teaney, *Parton energy loss and momentum broadening at NLO in high temperature QCD plasmas*, *Int. J. Mod. Phys. E* **24** (2015) 1530013 [[arXiv:1502.03730](#)] [[INSPIRE](#)].
- [11] H.A. Andrews et al., *Novel tools and observables for jet physics in heavy-ion collisions*, *J. Phys. G* **47** (2020) 065102 [[arXiv:1808.03689](#)] [[INSPIRE](#)].
- [12] N. Armesto and E. Scapparini, *Heavy-ion collisions at the Large Hadron Collider: a review of the results from Run 1*, *Eur. Phys. J. Plus* **131** (2016) 52 [[arXiv:1511.02151](#)] [[INSPIRE](#)].
- [13] M. Connors, C. Nattrass, R. Reed and S. Salur, *Jet measurements in heavy ion physics*, *Rev. Mod. Phys.* **90** (2018) 025005 [[arXiv:1705.01974](#)] [[INSPIRE](#)].

- [14] R. Kogler et al., *Jet Substructure at the Large Hadron Collider: Experimental Review*, *Rev. Mod. Phys.* **91** (2019) 045003 [[arXiv:1803.06991](#)] [[INSPIRE](#)].
- [15] L. Cunqueiro and A.M. Sickles, *Studying the QGP with Jets at the LHC and RHIC*, *Prog. Part. Nucl. Phys.* **124** (2022) 103940 [[arXiv:2110.14490](#)] [[INSPIRE](#)].
- [16] L. Apolinário, Y.-J. Lee and M. Winn, *Heavy quarks and jets as probes of the QGP*, *Prog. Part. Nucl. Phys.* **127** (2022) 103990 [[arXiv:2203.16352](#)] [[INSPIRE](#)].
- [17] Y.-T. Chien and I. Vitev, *Towards the understanding of jet shapes and cross sections in heavy ion collisions using soft-collinear effective theory*, *JHEP* **05** (2016) 023 [[arXiv:1509.07257](#)] [[INSPIRE](#)].
- [18] Y. Mehtar-Tani and K. Tywoniuk, *Groomed jets in heavy-ion collisions: sensitivity to medium-induced bremsstrahlung*, *JHEP* **04** (2017) 125 [[arXiv:1610.08930](#)] [[INSPIRE](#)].
- [19] R. Kunnawalkam Elayavalli and K.C. Zapp, *Medium response in JEWEL and its impact on jet shape observables in heavy ion collisions*, *JHEP* **07** (2017) 141 [[arXiv:1707.01539](#)] [[INSPIRE](#)].
- [20] P. Caucal, E. Iancu and G. Soyez, *Deciphering the z_g distribution in ultrarelativistic heavy ion collisions*, *JHEP* **10** (2019) 273 [[arXiv:1907.04866](#)] [[INSPIRE](#)].
- [21] J. Casalderrey-Solana, G. Milhano, D. Pablos and K. Rajagopal, *Modification of Jet Substructure in Heavy Ion Collisions as a Probe of the Resolution Length of Quark-Gluon Plasma*, *JHEP* **01** (2020) 044 [[arXiv:1907.11248](#)] [[INSPIRE](#)].
- [22] F. Ringer, B.-W. Xiao and F. Yuan, *Can we observe jet P_T -broadening in heavy-ion collisions at the LHC?*, *Phys. Lett. B* **808** (2020) 135634 [[arXiv:1907.12541](#)] [[INSPIRE](#)].
- [23] P. Caucal, E. Iancu, A.H. Mueller and G. Soyez, *Nuclear modification factors for jet fragmentation*, *JHEP* **10** (2020) 204 [[arXiv:2005.05852](#)] [[INSPIRE](#)].
- [24] P. Caucal, A. Soto-Ontoso and A. Takacs, *Dynamically groomed jet radius in heavy-ion collisions*, *Phys. Rev. D* **105** (2022) 114046 [[arXiv:2111.14768](#)] [[INSPIRE](#)].
- [25] Y. Mehtar-Tani, D. Pablos and K. Tywoniuk, *Cone-Size Dependence of Jet Suppression in Heavy-Ion Collisions*, *Phys. Rev. Lett.* **127** (2021) 252301 [[arXiv:2101.01742](#)] [[INSPIRE](#)].
- [26] A. Takacs and K. Tywoniuk, *Quenching effects in the cumulative jet spectrum*, *JHEP* **10** (2021) 038 [[arXiv:2103.14676](#)] [[INSPIRE](#)].
- [27] M. Attems, J. Brewer, G.M. Innocenti, A. Mazeliauskas, S. Park, W. van der Schee et al., *The medium-modified $g \rightarrow c\bar{c}$ splitting function in the BDMPS-Z formalism*, *JHEP* **01** (2023) 080 [[arXiv:2203.11241](#)] [[INSPIRE](#)].
- [28] J. Casalderrey-Solana, Y. Mehtar-Tani, C.A. Salgado and K. Tywoniuk, *New picture of jet quenching dictated by color coherence*, *Phys. Lett. B* **725** (2013) 357 [[arXiv:1210.7765](#)] [[INSPIRE](#)].
- [29] P. Caucal, E. Iancu, A.H. Mueller and G. Soyez, *Vacuum-like jet fragmentation in a dense QCD medium*, *Phys. Rev. Lett.* **120** (2018) 232001 [[arXiv:1801.09703](#)] [[INSPIRE](#)].
- [30] V. Vaidya, *Effective Field Theory for jet substructure in heavy ion collisions*, *JHEP* **11** (2021) 064 [[arXiv:2010.00028](#)] [[INSPIRE](#)].
- [31] Y. Mehtar-Tani and K. Tywoniuk, *Sudakov suppression of jets in QCD media*, *Phys. Rev. D* **98** (2018) 051501 [[arXiv:1707.07361](#)] [[INSPIRE](#)].
- [32] R. Baier, Y.L. Dokshitzer, A.H. Mueller, S. Peigne and D. Schiff, *Radiative energy loss of high-energy quarks and gluons in a finite volume quark-gluon plasma*, *Nucl. Phys. B* **483** (1997) 291 [[hep-ph/9607355](#)] [[INSPIRE](#)].

- [33] B.G. Zakharov, *Radiative energy loss of high-energy quarks in finite size nuclear matter and quark-gluon plasma*, *JETP Lett.* **65** (1997) 615 [[hep-ph/9704255](#)] [[INSPIRE](#)].
- [34] P.B. Arnold, G.D. Moore and L.G. Yaffe, *Photon and gluon emission in relativistic plasmas*, *JHEP* **06** (2002) 030 [[hep-ph/0204343](#)] [[INSPIRE](#)].
- [35] M. Gyulassy, P. Levai and I. Vitev, *Jet quenching in thin quark gluon plasmas I: Formalism*, *Nucl. Phys. B* **571** (2000) 197 [[hep-ph/9907461](#)] [[INSPIRE](#)].
- [36] U.A. Wiedemann, *Gluon radiation off hard quarks in a nuclear environment: Opacity expansion*, *Nucl. Phys. B* **588** (2000) 303 [[hep-ph/0005129](#)] [[INSPIRE](#)].
- [37] M. Djordjevic and M. Gyulassy, *Heavy quark radiative energy loss in QCD matter*, *Nucl. Phys. A* **733** (2004) 265 [[nucl-th/0310076](#)] [[INSPIRE](#)].
- [38] M.D. Sievert and I. Vitev, *Quark branching in QCD matter to any order in opacity beyond the soft gluon emission limit*, *Phys. Rev. D* **98** (2018) 094010 [[arXiv:1807.03799](#)] [[INSPIRE](#)].
- [39] C.A. Salgado and U.A. Wiedemann, *Calculating quenching weights*, *Phys. Rev. D* **68** (2003) 014008 [[hep-ph/0302184](#)] [[INSPIRE](#)].
- [40] N. Armesto, C.A. Salgado and U.A. Wiedemann, *Medium induced gluon radiation off massive quarks fills the dead cone*, *Phys. Rev. D* **69** (2004) 114003 [[hep-ph/0312106](#)] [[INSPIRE](#)].
- [41] P.B. Arnold, *Simple Formula for High-Energy Gluon Bremsstrahlung in a Finite, Expanding Medium*, *Phys. Rev. D* **79** (2009) 065025 [[arXiv:0808.2767](#)] [[INSPIRE](#)].
- [42] P.B. Arnold, *High-energy gluon bremsstrahlung in a finite medium: harmonic oscillator versus single scattering approximation*, *Phys. Rev. D* **80** (2009) 025004 [[arXiv:0903.1081](#)] [[INSPIRE](#)].
- [43] J.-P. Blaizot, F. Domínguez, E. Iancu and Y. Mehtar-Tani, *Medium-induced gluon branching*, *JHEP* **01** (2013) 143 [[arXiv:1209.4585](#)] [[INSPIRE](#)].
- [44] A. Kurkela and U.A. Wiedemann, *Picturing perturbative parton cascades in QCD matter*, *Phys. Lett. B* **740** (2015) 172 [[arXiv:1407.0293](#)] [[INSPIRE](#)].
- [45] F. Domínguez, J.G. Milhano, C.A. Salgado, K. Tywoniuk and V. Vila, *Mapping collinear in-medium parton splittings*, *Eur. Phys. J. C* **80** (2020) 11 [[arXiv:1907.03653](#)] [[INSPIRE](#)].
- [46] C. Andres, F. Domínguez and M. Gonzalez Martinez, *From soft to hard radiation: the role of multiple scatterings in medium-induced gluon emissions*, *JHEP* **03** (2021) 102 [[arXiv:2011.06522](#)] [[INSPIRE](#)].
- [47] B.G. Zakharov, *Radiative parton energy loss and jet quenching in high-energy heavy-ion collisions*, *JETP Lett.* **80** (2004) 617 [[hep-ph/0410321](#)] [[INSPIRE](#)].
- [48] S. Caron-Huot and C. Gale, *Finite-size effects on the radiative energy loss of a fast parton in hot and dense strongly interacting matter*, *Phys. Rev. C* **82** (2010) 064902 [[arXiv:1006.2379](#)] [[INSPIRE](#)].
- [49] X. Feal and R. Vazquez, *Intensity of gluon bremsstrahlung in a finite plasma*, *Phys. Rev. D* **98** (2018) 074029 [[arXiv:1811.01591](#)] [[INSPIRE](#)].
- [50] W. Ke, Y. Xu and S.A. Bass, *Modified Boltzmann approach for modeling the splitting vertices induced by the hot QCD medium in the deep Landau-Pomeranchuk-Migdal region*, *Phys. Rev. C* **100** (2019) 064911 [[arXiv:1810.08177](#)] [[INSPIRE](#)].
- [51] C. Andres, L. Apolinário and F. Domínguez, *Medium-induced gluon radiation with full resummation of multiple scatterings for realistic parton-medium interactions*, *JHEP* **07** (2020) 114 [[arXiv:2002.01517](#)] [[INSPIRE](#)].

- [52] S. Schlichting and I. Soudi, *Medium-induced fragmentation and equilibration of highly energetic partons*, *JHEP* **07** (2021) 077 [[arXiv:2008.04928](#)] [[INSPIRE](#)].
- [53] Y. Mehtar-Tani, *Gluon bremsstrahlung in finite media beyond multiple soft scattering approximation*, *JHEP* **07** (2019) 057 [[arXiv:1903.00506](#)] [[INSPIRE](#)].
- [54] Y. Mehtar-Tani and K. Tywoniuk, *Improved opacity expansion for medium-induced parton splitting*, *JHEP* **06** (2020) 187 [[arXiv:1910.02032](#)] [[INSPIRE](#)].
- [55] J.a. Barata and Y. Mehtar-Tani, *Improved opacity expansion at NNLO for medium induced gluon radiation*, *JHEP* **10** (2020) 176 [[arXiv:2004.02323](#)] [[INSPIRE](#)].
- [56] J.a. Barata, Y. Mehtar-Tani, A. Soto-Ontoso and K. Tywoniuk, *Revisiting transverse momentum broadening in dense QCD media*, *Phys. Rev. D* **104** (2021) 054047 [[arXiv:2009.13667](#)] [[INSPIRE](#)].
- [57] J.a. Barata, Y. Mehtar-Tani, A. Soto-Ontoso and K. Tywoniuk, *Medium-induced radiative kernel with the Improved Opacity Expansion*, *JHEP* **09** (2021) 153 [[arXiv:2106.07402](#)] [[INSPIRE](#)].
- [58] P.B. Arnold, G.D. Moore and L.G. Yaffe, *Effective kinetic theory for high temperature gauge theories*, *JHEP* **01** (2003) 030 [[hep-ph/0209353](#)] [[INSPIRE](#)].
- [59] J.-P. Blaizot, F. Domínguez, E. Iancu and Y. Mehtar-Tani, *Probabilistic picture for medium-induced jet evolution*, *JHEP* **06** (2014) 075 [[arXiv:1311.5823](#)] [[INSPIRE](#)].
- [60] Y. Mehtar-Tani, C.A. Salgado and K. Tywoniuk, *Anti-angular ordering of gluon radiation in QCD media*, *Phys. Rev. Lett.* **106** (2011) 122002 [[arXiv:1009.2965](#)] [[INSPIRE](#)].
- [61] Y. Mehtar-Tani, C.A. Salgado and K. Tywoniuk, *The Radiation pattern of a QCD antenna in a dense medium*, *JHEP* **10** (2012) 197 [[arXiv:1205.5739](#)] [[INSPIRE](#)].
- [62] S. Schlichting and I. Soudi, *Splitting rates in QCD plasmas from a nonperturbative determination of the momentum broadening kernel $C(q \perp)$* , *Phys. Rev. D* **105** (2022) 076002 [[arXiv:2111.13731](#)] [[INSPIRE](#)].
- [63] G.D. Moore, S. Schlichting, N. Schlusser and I. Soudi, *Non-perturbative determination of collisional broadening and medium induced radiation in QCD plasmas*, *JHEP* **10** (2021) 059 [[arXiv:2105.01679](#)] [[INSPIRE](#)].
- [64] M. Gyulassy and X.-n. Wang, *Multiple collisions and induced gluon Bremsstrahlung in QCD*, *Nucl. Phys. B* **420** (1994) 583 [[nucl-th/9306003](#)] [[INSPIRE](#)].
- [65] P. Aurenche, F. Gelis and H. Zaraket, *A Simple sum rule for the thermal gluon spectral function and applications*, *JHEP* **05** (2002) 043 [[hep-ph/0204146](#)] [[INSPIRE](#)].
- [66] M. Gyulassy, P. Levai and I. Vitev, *Reaction operator approach to nonAbelian energy loss*, *Nucl. Phys. B* **594** (2001) 371 [[nucl-th/0006010](#)] [[INSPIRE](#)].
- [67] M. Gyulassy, P. Levai and I. Vitev, *NonAbelian energy loss at finite opacity*, *Phys. Rev. Lett.* **85** (2000) 5535 [[nucl-th/0005032](#)] [[INSPIRE](#)].
- [68] C. Andres, F. Domínguez and M. Gonzalez Martinez, private communication (2022).
- [69] B.G. Zakharov, *Fully quantum treatment of the Landau-Pomeranchuk-Migdal effect in QED and QCD*, *JETP Lett.* **63** (1996) 952 [[hep-ph/9607440](#)] [[INSPIRE](#)].
- [70] P. Arnold and S. Iqbal, *The LPM effect in sequential bremsstrahlung*, *JHEP* **04** (2015) 070 [[arXiv:1501.04964](#)] [[INSPIRE](#)].
- [71] P. Arnold, T. Gorda and S. Iqbal, *The LPM effect in sequential bremsstrahlung: nearly complete results for QCD*, *JHEP* **11** (2020) 053 [[arXiv:2007.15018](#)] [[INSPIRE](#)].

- [72] P. Arnold, T. Gorda and S. Iqbal, *The LPM effect in sequential bremsstrahlung: analytic results for sub-leading (single) logarithms*, *JHEP* **04** (2022) 085 [[arXiv:2112.05161](#)] [[INSPIRE](#)].
- [73] A. Banfi, F.A. Dreyer and P.F. Monni, *Higher-order non-global logarithms from jet calculus*, *JHEP* **03** (2022) 135 [[arXiv:2111.02413](#)] [[INSPIRE](#)].
- [74] J.a. Barata, F. Domínguez, C.A. Salgado and V. Vila, *A modified in-medium evolution equation with color coherence*, *JHEP* **05** (2021) 148 [[arXiv:2101.12135](#)] [[INSPIRE](#)].
- [75] Y. Mehtar-Tani and S. Schlichting, *Universal quark to gluon ratio in medium-induced parton cascade*, *JHEP* **09** (2018) 144 [[arXiv:1807.06181](#)] [[INSPIRE](#)].
- [76] J.-P. Blaizot, E. Iancu and Y. Mehtar-Tani, *Medium-induced QCD cascade: democratic branching and wave turbulence*, *Phys. Rev. Lett.* **111** (2013) 052001 [[arXiv:1301.6102](#)] [[INSPIRE](#)].
- [77] J.-P. Blaizot and Y. Mehtar-Tani, *Energy flow along the medium-induced parton cascade*, *Annals Phys.* **368** (2016) 148 [[arXiv:1501.03443](#)] [[INSPIRE](#)].
- [78] *Medium-induced kernels*, <https://github.com/adam-takacs/kernels.git>.
- [79] B. Schenke, C. Gale and S. Jeon, *MARTINI: An Event generator for relativistic heavy-ion collisions*, *Phys. Rev. C* **80** (2009) 054913 [[arXiv:0909.2037](#)] [[INSPIRE](#)].
- [80] K. Kutak, W. Flaczek and R. Straka, *Solutions of evolution equations for medium-induced QCD cascades*, *Eur. Phys. J. C* **79** (2019) 317 [[arXiv:1811.06390](#)] [[INSPIRE](#)].
- [81] E. Blanco, K. Kutak, W. Flaczek, M. Rohrmoser and R. Straka, *Medium induced QCD cascades: broadening and rescattering during branching*, *JHEP* **04** (2021) 014 [[arXiv:2009.03876](#)] [[INSPIRE](#)].
- [82] A. Idilbi and A. Majumder, *Extending Soft-Collinear-Effective-Theory to describe hard jets in dense QCD media*, *Phys. Rev. D* **80** (2009) 054022 [[arXiv:0808.1087](#)] [[INSPIRE](#)].
- [83] G. Ovanessian and I. Vitev, *An effective theory for jet propagation in dense QCD matter: jet broadening and medium-induced bremsstrahlung*, *JHEP* **06** (2011) 080 [[arXiv:1103.1074](#)] [[INSPIRE](#)].
- [84] A. Majumder, *Incorporating Space-Time Within Medium-Modified Jet Event Generators*, *Phys. Rev. C* **88** (2013) 014909 [[arXiv:1301.5323](#)] [[INSPIRE](#)].
- [85] X.-f. Guo and X.-N. Wang, *Multiple scattering, parton energy loss and modified fragmentation functions in deeply inelastic $e A$ scattering*, *Phys. Rev. Lett.* **85** (2000) 3591 [[hep-ph/0005044](#)] [[INSPIRE](#)].
- [86] X.-N. Wang and Y. Zhu, *Medium Modification of γ -jets in High-energy Heavy-ion Collisions*, *Phys. Rev. Lett.* **111** (2013) 062301 [[arXiv:1302.5874](#)] [[INSPIRE](#)].
- [87] J. Ghiglieri, G.D. Moore and D. Teaney, *Jet-Medium Interactions at NLO in a Weakly-Coupled Quark-Gluon Plasma*, *JHEP* **03** (2016) 095 [[arXiv:1509.07773](#)] [[INSPIRE](#)].
- [88] S.P. Adhya, C.A. Salgado, M. Spousta and K. Tywoniuk, *Medium-induced cascade in expanding media*, *JHEP* **07** (2020) 150 [[arXiv:1911.12193](#)] [[INSPIRE](#)].
- [89] S.P. Adhya, C.A. Salgado, M. Spousta and K. Tywoniuk, *Multi-partonic medium induced cascades in expanding media*, *Eur. Phys. J. C* **82** (2022) 20 [[arXiv:2106.02592](#)] [[INSPIRE](#)].

Article III

Precise description of medium-induced emissions

J. H. Isaksen and K. Tywoniuk

Submitted to *Journal of High Energy Physics*, (2023)

Precise description of medium-induced emissions

Johannes Hamre Isaksen^a and Konrad Tywoniuk^a

^a*Department of Physics and Technology, University of Bergen, 5007 Bergen, Norway*

E-mail: johannes.isaksen@uib.no, konrad.tywoniuk@uib.no

ABSTRACT: We study jet fragmentation via final-state parton splittings in the medium. These processes are usually calculated theoretically by invoking the large- N_c limit. In this paper we perform the first computation of a $1 \rightarrow 2$ parton splitting in a thermal medium at finite numbers of colors N_c , for arbitrary momentum-sharing fraction z and with full transverse dynamics. We show how the problem can be transformed into a system of coupled Schrödinger equations, that we solve numerically. The novel numerical results are used to estimate the accuracy of several widely used approximations. We check the error introduced while going from finite N_c (i.e. $N_c = 3$) to the large- N_c limit, which we find to be small. For unbalanced splittings, e.g. when $z \rightarrow 0$, only one of the partons is affected by transverse momentum exchanges with the medium. The emission process then separates into a term responsible for the $1 \rightarrow 2$ splitting and the subsequent independent broadening of the daughter partons. This is also referred to as the factorizable term. For finite z , further contributions arise that are responsible for the coherent color dynamics of the two-parton system, and these are referred to as non-factorizable terms. These were argued to be small for soft (unbalanced) splittings and for large media. In this work we therefore determine the accuracy of keeping only the factorizable term of the large- N_c solution. We find that the error is insignificant at a small splitting fraction $z \sim 0$, but can be sizable in a more balanced splitting with $z \sim 0.5$. Finally, we also examine the eikonal approximation, which amounts to approximating the partons' paths through the medium as straight lines. We find that it is associated with a substantial error for the parameter values we explored in this work.

Contents

1	Introduction	2
2	Basic elements and notation	4
3	Describing parton splitting in the medium	6
3.1	Derivation of the emissions spectrum	6
3.2	Isolating the medium contribution	11
3.3	The energy spectrum	14
4	Photon splitting in the harmonic oscillator approximation	15
4.1	Harmonic oscillator approximation	15
4.2	Pair production	16
4.3	The large- N_c limit	18
4.4	Factorizable and non-factorizable contributions to the spectrum	20
5	Numerical results	21
5.1	The in-in contribution	23
5.2	Validation of the numerical results and comparison to approximate solutions	25
5.3	Precision calculation of splitting function in the Lund plane	30
6	Conclusion and outlook	32
A	Simplifying n-point functions	33
A.1	Four-point function	33
A.2	Three-point function	35
A.3	Two-point function	37
A.4	Summary of color structure	38
B	Calculation of different processes	38
B.1	Pair production	38
B.2	Gluon-gluon splitting	40
C	Deriving the Schrödinger equation	42
D	The eikonal limit	44

1 Introduction

High energy heavy-ion collisions provide a glimpse of a new state of nuclear matter that emerge only when extreme energy densities are achieved. Under these conditions color degrees of freedom, carried by the fundamental quark and gluon excitations, are released and influence the material properties of the system, hence the name quark-gluon plasma (QGP) [1]. One way of measuring the properties of the QGP is to rely on internal probes that were created concurrently with the plasma. So-called “hard” probes refer to a class of observables that, due to the large energy or mass scale involved, are created at very short time scales such that their production mechanism is independent of the complicated processes leading to the formation of a QGP and, therefore, are effectively happening in the vacuum. However, in subsequent stages, when these probes traverse a spatially extended and evolving QGP to reach the detector, modifications of their properties can occur. By comparing the same “hard” observable in proton-proton (p - p) collisions and in heavy-ion collisions (A - A), one can extract information that can be compared to first-principle calculations of the QGP dynamics.

One of the most useful internal probes in the pursuit of studying QCD and the QGP are so-called jets. These are collimated sprays of energetic hadrons originating from the fragmentation of a highly virtual initial parton [2, 3]. Jets are produced both in p - p collisions and in heavy ion collisions. In p - p collisions the fragmentation process brings the initial high virtuality of the parton, which is of the order of its transverse momentum p_T , down to the hadronization scale where non-perturbative effects dominate [4–6]. In heavy-ion collisions, however, the medium provides a scale related to the achieved energy density that interferes with the vacuum-like fragmentation. The induced interactions modify the jet properties compared to the vacuum baseline, leading to a set of phenomena that are usually referred to as *jet quenching* [7, 8], for reviews see [9–14]. Given that jets probe a wide range of scales of heavy-ion collisions, they can serve as probes of the initial pre-equilibrium dynamics [15, 16] and anisotropy of the medium [17, 18], as well as of the late hydrodynamic evolution [19]. There is a substantial experimental effort at RHIC and the LHC in quantifying the effects of jet quenching, focusing on a range of different observables [14, 20–24].

The dominant driver of jet-medium modifications is induced radiative processes. In dense media, where multiple scatterings are important, the in-medium splitting functions can be understood from the underlying scales that separate the limiting cases [25–31]. This is true whether the spectra are differential in both the longitudinal momentum splitting variable z and the relative transverse momentum $dI/[dz d^2\mathbf{p}]$ or simply dI/dz . The full problem can be tackled by numerical [32–37] or analytical techniques [38–43].

Medium-induced radiation is mainly responsible for the diffusion of jet energy to large angles, leading to energy loss of jets which induces a bias on the observed jet samples. The total jet energy loss is also sensitive to the medium parameters through the number of resolved substructures acting as sources for medium-induced emissions [44, 45]. When emitted at small angles, medium-induced emissions can also modify jet substructure [46–49]. In both cases described above, it is desirable to have a precise description of medium-

induced emissions to exploit to a maximal extent jet observables as probes of the QGP.

It is well understood that radiative processes in the medium are non-local, meaning that they extend over finite longitudinal distances in the medium [25, 50–53]. The characteristic *branching*, or *formation*, time arises from the transverse momentum accumulated during the splitting. In dense media, dominated by Gaussian diffusion, the dispersion in transverse momentum grows linearly with time, i.e. $\langle k_{\perp}^2 \rangle = \hat{q}t$, where \hat{q} is the so-called jet quenching parameter. The resulting branching time, scaling as $t_{\text{br}} \sim \omega/\langle k_{\perp}^2 \rangle \sim \sqrt{\omega/\hat{q}}$, can therefore extend up to the length of the medium, $t_{\text{br}} \sim L$, for sufficiently energetic splittings, with $\omega \sim \hat{q}L^2$. On the contrary, sufficiently soft splitting splittings should occur quasi-instantaneously in the medium, i.e. with $t_{\text{br}} \ll L$.

However, the non-locality of medium-induced emissions also has a more profound consequence. It turns out [28] that the splitting products can remain *color* correlated to each other over an extended period of time. During this time, the pair interacts coherently with the medium as it is allowed to explore different color representations. After the pair decorrelates, both daughters continue to broaden independently until they exit the medium. Using analytical calculations in the large- N_c limit for gluon-to-gluon branching, the decoherence time was estimated to be of the same order as the branching time t_{br} [28], see also [54] for a similar discussion. The large- N_c approximation consists of taking the number of colors, N_c , to infinity which greatly simplifies the color structure of the problem, making it easier to solve. Hence, for sufficiently short branching (and decoherence) times, non-factorizable contributions are expected to scale as t_{br}/L and quasi-instantaneous $1 \rightarrow 2$ splittings factorize from long-distance transverse momentum broadening. This factorization, which we will critically examine below, lends support to a probabilistic, Markovian picture of multiple emissions [55], see also [37] for similar rate equations in the context of thermal effects.

Contributions that violate this probabilistic picture become important for long formation, or branching, times. Multiple emissions with overlapping formation times lead to interesting factorization-breaking effects [56–61]. In particular, in the regime of strongly ordered formation times, one can reinterpret part of these effects, namely the ones as contribute with logarithms of the medium length, i.e. $\log^2 L$ and $\log L$, as radiative corrections to the jet quenching parameter \hat{q} [62–66]. It is still an open question how to extend the description of multiple in-medium splitting beyond the probabilistic picture, see e.g. [43, 67, 68].

Kinematically, large formation times correspond to balanced splittings occurring at large relative angles. In order to overcome some of these problems and to focus on hard $1 \rightarrow 2$ emissions in the medium, i.e. when both daughter partons carry a large longitudinal momentum ($z \approx 1/2$ and $E \rightarrow \infty$), one introduced the eikonal approximation [30]. This consists of fixing the straight-line trajectories of the partons through the medium, thus neglecting completely their transverse momentum broadening. In this approximation, the problem reduces most clearly to that of decoherence of the intermediate partons that move apart from each other in transverse space as $\sim \theta t$, where θ is the relative angle of the pair. Going beyond the large- N_c approximation was then achieved in [69]. For a further discussion of color dynamics in the QGP, see also [70–72]. Nevertheless, the eikonal

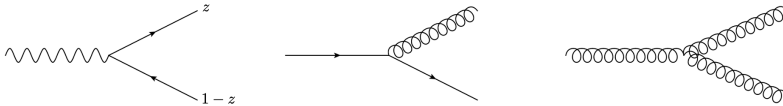


Figure 1. Three different splitting processes where a parton with LC longitudinal momentum $p^+ \equiv E$ splits into two partons with momenta zE and $(1-z)E$. The processes shown are $\gamma \rightarrow q\bar{q}$, $q \rightarrow gq$, and $g \rightarrow gg$.

approximation becomes unreliable exactly where the medium scales become important, where transverse momentum broadening starts playing an important role.

In this work, we address the full calculation of the medium-induced splitting function in relative angle θ (or transverse momentum \mathbf{p}) and longitudinal momentum-sharing fraction z of one single parton into two, for some relevant examples see Fig. 1, for dilute as well as dense media, surpassing all previous approximations.¹ This includes effects from a finite number of colors N_c and comprises all non-factorizable contributions. We arrive at a simple formula that generalizes well-known results obtained earlier only in the limit of soft emissions, i.e. $z \ll 1$ [36, 42, 52], and resembles the heuristic picture of a two-step process of emission and subsequent broadening argued for above. However, it involves a novel building block, the quadrupole correlation function, that describes the full dynamics of the daughter parton pair after the splitting. The quadrupole function is governed by a hierarchy of coupled Schrödinger equations, which describes all possible intermediate color representations of the daughter parton pair. Our novel approach allows us to critically examine the conventional approximations and shed light on the dynamics of large-angle and balanced emissions.

We also analyze the deviations from the *factorization* of the two-parton emission spectrum, and examine the size of the corrections stemming from non-factorizable processes, whether at large- or finite- N_c , in a wide kinematic range.

The paper is structured in the following way: in Sec. 2 we will introduce the basic elements and notation that we will use throughout the paper. In Sec. 3.1 we will derive the spectrum for medium-induced emissions on general grounds, and show how the different approximations simplify the calculations. Lastly, in Sec. 4 we do the calculation for a specific splitting process, and in Sec. 5 we show the results of our numerical calculation.

2 Basic elements and notation

To describe the medium interaction we consider how hard QCD partons behave in an external classical colored field. We work in light-cone gauge $A^+ = 0$.² A parton with large light-cone (LC) “energy” $E \equiv p^+$ (or, more precisely, longitudinal momentum) couples mainly to the reciprocal background field component $\mathcal{A}(t, \mathbf{r}) \equiv A^-(x^+, x^- \simeq 0, \mathbf{r})$, where

¹In-medium splitting functions (or exclusive two-particle cross sections) were also computed in the so-called *opacity* expansion [73, 74], appropriate for dilute media [43].

²We use the conventions $x^\mu = (x^+, x^-, \mathbf{x})$, where $x^+ = (x^0 + x^3)/2$, $x^- = x^0 - x^3$ and $\mathbf{x} = (x^1, x^2)$, and similarly for other variables.

we have introduced the light-cone “time” $t \equiv x^+$ and we have neglected the extent of the background field in the x^- direction. This immediately guarantees that no longitudinal momentum is exchanged between the parton and the background field, restricting the dynamics to the two-dimensional transverse space at each instant of light-cone time.

Then, the in-medium propagation is described by the propagator,

$$(\mathbf{x}|\mathcal{G}_R(t, t_0)|\mathbf{x}_0) = \int_{\mathbf{x}_0}^{\mathbf{x}} \mathcal{D}\mathbf{r} \exp \left[i \frac{E}{2} \int_0^t ds \dot{\mathbf{r}}^2(s) \right] V_R(t, t_0; [\mathbf{r}]), \quad (2.1)$$

describing the transition of a parton from transverse position \mathbf{x}_0 at time t_0 to the transverse position \mathbf{x} at time t (it is implicitly assumed that $t > t_0$). The parton is constantly “kicked” in the transverse plane by the medium interaction, and it can therefore take an infinite number of possible paths through the medium. These are summed up in the path integral.³

The interaction with the medium also involves an exchange of color. The color rotation is encapsulated in a Wilson line along the parton trajectory, given by

$$V_R(t, t_0; [\mathbf{r}]) = \mathcal{P} \exp \left[ig \int_{t_0}^t ds \mathcal{A}^a(s, \mathbf{r}(s)) T_R^a \right]. \quad (2.2)$$

Here, the label R refers to the fundamental representation of $SU(3)$ for quarks, i.e. $R = F$ with $(T^a)_{ij} \equiv t_{ij}^a$, and the adjoint representation for gluons, i.e. $R = A$ with $(T^b)^{ac} \equiv if^{abc}$.

Finally, for the anti-quark, the propagator is given by

$$(\mathbf{x}_0|\bar{\mathcal{G}}_R(t_0, t)|\mathbf{x}) = \int_{\mathbf{x}_0}^{\mathbf{x}} \mathcal{D}\mathbf{r} \exp \left[i \frac{E}{2} \int_0^t ds \dot{\mathbf{r}}^2(s) \right] V_R^\dagger(t, t_0; [\mathbf{r}]). \quad (2.3)$$

Here, we have used the fact that the background field is real, i.e. $\mathcal{A}^{a*}(s, \mathbf{r}) = \mathcal{A}^a(s, \mathbf{r})$.

In vacuum, i.e. setting $\mathcal{A} = 0$, the propagator simply reduces to its vacuum counterpart

$$(\mathbf{x}|\mathcal{G}_0(t, t_0)|\mathbf{x}_0) = \frac{E}{2\pi i(t-t_0)} e^{i \frac{E}{2} \frac{(\mathbf{x}-\mathbf{x}_0)^2}{(t-t_0)}}. \quad (2.4)$$

This can be written in momentum space as

$$(\mathbf{p}|\mathcal{G}_0(t, t_0)|\mathbf{p}_0) = (2\pi)^2 \delta(\mathbf{p} - \mathbf{p}_0) e^{-i \frac{\mathbf{p}^2}{2E}(t-t_0)}. \quad (2.5)$$

Although we have skimmed over some details, the adiabatic turn-off prescription, which is crucial when the time arguments tend to $\pm\infty$, can easily be reinstated.

At high energy, i.e. $E \rightarrow \infty$, the parton becomes increasingly constrained to the classical trajectory between the end-points, and the path integral in Eq. (2.1) becomes trivial, reducing to a product of a free propagator and a Wilson line,

$$\mathcal{G}_R(t, t_0) \simeq \mathcal{G}_0(t, t_0) V_R(t, t_0; [\mathbf{x}_{cl}]), \quad (2.6)$$

³Switching between transverse coordinate basis and transverse momentum basis is straightforward by applying $|\mathbf{x}\rangle = \int_{\mathbf{p}} e^{-i\mathbf{p}\cdot\mathbf{x}}|\mathbf{p}\rangle$ and $\langle\mathbf{x}| = \int_{\mathbf{p}} e^{i\mathbf{p}\cdot\mathbf{x}}\langle\mathbf{p}|$ for the initial and final state bases, respectively. Throughout, we use the notation $\int_q \equiv \int \frac{d^2q}{(2\pi)^2}$.

where $\mathbf{x}_{\text{cl}}(s) = \frac{t-s}{t-t_0}\mathbf{x}_0 + \frac{s-t_0}{t-t_0}\mathbf{x}$. This is called the eikonal approximation and can be used to simplify calculations when considering highly energetic partons. Correspondingly, deviations from the straight-line trajectory are called non-eikonal corrections, see also [75, 76] for a systematic expansion in non-eikonal corrections. However, in the general case for jet quenching observables in dense heavy-ion collisions the full propagators, as given in Eq. (2.1), are used.

When computing observables, combining the parton evolution in the amplitude and the complex-conjugate amplitude, one has to account for the fluctuations of the background field. Assuming that the amplitude of the background field is Gaussian, the medium average over the classical field is given by

$$\langle \mathcal{A}^a(t, \mathbf{r}) \mathcal{A}^{b*}(t', \mathbf{r}') \rangle = \delta^{ab} n(t) \delta(t-t') \gamma(\mathbf{r} - \mathbf{r}'), \quad (2.7)$$

where $n(t)$ is the density of scattering centers and the function $\gamma(\mathbf{r})$ is given by

$$\gamma(\mathbf{r}) = \int_{\mathbf{q}} e^{i\mathbf{q}\cdot\mathbf{r}} \frac{d^2\sigma_{\text{el}}}{d^2\mathbf{q}}, \quad (2.8)$$

and $d^2\sigma_{\text{el}}/d^2\mathbf{q}$ is the elastic scattering cross-section in the medium.

3 Describing parton splitting in the medium

3.1 Derivation of the emissions spectrum

In this section, we discuss the $1 \rightarrow 2$ splitting process on the partonic level in a deconfined medium. We consider the splitting of a parton of type a with initial transverse momentum \mathbf{p}_0 and energy E into two partons of types b and c , with transverse momenta and energies $(k^+ = zE, \mathbf{k})$ and $(q^+ = (1-z)E, \mathbf{q})$, respectively, where z is the energy sharing fraction. The conservation of energy is implicitly accounted for in all the vertices. This is depicted in Fig. 2, where we have placed the process occurring in the amplitude upstairs, and the corresponding process in the complex-conjugate amplitude downstairs. It could be one of many possible splitting processes involving photons, quarks and gluons, but here we choose to keep the notation general and postpone the discussion of a concrete process, namely $\gamma \rightarrow q\bar{q}$, to Sec. 4.2. For further details about the calculation, we refer to App. B, where we explicitly have derived the double-inclusive cross sections for $\gamma \rightarrow q\bar{q}$ and $g \rightarrow gg$ splittings.

After performing the medium averages and simplifying the color structure, we can write the inclusive splitting cross section as

$$\begin{aligned} \frac{d\sigma}{d\Omega_{\mathbf{k}} d\Omega_{\mathbf{q}}} &= \frac{g^2 C_R}{(2E)^2} \text{Re} \int_0^\infty dt_2 \int_0^{t_2} dt_1 \int_{\mathbf{p}_0 \mathbf{p}_1 \mathbf{k}_1 \mathbf{k}_2 \bar{\mathbf{p}}_0 \bar{\mathbf{p}}_2 \bar{\mathbf{k}}_2} \Gamma^i(\mathbf{k}_1 - z\mathbf{p}_1) \cdot \Gamma^{\bar{i}}(\bar{\mathbf{k}}_2 - z\bar{\mathbf{p}}_2) \\ &\quad \times (\mathbf{k}, \mathbf{q}; \mathbf{k}, \mathbf{q} | S^{(4)}(t_\infty, t_2) | \mathbf{k}_2, \mathbf{q}_2; \bar{\mathbf{k}}_2, \bar{\mathbf{p}}_2 - \bar{\mathbf{k}}_2) \\ &\quad \times (\mathbf{k}_2, \mathbf{q}_2; \bar{\mathbf{p}}_2 | S^{(3)}(t_2, t_1) | \mathbf{k}_1, \mathbf{p}_1 - \mathbf{k}_1; \bar{\mathbf{p}}_1) \\ &\quad \times (\mathbf{p}_1; \bar{\mathbf{p}}_1 | S^{(2)}(t_1, 0) | \mathbf{p}_0; \bar{\mathbf{p}}_0) \langle \mathcal{M}_0^i(E, \mathbf{p}_0) \mathcal{M}_0^{\bar{i}*}(E, \bar{\mathbf{p}}_0) \rangle, \end{aligned} \quad (3.1)$$

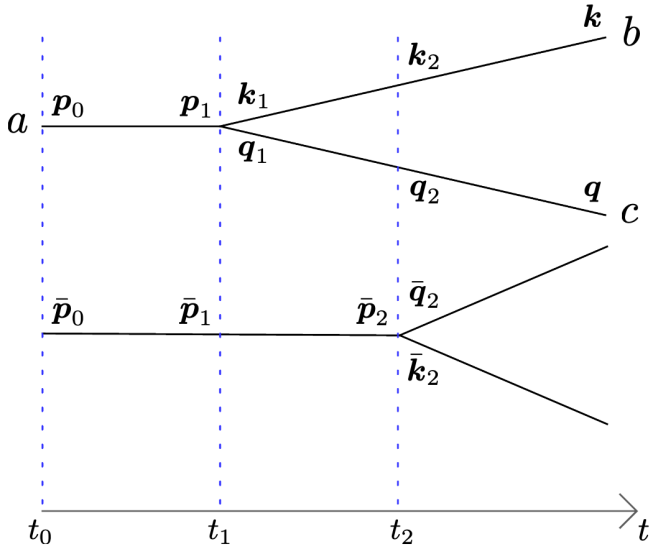


Figure 2. The process of a parton splitting into two, where the time runs from left to right. The amplitude is depicted on the top and the complex conjugate amplitude is on the bottom. All lines refer to propagators that include arbitrarily many medium interactions. Due to the lack of exchange of longitudinal momentum with the medium, the energy stays constant along the lines but the transverse momentum (or transverse position) is continuously updated according to Eq. (2.1). The parton is created at the initial time $t_0 = 0$, and the splitting occurs at time t_1 in the amplitude and at a later time t_2 in the complex conjugate amplitude. Due to the transverse momentum conservation in the vertices, $\mathbf{q}_1 = \mathbf{p}_1 - \mathbf{k}_1$ and $\bar{\mathbf{q}}_2 = \bar{\mathbf{p}}_2 - \bar{\mathbf{k}}_2$.

where the invariant phase space element is $d\Omega_p = dE d^2\mathbf{p}/(2E(2\pi)^3)$. Here, C_R is the squared Casimir operator of the initial parton, or in other words the color charge of the emitter.⁴ The index “i” represents the spin/polarization state of the initial parton before the splitting, which is averaged over, and the product of vertices, i.e. $\Gamma^i \cdot \Gamma^{\bar{i}}$, involves a further summation over the final spin/polarization states.

Since we will be interested in the cross section averaged over azimuthal angles, we can simplify the vertex structure as

$$C_R \Gamma^i(\mathbf{k}_1 - z\mathbf{p}_1) \cdot \Gamma^{\bar{i}}(\bar{\mathbf{k}}_2 - z\bar{\mathbf{p}}_2) = \frac{4P_{ba}(z)}{z(1-z)} (\mathbf{k}_1 - z\mathbf{p}_1) \cdot (\bar{\mathbf{k}}_2 - z\bar{\mathbf{p}}_2) \delta^{i\bar{i}}, \quad (3.2)$$

for further details see App. B. In effect, the product of fundamental vertices becomes directly proportional to the Altarelli-Parisi splitting function $P_{ba}(z)$ [77–79]. The sum over initial polarizations now becomes trivial, allowing to isolate the cross section for the Born process, as $d\sigma_0/d\Omega_{p_0} = \langle |\mathcal{M}_0(E, \mathbf{p}_0)|^2 \rangle$. Then, we can finally write

$$\frac{d\sigma}{d\Omega_q d\Omega_k} = 2E \int d\Omega_{p_0} 2\pi \delta(E - k^+ - q^+) P_2(\mathbf{k}, \mathbf{q}; \mathbf{p}_0) \frac{d\sigma_0}{d\Omega_{p_0}}. \quad (3.3)$$

⁴Concretely, $C_R = N_c$ for $g \rightarrow gg$, $C_R = C_F$ for $q \rightarrow qg$ and $C_R = T_R = \frac{1}{2}$ for $g \rightarrow q\bar{q}$ and $\gamma \rightarrow q\bar{q}$.

This is the final answer for the two-body cross section in terms of the momenta of the two final-state particles.

The propagation of the partons in amplitude and complex-conjugate amplitude during the various stages of the splitting process, as depicted in Fig. 2, is encoded in the two-point, three-point, and four-point functions. These are in turn given by correlators of the dressed propagators, namely

$$(\mathbf{p}_1; \bar{\mathbf{p}}_1 | S^{(2)}(t_1, t_0) | \mathbf{p}_0; \bar{\mathbf{p}}_0) = d_a^{(2)} \langle (\mathbf{p}_1 | \mathcal{G}_a | \mathbf{p}_0) (\bar{\mathbf{p}}_0 | \mathcal{G}_a^\dagger | \bar{\mathbf{p}}_1) \rangle, \quad (3.4)$$

$$(\mathbf{k}_2, \mathbf{q}_2; \bar{\mathbf{p}}_2 | S^{(3)}(t_2, t_1) | \mathbf{k}_1, \mathbf{p}_1 - \mathbf{k}_1; \bar{\mathbf{p}}_1) = d_{abc}^{(3)} \langle (\mathbf{k}_2 | \mathcal{G}_b | \mathbf{k}_1) (\mathbf{q}_2 | \mathcal{G}_c | \mathbf{p}_1 - \mathbf{k}_1) (\bar{\mathbf{p}}_1 | \mathcal{G}_a^\dagger | \bar{\mathbf{p}}_2) \rangle, \quad (3.5)$$

and finally,

$$\begin{aligned} & (\mathbf{k}, \mathbf{q}; \mathbf{k}, \mathbf{q} | S^{(4)}(t_\infty, t_2) | \mathbf{k}_2, \mathbf{q}_2; \bar{\mathbf{k}}_2, \bar{\mathbf{p}}_2 - \bar{\mathbf{k}}_2) \\ &= d_{bc}^{(4)} \langle (\mathbf{k} | \mathcal{G}_b | \mathbf{k}_2) (\mathbf{q} | \mathcal{G}_c | \mathbf{q}_2) (\bar{\mathbf{p}}_2 - \bar{\mathbf{k}}_2 | \mathcal{G}_c^\dagger | \mathbf{q}) (\bar{\mathbf{k}}_2 | \mathcal{G}_b^\dagger | \mathbf{k}) \rangle, \end{aligned} \quad (3.6)$$

where we have dropped the time dependence of the propagators on the right-hand side of the equations. The process-dependent color factors $d_a^{(2)}$, $d_{abc}^{(3)}$ and $d_{bc}^{(4)}$ are responsible for color connecting the propagators and normalizing to the total color charge. We have here also neglected all color indices to be as general as possible. The various color structures for several concrete splitting processes can be inspected in App. A.4.

The n -point correlators possess a translation symmetry which renders them invariant under the simultaneous transverse shift of all the coordinates. In momentum space, this becomes manifest as the conservation of momentum incoming and outgoing legs, see App. A for details. Concretely, the four-point function then becomes

$$\begin{aligned} & (\mathbf{k}, \mathbf{q}; \mathbf{k}, \mathbf{q} | S^{(4)}(t_\infty, t_2) | \mathbf{k}_2, \mathbf{q}_2; \bar{\mathbf{k}}_2, \bar{\mathbf{p}}_2 - \bar{\mathbf{k}}_2) \\ &= (2\pi)^2 \delta^2(\mathbf{q}_2 + \mathbf{k}_2 - \bar{\mathbf{p}}_2) \\ &\times \mathcal{S}^{(4)}((1-z)\mathbf{k} - z\mathbf{q}, \mathbf{k}_2 - z\bar{\mathbf{p}}_2, \bar{\mathbf{k}}_2 - z\bar{\mathbf{p}}_2, \bar{\mathbf{p}}_2 - \mathbf{k} - \mathbf{q} | t_\infty, t_2), \end{aligned} \quad (3.7)$$

see Eq. (A.11). Enforcing the delta-function appearing in (3.7), i.e. $\bar{\mathbf{p}}_2 = \mathbf{q}_2 + \mathbf{k}_2$, the three-point function (3.5) further becomes

$$\begin{aligned} & (\mathbf{k}_2, \bar{\mathbf{p}}_2 - \mathbf{k}_2; \bar{\mathbf{p}}_2 | S^{(3)}(t_2, t_1) | \mathbf{k}_1, \mathbf{p}_1 - \mathbf{k}_1; \bar{\mathbf{p}}_1) \\ &= (2\pi)^2 \delta(\mathbf{p}_1 - \bar{\mathbf{p}}_1) \mathcal{S}^{(3)}(\mathbf{k}_2 - z\bar{\mathbf{p}}_2, \mathbf{k}_1 - z\mathbf{p}_1, \mathbf{p}_1 - \bar{\mathbf{p}}_2 | t_2, t_1). \end{aligned} \quad (3.8)$$

At this point, it becomes apparent that it makes sense to introduce new momentum variables, namely

$$\mathbf{l}_1 = \mathbf{k}_1 - z\mathbf{p}_1, \quad \mathbf{l}_2 = \mathbf{k}_2 - z\bar{\mathbf{p}}_2, \quad \text{and} \quad \bar{\mathbf{l}}_2 = \bar{\mathbf{k}}_2 - z\bar{\mathbf{p}}_2. \quad (3.9)$$

Finally, using that $\mathbf{p}_1 = \bar{\mathbf{p}}_1$ in (3.4), the two-point function becomes

$$(\mathbf{p}_1; \mathbf{p}_1 | S^{(2)}(t_1 - t_0) | \mathbf{p}_0; \bar{\mathbf{p}}_0) = (2\pi)^2 \delta(\mathbf{p}_0 - \bar{\mathbf{p}}_0) \mathcal{P}(\mathbf{p}_1 - \mathbf{p}_0 | t_1, t_0). \quad (3.10)$$

where $\mathcal{P}(\mathbf{p}|t_1, t_0)$ is the broadening function. In the new momentum variables, the splitting function becomes

$$\begin{aligned}
P_2(\mathbf{p}, \mathbf{P}; \mathbf{p}_0) &= \frac{g^2 P_{ba}(z)}{z(1-z)E^2} \text{Re} \int_0^\infty dt_1 \int_{t_1}^\infty dt_2 \\
&\times \int_{\mathbf{p}_1 \mathbf{l}_1 \mathbf{l}_2 \bar{\mathbf{p}}_2 \bar{\mathbf{l}}_2} \mathbf{l}_1 \cdot \bar{\mathbf{l}}_2 \mathcal{S}^{(4)}(\mathbf{p}, \mathbf{l}_2, \bar{\mathbf{l}}_2, \bar{\mathbf{p}}_2 - \mathbf{P} | t_\infty, t_2) \\
&\times \mathcal{S}^{(3)}(\mathbf{l}_2, \mathbf{l}_1, \mathbf{p}_1 - \bar{\mathbf{p}}_2 | t_2, t_1) \mathcal{P}(\mathbf{p}_1 - \mathbf{p}_0 | t_1, t_0), \tag{3.11}
\end{aligned}$$

where we have introduced the total and the relative transverse momentum of the pair,

$$\mathbf{P} \equiv \mathbf{k} + \mathbf{q}, \quad \text{and} \quad \mathbf{p} \equiv (1-z)\mathbf{k} - z\mathbf{q}, \tag{3.12}$$

respectively.

In what follows, we will be interested in the information about the relative transverse momentum, while the total momentum \mathbf{P} can be integrated out. The Jacobian from the change of variables yields $d\sigma/[d\Omega_k d\Omega_q] = (2\pi)^6 4z(1-z)E d\sigma/[dz dE d^2\mathbf{p} d^2\mathbf{P}]$. The reduced differential cross section in (3.3) then becomes

$$\int_{\mathbf{P}} \frac{d\sigma}{d\Omega_k d\Omega_q} = \frac{dI}{dz d^2\mathbf{p}} \frac{d\sigma_0}{dE}. \tag{3.13}$$

The integrals over $\bar{\mathbf{p}}_2$ and \mathbf{p}_1 can now be dealt with independently, by shifting separately the integration variables $\bar{\mathbf{p}}_2 - \mathbf{P} \rightarrow \mathbf{P}$ and $\bar{\mathbf{p}}_2 \rightarrow \mathbf{p}_1 - \bar{\mathbf{p}}_2$, and we end up with a rather compact formula from the emission spectrum in momentum space

$$\begin{aligned}
(2\pi)^2 \frac{dI}{dz d^2\mathbf{p}} &= \frac{1}{4\pi z(1-z)} \int_{\mathbf{P}} P_2(\mathbf{p}, \mathbf{P}; \mathbf{p}_0) \\
&= \frac{\alpha_s P_{ba}(z)}{\omega^2} \text{Re} \int_0^\infty dt_1 \int_{t_1}^\infty dt_2 \int_{\mathbf{l}_1 \mathbf{l}_2 \bar{\mathbf{l}}_2} \mathbf{l}_1 \cdot \bar{\mathbf{l}}_2 \mathcal{Q}(\mathbf{p}, \mathbf{l}_2, \bar{\mathbf{l}}_2 | t_\infty, t_2) \mathcal{K}(\mathbf{l}_2, \mathbf{l}_1 | t_2, t_1). \tag{3.14}
\end{aligned}$$

Here we have defined the quadrupole

$$\mathcal{Q}(\mathbf{p}, \mathbf{l}_2, \bar{\mathbf{l}}_2 | t_\infty, t_2) = \int_{\mathbf{P}} \mathcal{S}^{(4)}(\mathbf{p}, \mathbf{l}_2, \bar{\mathbf{l}}_2, \mathbf{P} | t_\infty, t_2), \tag{3.15}$$

the splitting kernel,

$$\mathcal{K}(\mathbf{l}_2, \mathbf{l}_1 | t_2, t_1) = \int_{\bar{\mathbf{p}}_2} \mathcal{S}^{(3)}(\mathbf{l}_2, \mathbf{l}_1, \bar{\mathbf{p}}_2 | t_2, t_1), \tag{3.16}$$

and used that $\int_{\mathbf{p}_1} \mathcal{P}(\mathbf{p}_1 - \mathbf{p}_0 | t_1, t_0) = 1$.

Switching to a formulation in transverse position, we apply Fourier transforms of both correlators, to arrive at

$$\begin{aligned}
(2\pi)^2 \frac{dI}{dz d^2\mathbf{p}} &= \frac{\alpha_s P_{ba}(z)}{\omega^2} \text{Re} \int_0^\infty dt_1 \int_{t_1}^\infty dt_2 \int_{\mathbf{u}_2 \bar{\mathbf{u}}_2} e^{-i(\mathbf{u} - \bar{\mathbf{u}}) \cdot \mathbf{p}} \\
&\times (\partial_{\mathbf{u}_1} \cdot \partial_{\bar{\mathbf{u}}_2}) \mathcal{Q}(\mathbf{u}, \bar{\mathbf{u}}; \mathbf{u}_2, \bar{\mathbf{u}}_2 | t_\infty, t_2) \mathcal{K}(\mathbf{u}_2, \mathbf{u}_1 | t_2, t_1) \Big|_{\mathbf{u}_1 = \bar{\mathbf{u}}_2 = 0}, \tag{3.17}
\end{aligned}$$

where we introduced the notation $\omega \equiv z(1-z)E$. The $(\mathbf{u}, \bar{\mathbf{u}})$ spatial coordinates are given in terms of the original coordinates in (A.7). In this work, we will concretely use Eq. (3.17) to find a numerical solution. Both Eqs. (3.14) and (3.17) are extremely compact formulas that account for the full kinematics of medium-induced splitting in an arbitrarily dense medium, see also [80].

The quadrupole $\mathcal{Q}(t_\infty, t_2)$ and splitting kernel $\mathcal{K}(t_2, t_1)$ are given by the path integrals

$$\mathcal{Q}(\mathbf{u}_f, \bar{\mathbf{u}}_f; \mathbf{u}_2, \bar{\mathbf{u}}_2 | t_\infty, t_2) = \int_{\mathbf{u}_2}^{\mathbf{u}_f} \mathcal{D}\mathbf{u} \int_{\bar{\mathbf{u}}_2}^{\bar{\mathbf{u}}_f} \mathcal{D}\bar{\mathbf{u}} e^{i\frac{\omega}{2} \int_{t_2}^{t_\infty} ds (\dot{\mathbf{u}}^2 - \dot{\bar{\mathbf{u}}}^2)} \mathcal{C}^{(4)}(\mathbf{u}, \bar{\mathbf{u}}), \quad (3.18)$$

$$\mathcal{K}(\mathbf{u}_2, \mathbf{u}_1 | t_2, t_1) = \int_{\mathbf{u}_1}^{\mathbf{u}_2} \mathcal{D}\mathbf{u} e^{i\frac{\omega}{2} \int_{t_1}^{t_2} ds \dot{\mathbf{u}}^2} \mathcal{C}^{(3)}(\mathbf{u}). \quad (3.19)$$

Hence, after exploiting symmetries of the problem, we have arrived at a description of the problem in terms of a one-body quantum-mechanical propagator $\mathcal{K}(t_2, t_1)$, that lives in the time-interval between the splitting time in the amplitude and in the complex-conjugate amplitude, and a two-body propagator $\mathcal{Q}(t_\infty, t_2)$, that describes the system after the latter splitting time until the end of the medium.⁵

The correlators $\mathcal{C}^{(n)}$ are given by process-dependent configurations of Wilson lines, e.g.

$$\begin{aligned} \mathcal{C}^{(3)} &= d_{abc}^{(3)} \langle V_b V_c V_a^\dagger \rangle \\ \mathcal{C}^{(4)} &= d_{bc}^{(4)} \langle V_b V_b^\dagger V_c V_c^\dagger \rangle. \end{aligned} \quad (3.20)$$

In these correlators the color indices are traced over, and the specific form of the color factors $d_{abc}^{(3)}$ and $d_{bc}^{(4)}$ depends on the process.

It turns out that the three-point function can be represented as a single exponential, namely

$$\mathcal{C}^{(3)}(\mathbf{u} | t_2, t_1) = e^{-\int_{t_1}^{t_2} ds v_{ba}(\mathbf{u})}, \quad (3.21)$$

where $v_{ba}(\mathbf{u})$ is the process-dependent potential of a splitting $a \rightarrow bc$, and is given as

$$v_{ba}(\mathbf{r}, t) = n(t) \left[\frac{c_{cba}}{2} \sigma(\mathbf{r}) + \frac{c_{acb}}{2} \sigma(z\mathbf{r}) + \frac{c_{bac}}{2} \sigma((1-z)\mathbf{r}) \right], \quad (3.22)$$

where the color factors are $c_{cba} \equiv C_c + C_b - C_a$ etc., and $C_a \equiv C_R$ are the individual color charges of the three partons. The broadening potential σ is a combination of real and virtual interactions $\sigma(\mathbf{r}) = g^2[\gamma(0) - \gamma(\mathbf{r})]$, where $\gamma(\mathbf{r})$ is defined in Eq. (2.8).

The four-point function, or quadrupole, is more complicated since it allows for the mixing between color states [72]. It therefore corresponds not only to a two-body but also a *multi-level* quantum-mechanical problem. It can be calculated through a coupled system of Schrödinger-like differential equations, which is derived in App. C. The specific details of this many-level system depend on the color charges of the involved particles. The correlator $\mathcal{C}^{(4)}$ is itself a color singlet, and therefore the number of coupled equations corresponds to the number of possible color singlets one can make out of four partons.

⁵In the vacuum, the quadrupole in momentum space reduce to a product of delta functions implying the absence of any further transverse momentum broadening of either of the legs.

Analytical solutions exist only in the large- N_c limit, where the system of coupled equations drastically simplifies. Will discuss different approximations of $\mathcal{Q}(t_\infty, t_2)$ as well as solve it exactly numerically for the $\gamma \rightarrow q\bar{q}$ process in the following sections.

3.2 Isolating the medium contribution

To continue it is convenient to divide the process into three regions, depending on whether the splittings in the amplitude and complex conjugate amplitude happen before or after the system exits the medium. These regions are: 1) $t_1 < t_2 < L$ (in-in region), 2) $t_1 < L < t_2$ (in-out region) and 3) $L < t_1 < t_2$ (out-out region). The spectrum then separates into

$$\frac{dI^{\text{full}}}{dzd^2\mathbf{p}} = \frac{dI^{\text{in-in}}}{dzd^2\mathbf{p}} + \frac{dI^{\text{in-out}}}{dzd^2\mathbf{p}} + \frac{dI^{\text{out-out}}}{dzd^2\mathbf{p}} \quad (3.23)$$

In many cases we want to study the medium contribution, which can be gotten by simply subtracting the vacuum spectrum. The out-out contribution describes a splitting happening entirely out of the medium, which means that it is equivalent to the vacuum spectrum. The medium contribution to the spectrum is then given by

$$\begin{aligned} \frac{dI^{\text{med}}}{dzd^2\mathbf{p}} &= \frac{dI^{\text{full}}}{dzd^2\mathbf{p}} - \frac{dI^{\text{vac}}}{dzd^2\mathbf{p}} \\ &= \frac{dI^{\text{in-in}}}{dzd^2\mathbf{p}} + \frac{dI^{\text{in-out}}}{dzd^2\mathbf{p}} \end{aligned} \quad (3.24)$$

One way of isolating the medium contribution to the spectrum is to calculate the so-called medium modification factor F_{med} , given by

$$\frac{dI^{\text{full}}}{dzd^2\mathbf{p}} = \frac{dI^{\text{vac}}}{dzd^2\mathbf{p}} (1 + F_{\text{med}}). \quad (3.25)$$

We will put some effort into calculating the three contributions individually, and will in the end use that knowledge to calculate F_{med} .

We can immediately deal with the out-out contribution, which is equivalent to the vacuum contribution. Outside of the medium the three- and four-point correlators simply reduce to $\mathcal{C}^{(3)} = \mathcal{C}^{(4)} = 1$, meaning that the path integrals are free. The three-point function becomes the free propagator, i.e. $\mathcal{K}(\mathbf{u}_2, \mathbf{u}_1|t_2, t_1)_{g \rightarrow 0} = \mathcal{K}_0(\mathbf{u}_2 - \mathbf{u}_1, t_2 - t_1)$, where

$$\mathcal{K}_0(\mathbf{u}, \Delta t) = \frac{\omega}{2\pi i \Delta t} e^{i \frac{\omega}{2\Delta t} \mathbf{u}^2}, \quad (3.26)$$

or, in momentum space

$$\mathcal{K}_0(\mathbf{p} - \mathbf{p}_0, \Delta t) = (2\pi)^2 \delta^2(\mathbf{p} - \mathbf{p}_0) e^{-i \frac{\mathbf{p}^2}{2\omega} \Delta t}. \quad (3.27)$$

The quadrupole becomes a product of two free propagators, i.e. $\mathcal{Q}(t_\infty, t_2)_{g \rightarrow 0} = \mathcal{Q}_0(t_\infty, t_2)$, where

$$\mathcal{Q}_0(\mathbf{u}_r, \bar{\mathbf{u}}_r, \mathbf{u}_2, \bar{\mathbf{u}}_2|t_\infty, t_2) = \mathcal{K}_0(\mathbf{u}_r - \mathbf{u}_2, t_\infty - t_2) \mathcal{K}_0^*(\bar{\mathbf{u}}_r - \bar{\mathbf{u}}_2, t_\infty - t_2). \quad (3.28)$$

In momentum space this simply becomes

$$\mathcal{Q}_0(\mathbf{p}, \mathbf{l}_2, \bar{\mathbf{l}}_2 | t_\infty, t_2) = (2\pi)^4 \delta(\mathbf{p} - \mathbf{l}_2) \delta(\mathbf{p} - \bar{\mathbf{l}}_2). \quad (3.29)$$

This simply represents the fact that, in the absence of further transverse momentum exchanges, the transverse momentum of the pair remains the same after the splitting has taken place, i.e. after t_2 .

The out-out, or vacuum, contribution is reached by inserting the free propagators into (3.14), which simply becomes

$$\begin{aligned} (2\pi)^2 \frac{dI^{\text{out-out}}}{dz d^2\mathbf{p}} &= \frac{\alpha_s}{\omega^2} P_{ba}(z) \text{Re} \int_L^\infty dt_1 \int_{t_1}^\infty dt_2 \mathbf{p}^2 e^{-i\frac{\mathbf{p}^2}{2\omega}(t_2-t_1)} \\ &= \frac{2\alpha_s}{\mathbf{p}^2} P_{ba}(z). \end{aligned} \quad (3.30)$$

In a more familiar form, it reads

$$\frac{dI^{\text{out-out}}}{dz d p_t^2} = \frac{\alpha_s}{2\pi} \frac{P_{ba}(z)}{p_t^2}, \quad (3.31)$$

where $p_t \equiv |\mathbf{p}| = \omega\theta$ in the small-angle approximation, which is nothing else than the well-known vacuum splitting function.

Similarly, the in-out contribution is immediately found to be given by

$$(2\pi)^2 \frac{dI^{\text{in-out}}}{dz d^2\mathbf{p}} = \frac{2\alpha_s}{\omega} \frac{1}{\mathbf{p}^2} P_{ba}(z) \text{Re} \int_0^L dt_1 \int_{\mathbf{u}} e^{-i\mathbf{u}\cdot\mathbf{p}} \mathbf{p} \cdot \partial_{\mathbf{u}_1} \mathcal{K}(\mathbf{u}, \mathbf{u}_1 | L, t_1) |_{\mathbf{u}_1=0}. \quad (3.32)$$

The equation for $\mathcal{K}(L, t_1)$ is given in (3.19) and describes a splitting process that starts at time t_1 and extends all the way to the end of the medium L . For general medium potentials in (3.21), the path integral has no analytical solution, and it is more useful to reformulate the problem as an evolution equation on $\mathcal{K}(t, t_1)$, that reads

$$\left[i \frac{\partial}{\partial t} + \frac{\partial_{\mathbf{u}}^2}{2\omega} + i v_{ba}(\mathbf{u}) \right] \mathcal{K}(\mathbf{u}, \mathbf{u}_1 | t, t_1) = i \delta(\mathbf{u} - \mathbf{u}_1) \delta(t - t_1), \quad (3.33)$$

where $v_{va}(\mathbf{u})$ is a process dependent potential, see Eq. (3.22). This correlator is a Green's function, whose evolution equation takes the form of a Schrödinger equation in 2+1 dimensions, describing the transition between initial time t_1 and the final time t . The evolution can be solved using analytical [38–43] or numerical methods [32–37], and is the basic building block for computing the energy emission spectrum dI/dz , differential only in the momentum-sharing fraction z , see Sec. 3.3.

Lastly, the in-in contribution is given by

$$\begin{aligned} (2\pi)^2 \frac{dI^{\text{in-in}}}{dz d^2\mathbf{p}} &= \frac{\alpha_s}{\omega^2} P_{ba}(z) \text{Re} \int_0^L dt_1 \int_{t_1}^L dt_2 \\ &\times \int_{\mathbf{u}_2 \bar{\mathbf{u}}} e^{-i(\mathbf{u}-\bar{\mathbf{u}})\cdot\mathbf{p}} (\partial_{\mathbf{u}_1} \cdot \partial_{\bar{\mathbf{u}}_2}) \mathcal{Q}(\mathbf{u}, \bar{\mathbf{u}}, \mathbf{u}_2, \bar{\mathbf{u}}_2 | L, t_2) \mathcal{K}(\mathbf{u}_2, \mathbf{u}_1 | t_2, t_1) |_{\mathbf{u}_1=\bar{\mathbf{u}}_2=0}. \end{aligned} \quad (3.34)$$

It is clear that to calculate the in-in spectrum, we have to be able to calculate the quadrupole $\mathcal{Q}(\mathbf{u}, \bar{\mathbf{u}}, \mathbf{u}_2, \bar{\mathbf{u}}_2|L, t_2)$. In the next subsection we will show one way of doing this numerically.

Now we will show how to calculate the four-point function in position space

$$\mathcal{Q}(\mathbf{u}_L, \bar{\mathbf{u}}_L, \mathbf{u}_2, \bar{\mathbf{u}}_2|L, t_2) = \int_{\mathbf{u}_2}^{\mathbf{u}_L} \mathcal{D}\mathbf{u} \int_{\bar{\mathbf{u}}_2}^{\bar{\mathbf{u}}_L} \mathcal{D}\bar{\mathbf{u}} e^{i\frac{\omega}{2} \int_{t_2}^L ds (\dot{\mathbf{u}}^2 - \dot{\bar{\mathbf{u}}}^2)} \mathcal{C}^{(4)}(\mathbf{u}, \bar{\mathbf{u}}). \quad (3.35)$$

The four-point correlator $\mathcal{C}^{(4)}$ is a medium-averaged trace of Wilson lines. In our approach, all adjoint Wilson lines are turned into fundamental ones using the identity $U_A^{ab} = 2 \text{tr} [t^a V_F t^b V_F^\dagger]$.⁶ If $\mathcal{C}^{(4)}$ contains n pairs of Wilson lines in the fundamental representation there will be $n!$ different ways to connect the color of these Wilson lines. The correlator we are interested in calculating is only one of these states $\mathcal{C}^{(4)} = \mathcal{C}_i^{(4)}$, and can be found through a system of differential equations that involves all of the states

$$\frac{d}{dt} \mathcal{C}_i(\mathbf{u}, \bar{\mathbf{u}}) = \mathbb{M}_{ij}(\mathbf{u}, \bar{\mathbf{u}}) \mathcal{C}_j(\mathbf{u}, \bar{\mathbf{u}}). \quad (3.36)$$

The sum runs over all of the $n!$ color states. In [69] we derived a general method of calculating the evolution matrix \mathbb{M} , which we refer the readers to for more details. In the large- N_c limit the matrix \mathbb{M} simplifies greatly and the system becomes analytically solvable. We will show a concrete example of this in Sec. 4.2.

The quadrupole \mathcal{Q}_i is a double path integral over the correlator \mathcal{C}_i . In appendix C it is shown that the path integral can be given equivalently in terms of a system of Schrödinger equations, namely

$$\left[i\delta_{ij} \frac{\partial}{\partial t} + \delta_{ij} \frac{\partial_{\mathbf{u}}^2 - \partial_{\bar{\mathbf{u}}}^2}{2\omega} - i\mathbb{M}_{ij}(\mathbf{u}, \bar{\mathbf{u}}) \right] \mathcal{Q}_j(\mathbf{U}, \mathbf{U}_2) = i\mathbf{1}_i \delta(t - t_2) \delta^2(\mathbf{u} - \mathbf{u}_2) \delta^2(\bar{\mathbf{u}} - \bar{\mathbf{u}}_2), \quad (3.37)$$

where $\mathbf{1}_i = [1, 1, \dots, 1]$ and we have defined $\mathbf{U} = (t, \mathbf{u}, \bar{\mathbf{u}})$.

From this it is possible to derive Schrödinger equations for objects that contain the four-point function. Defining

$$\begin{aligned} \mathcal{F}(\mathbf{u}, \bar{\mathbf{u}}|L) &= \int_0^L dt_2 \int_0^{t_2} dt_1 \int_{\mathbf{u}_2} \\ &\times (\partial_{\mathbf{u}_1} \cdot \partial_{\bar{\mathbf{u}}_2}) \mathcal{Q}(\mathbf{u}, \bar{\mathbf{u}}, \mathbf{u}_2, \bar{\mathbf{u}}_2|L, t_2) \mathcal{K}(\mathbf{u}_2, \mathbf{u}_1|t_2, t_1) \Big|_{\mathbf{u}_1 = \bar{\mathbf{u}}_2 = 0}. \end{aligned} \quad (3.38)$$

and acting on this object with the derivative operator $\hat{\mathbb{D}}[\cdot] = i\frac{\partial}{\partial t} + \frac{\partial_{\mathbf{u}}^2 - \partial_{\bar{\mathbf{u}}}^2}{2\omega} - i\mathbb{M}(\mathbf{u}, \bar{\mathbf{u}})$ it turns into a non-homogeneous differential equation

$$\hat{\mathbb{D}}[\mathcal{F}(\mathbf{u}, \bar{\mathbf{u}}|L)] = -i\partial_{\bar{\mathbf{u}}} \delta^2(\bar{\mathbf{u}}) \cdot \partial_{\mathbf{u}_1} \int_0^L dt_1 \mathcal{K}(\mathbf{u}, \mathbf{u}_1|L, t_1) \Big|_{\mathbf{u}_1 = 0}, \quad (3.39)$$

⁶For problems involving only gluon lines, alternatively one can work entirely in the adjoint representation [72].

where we have omitted the explicit form of the initial condition. The derivative of the Dirac delta might look odd, but it can be dealt with numerically by simply choosing some representation of the delta function. Using this object the in-in spectrum becomes

$$(2\pi)^2 \frac{dI^{\text{in-in}}}{dz d^2\mathbf{p}} = \frac{\alpha_s P_{ba}(z)}{\omega^2} \text{Re} \int_{u\bar{u}} e^{-i(\mathbf{u}-\bar{\mathbf{u}})\cdot\mathbf{p}} \mathcal{F}(\mathbf{u}, \bar{\mathbf{u}}|L). \quad (3.40)$$

The recipe for calculating the spectrum is then the following: Calculate $\mathcal{F}(\mathbf{u}, \bar{\mathbf{u}}|L)$ numerically through the Schrödinger equation (3.39), then do a numerical Fourier transform and insert the result into Eq.(3.40). In the next section we will do this for a specific splitting process.

3.3 The energy spectrum

In many cases we are not interested in the transverse momentum of the splitting, but only in the energy fraction carried by each parton. That is, we want to calculate $\frac{dI}{dz} = \int_{\mathbf{p}} (2\pi)^2 \frac{dI}{dz d^2\mathbf{p}}$. For now, we take the integral without any restriction on the phase space. Starting with the expression for the fully differential spectrum in momentum space (3.14), we write

$$\frac{dI}{dz} = \frac{\alpha_s}{\omega^2} P_{ba}(z) \text{Re} \int_0^\infty dt_1 \int_{t_1}^\infty dt_2 \int_{\mathbf{p}} \int_{\mathbf{l}_1 \mathbf{l}_2 \bar{\mathbf{l}}_2} \mathbf{l}_1 \cdot \bar{\mathbf{l}}_2 \mathcal{Q}(\mathbf{p}, \mathbf{l}_2, \bar{\mathbf{l}}_2 | t_\infty, t_2) \mathcal{K}(\mathbf{l}_2, \mathbf{l}_1 | t_2, t_1). \quad (3.41)$$

The relevant part to study is the part involving the quadrupole. Making use of the definitions of $\mathcal{Q}(t, t_2)$, we find that

$$\begin{aligned} \int_{\mathbf{p}} \mathcal{Q}(\mathbf{p}, \mathbf{l}_2, \bar{\mathbf{l}}_2 | t, t_2) &= \int_{\mathbf{P}, \mathbf{p}} S^{(4)}(\mathbf{p}, \mathbf{l}_2, \bar{\mathbf{l}}_2, \bar{\mathbf{p}}_2 - \mathbf{P}), \\ &= \int_{\mathbf{P}, \mathbf{p}, \mathbf{q}_2} (\mathbf{k}, \mathbf{q}; \mathbf{k}, \mathbf{q} | S^{(4)} | \mathbf{k}_2, \mathbf{q}_2; \bar{\mathbf{k}}_2, \bar{\mathbf{p}}_2 - \bar{\mathbf{k}}_2), \end{aligned} \quad (3.42)$$

where in the first line we have reinstated the original combination of momenta $\bar{\mathbf{p}}_2 - \mathbf{P}$. Using the definition of $S^{(4)}(t, t_2)$ in terms of the dressed in-medium propagators, see Eq. (3.6), and using that $\int_{\mathbf{q}} (\bar{\mathbf{q}}_2 | \mathcal{G}^\dagger | \mathbf{q})(\mathbf{q} | \mathcal{G} | \mathbf{q}_2) = (2\pi)^2 \delta(\bar{\mathbf{q}}_2 - \mathbf{q}_2)$ and is diagonal in color space, we can finally show that

$$\int_{\mathbf{p}} \mathcal{Q}(\mathbf{p}, \mathbf{l}_2, \bar{\mathbf{l}}_2 | t, t_2) = (2\pi)^2 \delta(\mathbf{l}_2 - \bar{\mathbf{l}}_2). \quad (3.43)$$

The integral over the quadrupole has been reduced to a Dirac delta, and only the splitting kernel $\mathcal{K}(t_2, t_1)$ actually contributes to the energy spectrum, which now reads

$$\frac{dI}{dz} = \frac{\alpha_s}{\omega^2} P_{ba}(z) \text{Re} \int_0^\infty dt_1 \int_{t_1}^\infty dt_2 \int_{\mathbf{l}_1 \mathbf{l}_2} \mathbf{l}_1 \cdot \mathbf{l}_2 \mathcal{K}(\mathbf{l}_2, \mathbf{l}_1 | t_2, t_1), \quad (3.44)$$

$$= \frac{\alpha_s}{\omega^2} P_{ba}(z) \text{Re} \int_0^\infty dt_1 \int_{t_1}^\infty dt_2 \partial_{\mathbf{x}} \cdot \partial_{\mathbf{y}} \mathcal{K}(\mathbf{x}, \mathbf{y} | t_2, t_1)_{\mathbf{x}=\mathbf{y}=0}, \quad (3.45)$$

in momentum and transverse-coordinate representation, respectively.

4 Photon splitting in the harmonic oscillator approximation

So far our results have been completely general, valid for any potential and splitting process. In this section, we will employ our formalism to calculate a specific process in the medium and plot the results. For the potential we will use the harmonic oscillator (HO) approximation [25, 50]. Then we will narrow our calculation further and study the specific case of a photon splitting to a quark-antiquark pair.

4.1 Harmonic oscillator approximation

The elastic scattering potential $\sigma(\mathbf{r})$ can be expanded at short distances $|\mathbf{r}| \rightarrow 0$ as

$$n(t)C_R\sigma(\mathbf{r}) = g^2 n(t)C_R \int_q \frac{d\sigma_{\text{el}}}{d^2\mathbf{q}} \left(1 - e^{i\mathbf{q}\cdot\mathbf{r}}\right) \approx \frac{1}{4} \mathbf{r}^2 \hat{q}_R \log \frac{1}{\mu_*^2 \mathbf{r}^2} + \mathcal{O}(\mathbf{r}^4 \mu_*^2), \quad (4.1)$$

where the form of the first term is universal for the scattering potentials used in the literature, while the scale μ_* is model-specific and depends on how the IR divergence of the scattering is screened by medium effects [40]. Assuming the logarithm is a slowly varying function, we drop it to arrive at

$$n(t)C_R\sigma(\mathbf{r}) \simeq \frac{1}{4} \hat{q}_R \mathbf{r}^2, \quad (4.2)$$

which is the so-called harmonic oscillator (HO) approximation [25, 50], see [38–43] for a consistent treatment of the logarithmic corrections. The HO approximation is appropriate for accounting for multiple, soft interactions with the medium. This is usually what mainly governs the dynamics of soft splittings. Besides, it is a very useful approximation since it allows for analytical solutions, in particular for the three-point function $\mathcal{K}(t_2, t_1)$ in governing the splitting process.

Focusing solely on the three-point function for now, it follows that the potential of the path integral, given in Eq. (3.22), becomes

$$v_{ba}(\mathbf{r}, t) = \frac{1}{4} \hat{q}_{ba} \mathbf{r}^2, \quad (4.3)$$

where

$$\hat{q}_{ba} = \left[\frac{c_{cba}}{2C_R} + \frac{c_{acb}}{2C_R} z^2 + \frac{c_{bac}}{2C_R} (1-z)^2 \right] \hat{q}_R. \quad (4.4)$$

For the process that we will consider in this paper, see Sec. 4.2, $\gamma \rightarrow q\bar{q}$ we have $\hat{q}_{q\gamma} = \hat{q}_F$.

Finally, the parameter \hat{q} is in general a function of time. In this paper we will simplify this and use brick medium $\hat{q}(t) = \Theta(L-t)\hat{q}$, where we treat $\hat{q} \equiv \hat{q}_F$ as constant.

In this approximation the splitting kernel becomes $\mathcal{K}(t_2, t_1) = \mathcal{K}_{\text{HO}}(t_2, t_1)$, where

$$\mathcal{K}_{\text{HO}}(\mathbf{u}_2, \mathbf{u}_1 | t_2, t_1) = \frac{\omega\Omega}{2\pi i \sin(\Omega\Delta t)} e^{\frac{i\omega\Omega}{2\sin(\Omega\Delta t)} [\cos(\Omega\Delta t) (\mathbf{u}_1^2 + \mathbf{u}_2^2) - 2\mathbf{u}_1 \cdot \mathbf{u}_2]}, \quad (4.5)$$

where $\Delta t = t_2 - t_1$ and $\Omega = \frac{1-i}{2} \sqrt{\hat{q}_{ba}/\omega}$.

Hence, in the HO approximation one can obtain analytic expressions for the in-out spectrum and part of the in-in spectrum. The in-out spectrum, given in Eq. (3.32), can be simplified by using the relation

$$\int_0^t dt_1 \partial_{\mathbf{u}_1} \mathcal{K}_{\text{HO}}(\mathbf{u}, \mathbf{u}_1 | t, t_1) |_{\mathbf{u}_1=0} = \frac{\omega}{i\pi} \frac{\mathbf{u}}{\mathbf{u}^2} e^{i\frac{\omega\Omega}{2} \cot \Omega t \mathbf{u}^2}. \quad (4.6)$$

After doing the integral over \mathbf{u} the in-out contribution in the HO approximation becomes

$$\begin{aligned} (2\pi)^2 \frac{dI^{\text{in-out}}}{dz d^2\mathbf{p}} &= -\frac{2\alpha_s}{\omega} P_{ba}(z) \text{Re} i \int_0^L dt \frac{1}{\cos^2(\Omega t)} e^{-i\frac{\tan(\Omega t)}{2\omega\Omega} \mathbf{p}^2} \\ &= -\frac{4\alpha_s}{\mathbf{p}^2} P_{ba}(z) \text{Re} \left[1 - e^{-i\frac{\tan(\Omega L)}{2\omega\Omega} \mathbf{p}^2} \right]. \end{aligned} \quad (4.7)$$

Similarly, the in-in spectrum can also be simplified. Again the first time integral can be done in the HO approximation, and Eq. (3.34) becomes

$$\begin{aligned} (2\pi)^2 \frac{dI^{\text{in-in}}}{dz d^2\mathbf{p}} &= \frac{\alpha_s}{\pi\omega} P_{ba}(z) \text{Im} \int_0^L dt_2 \int_{\mathbf{u}_2 \mathbf{u}_L \bar{\mathbf{u}}_L} e^{-i(\mathbf{u}_L - \bar{\mathbf{u}}_L) \cdot \mathbf{p}} e^{i\frac{\omega\Omega}{2} \cot \Omega t_2 \mathbf{u}_2^2} \\ &\quad \times \frac{\mathbf{u}_2}{\mathbf{u}_2^2} \cdot \partial_{\bar{\mathbf{u}}_2} \mathcal{Q}(\mathbf{u}_L, \bar{\mathbf{u}}_L, \mathbf{u}_2, \bar{\mathbf{u}}_2 | L, t_2) |_{\bar{\mathbf{u}}_2=0}. \end{aligned} \quad (4.8)$$

Again the last phase in the relation (4.6) drops out, leaving only the first term.

In our numerical calculations we will compute the object $\mathcal{F}(\mathbf{u}, \bar{\mathbf{u}} | L)$ given in Eq. (3.38). In the harmonic oscillator picture this is given by

$$\mathcal{F}(\mathbf{u}, \bar{\mathbf{u}} | L) = -i\frac{\omega}{\pi} \int_0^t dt_2 \int_{\mathbf{u}_2} e^{i\frac{\omega\Omega}{2} \cot(\Omega t_2) \mathbf{u}_2^2} \left(\frac{\mathbf{u}_2}{\mathbf{u}_2^2} \cdot \partial_{\bar{\mathbf{u}}_2} \right) \mathcal{Q}(\mathbf{u}, \bar{\mathbf{u}}, \mathbf{u}_2, \bar{\mathbf{u}}_2 | t, t_2) |_{\bar{\mathbf{u}}_2=0}. \quad (4.9)$$

This object can be computed through the Schrödinger equation

$$\left[i\frac{\partial}{\partial t} + \frac{\partial_{\mathbf{u}}^2 - \partial_{\bar{\mathbf{u}}}^2}{2\omega} - i\mathbb{M}(\mathbf{u}, \bar{\mathbf{u}}) \right] \mathcal{F}(\mathbf{u}, \bar{\mathbf{u}} | L) = -\frac{\omega}{\pi} \frac{\mathbf{u}}{\mathbf{u}^2} \cdot \partial_{\bar{\mathbf{u}}} \delta^2(\bar{\mathbf{u}}) e^{i\frac{\omega\Omega}{2} \cot(\Omega L) \mathbf{u}^2}. \quad (4.10)$$

We finally stress that the HO approximation is not a necessary ingredient for our numerical procedure. When dealing with the full expression in (4.1), we would need to solve the three-point function $\mathcal{K}(t_2, t_1)$ with advanced resummation techniques or numerically, and provide numerical data as the non-homogeneous contribution to the evolution equation (4.10).

4.2 Pair production

Turning finally to the concrete goal of our numerical calculation, let us examine the process of a photon splitting into a quark-antiquark pair, $\gamma \rightarrow q\bar{q}$. The full derivation of this cross section is done in App. B.1.

The reason for choosing this process to study is mainly a practical one. We have to solve a system of differential equations numerically. For $\gamma \rightarrow q\bar{q}$ the system is 2×2 , while for $q \rightarrow qg$ it is 6×6 , and for $g \rightarrow gg$ it is 24×24 . Therefore, the numerical complexity increases drastically with increasing color content in the process, so with limited computing resources, we chose the least complicated one.

Another reason is that $\gamma \rightarrow q\bar{q}$ is a pretty good proxy for studying both $q \rightarrow qg$ and $g \rightarrow gg$. The difference between the three cases is the Wilson line correlator $\mathcal{C}^{(4)}$ in Eq. (3.35). For $\gamma \rightarrow q\bar{q}$ this is

$$\mathcal{C}_{q\bar{q}}^{(4)}(L, t_2) = \frac{1}{N_c} \langle \text{tr}[V_1 V_2^\dagger V_2 V_1^\dagger] \rangle, \quad (4.11)$$

while for $q \rightarrow qg$ and $g \rightarrow gg$ it is [28, 54]

$$\mathcal{C}_{gq}^{(4)}(L, t_2) = \frac{1}{N_c^2 - 1} \langle \text{tr}[V_1^\dagger V_1 V_2^\dagger V_2] \text{tr}[V_2^\dagger V_2] - \frac{1}{N_c} \text{tr}[V_1^\dagger V_1] \rangle \quad (4.12)$$

$$\mathcal{C}_{gg}^{(4)}(L, t_2) = \frac{1}{N_c(N_c^2 - 1)} \left\langle \text{tr}[V_1^\dagger V_1] \text{tr}[V_2^\dagger V_2 V_1^\dagger V_1] \text{tr}[V_2^\dagger V_2] - \text{tr}[V_1^\dagger V_1 V_2^\dagger V_2 V_1^\dagger V_1 V_2^\dagger V_2] \right\rangle. \quad (4.13)$$

There is obviously a big difference in color complexity between these three systems. However, the large- N_c limit can be used to simplify $\mathcal{C}_{gq}^{(4)}$ and $\mathcal{C}_{gg}^{(4)}$. In both cases the first term goes as N_c^0 , while the second goes as N_c^{-2} , meaning that the latter is subleading in N_c . Additionally, in the large- N_c limit, the first term becomes a product of several factors, namely

$$\mathcal{C}_{gq}^{(4)}(L, t_2) \simeq \frac{1}{N_c^2} \langle \text{tr}[V_1 V_2^\dagger V_2 V_1^\dagger] \rangle \langle \text{tr}[V_2^\dagger V_2] \rangle \quad (4.14)$$

$$\mathcal{C}_{gg}^{(4)}(L, t_2) \simeq \frac{1}{N_c^3} \langle \text{tr}[V_1^\dagger V_1] \rangle \langle \text{tr}[V_1 V_2^\dagger V_2 V_1^\dagger] \rangle \langle \text{tr}[V_2^\dagger V_2] \rangle. \quad (4.15)$$

These consist of products of dipoles and a quadrupole. The dipoles are easily calculable

$$\mathcal{P}_{1\bar{1}}(t, t_2) \equiv \frac{1}{N_c} \langle \text{tr}[V_1^\dagger V_1] \rangle = e^{-C_F \int_{t_2}^t ds n(s) \sigma_{1\bar{1}}}, \quad (4.16)$$

where we have introduced the notation $\sigma_{1\bar{1}} = \sigma(\mathbf{r}_1 - \mathbf{r}_{\bar{1}})$. However, the quadrupole is not trivial. Notice that the quadrupole that appears in the $q \rightarrow qg$ and $g \rightarrow gg$ splittings is the same as the one for the $\gamma \rightarrow q\bar{q}$ process. One can therefore write

$$\mathcal{C}_{gq}^{(4)}(L, t_2) \simeq \mathcal{P}_{2\bar{2}}(L, t_2) \mathcal{C}_{q\bar{q}}^{(4)}(L, t_2) \quad (4.17)$$

$$\mathcal{C}_{gg}^{(4)}(L, t_2) \simeq \mathcal{P}_{1\bar{1}}(L, t_2) \mathcal{P}_{2\bar{2}}(L, t_2) \mathcal{C}_{q\bar{q}}^{(4)}(L, t_2). \quad (4.18)$$

Hence, by calculating the $\gamma \rightarrow q\bar{q}$ process we also calculate the non-trivial part of the $q \rightarrow qg$ and $g \rightarrow gg$ processes.

In the pair production case the potential in the path integral for the four-point function in (3.35) is a correlator of four Wilson lines, given in (4.11). There are two ways of connecting the color of these two Wilson lines, leading to a system of Schrödinger equations (3.37) with two states. The two states are defined as $\mathcal{C}_1^{(4)} = 1/N_c^2 \langle \text{tr}[V_1 V_2^\dagger][V_2 V_1^\dagger] \rangle$ and $\mathcal{C}_2^{(4)} = 1/N_c \langle \text{tr}[V_1 V_2^\dagger V_2 V_1^\dagger] \rangle$, where the latter represents the physical state that we are interested in.

To solve the Schrödinger equation given in Eq. (4.10) we need to know the explicit form of the potential matrix \mathbb{M} . In the $\gamma \rightarrow q\bar{q}$ case the indices are $i = 1, 2$ and the states

\mathcal{Q}_i are defined through Eq. (3.35) with the potentials $\mathcal{C}_i^{(4)}$. The second solution \mathcal{Q}_2 is the physical state that is part of the emission spectrum, but it is coupled with the state \mathcal{Q}_1 through the potential matrix in the Schrödinger equation. The potential matrix was derived in [69], and for an arbitrary potential it is

$$\mathbb{M} = -\frac{1}{2}n(t) \begin{bmatrix} 2C_F(\sigma_{12} + \sigma_{\bar{2}\bar{1}}) + \frac{1}{N_c}\Sigma_1 & -\frac{1}{N_c}\Sigma_1 \\ -N_c\Sigma_2 & 2C_F(\sigma_{\bar{1}\bar{1}} + \sigma_{\bar{2}2}) + \frac{1}{N_c}\Sigma_2 \end{bmatrix}. \quad (4.19)$$

Here we have introduced

$$\begin{aligned} \Sigma_1 &\equiv \sigma_{1\bar{2}} + \sigma_{\bar{2}\bar{1}} - \sigma_{\bar{1}\bar{1}} - \sigma_{2\bar{2}} \\ \Sigma_2 &\equiv \sigma_{1\bar{2}} + \sigma_{\bar{1}2} - \sigma_{12} - \sigma_{\bar{1}\bar{2}}. \end{aligned} \quad (4.20)$$

In the HO approximation, the potential matrix is given by

$$\mathbb{M} = -\frac{\hat{q}}{4C_F} \begin{bmatrix} C_F[\mathbf{u}^2 + \bar{\mathbf{u}}^2] + \frac{1}{N_c}\mathbf{u} \cdot \bar{\mathbf{u}} & -\frac{1}{N_c}\mathbf{u} \cdot \bar{\mathbf{u}} \\ N_c z(1-z)(\mathbf{u} - \bar{\mathbf{u}})^2 & [C_F - N_c z(1-z)](\mathbf{u} - \bar{\mathbf{u}})^2 \end{bmatrix}. \quad (4.21)$$

The parameter \hat{q} that appears here is in the fundamental representation $\hat{q}_F = \hat{q}_{q\gamma}$. In the potential matrix we have used the coordinate transformation (A.7) to go to the $(\mathbf{u}, \bar{\mathbf{u}})$ coordinates. To get the full solution of the system we plug this matrix into Eq. (4.10) and solve the differential equation numerically. This finite- N_c result can then be compared to the large- N_c calculation, which we will discuss now.

4.3 The large- N_c limit

In the large- N_c limit the potential matrix simplifies to

$$\mathbb{M} = -\frac{\hat{q}}{4} \begin{bmatrix} \mathbf{u}^2 + \bar{\mathbf{u}}^2 & 0 \\ 2z(1-z)(\mathbf{u} - \bar{\mathbf{u}})^2 & [z^2 + (1-z)^2](\mathbf{u} - \bar{\mathbf{u}})^2 \end{bmatrix}. \quad (4.22)$$

This simplification actually makes it possible to reach analytical solutions for both of the states.

Calculating \mathcal{Q}_1 . In the large- N_c limit the equation for \mathcal{Q}_1 decouples from \mathcal{Q}_2 , and in the path integral formulation it becomes a product of two independent path integrals

$$\begin{aligned} \mathcal{Q}_1(\mathbf{U}_L, \mathbf{U}_2) &= \int_{\mathbf{u}_2}^{\mathbf{u}_L} \mathcal{D}\mathbf{u} \int_{\bar{\mathbf{u}}_2}^{\bar{\mathbf{u}}_L} \mathcal{D}\bar{\mathbf{u}} e^{i \int_{t_2}^L ds \left[\frac{\omega}{2}(\dot{\mathbf{u}}^2 - \dot{\bar{\mathbf{u}}}^2) + i\frac{\hat{q}}{4}(\mathbf{u}^2 + \bar{\mathbf{u}}^2) \right]} \\ &= \mathcal{K}_{\text{HO}}(\mathbf{u}_L, \mathbf{u}_2|L, t_2) \mathcal{K}_{\text{HO}}^*(\bar{\mathbf{u}}_L, \bar{\mathbf{u}}_2|L, t_2), \end{aligned} \quad (4.23)$$

with \mathcal{K}_{HO} given in (4.5), and $\mathcal{K}_{\text{HO}}^*$ is the complex conjugate with $\Omega^* \equiv \frac{1+i}{2}\sqrt{\hat{q}/\omega}$.

Calculating \mathcal{Q}_2 . The second quadrupole \mathcal{Q}_2 is the one that is present in the emission spectrum, and its calculation is therefore of some importance. It is given by the non-homogeneous Schrödinger equation

$$\begin{aligned} &\left[i \frac{\partial}{\partial t} + \frac{\partial_{\mathbf{u}}^2 - \partial_{\bar{\mathbf{u}}}^2}{2\omega} + i\frac{\hat{q}}{4}[z^2 + (1-z)^2](\mathbf{u} - \bar{\mathbf{u}})^2 \right] \mathcal{Q}_2(\mathbf{U}, \mathbf{U}_2) \\ &= -i\frac{\hat{q}}{2}z(1-z)(\mathbf{u} - \bar{\mathbf{u}})^2 \mathcal{Q}_1(\mathbf{U}, \mathbf{U}_2), \end{aligned} \quad (4.24)$$

where $\mathcal{Q}_1(\mathbf{U}, \mathbf{U}_2)$ is given in (4.23). The solution to this

$$\mathcal{Q}_2(\mathbf{U}, \mathbf{U}_2) = \mathcal{Q}_2^{\text{fac}}(\mathbf{U}, \mathbf{U}_2) + \int_{t_2}^t dt_3 \int_{\mathbf{v}, \bar{\mathbf{v}}} \mathcal{Q}_2^{\text{fac}}(\mathbf{U}, \mathbf{V}) T(\mathbf{V}) \mathcal{Q}_1(\mathbf{V}, \mathbf{U}_2), \quad (4.25)$$

where the transition function is $T(\mathbf{V}) = -z(1-z)\hat{q}(\mathbf{v} - \bar{\mathbf{v}})^2/2$. These two terms were coined the factorizable and non-factorizable terms in [28]. Notice that the non-factorizable term is proportional to $z(1-z)$, so in the soft limit $z \rightarrow 0$ or $z \rightarrow 1$ it becomes negligible.

The factorizable problem is solved by a homogeneous Schrodinger equation

$$\left[i \frac{\partial}{\partial t} + \frac{\partial_{\mathbf{u}}^2 - \partial_{\bar{\mathbf{u}}}^2}{2\omega} + i \frac{\hat{q}}{4} [z^2 + (1-z)^2] (\mathbf{u} - \bar{\mathbf{u}})^2 \right] \mathcal{Q}_2^{\text{fac}}(\mathbf{U}, \mathbf{U}_2) = i\delta(t-t_2)\delta^2(\mathbf{u} - \mathbf{u}_2)\delta^2(\bar{\mathbf{u}} - \bar{\mathbf{u}}_2). \quad (4.26)$$

This is easier solved in the path integral form

$$\mathcal{Q}_2^{\text{fac}}(\mathbf{U}_L, \mathbf{U}_2) = \int_{\mathbf{u}_2}^{\mathbf{u}_L} \mathcal{D}\mathbf{u} \int_{\bar{\mathbf{u}}_2}^{\bar{\mathbf{u}}_L} \mathcal{D}\bar{\mathbf{u}} e^{i \int_{t_2}^t ds \left[\frac{\omega}{2} (\dot{\mathbf{u}}^2 - \dot{\bar{\mathbf{u}}}^2) + i \frac{\hat{q}}{4} [z^2 + (1-z)^2] (\mathbf{u} - \bar{\mathbf{u}})^2 \right]}. \quad (4.27)$$

After changing variables to $\mathbf{y} = \mathbf{u} - \bar{\mathbf{u}}$, $\mathbf{x} = 1/2(\mathbf{u} + \bar{\mathbf{u}})$ the potential becomes independent of \mathbf{x} , and the path integrals can be performed. The result is

$$\mathcal{Q}_2^{\text{fac}}(\mathbf{x}, \mathbf{y}, \mathbf{x}_2, \mathbf{y}_2 | L, t_2) = \left(\frac{\omega}{2\pi\Delta t} \right)^2 e^{i \frac{\omega}{\Delta t} [(\mathbf{x} - \mathbf{x}_2) \cdot (\mathbf{y} - \mathbf{y}_2)]} e^{-\frac{\hat{q}}{12} [z^2 + (1-z)^2] \Delta t [\mathbf{y}^2 + \mathbf{y} \cdot \mathbf{y}_2 + \mathbf{y}_2^2]}, \quad (4.28)$$

where $\Delta t = L - t_2$.

It is worth pausing at this point, and consider the form of this function in Fourier space, given by

$$\mathcal{Q}_2^{\text{fac}}(\mathbf{p}, \mathbf{l}_2, \bar{\mathbf{l}}_2) = \int_{\mathbf{x}, \mathbf{y}, \mathbf{x}_2, \mathbf{y}_2} e^{i(\mathbf{x}_2 + \frac{1}{2}\mathbf{y}_2) \cdot \mathbf{l}_2 - i(\mathbf{x}_2 - \frac{1}{2}\mathbf{y}_2) \cdot \bar{\mathbf{l}}_2 - i\mathbf{y} \cdot \mathbf{p}} \mathcal{Q}_2^{\text{fac}}(\mathbf{x}, \mathbf{y}; \mathbf{x}_2, \mathbf{y}_2). \quad (4.29)$$

We see that we can take the \mathbf{x} integral directly on the four-point function. After further simplifications, we find

$$\begin{aligned} \mathcal{Q}_2^{\text{fac}}(\mathbf{p}, \mathbf{l}_2, \bar{\mathbf{l}}_2) &= (2\pi)^2 \delta(\mathbf{l}_2 - \bar{\mathbf{l}}_2) \frac{4\pi}{\hat{q}_{\text{eff}}(L - t_2)} e^{-\frac{(\mathbf{p} - \mathbf{l}_2)^2}{\hat{q}_{\text{eff}}(L - t_2)}} \\ &\equiv (2\pi)^2 \delta(\mathbf{l}_2 - \bar{\mathbf{l}}_2) \mathcal{P}_{\text{eff}}(\mathbf{p} - \mathbf{l}_2 | L, t_2), \end{aligned} \quad (4.30)$$

where the effective \hat{q} parameter for the photon decay is $\hat{q}_{\text{eff}} = [z^2 + (1-z)^2]\hat{q}$.

The non-factorizable piece,

$$\mathcal{Q}_2^{\text{non-fac}}(\mathbf{U}, \mathbf{U}_2) = \int_{t_2}^t dt_3 \int_{\mathbf{v}, \bar{\mathbf{v}}} \mathcal{Q}_2^{\text{fac}}(\mathbf{U}, \mathbf{V}) T(\mathbf{V}) \mathcal{Q}_1(\mathbf{V}, \mathbf{U}_2), \quad (4.31)$$

is much more complicated since it depends on both of the color-states of the four-point function. In the large- N_c limit, we have an explicit solution for \mathcal{Q}_1 and can therefore solve Eq. (4.31). One can show that in momentum space it is given by

$$\begin{aligned} \mathcal{Q}_{\text{non-fac}}(\mathbf{p}, \mathbf{l}_2, \bar{\mathbf{l}}_2 | L, t_2) &= \int_{t_2}^L dt_3 \int_{\mathbf{l}_3} \int_{\mathbf{u}} e^{-i(\mathbf{p} - \mathbf{l}_3) \cdot \mathbf{u}} \tilde{\mathcal{P}}(z\mathbf{u} | L, t_3) \tilde{\mathcal{P}}((1-z)\mathbf{u} | L, t_3) \\ &\quad \times T(\mathbf{u} | t_3) \mathcal{Q}_1(\mathbf{l}_3, \mathbf{l}_2, \bar{\mathbf{l}}_2 | t_3, t_2), \end{aligned} \quad (4.32)$$

where we have written the two-point broadening functions in coordinate space, i.e. $\tilde{\mathcal{P}}(\mathbf{u}) = \int_{\mathbf{p}} e^{-i\mathbf{p}\cdot\mathbf{u}} \mathcal{P}(\mathbf{p})$. Since $T(\mathbf{u}) = -z(1-z)\hat{q}\mathbf{u}^2/2$, we can trade it for a double derivative and obtain

$$\begin{aligned} \mathcal{Q}_{\text{non-fac}}(\mathbf{p}, \mathbf{l}_2, \bar{\mathbf{l}}_2|L, t_2) &= \frac{1}{2}z(1-z)\hat{q} \int_{t_2}^L dt_3 \int_{\mathbf{l}_3} \\ &\times (\partial_{\mathbf{p}} \cdot \partial_{\mathbf{p}}) \mathcal{P}_{\text{eff}}(\mathbf{p} - \mathbf{l}_3|L, t_3) \mathcal{Q}_1(\mathbf{l}_3, \mathbf{l}_2, \bar{\mathbf{l}}_2|t_3, t_2). \end{aligned} \quad (4.33)$$

The quadrupole \mathcal{Q}_1 was given in (4.23), and in momentum space it is

$$\mathcal{Q}_1(\mathbf{l}_3, \mathbf{l}_2, \bar{\mathbf{l}}_2|t_3, t_2) = \mathcal{K}_{\text{HO}}(\mathbf{l}_3, \mathbf{l}_2|t_3, t_2) \mathcal{K}_{\text{HO}}^*(\mathbf{l}_3, \bar{\mathbf{l}}_2|t_3, t_2), \quad (4.34)$$

where the splitting kernel in momentum space is

$$\mathcal{K}_{\text{HO}}(\mathbf{l}_3, \mathbf{l}_2|t_3, t_2) = \frac{2\pi}{i\omega\Omega \sin(\Omega\Delta t)} e^{\frac{i}{2\omega\Omega \sin(\Omega\Delta t)} [\cos(\Omega\Delta t) (t_3^2 + t_2^2) - 2t_2 t_3]}. \quad (4.35)$$

After taking the double derivative and doing the last Gaussian integral you arrive at the somewhat complicated expression

$$\begin{aligned} \mathcal{Q}_{\text{non-fac}}(\mathbf{p}, \mathbf{l}_2, \bar{\mathbf{l}}_2|L, t_2) &= -\frac{1}{2}z(1-z)\hat{q} \int_{t_2}^L dt_3 \frac{c^2}{A} \\ &\times \mathcal{Q}_1(\mathbf{p}, \mathbf{l}_2, \bar{\mathbf{l}}_2|t_3, t_2) \left[1 - \frac{2c}{A} + \frac{c}{A^2} \mathbf{q}^2 \right] e^{-\frac{\mathbf{q}^2}{2A}}, \end{aligned} \quad (4.36)$$

where we have defined the time-dependent factors

$$c = \frac{2}{\hat{q}_{\text{eff}}(L - t_3)}, \quad (4.37)$$

$$A = \frac{2}{\hat{q}_{\text{eff}}(L - t_3)} - i\omega[\Omega \cot \Omega(t_3 - t_2) - \Omega^* \cot \Omega^*(t_3 - t_2)], \quad (4.38)$$

$$\mathbf{q} = \omega \left[\frac{\Omega}{\tan \Omega(t_3 - t_2)} \left(\mathbf{p} - \frac{\mathbf{l}_2}{\sin \Omega(t_3 - t_2)} \right) - \frac{\Omega^*}{\tan \Omega^*(t_3 - t_2)} \left(\mathbf{p} - \frac{\bar{\mathbf{l}}_2}{\sin \Omega^*(t_3 - t_2)} \right) \right]. \quad (4.39)$$

4.4 Factorizable and non-factorizable contributions to the spectrum

Hence, in this case, the factorizable part of the spectrum reads

$$(2\pi)^2 \frac{dJ_{\text{fac}}^{\text{in-in}}}{dz d^2\mathbf{p}} = \frac{\alpha_s}{\omega^2} P_{ba}(z) \text{Re} \int_0^L dt_2 \int_0^{t_2} dt_1 \int_{\mathbf{l}_2, \mathbf{l}_1} \mathbf{l}_1 \cdot \mathbf{l}_2 \mathcal{P}_{\text{eff}}(\mathbf{p} - \mathbf{l}_2|L, t_2) \mathcal{K}(\mathbf{l}_2, \mathbf{l}_1|t_2, t_1) \quad (4.40)$$

$$= \frac{\alpha_s}{\omega^2} P_{ba}(z) \text{Re} \int_0^L dt_2 \int_0^{t_2} dt_1 e^{-i\mathbf{p}\cdot\mathbf{x}} \mathcal{P}_{\text{eff}}(\mathbf{x}|L, t_2) \partial_{\mathbf{x}} \cdot \partial_{\mathbf{y}} \mathcal{K}(\mathbf{x}, \mathbf{y}|t_2, t_1)_{\mathbf{y}=0}. \quad (4.41)$$

This describes a splitting of one parton into two at times $t_1 < t < t_2$ and the subsequent incoherent broadening of the two-body system, described by the effective jet coefficient \hat{q}_{eff} , at times $t_2 < t < L$.

After doing the remaining momentum integrals the factorizable part of the spectrum becomes

$$(2\pi)^2 \frac{dJ_{\text{fac}}^{\text{in-in}}}{dz d^2\mathbf{p}} = \frac{2\alpha_s}{\omega} P_{ba}(z) \text{Re} i \int_0^L dt \frac{2\omega\Omega \cot(\Omega t)}{2\omega\Omega \cot(\Omega t) + i\hat{q}_{\text{eff}}\Delta t} e^{-i\frac{\mathbf{p}^2}{2\omega\Omega \cot(\Omega t) + i\hat{q}_{\text{eff}}\Delta t}}. \quad (4.42)$$

Similarly, the non-factorizable part of the spectrum is

$$(2\pi)^2 \frac{dJ_{\text{non-fac}}^{\text{in-in}}}{dz d^2\mathbf{p}} = \frac{\alpha_s z(1-z)\hat{q} P_{ba}(z)}{2\omega^2} \text{Re} \int_0^L dt_2 \int_0^{t_2} dt_1 \int_{t_2}^L dt_3 \int_{\mathbf{l}_1 \mathbf{l}_2 \bar{\mathbf{l}}_2 \mathbf{l}_3} \mathbf{l}_1 \cdot \bar{\mathbf{l}}_2 \\ \times (\partial_{\mathbf{p}} \cdot \partial_{\mathbf{p}}) \mathcal{P}_{\text{eff}}(\mathbf{p} - \mathbf{l}_3 | L, t_3) \mathcal{Q}_1(\mathbf{l}_3, \mathbf{l}_2, \bar{\mathbf{l}}_2 | t_3, t_2) \mathcal{K}(\mathbf{l}_2, \mathbf{l}_1 | t_2, t_1). \quad (4.43)$$

The two expressions (4.42) and (4.43) constitute the main, analytical results in the large- N_c limit. However, it is worth to stress that the full finite- N_c result can similarly be interpreted as a factorizable contribution, corresponding to the diagonal elements of the interaction matrix \mathbb{M} , see (4.21), and the remaining diagonal diagonal and non-diagonal, or non-factorizable, contributions.

It is interesting to study the time scales of the different parts of the spectrum. The splitting kernel $\mathcal{K}(t_2, t_1)$ is governed by the time scale $t_{\text{br}} = \sqrt{2\omega/\hat{q}}$, called the branching time. This which is evident from (4.5), which contains the combination $|\Omega\tau| \sim \tau/t_{\text{br}}$, where the time difference is $\tau = t_2 - t_1$. This constrains the extent of the time difference to be of the order of t_{br} . The scaling of the spectrum with the medium length can be clarified by shifting the time integrals as

$$\int_0^L dt_2 \int_0^{t_2} dt_1(\dots) \rightarrow \int_0^L dt \int_0^{L-t} d\tau(\dots). \quad (4.44)$$

For a large medium or for soft emissions, such that $L \gg t_{\text{br}}$, the integration over τ yields a factor $\sim t_{\text{br}}$, while the remaining integration over t scales with L . Hence, the factorizable piece is expected to scale linearly with L .

The time dependence of the non-factorizable piece is not so straightforward, as it is a convolution of two different quadrupoles, see Eq. (4.33). Between t_2 and t_3 the time dependence is set by $\mathcal{Q}_1(t_3, t_2)$, which exhibits the same characteristic time scale as $\mathcal{K}(t_3, t_2)$, namely at the order of the branching time t_{br} . One therefore expects the integration over the intermediate time t_3 to yield a factor t_{br} . It can be shown numerically that the non-factorizable term vanishes in the $z \rightarrow 0$ limit, see Figs. 9 and 12, since $t_{\text{br}} \propto \sqrt{z}$. This has to be compensated by another length scale, which should emerge from the remaining dynamics between $t_3 \sim t_2 + t_{\text{br}}$ and L . In [28] the authors argued that the non-factorizable part contributes only as t_{br}/L , suggesting that the non-factorizable contribution should become less relevant for large media. In Sec. 5 we will critically examine this proposed behavior.

5 Numerical results

In this section we will present the results of our numerical calculations for the $\gamma \rightarrow q\bar{q}$ splitting. The system of coupled Schrödinger equations is solved on a dense grid using the

fourth-order Runge-Kutta method. The coupled set of equations is defined in Eq. (4.10) and the potential matrix \mathbb{M} entering these equations is given in (4.21) at finite- N_c and (4.22) at large- N_c . The simulation error was estimated by comparing the simulated value of the factorizable problem with the analytical solution given in (4.42). The code we used to do these simulations can be found here: <https://github.com/johannesgutn/schrodinger>.

As mentioned above, we have chosen to focus on the $\gamma \rightarrow q\bar{q}$ process due to the small dimension of possible intermediate color states and, thus, the number of coupled equations; the $q\bar{q}$ pair can only be in two (singlet and octet) configurations. Our approach can be straightforwardly generalized to more complicated systems like $q \rightarrow qg$ and $g \rightarrow gg$, however, it is not a trivial task. The main problem is that in these cases the potential matrices \mathbb{M} have a much higher dimension than in the photon case, and the number of coupled evolution equations grows rapidly. This also comes with a much higher demand for computing power and time, which is one of the reasons why we decided to focus on the photon case. On the other hand, as discovered for the calculations in the eikonal approximation [69], one would expect more pronounced deviations from the large- N_c limit in splitting processes involving more color.

The object we end up with after doing our numerical calculation is

$$\mathcal{F}(\mathbf{p}|L) = \int_{\mathbf{u}\bar{\mathbf{u}}} e^{-i(\mathbf{u}-\bar{\mathbf{u}})\cdot\mathbf{p}} \mathcal{F}(\mathbf{u}, \bar{\mathbf{u}}|L), \quad (5.1)$$

where $\mathcal{F}(\mathbf{u}, \bar{\mathbf{u}}|L)$ is defined in Eq. (4.9). The code then simulates the time evolution of the object $\mathcal{F}(\mathbf{p}|L)$, as a function of the splitting fraction z and the transverse momentum \mathbf{p} , or equivalently splitting angle θ , as $|\mathbf{p}| \simeq \omega\theta$.

We focus on the medium modification factor F_{med} , introduced in (3.25). It measures how much the medium-induced emission spectrum differs from the vacuum spectrum, and is defined as

$$F_{\text{med}} = \left(\frac{dI^{\text{in-in}}}{dzd^2\mathbf{p}} + \frac{dI^{\text{in-out}}}{dzd^2\mathbf{p}} \right) / \frac{dI^{\text{vac}}}{dzd^2\mathbf{p}}. \quad (5.2)$$

This ratio cancels directly out the soft and collinear divergences contained in the vacuum spectrum. In particular, since the Altarelli-Parisi splitting function is canceled out in (5.2), we expect that F_{med} should give a measure of the medium modifications that is, at least *qualitatively*, universal among the medium-induced splitting processes (up to the magnitude of the effects).

In the previous sections we have computed the vacuum and in-out contributions analytically in the HO approximation, see Eqs. (3.30) and (4.7). For the in-in contribution we have as mentioned calculated the object $\mathcal{F}(\mathbf{p}|L)$ numerically. Inserting this into the above equation gives

$$F_{\text{med}} = \text{Re} \left(\frac{\mathbf{p}^2}{2\omega^2} \mathcal{F}(\mathbf{p}|L) - 2 \left[1 - e^{-i \frac{\tan(\Omega L)}{2\omega\Omega} \mathbf{p}^2} \right] \right). \quad (5.3)$$

We will now discuss some of the main observations from the results of our simulations.

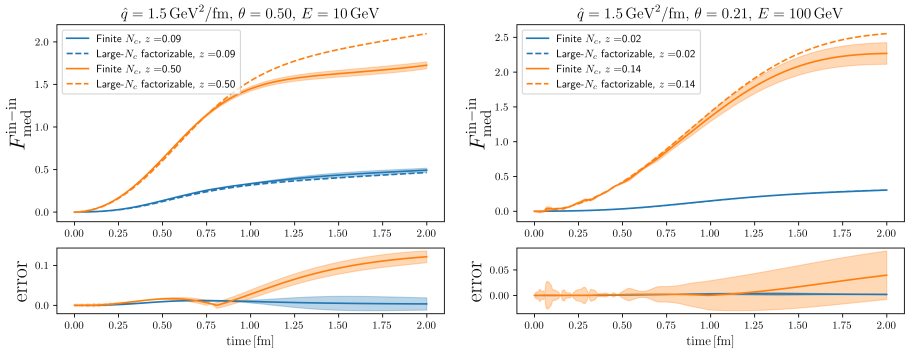


Figure 3. $F_{\text{med}}^{\text{in-in}}$ as a function of time for different values of ω .

5.1 The in-in contribution

To start, it is interesting to look at just the in-in contribution, as this is what was studied in [28]. To do this we define $F_{\text{med}}^{\text{in-in}} = \text{Re} \frac{p^2}{2\omega^2} \mathcal{F}(\mathbf{p}|L)$, and plot this as a function of time and θ in Figs. 3-5. In [28] the authors argue that the non-factorizable part should be negligible as long as $L \gg t_{\text{br}} = \sqrt{2\omega/\hat{q}}$. We can now use our numerical results to check this statement.

Looking at the left plot in Fig. 3 we have $t_{\text{br}} \simeq 0.5$ fm and $t_{\text{br}} \simeq 0.8$ fm for $z = 0.09$ and $z = 0.5$, respectively. We would therefore expect the finite- N_c and the factorizable results to match closely at late times. However, this is not what we see. For $z = 0.5$ the two solutions actually move away from each other at around 1 fm. The same is also true for the 100 GeV plot on the right, but since error bands are bigger it is harder to draw concrete conclusions.

To study the behavior at late times in more detail we have in Fig. 4 plotted $F_{\text{med}}^{\text{in-in}}$ up to 5 fm. Numerically this was only possible at 10 GeV, as the error blows up at late times for the 100 GeV case. In this figure we have used two different values of \hat{q} , which is a way of varying t_{br} while holding ω constant. From this figure it is clear that the difference between the finite- N_c and factorizable solutions grows at around 1 fm, and stabilizes to a constant value. This contradicts the notion from [28] that the non-factorizable should become less important at late times. However, it is consistent with [69], where we also found that the difference between the finite N_c and factorizable versions of the quadrupole amounted to a constant shift after some time.

On the other hand, it is interesting to note that the error in the case where $\hat{q} = 1.5$ GeV²/fm is bigger than the error when $\hat{q} = 3$ GeV²/fm. This does seem to support the claim that the non-factorizable piece is less important when \hat{q} is big, or equivalently t_{br} is small. Together, these observations seem to indicate that the size of the non-factorizable term as a function of the different parameters is more complicated than previously thought.

In Fig. 5 we have plotted the in-in contribution as a function of the splitting angle θ . This is also interesting to study, as the estimate that the non-factorizable piece should be

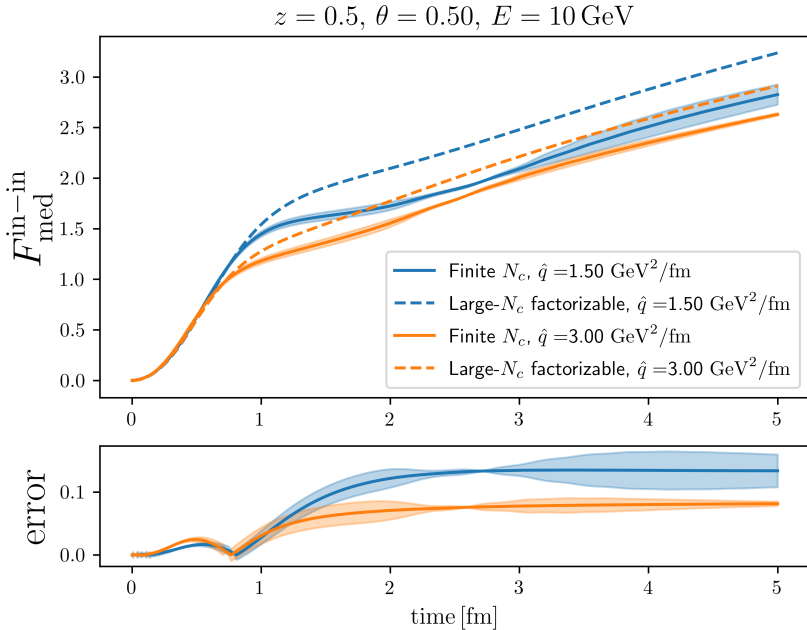


Figure 4. $F_{\text{med}}^{\text{in-in}}$ as a function of time for two different values of \hat{q} .

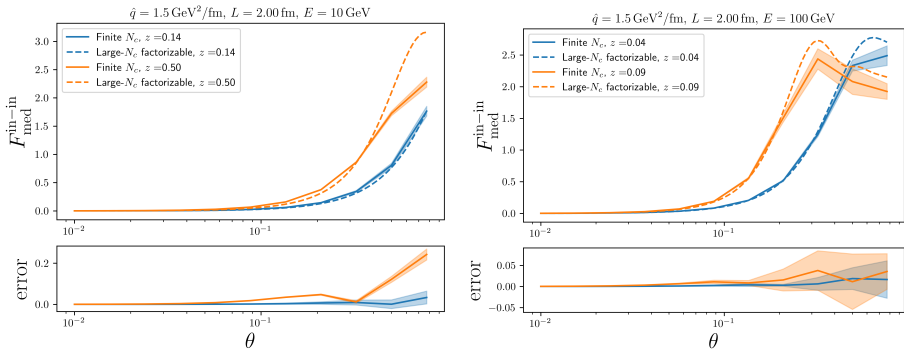


Figure 5. $F_{\text{med}}^{\text{in-in}}$ as a function of θ for different values of ω .

small when $L \gg t_{\text{br}}$ contains no information about the angle. We see that the factorizable piece matches the full solution one when F_{med} itself is small, while the two solutions show differences around the peaks in the distributions. Of the four curves in Fig. 5 only the one with $z = 0.5$ and $E = 10 \text{ GeV}$ ($t_{\text{br}} \simeq 0.8$) exhibits a significant difference between the factorizable and full solution. However, in the four plots the branching time t_{br} ranges

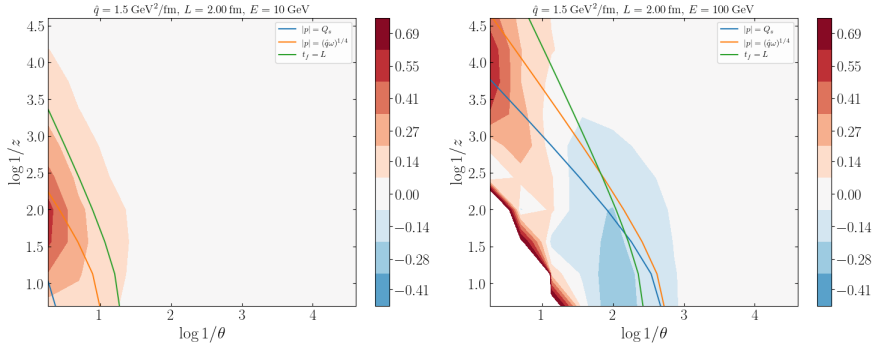


Figure 6. F_{med} , given in Eq. (5.2), simulated at finite- N_c for two different energies, i.e. for $E = 10$ GeV and $E = 100$ GeV. See text for further details. The two medium scales $|\mathbf{p}| = Q_s$ and $|\mathbf{p}| = (\omega\hat{q})^{1/4}$ are also plotted, as well as $t_f = L$.

from 0.8 fm to 1.4 fm, which is smaller than L , but not very much smaller, so it is hard to draw conclusions.

It is clear in both Figs. 3 and 5 that the non-factorizable part is small when z is small, which is what we expect from the analytic calculation (4.25).

5.2 Validation of the numerical results and comparison to approximate solutions

Armed with our numerical simulation we have the opportunity to study several approximations. From now we plot the full F_{med} , given in (5.2), which also includes the in-out term. As a first test case, we study going from the full finite- N_c result to the large- N_c solution. This amounts to simplifying the potential matrix in the Schrödinger equation from (4.21) to (4.22).

The next approximation we examine is comparing the magnitude of non-factorizable effects in the splitting. The factorizable piece corresponds to keeping only the first term of the quadrupole, see Eq. (4.25). This is what is usually done in most practical applications, and is therefore a very important test. For instance, for the special case of $g \rightarrow q\bar{q}$ (even with massive quarks), this is the *only* contribution at large- N_c [81].

Lastly, we will also compare our non-eikonal result to the fully eikonal approximation, where all the partons are put on classical paths. This is the approximation we used in [69], where we performed a similar study. Here, we put this approximation to the test.

We evaluate the numerics for the medium parameters $\hat{q} = 1.5$ GeV²/fm and $L = 2$ fm, and choose two, widely separated initial energies $E = 10$ GeV and $E = 100$ GeV as representative test cases. The simulated F_{med} at finite N_c is shown in Fig. 6, where we have plotted it in the two-dimensional $(\log \frac{1}{z}, \log \frac{1}{\theta})$ plane (or Lund plane) for a wide range of splitting fractions and angles. In this representation the vacuum spectrum alone, in the soft limit, would correspond to a constant $\propto \alpha_s C_R$. Hence, this provides a compact representation of where the medium effects are most pronounced.

In Fig. 6 we have also depicted the medium scales related to the transverse momentum scales from splitting, i.e. $|\mathbf{p}| = p_t = \omega\theta \sim (\omega\hat{q})^{1/4}$ (thick, red line), and broadening, i.e. $p_t = \omega\theta \sim Q_s = \sqrt{\hat{q}L}$ (thick, blue line). Finally, we also delineate where the formation time $t_f = 2\omega/p_t^2$ becomes equal to the medium length L (thick, green line). Clearly, as is most visible for the higher parton energy (Fig 6, right), medium effects are occurring at large angles and scale nicely with Q_s . However, whenever $Q_s \approx (\omega\hat{q})^{1/4}$, i.e. for long branching times, we note a net negative effect of medium interactions. In this regime, both of these scales also become comparable to the condition on the formation time $t_f < L$, or $p_t > \sqrt{2\omega/L}$. Note, however, that the full spectrum, i.e. vacuum plus medium, is positive.

Finally, we note that the simulation errors become quite large for large angles and large z for $E = 100$ GeV, and our results are therefore not shown in the lower, left corner of Fig 6 (right). We now turn to discuss exactly the simulation errors.

Estimating the simulation error. Before we do any of these comparisons we will discuss the error in our simulation. In this work, we have done three numerical simulations, corresponding to i) the finite- N_c result, ii) the large- N_c result, and iii) the factorizable part of the large- N_c result. The third point corresponds to a special case where we solve the coupled Schrödinger equations with the potential matrix \mathbb{M} at large- N_c , Eq. (4.22), while also setting the non-diagonal contributions to zero. In this case we also have an analytic formula, Eq. (4.42). This gives us a way to compare our numerical simulations, in this special case, to a well-defined answer and the difference between these two will then give us an estimate of the simulation error.

Hence, as a proxy for the full numerical error, we define the error of the simulation as $1 + F_{\text{med}}$ calculated analytically and numerically, according to prescription iii) above. Hence, we define the accuracy as,

$$\Delta_{\text{num}} \equiv \frac{|F_{\text{med,analytic}} - F_{\text{med,simulated}}|}{1 + |F_{\text{med,analytic}}|}. \quad (5.4)$$

This quantity is plotted on the Lund plane in Fig. 7.

As one can see from Fig. 7 the simulation error is generally small for the 10 GeV case. For the 100 GeV case the error grows large for big θ and $z \sim 0.5$. We therefore do not

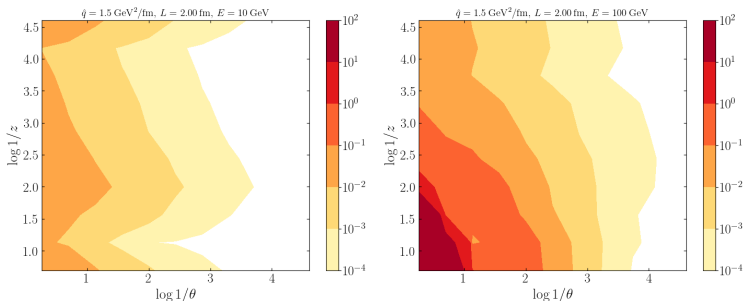


Figure 7. The simulation error Δ_{num} , defined in Eq. (5.4), for two different energies.

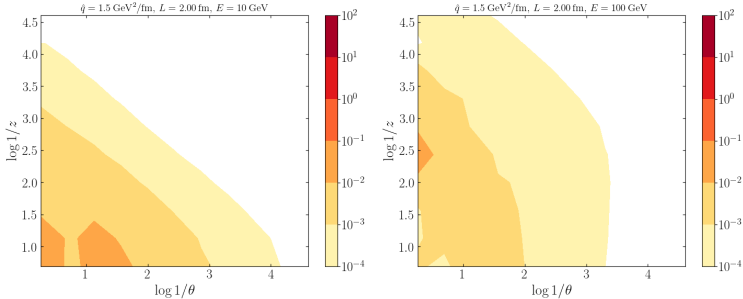


Figure 8. The difference Δ_{N_c} between $1 + F_{\text{med}}$ simulated at finite N_c and large- N_c , defined in Eq. (5.5).

expect to get accurate results in this part of the phase space. This comes from the fact that the Schrödinger equation (4.10) contains a non-homogeneous term with a complex phase which is proportional to $\sqrt{\omega}$. This phase will oscillate rapidly when ω is big, meaning we need an increasingly detailed grid to capture these oscillations. Further work is needed to address this corner of the phase space.

However, except for this corner of the phase space for the 100 GeV case, the simulation error is sufficiently small to be able to draw meaningful conclusions from the numerical results.

Comparing finite- N_c and large- N_c . In [69] we found that there is only a very small difference between the spectrum for finite N_c and large- N_c in the $\gamma \rightarrow q\bar{q}$ case. In that paper we used the eikonal approximation for all the partons, so it is interesting to see if anything changes when we here include the possibility to accumulate transverse momentum along the partonic lines. Again we define the difference between the two schemes on the level of $1 + F_{\text{med}}$, and plot

$$\Delta_{N_c} \equiv \frac{|F_{\text{med,finite-}N_c} - F_{\text{med,large-}N_c}|}{1 + |F_{\text{med,finite-}N_c}|}, \quad (5.5)$$

in Fig. 8. As we can see from the difference between the finite- N_c and large- N_c results are very small in the whole (θ, z) plane, mostly under 1 %. This is consistent with our earlier findings in [69]. However, in that work we found substantial differences in the cases of $q \rightarrow qg$ and $g \rightarrow gg$, so we would expect the same in this case.

Since the difference between the results at finite N_c and large- N_c is so small we will subsequently only plot the result at finite N_c .

Comparing large- N_c and the factorizable contribution. The quadrupole at large- N_c is given in Eq. (4.25). In most analytic calculations of the emission spectrum the second non-factorizable term is dropped, and only the first term is considered. We directly see from the definition that the non-factorizable term vanishes for soft emissions $z \rightarrow 0$. For soft or unbalanced splittings, $z \ll 1$, we expect the non-factorizable contributions to be

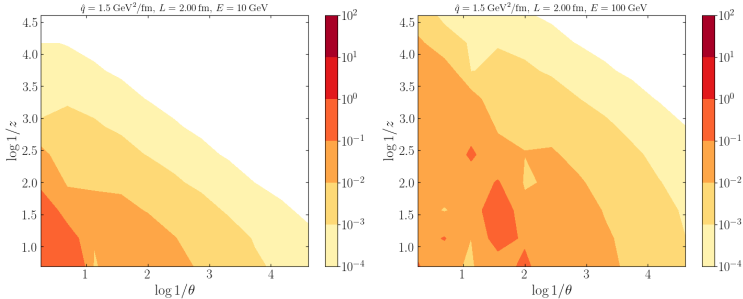


Figure 9. The difference $\Delta_{\text{non-fac}}$ between $1 + F_{\text{med}}$ calculated at large- N_c and keeping only the factorizable term of the large- N_c solution, defined in Eq. (5.6).

suppressed by an inverse length, i.e. t_{br}/L (at least this was argued in the large- N_c limit) [28]. However, there could be important differences at finite z and large angles.

In order to gauge the importance of the full range of non-factorizable contributions at finite- N_c , we define

$$\Delta_{\text{non-fac}} \equiv \frac{|F_{\text{med,large-}N_c} - F_{\text{med,factorizable}}|}{1 + |F_{\text{med,large-}N_c}|}. \quad (5.6)$$

which is plotted in Fig. 9. We see from comparing Figs. 8 and 9 that dropping the non-factorizable part of the large- N_c solution introduces a considerably bigger error than what is introduced by going from finite- N_c to large- N_c .

It is also clear that this approximation works well in the soft limit, as expected. This indicates that it is safe to only use the factorizable piece when calculating soft emissions. However, for finite z one should be more careful, as there might be significant contributions from the non-factorizable term, leading to significant deviations.

Comparing the eikonal approximation and non-eikonal corrections. In [69] we also studied many of the same effects we have presented here. However, in that paper we used the eikonal approximation, where all the partons travel on straight lines through the medium. In App. D we show how the calculation simplifies in the eikonal limit. It is interesting to examine how well the eikonal approximation actually works. We will compare the factorizable term of the large- N_c solution in the eikonal limit and with full transverse behavior. This comparison is convenient, as we have analytical solutions for both, see Eqs. (D.15) and (4.42), respectively. That means we are not limited by the simulation and the error bands that come with it. We expect that the eikonal approximation works best when ω is big, or when $z \sim 0.5$. In Fig. 10 we have plotted the error introduced by using the eikonal approximation, compared to the non-eikonal version, defined as

$$\Delta_{\text{eik}} \equiv \frac{|F_{\text{med,non-eikonal}} - F_{\text{med,eikonal}}|}{1 + |F_{\text{med,non-eikonal}}|}. \quad (5.7)$$

As one can see the eikonal approximation overestimates the contribution by a big margin, especially along the line $\omega\theta \sim Q_s$, i.e. around the peak of the spectrum. We can therefore

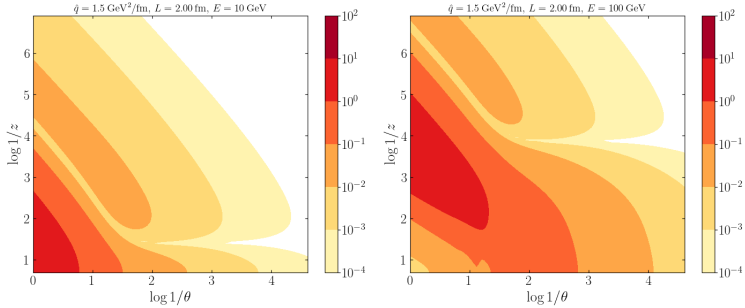


Figure 10. The difference Δ_{eik} between eikonal and non-eikonal $1 + F_{\text{med}}$, calculated analytically for the factorizable piece of the large- N_c solution, defined in Eq. (5.7).

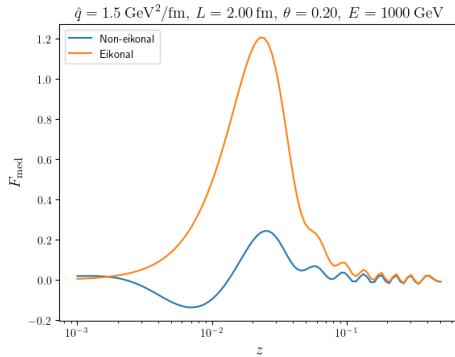


Figure 11. Comparison of the non-eikonal and fully eikonal F_{med} , calculated using the factorizable part of the large- N_c solution, as a function of z , for a much higher energy $E = 1000$ GeV.

conclude that using the eikonal approximation does not work well for the values of the parameters we have chosen in this paper.

In Fig. 11 we have plotted F_{med} as a function of z at a higher energy of $E = 1000$ GeV, to study whether the eikonal approximation is accurate at this energy scale. From the figure it is clear that it does indeed work well for z close to 0.5. However, it still fails to capture the main contribution of F_{med} , which is present at lower z .

We would also like to point out that we have here used the eikonal approximation on all of the partons. It is common to study the case where one of the emitted partons is soft, while the other is hard. In that case the eikonal approximation could be used on the hard partons, while the full transverse dependence of the soft parton should be kept. We expect this to give a more accurate result than the fully eikonal case, but we have decided not to pursue this scheme further here.

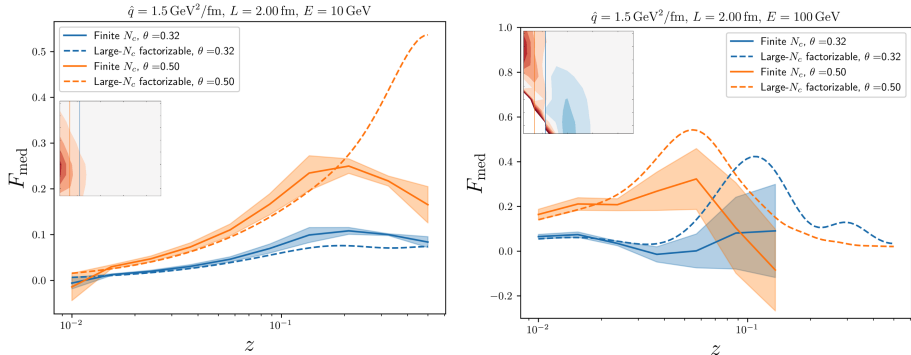


Figure 12. F_{med} calculated at finite N_c and the factorizable part of the large- N_c solution. On the Lund plane we have indicated constant θ slices that we plot as a function of z .

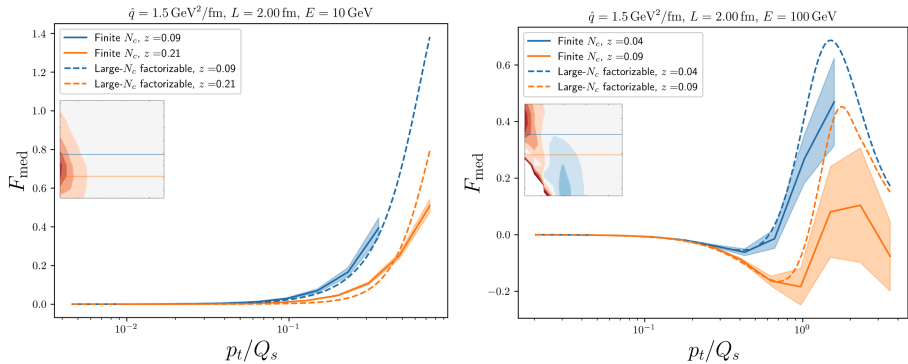


Figure 13. F_{med} calculated at finite N_c and the factorizable part of the large- N_c solution. On the Lund plane we have indicated constant z slices that we plot as a function of p_t/Q_s .

5.3 Precision calculation of splitting function in the Lund plane

Finally, we turn to the state-of-the-art calculations of the splitting function, evaluated in the HO approximation without any other further approximations. In this section we discuss our results, and plot slices of the Lund plane as a function of different parameters.

In Fig. 12 we have plotted F_{med} simulated at finite N_c . We have plotted a slice of this at constant θ , as a function of z . We have plotted both the simulated finite- N_c result and the analytical formula for the factorizable piece of the large- N_c solution. It is interesting to note that the two different solutions are within error bands of each other at low- z , i.e. $z < 0.1$.

However, as z approaches 0.5 the two solutions diverge. The factorizable part overestimates the finite- N_c value by a significant margin. In addition, the two solutions peak at different z -values. This again shows that the factorizable part is not as accurate at finite $z > 0.1$.

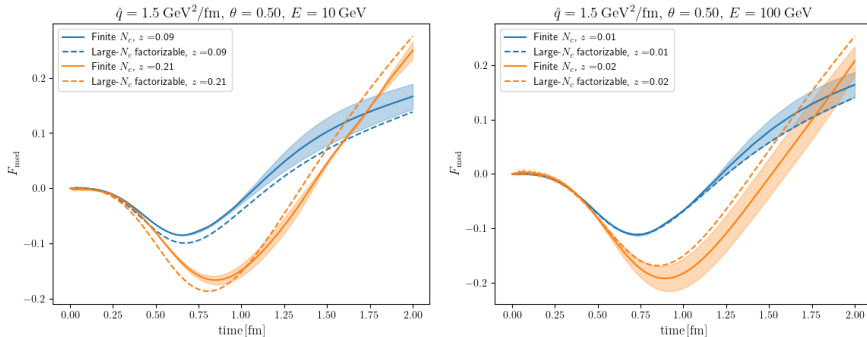


Figure 14. F_{med} as a function of time for two different energies.

Next, in Fig. 13, we plot the medium modification F_{med} for two slices of constant z , as indicated on the Lund plane in the inset. We plot this as a function of the dimensionless ratio p_t/Q_s , where $p_t \equiv |\mathbf{p}| = \omega\theta$. In the soft limit, $z \ll 1$, one expects that the distribution should peak around $p_t/Q_s \approx 1$ [41]. This is indeed the case for both the factorizable part (now at finite- z) and for the full, finite- N_c simulation, although the peak is less distinguishable due to the numerical errors. However, the factorizable solution again overshoots the true value, especially at large p_t or angles.

As our last numerical results, we show the time evolution of F_{med} in Fig. 14. Here we have chosen z and θ to be close to the respective peaks in the distributions at $L = 2$ fm. From these plots it is clear that the peak of the distribution moves with time. As we sit in a constant point in the (θ, z) plane the distribution is first negative, and then becomes positive as time progresses.

We note also that the large- N_c /factorizable result agrees with the full calculation at early times, to diverge from it at later times. This is related to the physics of multiple scattering. At early times in the medium, there were simply not enough scatterings to cause strong color rotations so as to probe the many possible intermediate states of the two-body final particle system. This, however, changes when time progresses and the full color dynamics become apparent.

Furthermore, Fig. 14 provides an *a posteriori* justification for using the HO approximation in this work. As is well known [42], hard medium-induced emissions occur mostly at early times in the medium. It can be explicitly checked that the mixing of different color states only occurs at higher orders ($N > 1$) in the opacity expansion. In order to induce the color dynamics responsible for factorization-breaking effects one needs frequent scatterings to occur; some to induce the splitting and others in charge of de-correlating and broadening the final splitting products.

6 Conclusion and outlook

In this paper we have derived the spectrum for a medium-induced emission without invoking the large- N_c or eikonal approximations. This was done in Sec. 3.1. The spectrum can be divided into a vacuum component (called out-out) and a medium component, consisting of an in-out piece and in-in piece, which for a general potential are given in Eqs. (3.30), (3.32) and (3.34), respectively. The in-in contribution contains the quadrupole correlation function $\mathcal{Q}(L, t)$, which currently cannot be solved analytically without using the large- N_c approximation. We then showed how the in-in contribution can be solved through a Schrödinger equation in Eq. (3.39).

In Sec. 4, we focused our efforts by applying the general results we derived in the previous sections to a state-of-the-art calculation of a concrete splitting process. We chose to study the process $\gamma \rightarrow q\bar{q}$, in the harmonic oscillator approximation. We here found that the large- N_c approximation works extremely well for the photon case, which also echoes the results we found in [69]. Our main result of this calculation was shown in Fig. 8.

We also examined how well the full spectrum can be approximated using only the first of the two terms in the large- N_c solution of the quadrupole, given in Eq. (4.25). This is important, as usually only the first term, referred to as the factorizable term, is kept in calculations of the emission spectrum, as the quadrupole then simplifies substantially. The factorizable and full solutions were shown in Fig. 9 and also Figs. 12-5. As expected from the analytical formula (4.25) we found that the factorizable term provides an excellent approximation of the full solution in the soft limit when $z \sim 0$. However, we do see a small deviation at finite z , at the order of 10 %, and even higher at large angles. It could therefore be important to include both terms in studies that focus on corrections where z is not small. Our results, also summarized in Fig. 4, seem to indicate that the non-factorizable terms are sizable and persistent even for large media even for small branching times, while their impact overall decreases when decreasing the branching time. This indicates that the color-dynamics taking place from moment of the branching to the end of the medium is non-trivial. These effects are expected to be bigger for partons with a higher color charge, such as $g \rightarrow gg$ branching, and deserves further studies.

We also compared our result to the fully eikonal result, where all the partons are put on straight lines. This is what was done in [69], so keeping the full transverse dynamics is the main improvement over that paper. We found in Fig. 10 that the fully eikonal approximation is not generally very effective at capturing the spectrum, especially at low ω . However, it should be noted that in many calculations the soft limit is used, where you keep the non-eikonal behavior of the soft line, while putting the rest on straight lines. We expect this to work better for small z , and is something that could be studied in future work.

Having established a working methodology, this work therefore paves the way for precise calculations of all QCD and QED/EW splitting functions in the medium. As a next important step, we will attempt to solve the necessary evolution equations for $g \rightarrow gg$ and $q \rightarrow qg$ which both contain soft divergences and should therefore occur frequently in the QGP. On the level of spectra differential only in the momentum-sharing fractions,

this would also be relevant for studying overlapping formation times in $g \rightarrow ggg$ splitting beyond the soft and/or large- N_c limits [72]. A further perspective worth considering is to simulate more partons as many-body and multi-level (in the sense of color) quantum-mechanical systems in a background field. This effort seems however daunting due to the exponentially growing size of the system of coupled evolution equations, describing the available color representations of the involved partons.

Going beyond the HO approximation is also, in principle, straightforward. In order to achieve a full resummation one should use the complete elastic medium scattering potential, and use the most general interaction matrix \mathbb{M} as given in Eq. (4.19). In this case, one also needs to evaluate the three-point function $\mathcal{K}(\mathbf{u}, \mathbf{u}_2|t_2, t_1)$ numerically with a completely analogous numerical Schrödinger equation. Hence, the non-homogeneous contribution to \mathcal{F} , as in Eq. (3.39), would be provided as numerical data. In principle, one could also use scattering potentials extracted from lattice simulations of high-temperature QCD [82].

Acknowledgments

We would like to thank Fabio Dominguez for helpful discussions and private communication on this subject. We would also like to thank Adam Takacs and Alexandre Falcão for useful discussions and feedback. Finally, we acknowledge financial support from the Trond Mohn Foundation (BFS2018REK01).

A Simplifying n-point functions

Here we will show how the n-point functions present in Eq. (3.1) can be simplified. It is adapted from the procedure shown in [28].

A.1 Four-point function

The four-point function up to some final time t_f is given by

$$(\mathbf{k}, \mathbf{q}; \mathbf{k}, \mathbf{q}|S^{(4)}(t_f, t_2)|\mathbf{k}_2, \mathbf{q}_2; \bar{\mathbf{k}}_2, \bar{\mathbf{p}}_2 - \bar{\mathbf{k}}_2) = d_{bc} \left\langle (\mathbf{k}|\mathcal{G}_b|\mathbf{k}_2)(\mathbf{q}|\mathcal{G}_c|\mathbf{q}_2)(\bar{\mathbf{p}}_2 - \bar{\mathbf{k}}_2|\mathcal{G}_c^\dagger|\mathbf{q})(\bar{\mathbf{k}}_2|\mathcal{G}_b^\dagger|\mathbf{k}) \right\rangle, \quad (\text{A.1})$$

where the color factor d_{bc} is process dependent, and we have neglected all color indices. The propagators are usually formulated in position space, see Eq. (2.1), so after a Fourier transform it becomes

$$\begin{aligned} & (\mathbf{k}, \mathbf{q}; \bar{\mathbf{k}}, \mathbf{q}|S^{(4)}(t_f, t_2)|\mathbf{k}_2, \mathbf{q}_2; \bar{\mathbf{k}}_2, \bar{\mathbf{p}}_2 - \bar{\mathbf{k}}_2) = \\ & \int_{x_2 y_2 \bar{y}_2 \bar{x}_2 x y \bar{y} \bar{x}} e^{i\mathbf{k}_2 \cdot \mathbf{x}_2 - i\bar{\mathbf{k}}_2 \cdot \bar{\mathbf{x}}_2 + i\mathbf{q}_2 \cdot \mathbf{y}_2 - i(\bar{\mathbf{p}}_2 - \bar{\mathbf{k}}_2) \cdot \bar{\mathbf{y}}_2 - i\mathbf{k} \cdot (\mathbf{x} - \bar{\mathbf{x}}) - i\mathbf{q} \cdot (\mathbf{y} - \bar{\mathbf{y}})} \\ & \times (\mathbf{x}, \mathbf{y}; \bar{\mathbf{x}}, \bar{\mathbf{y}}|S^{(4)}(t_f, t_2)|x_2, y_2; \bar{x}_2, \bar{y}_2). \end{aligned} \quad (\text{A.2})$$

The four-point function in position space is then given by

$$\begin{aligned}
(\mathbf{x}, \mathbf{y}; \bar{\mathbf{x}}, \bar{\mathbf{y}} | S^{(4)}(t_f, t_2) | \mathbf{x}_2, \mathbf{y}_2; \bar{\mathbf{x}}_2, \bar{\mathbf{y}}_2) &= d_{bc} \langle (\mathbf{x} | \mathcal{G}_b | \mathbf{x}_2) (\mathbf{y} | \mathcal{G}_c | \mathbf{y}_2) (\bar{\mathbf{y}}_2 | \mathcal{G}_c^\dagger | \bar{\mathbf{y}}) (\bar{\mathbf{x}}_2 | \mathcal{G}_b^\dagger | \bar{\mathbf{x}}) \rangle \\
&= \int_{\mathbf{x}_2}^{\mathbf{x}} \mathcal{D}\mathbf{r}_1 \int_{\mathbf{y}_2}^{\mathbf{y}} \mathcal{D}\mathbf{r}_2 \int_{\bar{\mathbf{y}}_2}^{\bar{\mathbf{y}}} \mathcal{D}\bar{\mathbf{r}}_2 \int_{\bar{\mathbf{x}}_2}^{\bar{\mathbf{x}}} \mathcal{D}\bar{\mathbf{r}}_1 e^{i\frac{E}{2} \int_{t_2}^{t_f} ds [z(\dot{\mathbf{r}}_1^2 - \dot{\bar{\mathbf{r}}}_1^2) + (1-z)(\dot{\mathbf{r}}_2^2 - \dot{\bar{\mathbf{r}}}_2^2)]} \mathcal{C}^{(4)}(\mathbf{r}_1, \mathbf{r}_2, \bar{\mathbf{r}}_2, \bar{\mathbf{r}}_1),
\end{aligned} \tag{A.3}$$

where the potential term $\mathcal{C}^{(4)}$ is a correlator of Wilson lines

$$\mathcal{C}^{(4)}(\mathbf{r}_1, \mathbf{r}_2, \bar{\mathbf{r}}_2, \bar{\mathbf{r}}_1) = d_{bc} \langle V_b(\mathbf{r}_1) V_c(\mathbf{r}_2) V_c^\dagger(\bar{\mathbf{r}}_2) V_b^\dagger(\bar{\mathbf{r}}_1) \rangle. \tag{A.4}$$

The Wilson lines $V(\mathbf{r})$ can be in the fundamental or adjoint representations depending on the process.

In [69] it was shown that all Wilson line correlators can be written as a system of differential equations

$$\frac{d}{dt} \mathcal{C}_i^{(4)} = \mathbb{M}_{ij} \mathcal{C}_j^{(4)}. \tag{A.5}$$

Here \mathcal{C}_j indicates some other color configuration of the same Wilson lines. It was also shown in [69] that the evolution matrix only depends on the differences of the coordinates

$$\mathbb{M}_{ij} = \mathbb{M}_{ij}(\sigma_{12}, \sigma_{\bar{1}\bar{2}}, \sigma_{1\bar{1}}, \sigma_{2\bar{2}}, \sigma_{1\bar{2}}, \sigma_{\bar{1}2}). \tag{A.6}$$

Here we have used the notation $\sigma_{12} \equiv \sigma(\mathbf{r}_1 - \mathbf{r}_2)$. This implies that $\mathcal{C}^{(4)}$ also only depends on the differences of the coordinates. It is therefore natural to change to the following coordinates, with unit Jacobian

$$\begin{aligned}
\mathbf{u} &= \mathbf{r}_1 - \mathbf{r}_2 \\
\bar{\mathbf{u}} &= \bar{\mathbf{r}}_1 - \bar{\mathbf{r}}_2 \\
\mathbf{v} &= z(\mathbf{r}_1 - \bar{\mathbf{r}}_1) + (1-z)(\mathbf{r}_2 - \bar{\mathbf{r}}_2) \\
\mathbf{w} &= \frac{1}{2}[z(\mathbf{r}_1 + \bar{\mathbf{r}}_1) + (1-z)(\mathbf{r}_2 + \bar{\mathbf{r}}_2)].
\end{aligned} \tag{A.7}$$

Now the correlator $\mathcal{C}^{(4)}$ only depends on the coordinates $\mathbf{u}, \bar{\mathbf{u}}$ and \mathbf{v} , and there is no dependence on \mathbf{w} . The four-point function then becomes

$$\begin{aligned}
(\mathbf{x}, \mathbf{y}; \bar{\mathbf{x}}, \bar{\mathbf{y}} | S^{(4)}(t_f, t_2) | \mathbf{x}_2, \mathbf{y}_2; \bar{\mathbf{x}}_2, \bar{\mathbf{y}}_2) &= \\
&= \int \mathcal{D}\mathbf{w} \int \mathcal{D}\mathbf{v} \int \mathcal{D}\mathbf{u} \int \mathcal{D}\bar{\mathbf{u}} e^{i\frac{E}{2} \int_{t_2}^{t_f} ds [2\dot{\mathbf{v}} \cdot \dot{\mathbf{w}} + z(1-z)(\dot{\mathbf{u}}^2 - \dot{\bar{\mathbf{u}}}^2)]} \mathcal{C}^{(4)}(\mathbf{u}, \bar{\mathbf{u}}, \mathbf{v}).
\end{aligned} \tag{A.8}$$

Since the potential does not depend on \mathbf{w} the path integral over \mathbf{w} can be done, which has the effect of forcing \mathbf{v} to be on the classical path $\mathbf{v} \rightarrow \mathbf{v}_{\text{cl}}$. The result is

$$\begin{aligned}
&(\mathbf{x}, \mathbf{y}; \bar{\mathbf{x}}, \bar{\mathbf{y}} | S^{(4)}(t_f, t_2) | \mathbf{x}_2, \mathbf{y}_2; \bar{\mathbf{x}}_2, \bar{\mathbf{y}}_2) \\
&= \left(\frac{E}{2\pi(t_f - t_2)} \right)^2 e^{i\frac{E}{(t_f - t_2)} \Delta \mathbf{v} \cdot \Delta \mathbf{w}} \int \mathcal{D}\mathbf{u} \int \mathcal{D}\bar{\mathbf{u}} e^{i\frac{E}{2} \int_{t_2}^{t_f} ds (\dot{\mathbf{u}}^2 - \dot{\bar{\mathbf{u}}}^2)} \mathcal{C}^{(4)}(\mathbf{u}, \bar{\mathbf{u}}, \mathbf{v}_{\text{cl}}),
\end{aligned} \tag{A.9}$$

where $\Delta \mathbf{w} = \mathbf{w}(t_f) - \mathbf{w}(t_2)$ and we have defined $\omega = z(1-z)E$. Now we can return to momentum space. After performing the same coordinate change on the Fourier components in Eq. (A.2) the integrals involving the \mathbf{w} components are

$$\begin{aligned} & \int_{\mathbf{w}_L \mathbf{w}_2} e^{i\mathbf{w}_2 \cdot (\mathbf{q}_2 + \mathbf{k}_2 - \bar{\mathbf{p}}_2)} e^{i\frac{E}{(t_f - t_2)} \Delta \mathbf{v} \cdot (\mathbf{w}_L - \mathbf{w}_2)} \\ &= \left(\frac{2\pi(t_f - t_2)}{E} \right)^2 (2\pi)^2 \delta^2(\Delta \mathbf{v}) (2\pi)^2 \delta^2(\mathbf{q}_2 + \mathbf{k}_2 - \bar{\mathbf{p}}_2). \end{aligned} \quad (\text{A.10})$$

Inserting this into the expression for the four-point function in momentum space Eq. (A.2) and doing one \mathbf{v} integral leads to Eq. (3.7)

$$\begin{aligned} & (\mathbf{k}, \mathbf{q}; \mathbf{k}, \mathbf{q} | S^{(4)}(t_f, t_2) | \mathbf{k}_2, \mathbf{q}_2; \bar{\mathbf{k}}_2, \bar{\mathbf{p}}_2 - \bar{\mathbf{k}}_2) = (2\pi)^2 \delta^2(\mathbf{q}_2 + \mathbf{k}_2 - \bar{\mathbf{p}}_2) \\ & \times \int_{\mathbf{u}_2 \mathbf{u}_f \bar{\mathbf{u}}_2 \bar{\mathbf{u}}_f \mathbf{v}} e^{i\mathbf{v} \cdot (\bar{\mathbf{p}}_2 - \mathbf{q} - \mathbf{k}) + i\mathbf{u}_2 \cdot (\mathbf{k}_2 - z\bar{\mathbf{p}}_2) - i\bar{\mathbf{u}}_2 \cdot (\bar{\mathbf{k}}_2 - z\bar{\mathbf{p}}_2) - i(\mathbf{u}_f - \bar{\mathbf{u}}_f) \cdot ((1-z)\mathbf{k} - z\mathbf{q})} \\ & \times \int_{\mathbf{u}_2}^{\mathbf{u}_f} \mathcal{D}\mathbf{u} \int_{\bar{\mathbf{u}}_2}^{\bar{\mathbf{u}}_f} \mathcal{D}\bar{\mathbf{u}} e^{i\frac{\omega}{2} \int_{t_2}^{t_f} ds (\dot{\mathbf{u}}^2 - \dot{\bar{\mathbf{u}}}^2)} \mathcal{C}^{(4)}(\mathbf{u}, \bar{\mathbf{u}}, \mathbf{v}) \\ & \equiv (2\pi)^2 \delta^2(\mathbf{q}_2 + \mathbf{k}_2 - \bar{\mathbf{p}}_2) S^{(4)}((1-z)\mathbf{k} - z\mathbf{q}, \mathbf{k}_2 - z\bar{\mathbf{p}}_2, \bar{\mathbf{k}}_2 - z\bar{\mathbf{p}}_2, \bar{\mathbf{p}}_2 - \mathbf{k} - \mathbf{q} | t_f, t_2). \end{aligned} \quad (\text{A.11})$$

Here it is clear that it is more convenient to use the momentum variables $\mathbf{l}_2 = \mathbf{k}_2 - z\bar{\mathbf{p}}_2$, $\bar{\mathbf{l}}_2 = \bar{\mathbf{k}}_2 - z\bar{\mathbf{p}}_2$, $\mathbf{p} = (1-z)\mathbf{k} - z\mathbf{q}$ and $\mathbf{P} = \mathbf{q} + \mathbf{k}$, where the four-point function is $S^{(4)}(\mathbf{p}, \mathbf{l}_2, \bar{\mathbf{l}}_2, \bar{\mathbf{p}}_2 - \mathbf{P} | t_f, t_2)$.

A.2 Three-point function

The three-point function is given by

$$(\mathbf{k}_2, \mathbf{q}_2; \bar{\mathbf{p}}_2 | S^{(3)}(t_2, t_1) | \mathbf{k}_1, \mathbf{p}_1 - \mathbf{k}_1; \bar{\mathbf{p}}_1) = d_{abc} \left\langle (\mathbf{k}_2 | \mathcal{G}_b | \mathbf{k}_1) (\mathbf{q}_2 | \mathcal{G}_c | \mathbf{p}_1 - \mathbf{k}_1) (\bar{\mathbf{p}}_1 | \mathcal{G}_a^\dagger | \bar{\mathbf{p}}_2) \right\rangle, \quad (\text{A.12})$$

where the color factor d_{abc} is process dependent, and we have neglected all color indices. The propagators are usually formulated in position space, see Eq. (2.1), so after a Fourier transform it becomes

$$\begin{aligned} & (\mathbf{k}_2, \mathbf{q}_2; \bar{\mathbf{p}}_2 | S^{(3)}(t_2, t_1) | \mathbf{k}_1, \mathbf{p}_1 - \mathbf{k}_1; \bar{\mathbf{p}}_1) = \\ & \int_{\mathbf{x}_1 \mathbf{x}_2 \mathbf{y}_1 \mathbf{y}_2 \bar{\mathbf{z}}_1 \bar{\mathbf{z}}_2} e^{i\mathbf{k}_1 \cdot \mathbf{x}_1 - i\mathbf{k}_2 \cdot \mathbf{x}_2 + i(\mathbf{p}_1 - \mathbf{k}_1) \cdot \mathbf{y}_1 - i\mathbf{q}_2 \cdot \mathbf{y}_2 - i\bar{\mathbf{p}}_1 \cdot \bar{\mathbf{z}}_1 + i\bar{\mathbf{p}}_2 \cdot \bar{\mathbf{z}}_2} \\ & \times (\mathbf{x}_2, \mathbf{y}_2; \bar{\mathbf{z}}_2 | S^{(3)}(t_2, t_1) | \mathbf{x}_1, \mathbf{y}_1; \bar{\mathbf{z}}_1). \end{aligned} \quad (\text{A.13})$$

The three-point function in position space is then given by

$$\begin{aligned} & (\mathbf{x}_2, \mathbf{y}_2; \bar{\mathbf{z}}_2 | S^{(3)}(t_2, t_1) | \mathbf{x}_1, \mathbf{y}_1; \bar{\mathbf{z}}_1) = d_{abc} \left\langle (\mathbf{x}_2 | \mathcal{G}_b | \mathbf{x}_1) (\mathbf{y}_2 | \mathcal{G}_c | \mathbf{y}_1) (\bar{\mathbf{z}}_1 | \mathcal{G}_a^\dagger | \bar{\mathbf{z}}_2) \right\rangle \\ & = \int_{\mathbf{x}_1}^{\mathbf{x}_2} \mathcal{D}\mathbf{r}_1 \int_{\mathbf{y}_1}^{\mathbf{y}_2} \mathcal{D}\mathbf{r}_2 \int_{\bar{\mathbf{z}}_1}^{\bar{\mathbf{z}}_2} \mathcal{D}\bar{\mathbf{r}}_0 e^{i\frac{E}{2} \int_{t_1}^{t_2} ds [z\dot{\mathbf{r}}_1^2 + (1-z)\dot{\mathbf{r}}_2^2 - \dot{\bar{\mathbf{r}}}_0^2]} \mathcal{C}^{(3)}(\mathbf{r}_1, \mathbf{r}_2, \bar{\mathbf{r}}_0), \end{aligned} \quad (\text{A.14})$$

where the correlator $\mathcal{C}^{(3)}$ is given by

$$\mathcal{C}^{(3)}(\mathbf{r}_1, \mathbf{r}_2, \bar{\mathbf{r}}_0) = d_{abc} \left\langle V_b(\mathbf{r}_1) V_c(\mathbf{r}_2) V_a^\dagger(\bar{\mathbf{r}}_0) \right\rangle. \quad (\text{A.15})$$

The Wilson lines $V(\mathbf{r})$ can be in the trivial, fundamental, or adjoint representations depending on the process.

In [69] it was shown that all Wilson line correlators can be written as a system of differential equations

$$\frac{d}{dt} \mathcal{C}_i^{(3)}(\mathbf{r}_1, \mathbf{r}_2, \bar{\mathbf{r}}_0) = \mathbb{M}_{ij}(\mathbf{r}_1 - \bar{\mathbf{r}}_0, \mathbf{r}_2 - \bar{\mathbf{r}}_0, \mathbf{r}_2 - \mathbf{r}_1) \mathcal{C}_j^{(3)}(\mathbf{r}_1, \mathbf{r}_2, \bar{\mathbf{r}}_0). \quad (\text{A.16})$$

Here $\mathcal{C}_j^{(3)}$ indicates some other color configuration of the same Wilson lines. The fact that the evolution matrix only depends on the differences of the coordinates implies that the same is true for the correlator: $\mathcal{C}(\mathbf{r}_1, \mathbf{r}_2, \bar{\mathbf{r}}_0) = \mathcal{C}(\mathbf{r}_1 - \bar{\mathbf{r}}_0, \mathbf{r}_2 - \bar{\mathbf{r}}_0, \mathbf{r}_2 - \mathbf{r}_1)$. This leads naturally to a variable change, with unit Jacobian

$$\begin{aligned} \mathbf{u} &= \mathbf{r}_1 - \mathbf{r}_2 \\ \mathbf{v} &= z\mathbf{r}_1 + (1-z)\mathbf{r}_2 - \bar{\mathbf{r}}_0 \end{aligned} \quad (\text{A.17})$$

Now the correlator $\mathcal{C}^{(3)}$ only depends on the coordinates \mathbf{u} and \mathbf{v} , and there is no dependence on $\bar{\mathbf{r}}_0$. The three-point function then becomes

$$\begin{aligned} (\mathbf{x}_2, \mathbf{y}_2; \bar{\mathbf{z}}_2 | S^{(3)}(t_2, t_1) | \mathbf{x}_1, \mathbf{y}_1; \bar{\mathbf{z}}_1) &= \\ \int \mathcal{D}\mathbf{u} \int \mathcal{D}\mathbf{v} \int \mathcal{D}\bar{\mathbf{r}}_0 e^{i\frac{E}{2} \int_{t_1}^{t_2} ds [z(1-z)\dot{\mathbf{u}}^2 + \dot{\mathbf{v}}^2 + 2\dot{\mathbf{v}} \cdot \dot{\bar{\mathbf{r}}_0}]} \mathcal{C}^{(3)}(\mathbf{u}, \mathbf{v}). \end{aligned} \quad (\text{A.18})$$

Since the potential does not depend on $\bar{\mathbf{r}}_0$ the path integral over $\bar{\mathbf{r}}_0$ can be done, which has the effect of forcing \mathbf{v} to be on the classical path $\mathbf{v} \rightarrow \mathbf{v}_c$. The result is

$$\begin{aligned} (\mathbf{x}_2, \mathbf{y}_2; \bar{\mathbf{z}}_2 | S^{(3)}(t_2, t_1) | \mathbf{x}_1, \mathbf{y}_1; \bar{\mathbf{z}}_1) &= \\ = \left(\frac{E}{2\pi(t_2 - t_1)} \right)^2 e^{i\frac{E}{(t_2 - t_1)} \Delta\mathbf{v} \cdot (\Delta\mathbf{v} + 2(\bar{\mathbf{z}}_2 - \bar{\mathbf{z}}_1))} \int \mathcal{D}\mathbf{u} e^{i\frac{E}{2} \int_{t_1}^{t_2} ds \dot{\mathbf{u}}^2} \mathcal{C}^{(3)}(\mathbf{u}, \mathbf{v}_c), \end{aligned} \quad (\text{A.19})$$

where $\Delta\mathbf{v} = \mathbf{v}_2 - \mathbf{v}_1$ and we have defined $\omega = z(1-z)E$. Now we can return to momentum space. After performing the same coordinate change on the Fourier components in Eq. (A.2) the integrals involving the z components are

$$\begin{aligned} \int_{\bar{\mathbf{z}}_1 \bar{\mathbf{z}}_2} e^{i\bar{\mathbf{z}}_1 \cdot (\mathbf{p}_1 - \bar{\mathbf{p}}_1)} e^{-i\bar{\mathbf{z}}_2 \cdot (\mathbf{k}_2 + \mathbf{q}_2 - \bar{\mathbf{p}}_2)} e^{i\frac{E}{(t_2 - t_1)} \Delta\mathbf{v} \cdot (\bar{\mathbf{z}}_2 - \bar{\mathbf{z}}_1)} &= \\ = \left(\frac{2\pi(t_2 - t_1)}{E} \right)^2 (2\pi)^2 \delta^2(\Delta\mathbf{v}) (2\pi)^2 \delta^2(\mathbf{p}_1 - \bar{\mathbf{p}}_1). \end{aligned} \quad (\text{A.20})$$

Here we have used that $\bar{\mathbf{p}}_2 = \mathbf{k}_2 + \mathbf{q}_2$, see Eq. (3.7). Inserting this into the expression for the three-point function in momentum space Eq. (A.13) and doing one \mathbf{v} integral leads to

Eq. (3.8)

$$\begin{aligned}
& (\mathbf{k}_2, \mathbf{q}_2; \bar{\mathbf{p}}_2 | S^{(3)}(t_2, t_1) | \mathbf{k}_1, \mathbf{p}_1 - \mathbf{k}_1; \bar{\mathbf{p}}_1) = (2\pi)^2 \delta^2(\mathbf{p}_1 - \bar{\mathbf{p}}_1) \\
& \times \int_{\mathbf{u}_1 \mathbf{u}_2 \mathbf{v}} e^{i\mathbf{v} \cdot (\mathbf{p}_1 - \bar{\mathbf{p}}_2) + i\mathbf{u}_1 \cdot (\mathbf{k}_1 - z\mathbf{p}_1) - i\mathbf{u}_2 \cdot (\mathbf{k}_2 - z\bar{\mathbf{p}}_2)} \int \mathcal{D}\mathbf{u} e^{i\frac{E}{2} \int_{t_1}^{t_2} ds \dot{\mathbf{u}}^2} \mathcal{C}^{(3)}(\mathbf{u}, \mathbf{v}) \\
& \equiv (2\pi)^2 \delta(\mathbf{p}_1 - \bar{\mathbf{p}}_1) \mathcal{S}^{(3)}(\mathbf{k}_2 - z\bar{\mathbf{p}}_2, \mathbf{k}_1 - z\mathbf{p}_1, \mathbf{p}_1 - \bar{\mathbf{p}}_2 | t_2, t_1). \tag{A.21}
\end{aligned}$$

After defining the momentum variables $\mathbf{l}_2 = \mathbf{k}_2 - z\bar{\mathbf{p}}_2$ and $\mathbf{l}_1 = \mathbf{k}_1 - z\mathbf{p}_1$ this becomes $\mathcal{S}^{(3)}(\mathbf{l}_2, \mathbf{l}_1, \mathbf{p}_1 - \bar{\mathbf{p}}_2 | t_2, t_1)$.

A.3 Two-point function

The two-point function is

$$(\mathbf{p}_1; \mathbf{p}_1 | S^{(2)}(t_1, t_0) | \mathbf{p}_0; \bar{\mathbf{p}}_0) = d_a^{(2)} \left\langle (\mathbf{p}_1 | \mathcal{G}_a(t_1, t_0) | \mathbf{p}_0) (\bar{\mathbf{p}}_0 | \mathcal{G}_a^\dagger(t_0, t_1) | \bar{\mathbf{p}}_1) \right\rangle, \tag{A.22}$$

where we have used that $\bar{\mathbf{p}}_1 = \mathbf{p}_1$ from (A.21). After Fourier transforming this becomes

$$(\mathbf{p}_1; \mathbf{p}_1 | S^2(t_1 - t_0) | \mathbf{p}_0; \bar{\mathbf{p}}_0) = \int_{\mathbf{x}_1 \mathbf{x}_0 \bar{\mathbf{x}}_1 \bar{\mathbf{x}}_0} e^{-i\mathbf{p}_1 \cdot (\mathbf{x}_1 - \bar{\mathbf{x}}_1) + i\mathbf{p}_0 \cdot \mathbf{x}_0 - i\bar{\mathbf{p}}_0 \cdot \bar{\mathbf{x}}_0} (\mathbf{x}_1; \bar{\mathbf{x}}_1 | S^2(t_1 - t_0) | \mathbf{x}_0; \bar{\mathbf{x}}_0). \tag{A.23}$$

In position space it can be written in terms of path integrals

$$\begin{aligned}
(\mathbf{x}_1; \bar{\mathbf{x}}_1 | S^2(t_1 - t_0) | \mathbf{x}_0; \bar{\mathbf{x}}_0) &= d_a^{(2)} \left\langle (\mathbf{x}_1 | \mathcal{G}_a(t_1, t_0) | \mathbf{x}_0) (\bar{\mathbf{x}}_0 | \mathcal{G}_a^\dagger(t_1, t_0) | \bar{\mathbf{x}}_1) \right\rangle \\
&= \int_{\mathbf{x}_0}^{\mathbf{x}_1} \mathcal{D}\mathbf{r} \int_{\bar{\mathbf{x}}_0}^{\bar{\mathbf{x}}_1} \mathcal{D}\bar{\mathbf{r}} e^{i\frac{E}{2} \int_{t_0}^{t_1} ds (\dot{\mathbf{r}}^2 - \dot{\bar{\mathbf{r}}}^2)} \mathcal{C}^{(2)}(\mathbf{r} - \bar{\mathbf{r}} | t_1, t_0), \tag{A.24}
\end{aligned}$$

where $\mathcal{C}^{(2)}$ is a Wilson line correlator that has a simple solution

$$\mathcal{C}^{(2)}(\mathbf{r} - \bar{\mathbf{r}} | t_1, t_0) = d_a^{(2)} \left\langle V_a V_a^\dagger \right\rangle = e^{-C_R \int_{t_0}^{t_1} ds n(s) \sigma(\mathbf{r} - \bar{\mathbf{r}})}. \tag{A.25}$$

Changing coordinates to $\mathbf{u} = \mathbf{r} - \bar{\mathbf{r}}$ and $\mathbf{v} = 1/2(\mathbf{r} + \bar{\mathbf{r}})$ the potential does not depend on \mathbf{v} , and the path integral over \mathbf{v} can be performed. This has the effect of forcing \mathbf{u} to be on the classical path, and the full two-point function becomes

$$\begin{aligned}
(\mathbf{p}_1; \mathbf{p}_1 | S^2(t_1 - t_0) | \mathbf{p}_0; \bar{\mathbf{p}}_0) &= \left(\frac{E}{2\pi \Delta t} \right)^2 \int_{\mathbf{u}_1 \mathbf{u}_0 \mathbf{v}_1 \mathbf{v}_0} e^{i\mathbf{v}_0 \cdot (\mathbf{p}_0 - \bar{\mathbf{p}}_0) - i\mathbf{u}_1 \cdot \mathbf{p}_1 + \frac{1}{2} i\mathbf{u}_0 \cdot (\mathbf{p}_0 + \bar{\mathbf{p}}_0)} \\
&\times e^{i\frac{E}{\Delta t} (\mathbf{u}_1 - \mathbf{u}_0) \cdot (\mathbf{v}_1 - \mathbf{v}_0) - C_R \int_{t_0}^{t_1} ds n(s) \sigma(\mathbf{u}_{cl})}. \tag{A.26}
\end{aligned}$$

All but one of the integrals can be done immediately, leading to a momentum-conserving delta function

$$(\mathbf{p}_1; \mathbf{p}_1 | S^{(2)}(t_1 - t_0) | \mathbf{p}_0; \bar{\mathbf{p}}_0) = (2\pi)^2 \delta(\mathbf{p}_0 - \bar{\mathbf{p}}_0) \mathcal{P}(\mathbf{p}_1 - \mathbf{p}_0 | t_1, t_0). \tag{A.27}$$

Here we have defined the broadening distribution \mathcal{P} as

$$\mathcal{P}(\mathbf{p}_1 - \mathbf{p}_0 | t_1, t_0) = \int_{\mathbf{u}} e^{-i\mathbf{u} \cdot (\mathbf{p}_1 - \mathbf{p}_0) - C_R \int_{t_0}^{t_1} ds n(s) \sigma(\mathbf{u})}. \tag{A.28}$$

A.4 Summary of color structure

In the main text we have written the n-point functions in a very general way, namely

$$\begin{aligned}
(\mathbf{p}_1; \bar{\mathbf{p}}_1 | S^{(2)}(t_1, t_0) | \mathbf{p}_0; \bar{\mathbf{p}}_0) &= d_a^{(2)} \langle (\mathbf{p}_1 | \mathcal{G}_a(t_1, t_0) | \mathbf{p}_0) (\bar{\mathbf{p}}_0 | \mathcal{G}_a^\dagger(t_0, t_1) | \bar{\mathbf{p}}_1) \rangle \\
(\mathbf{k}_2, \mathbf{q}_2; \bar{\mathbf{p}}_2 | S^{(3)}(t_2, t_1) | \mathbf{k}_1, \mathbf{p}_1 - \mathbf{k}_1; \bar{\mathbf{p}}_1) &= d_{abc}^{(3)} \langle (\mathbf{k}_2 | \mathcal{G}_b | \mathbf{k}_1) (\mathbf{q}_2 | \mathcal{G}_c | \mathbf{p}_1 - \mathbf{k}_1) (\bar{\mathbf{p}}_1 | \mathcal{G}_a^\dagger | \bar{\mathbf{p}}_2) \rangle \\
(\mathbf{k}, \mathbf{q}; \mathbf{k}, \mathbf{q} | S^{(4)}(t_\infty, t_2) | \mathbf{k}_2, \mathbf{q}_2; \bar{\mathbf{k}}_2, \bar{\mathbf{p}}_2 - \bar{\mathbf{k}}_2) &= d_{bc}^{(4)} \langle (\mathbf{k} | \mathcal{G}_b | \mathbf{k}_2) (\mathbf{q} | \mathcal{G}_c | \mathbf{q}_2) (\bar{\mathbf{p}}_2 - \bar{\mathbf{k}}_2 | \mathcal{G}_c^\dagger | \mathbf{q}) (\bar{\mathbf{k}}_2 | \mathcal{G}_b^\dagger | \mathbf{k}) \rangle.
\end{aligned} \tag{A.29}$$

Here we have neglected all the color indices. Here we present the n-point correlators for the two processes $\gamma \rightarrow q\bar{q}$ and $g \rightarrow gg$ with full color dependence. The process dependent color factors $d_a^{(2)}$, $d_{abc}^{(3)}$ and $d_{bc}^{(4)}$ then be inferred from this.

In the case of $\gamma \rightarrow q\bar{q}$ the two-, three-, and four-point functions are given as

$$\begin{aligned}
S^{(2)}(t_1, t_0) &= (\mathbf{p}_1 | \mathcal{G}_0 | \mathbf{p}_0) (\bar{\mathbf{p}}_0 | \mathcal{G}_0^\dagger | \bar{\mathbf{p}}_1) \\
S^{(3)}(t_2, t_1) &= \frac{1}{N_c} \langle \text{tr}[(\mathbf{k}_2 | \mathcal{G}_F | \mathbf{k}_1) (\mathbf{p}_0 - \mathbf{k}_1 | \bar{\mathcal{G}}_F | \mathbf{q}_2)] \rangle (\bar{\mathbf{p}}_0 | \mathcal{G}_0^\dagger(t_1, t_2) | \bar{\mathbf{p}}_2) \\
S^{(4)}(t_\infty, t_2) &= \frac{1}{N_c} \langle \text{tr}[(\mathbf{k} | \mathcal{G}_F | \mathbf{k}_2) (\mathbf{q}_2 | \bar{\mathcal{G}}_F | \mathbf{q}) (\mathbf{q} | \mathcal{G}_F^\dagger | \bar{\mathbf{p}}_2 - \bar{\mathbf{k}}_2) (\bar{\mathbf{k}}_2 | \bar{\mathcal{G}}_F^\dagger | \mathbf{k})] \rangle.
\end{aligned} \tag{A.30}$$

Finally, for the $g \rightarrow gg$ process we have

$$\begin{aligned}
S^{(2)}(t_1, t_0) &= \frac{1}{N_c^2 - 1} \langle \text{tr}[(\mathbf{p}_1 | \mathcal{G}_A | \mathbf{p}_0) (\bar{\mathbf{p}}_0 | \mathcal{G}_A | \bar{\mathbf{p}}_1)] \rangle \\
S^{(3)}(t_2, t_1) &= \frac{1}{N_c(N_c^2 - 1)} f^{\bar{a}_2 b_2 c_2} f^{a_1 b_1 c_1} \langle (\mathbf{k}_2 | \mathcal{G}_A^{b_2 b_1} | \mathbf{k}_1) (\mathbf{q}_2 | \mathcal{G}_A^{c_2 c_1} | \mathbf{p}_1 - \mathbf{k}_1) (\bar{\mathbf{p}}_1 | \mathcal{G}_A^{\dagger a_1 \bar{a}_2} | \bar{\mathbf{p}}_2) \rangle \\
S^{(4)}(t_\infty, t_2) &= \frac{1}{N_c(N_c^2 - 1)} f^{\bar{a}_2 b_2 c_2} f^{\bar{a}_2 \bar{b}_2 \bar{c}_2} \\
&\quad \times \langle (\mathbf{k} | \mathcal{G}_A^{bb_2} | \mathbf{k}_2) (\mathbf{q} | \mathcal{G}_A^{cc_2} | \mathbf{q}_2) (\bar{\mathbf{k}}_2 | \mathcal{G}_A^{\dagger \bar{b}_2 \bar{b}} | \mathbf{k}) (\bar{\mathbf{p}}_2 - \bar{\mathbf{k}}_2 | \mathcal{G}_A^{\dagger \bar{c}_2 c_1} | \mathbf{q}) \rangle.
\end{aligned} \tag{A.31}$$

Here we have neglected the momentum dependence on the left-hand side to make the color structure more clear.

B Calculation of different processes

Here we will show how to derive the emission spectrum for two different physical processes.

B.1 Pair production

The pair production matrix element is

$$\begin{aligned}
\mathcal{M}_{s_i, s_j}^{ij}(\mathbf{k}, \mathbf{q}) &= \int_0^\infty dt_1 \int_{\mathbf{p}_0 \mathbf{p}_1 \mathbf{k}_1 \mathbf{q}_1} e^{i \frac{\mathbf{k}^2}{2zE} t_\infty} (\mathbf{k} | \mathcal{G}_F^{i i_1}(t_\infty, t_1) | \mathbf{k}_1) e^{i \frac{\mathbf{q}^2}{2(1-z)E} t_\infty} (\mathbf{q}_1 | \bar{\mathcal{G}}_F^{j_1 j}(t_1, t_\infty) | \mathbf{q}) \\
&\quad \times (\mathbf{q}_1, \mathbf{k}_1 | V_{\lambda s_i s_j}^{i_1 j_1} | \mathbf{p}_1) \frac{1}{2E} (\mathbf{p}_1 | \mathcal{G}_0(t_1, t_0) | \mathbf{p}_0) \mathcal{M}_{0\lambda}(\mathbf{p}_0).
\end{aligned} \tag{B.1}$$

Here the photon propagator is simply the free propagator, given in (2.5). The vertex is given by

$$(\mathbf{q}_1, \mathbf{k}_1 | V_{\lambda s_i s_j}^{i_1 j_1} | \mathbf{p}_1) = \delta^{i_1 j_1} (2\pi)^2 \delta(\mathbf{p}_1 - \mathbf{k}_1 - \mathbf{q}_1) e \Gamma_{\lambda s_i s_j}(\mathbf{k}_1 - z\mathbf{p}_1), \tag{B.2}$$

where

$$\Gamma_{\lambda s_i s_j}(\mathbf{Q}) = \delta_{-s_j s_i} (z \delta_{\lambda s_i} - (1-z) \delta_{\lambda s_j}) \frac{2i}{\sqrt{z(1-z)}} \mathbf{Q} \cdot \epsilon_\lambda. \quad (\text{B.3})$$

The cross section is, after summing over flavor

$$\frac{d^2\sigma}{d\Omega_{\mathbf{k}} d\Omega_{\mathbf{q}}} = n_f \sum \langle |\mathcal{M}(\mathbf{k}, \mathbf{q})|^2 \rangle. \quad (\text{B.4})$$

After squaring the amplitude the cross section is

$$\begin{aligned} \frac{d^2\sigma}{d\Omega_{\mathbf{k}} d\Omega_{\mathbf{q}}} &= \frac{e^2 n_f}{(2E)^2} \text{Re} \int_0^\infty dt_2 \int_0^{t_2} dt_1 \int_{\mathbf{p}_0 \mathbf{p}_1 \mathbf{k}_1 \mathbf{q}_2 \mathbf{k}_2 \bar{\mathbf{p}}_0 \bar{\mathbf{p}}_2 \bar{\mathbf{k}}_2 \bar{\mathbf{p}}_1} \langle \mathcal{M}_{0\lambda}(\mathbf{p}_0) \mathcal{M}_{0\bar{\lambda}}^*(\bar{\mathbf{p}}_0) \rangle \\ &\times \Gamma_{\lambda s_i s_j}(\mathbf{k}_1 - z\mathbf{p}_1) \Gamma_{\bar{\lambda} s_i s_j}(\bar{\mathbf{k}}_2 - z\bar{\mathbf{p}}_2) \langle (\mathbf{p}_1 | \mathcal{G}_0(t_1, t_0) | \mathbf{p}_0) (\bar{\mathbf{p}}_0 | \mathcal{G}_0^\dagger(t_0, t_1) | \bar{\mathbf{p}}_1) \rangle \\ &\times \langle (\mathbf{k}_2 | \mathcal{G}_F^{i_2 i_1}(t_2, t_1) | \mathbf{k}_1) (\mathbf{p}_1 - \mathbf{k}_1 | \bar{\mathcal{G}}_F^{i_1 j_2}(t_1, t_2) | \mathbf{q}_2) (\bar{\mathbf{p}}_1 | \mathcal{G}_0^\dagger(t_1, t_2) | \bar{\mathbf{p}}_2) \rangle \\ &\times \langle (\mathbf{k} | \mathcal{G}_F^{i_2 i_2}(t_\infty, t_2) | \mathbf{k}_2) (\mathbf{q}_2 | \bar{\mathcal{G}}_F^{j_2 j_2}(t_\infty, t_2) | \mathbf{q}) (\mathbf{q} | \mathcal{G}_F^{\dagger j_2 i_2}(t_2, t_\infty) | \bar{\mathbf{p}}_2 - \bar{\mathbf{k}}_2) (\bar{\mathbf{k}}_2 | \bar{\mathcal{G}}_F^{\dagger i_2 i_2}(t_2, t_\infty) | \mathbf{k}) \rangle. \end{aligned} \quad (\text{B.5})$$

This equation contains a lot of information and should be understood in the following way: The two-point function between t_0 and t_1 describes the propagation of the initial photon. Then the splitting happens in the amplitude at t_1 , and in the complex conjugate amplitude at t_2 , which is described by the three-point function. Finally, the quark-antiquark system broadens until the end of the medium and propagates until t_∞ .

The two-point function is simply

$$\langle (\mathbf{p}_1 | \mathcal{G}_0(t_1, t_0) | \mathbf{p}_0) (\bar{\mathbf{p}}_0 | \mathcal{G}_0^\dagger(t_0, t_1) | \bar{\mathbf{p}}_1) \rangle = (2\pi)^4 \delta(\mathbf{p}_1 - \mathbf{p}_0) \delta(\bar{\mathbf{p}}_1 - \bar{\mathbf{p}}_0) e^{-i \frac{\mathbf{p}_0^2 - \bar{\mathbf{p}}_0^2}{2E} (t_1 - t_0)}. \quad (\text{B.6})$$

The three-point function is

$$\begin{aligned} &\langle (\mathbf{k}_2 | \mathcal{G}_F^{i_2 i_1}(t_2, t_1) | \mathbf{k}_1) (\mathbf{p}_0 - \mathbf{k}_1 | \bar{\mathcal{G}}_F^{i_1 j_2}(t_1, t_2) | \mathbf{q}_2) (\bar{\mathbf{p}}_0 | \mathcal{G}_0^\dagger(t_1, t_2) | \bar{\mathbf{p}}_2) \rangle \\ &= \frac{\delta^{i_2 j_2}}{N_c} \langle \text{tr}[(\mathbf{k}_2 | \mathcal{G}_F(t_2, t_1) | \mathbf{k}_1) (\mathbf{p}_0 - \mathbf{k}_1 | \bar{\mathcal{G}}_F(t_1, t_2) | \mathbf{q}_2) (\bar{\mathbf{p}}_0 | \mathcal{G}_0^\dagger(t_1, t_2) | \bar{\mathbf{p}}_2)] \rangle \\ &= \delta^{i_2 j_2} \langle \mathbf{k}_2, \mathbf{q}_2; \bar{\mathbf{p}}_2 | S^{(3)}(t_2, t_1) | \mathbf{k}_1, \mathbf{p}_0 - \mathbf{k}_1; \bar{\mathbf{p}}_0 \rangle \\ &= \delta^{i_2 j_2} (2\pi)^2 \delta(\bar{\mathbf{p}}_0 - \mathbf{p}_0) S^{(3)}(\mathbf{k}_2 - z\bar{\mathbf{p}}_2, \mathbf{k}_1 - z\mathbf{p}_0, \mathbf{p}_0 - \bar{\mathbf{p}}_2 | t_2, t_1). \end{aligned} \quad (\text{B.7})$$

Finally, the four-point function becomes

$$\begin{aligned} &\langle \text{tr}[(\mathbf{k} | \mathcal{G}_F(t_\infty, t_2) | \mathbf{k}_2) (\mathbf{q}_2 | \bar{\mathcal{G}}_F(t_\infty, t_2) | \mathbf{q}) (\mathbf{q} | \mathcal{G}_F^\dagger(t_2, t_\infty) | \bar{\mathbf{p}}_2 - \bar{\mathbf{k}}_2) (\bar{\mathbf{k}}_2 | \bar{\mathcal{G}}_F^\dagger(t_2, t_\infty) | \mathbf{k})] \rangle \\ &= N_c \langle \mathbf{k}, \mathbf{q}; \mathbf{k}, \mathbf{q} | S^{(4)}(t_\infty, t_2) | \mathbf{k}_2, \mathbf{q}_2; \bar{\mathbf{k}}_2, \bar{\mathbf{p}}_2 - \bar{\mathbf{k}}_2 \rangle \\ &= N_c (2\pi)^2 \delta(\bar{\mathbf{p}}_2 - \mathbf{k}_2 - \mathbf{q}_2) S^{(4)}((1-z)\mathbf{k} - z\mathbf{q}, \mathbf{k}_2 - z\bar{\mathbf{p}}_2, \bar{\mathbf{k}}_2 - z\bar{\mathbf{p}}_2, \bar{\mathbf{p}}_2 - \mathbf{k} - \mathbf{q} | t_\infty, t_2). \end{aligned} \quad (\text{B.8})$$

Plugging this into the cross section we get

$$\begin{aligned} \frac{d^2\sigma}{d\Omega_{\mathbf{k}} d\Omega_{\mathbf{q}}} &= \frac{n_f e^2}{(2E)^2} N_c \text{Re} \int_0^\infty dt_2 \int_0^{t_2} dt_1 \int_{\mathbf{p}_0 \mathbf{k}_1 \mathbf{k}_2 \bar{\mathbf{k}}_2 \bar{\mathbf{p}}_2} \langle \mathcal{M}_{0\lambda}(\mathbf{p}_0) \mathcal{M}_{0\bar{\lambda}}^*(\bar{\mathbf{p}}_0) \rangle \\ &\times \Gamma_{\lambda s_i s_j}(\mathbf{k}_1 - z\mathbf{p}_0) \Gamma_{\bar{\lambda} s_i s_j}(\bar{\mathbf{k}}_2 - z\bar{\mathbf{p}}_2) \\ &\times S^{(3)}(\mathbf{k}_2 - z\bar{\mathbf{p}}_2, \mathbf{k}_1 - z\mathbf{p}_0, \mathbf{p}_0 - \bar{\mathbf{p}}_2 | t_2, t_1) \\ &\times S^{(4)}((1-z)\mathbf{k} - z\mathbf{q}, \mathbf{k}_2 - z\bar{\mathbf{p}}_2, \bar{\mathbf{k}}_2 - z\bar{\mathbf{p}}_2, \bar{\mathbf{p}}_2 - \mathbf{k} - \mathbf{q} | t_\infty, t_2). \end{aligned} \quad (\text{B.9})$$

After using that the vertices combine as

$$\Gamma_{\lambda s_i s_j}(\mathbf{Q}_1) \Gamma_{\bar{\lambda} s_i s_j}(\mathbf{Q}_2) = \delta^{\lambda \bar{\lambda}} (z^2 + (1-z)^2) \frac{4}{z(1-z)} \mathbf{Q}_1 \cdot \mathbf{Q}_2, \quad (\text{B.10})$$

we end up with

$$\begin{aligned} P_2(\mathbf{k}, \mathbf{q}; \mathbf{p}_0) &= \frac{e^2}{z(1-z)E^2} P_{q\gamma}(z) \text{Re} \int_0^\infty dt_2 \int_0^{t_2} dt_1 \int_{\mathbf{k}_1 \mathbf{k}_2 \bar{\mathbf{k}}_2 \bar{\mathbf{p}}_2} (\mathbf{k}_1 - z\mathbf{p}_0) \cdot (\bar{\mathbf{k}}_2 - z\bar{\mathbf{p}}_2) \\ &\times \mathcal{S}^{(3)}(\mathbf{k}_2 - z\bar{\mathbf{p}}_2, \mathbf{k}_1 - z\mathbf{p}_0, \mathbf{p}_0 - \bar{\mathbf{p}}_2 | t_2, t_1) \\ &\times \mathcal{S}^{(4)}((1-z)\mathbf{k} - z\mathbf{q}, \mathbf{k}_2 - z\bar{\mathbf{p}}_2, \bar{\mathbf{k}}_2 - z\bar{\mathbf{p}}_2, \bar{\mathbf{p}}_2 - \mathbf{k} - \mathbf{q} | t_\infty, t_2), \end{aligned} \quad (\text{B.11})$$

where we have introduced the Altarelli-Parisi splitting function

$$P_{q\gamma}(z) = n_f N_c [z^2 + (1-z)^2]. \quad (\text{B.12})$$

B.2 Gluon-gluon splitting

This is calculated in detail in [28], but we will repeat the most relevant parts here. The matrix element is

$$\begin{aligned} \mathcal{M}_{\lambda_b, \lambda_c}^{bc}(\mathbf{k}, \mathbf{q}) &= \int_0^\infty dt_1 \int_{\mathbf{p}_0 \mathbf{p}_1 \mathbf{k}_1 \mathbf{q}_1} \epsilon_{\lambda_b}^{*j} e^{i \frac{\mathbf{k} \cdot \mathbf{k}_2}{2zE} t_\infty} (\mathbf{k} | \mathcal{G}^{bb_1}(t_\infty, t_1) | \mathbf{k}_1) \\ &\times \epsilon_{\lambda_c}^{*l} e^{i \frac{\mathbf{q}^2}{2(1-z)E} t_\infty} (\mathbf{q} | \mathcal{G}^{cc_1}(t_\infty, t_1) | \mathbf{q}_1) (\mathbf{q}_1, \mathbf{k}_1 | V_{a_1 b_1 c_1}^{ijl} | \mathbf{p}_1) \frac{1}{2E} (\mathbf{p}_1 | \mathcal{G}^{a_1 a_0}(t_1, t_0) | \mathbf{p}_0) \mathcal{M}_0^{ia_0}(\mathbf{p}_0), \end{aligned} \quad (\text{B.13})$$

where all the propagators are gluon propagators. The vertex is given by

$$(\mathbf{q}_1, \mathbf{k}_1 | V_{a_1 b_1 c_1}^{ijl} | \mathbf{p}_1) = (2\pi)^2 \delta(\mathbf{p}_1 - \mathbf{k}_1 - \mathbf{q}_1) g f^{a_1 b_1 c_1} \Gamma^{ijk}(\mathbf{k}_1 - z\mathbf{p}_1), \quad (\text{B.14})$$

and

$$\Gamma^{ijk}(\mathbf{Q}) = 2 \left(\frac{1}{z} \mathbf{Q}^j \delta^{il} + \frac{1}{1-z} \mathbf{Q}^l \delta^{ij} - \mathbf{Q}^i \delta^{jl} \right). \quad (\text{B.15})$$

The cross section is simply achieved by squaring the amplitude and averaging over the initial and summing over the final quantum numbers

$$\frac{d^2\sigma}{d\Omega_{\mathbf{k}} d\Omega_{\mathbf{q}}} = \sum \langle |\mathcal{M}(\mathbf{k}, \mathbf{q})|^2 \rangle. \quad (\text{B.16})$$

After squaring the amplitude and use polarization sums $\sum_\lambda \epsilon_\lambda^i \epsilon_\lambda^{*j} = \delta^{ij}$ this is

$$\begin{aligned} \frac{d^2\sigma}{d\Omega_{\mathbf{k}} d\Omega_{\mathbf{q}}} &= \frac{g^2}{(2E)^2} \text{Re} \int_0^\infty dt_2 \int_0^{t_2} dt_1 \int_{\mathbf{p}_0 \mathbf{p}_1 \mathbf{k}_1 \mathbf{q}_2 \mathbf{k}_2 \bar{\mathbf{p}}_0 \bar{\mathbf{p}}_2 \bar{\mathbf{k}}_2 \bar{\mathbf{p}}_1} \Gamma^{ijk}(\mathbf{k}_1 - z\mathbf{p}_1) \Gamma^{\bar{i}\bar{j}\bar{k}}(\bar{\mathbf{k}}_2 - z\bar{\mathbf{p}}_2) \\ &\times f^{a_1 b_1 c_1} f^{\bar{a}_2 \bar{b}_2 \bar{c}_2} \mathcal{M}_0^{ia_0}(\mathbf{p}_0) \mathcal{M}_0^{*\bar{i}\bar{a}_0}(\bar{\mathbf{p}}_0) (\mathbf{p}_1 | \mathcal{G}^{a_1 a_0}(t_1, t_0) | \mathbf{p}_0) (\bar{\mathbf{p}}_0 | \mathcal{G}^{\bar{a}_0 \bar{a}_1}(t_0, t_1) | \bar{\mathbf{p}}_1) \\ &\times (\mathbf{k}_2 | \mathcal{G}^{b_2 b_1}(t_2, t_1) | \mathbf{k}_1) (\mathbf{q}_2 | \mathcal{G}^{c_2 c_1}(t_2, t_1) | \mathbf{p}_1 - \mathbf{k}_1) (\bar{\mathbf{p}}_1 | \mathcal{G}^{\bar{a}_1 \bar{a}_2}(t_1, t_2) | \bar{\mathbf{p}}_2) \\ &\times (\mathbf{k} | \mathcal{G}^{bb_2}(t_\infty, t_2) | \mathbf{k}_2) (\mathbf{q} | \mathcal{G}^{cc_2}(t_\infty, t_2) | \mathbf{q}_2) (\bar{\mathbf{k}}_2 | \mathcal{G}^{\bar{i}\bar{b}_2 \bar{b}}(t_2, t_\infty) | \bar{\mathbf{k}}) (\bar{\mathbf{p}}_2 - \bar{\mathbf{k}}_2 | \mathcal{G}^{\bar{c}_2 \bar{c}}(t_2, t_\infty) | \mathbf{q}). \end{aligned} \quad (\text{B.17})$$

We have divided into three regions by using the property

$$(\mathbf{k}|\mathcal{G}^{bb_1}(t_\infty, t_1)|\mathbf{k}_1) = \int_{\mathbf{k}_2} (\mathbf{k}|\mathcal{G}^{bb_2}(t_\infty, t_2)|\mathbf{k}_2)(\mathbf{k}_2|\mathcal{G}^{b_2b_1}(t_2, t_1)|\mathbf{k}_1). \quad (\text{B.18})$$

The cross section again looks quite complicated, but it can be divided into three distinct physical processes.

The initial state can be simplified by using

$$\mathcal{M}_0^{ia_0}(\mathbf{p}_0)\mathcal{M}_0^{*\bar{i}\bar{a}_0}(\bar{\mathbf{p}}_0) = \frac{\delta^{a_0\bar{a}_0}}{N_c^2 - 1}\mathcal{M}_0^i(\mathbf{p}_0)\mathcal{M}_0^{*\bar{i}}(\bar{\mathbf{p}}_0). \quad (\text{B.19})$$

This makes it possible to simplify the 2-point function

$$\begin{aligned} \delta^{a_0\bar{a}_0}(\mathbf{p}_1|\mathcal{G}^{a_1a_0}(t_1, t_0)|\mathbf{p}_0)(\bar{\mathbf{p}}_0|\mathcal{G}^{\dagger\bar{a}_0\bar{a}_1}(t_0, t_1)|\bar{\mathbf{p}}_1) &= \delta^{a_1\bar{a}_1}(\mathbf{p}_1; \bar{\mathbf{p}}_1|S^{(2)}(t_1, t_0)|\mathbf{p}_0; \bar{\mathbf{p}}_0) \\ &= \delta^{a_1\bar{a}_1}(2\pi)^2\delta(\bar{\mathbf{p}}_0 - \mathbf{p}_0)\mathcal{P}(\mathbf{p}_1 - \mathbf{p}_0|t_1, t_0). \end{aligned} \quad (\text{B.20})$$

With this, the 3-point function becomes

$$\begin{aligned} f^{a_1b_1c_1}(\mathbf{k}_2|\mathcal{G}^{b_2b_1}(t_2, t_1)|\mathbf{k}_1)(\mathbf{q}_2|\mathcal{G}^{c_2c_1}(t_2, t_1)|\mathbf{p}_1 - \mathbf{k}_1)(\bar{\mathbf{p}}_1|\mathcal{G}^{\dagger a_1\bar{a}_2}(t_1, t_2)|\bar{\mathbf{p}}_2) \\ = f^{\bar{a}_2b_2c_2}(\mathbf{k}_2, \mathbf{q}_2; \bar{\mathbf{p}}_2|S^{(3)}(t_2, t_1)|\mathbf{k}_1, \mathbf{p}_1 - \mathbf{k}_1; \bar{\mathbf{p}}_1) \\ = f^{\bar{a}_2b_2c_2}(2\pi)^2\delta(\bar{\mathbf{p}}_1 - \mathbf{p}_1)\mathcal{S}^{(3)}(\mathbf{k}_2 - z\bar{\mathbf{p}}_2, \mathbf{k}_1 - z\mathbf{p}_1, \mathbf{p}_1 - \bar{\mathbf{p}}_2|t_2, t_1), \end{aligned} \quad (\text{B.21})$$

Finally, the 4-point function is

$$\begin{aligned} f^{\bar{a}_2b_2c_2}f^{\bar{a}_2\bar{b}_2\bar{c}_2}(\mathbf{k}|\mathcal{G}^{bb_2}(t_\infty, t_2)|\mathbf{k}_2)(\mathbf{q}|\mathcal{G}^{cc_2}(t_\infty, t_2)|\mathbf{q}_2)(\bar{\mathbf{k}}_2|\mathcal{G}^{\dagger\bar{b}_2\bar{b}}(t_2, t_\infty)|\bar{\mathbf{k}})(\bar{\mathbf{p}}_2 - \bar{\mathbf{k}}_2|\mathcal{G}^{\dagger\bar{c}_2\bar{c}}(t_2, t_\infty)|\bar{\mathbf{q}}) \\ = N_c(N_c^2 - 1)(\mathbf{k}, \mathbf{q}; \mathbf{k}, \mathbf{q}|S^{(4)}(t_\infty, t_2)|\mathbf{k}_2, \mathbf{q}_2; \bar{\mathbf{k}}_2, \bar{\mathbf{p}}_2 - \bar{\mathbf{k}}_2) \\ = N_c(N_c^2 - 1)(2\pi)^2\delta(\bar{\mathbf{p}}_2 - \mathbf{k}_2 - \mathbf{q}_2)\mathcal{S}^{(4)}((1 - z)\mathbf{k} - z\mathbf{q}, \mathbf{k}_2 - z\bar{\mathbf{p}}_2, \bar{\mathbf{k}}_2 - z\bar{\mathbf{p}}_2, \bar{\mathbf{p}}_2 - \mathbf{k} - \mathbf{q}|t_\infty, t_2). \end{aligned} \quad (\text{B.22})$$

After using these relations the cross section becomes

$$\begin{aligned} \frac{d^2\sigma}{d\Omega_{\mathbf{k}}d\Omega_{\mathbf{q}}} &= \frac{g^2}{(2E)^2}N_c\text{Re}\int_0^\infty dt_2\int_0^{t_2} dt_1\int_{\mathbf{p}_0\mathbf{p}_1\mathbf{k}_1\mathbf{k}_2\bar{\mathbf{p}}_2\bar{\mathbf{k}}_2}\Gamma^{ijk}(\mathbf{k}_1 - z\mathbf{p}_1)\Gamma^{\bar{i}jk}(\bar{\mathbf{k}}_2 - z\bar{\mathbf{p}}_2) \\ &\quad \times \mathcal{M}_0^i(\mathbf{p}_0)\mathcal{M}_0^{*\bar{i}}(\mathbf{p}_0)\mathcal{P}(\mathbf{p}_1 - \mathbf{p}_0|t_1, t_0) \\ &\quad \times \mathcal{S}^{(3)}(\mathbf{k}_2 - z\bar{\mathbf{p}}_2, \mathbf{k}_1 - z\mathbf{p}_1, \mathbf{p}_1 - \bar{\mathbf{p}}_2|t_2, t_1) \\ &\quad \times \mathcal{S}^{(4)}((1 - z)\mathbf{k} - z\mathbf{q}, \mathbf{k}_2 - z\bar{\mathbf{p}}_2, \bar{\mathbf{k}}_2 - z\bar{\mathbf{p}}_2, \bar{\mathbf{p}}_2 - \mathbf{k} - \mathbf{q}|t_\infty, t_2). \end{aligned} \quad (\text{B.23})$$

$$\begin{aligned} N_c\Gamma^{ijk}(\mathbf{Q}_1)\Gamma^{\bar{i}jk}(\mathbf{Q}_2) &= \left[\frac{1}{z^2} + \frac{1}{(1 - z)^2}\right]\mathbf{Q}_1 \cdot \mathbf{Q}_2\delta^{i\bar{i}} + 2Q_1^iQ_2^{\bar{i}} \\ &= \frac{4}{z(1 - z)}P_{\text{gg}}(z)\delta^{i\bar{i}}\mathbf{Q}_1 \cdot \mathbf{Q}_2 \end{aligned} \quad (\text{B.24})$$

The last step is true if we only consider inclusive cross sections and average over azimuthal angles.

We can now combine the initial hard processes in $\frac{d\sigma_0}{d\Omega_{\mathbf{p}_0}} = |\mathcal{M}_0(\mathbf{p}_0)|^2$, and extract this from the equation. Using this together with Eqs. (3.3) we get the generalized splitting function

$$\begin{aligned}
P_2(\mathbf{k}, \mathbf{q}; \mathbf{p}_0) &= \frac{g^2}{z(1-z)E_s^2} P_{gg}(z) \text{Re} \int_0^\infty dt_2 \int_0^{t_2} dt_1 \int_{\mathbf{p}_1 \mathbf{k}_1 \mathbf{k}_2 \bar{\mathbf{p}}_2 \bar{\mathbf{k}}_2} \\
&\times (\mathbf{k}_1 - z\mathbf{p}_1) \cdot (\bar{\mathbf{k}}_2 - z\bar{\mathbf{p}}_2) \mathcal{P}(\mathbf{p}_1 - \mathbf{p}_0 | t_1, t_0) \\
&\times \mathcal{S}^{(3)}(\mathbf{k}_2 - z\bar{\mathbf{p}}_2, \mathbf{k}_1 - z\mathbf{p}_1, \mathbf{p}_1 - \bar{\mathbf{p}}_2 | t_2, t_1) \\
&\times \mathcal{S}^{(4)}((1-z)\mathbf{k} - z\mathbf{q}, \mathbf{k}_2 - z\bar{\mathbf{p}}_2, \bar{\mathbf{k}}_2 - z\bar{\mathbf{p}}_2, \bar{\mathbf{p}}_2 - \mathbf{k} - \mathbf{q} | t_\infty, t_2). \tag{B.25}
\end{aligned}$$

Here we have introduced the Altarelli-Parisi splitting function

$$P_{gg}(z) = N_c \frac{[1 - z(1-z)]^2}{z(1-z)}. \tag{B.26}$$

C Deriving the Schrödinger equation

Here we show how to derive the Schrödinger equation (3.37) starting with the path integral (3.35). We will do this for a general system, which the specific system in question is only a special case of. Let the path integral go from some initial state at $(t_0, \mathbf{u}_0, \bar{\mathbf{u}}_0)$ to some final state at $(t + \epsilon, \mathbf{u}_f, \bar{\mathbf{u}}_f)$.

$$\mathcal{Q}_i(\mathbf{u}_f, \bar{\mathbf{u}}_f, \mathbf{u}_0, \bar{\mathbf{u}}_0 | t + \epsilon, t_0) \equiv \int_{\mathbf{u}_0}^{\mathbf{u}_f} \mathcal{D}\mathbf{u} \int_{\bar{\mathbf{u}}_0}^{\bar{\mathbf{u}}_f} \mathcal{D}\bar{\mathbf{u}} e^{i\frac{\omega}{2} \int_{t_0}^{t+\epsilon} ds (\dot{\mathbf{u}}^2 - \dot{\bar{\mathbf{u}}}^2)} \mathcal{C}_i(\mathbf{u}, \bar{\mathbf{u}} | t + \epsilon). \tag{C.1}$$

In this equation \mathcal{C}_i indicates some Wilson line correlator. In [69] it was shown that all Wilson line correlators can be written as a system of differential equations.

$$\frac{d}{dt} \mathcal{C}_i(t) = \mathbb{M}_{ij} \mathcal{C}_j(t). \tag{C.2}$$

Here \mathcal{C}_j indicates some other color configuration of the same Wilson lines. Notice that this implies that $\mathcal{C}_i(t + \epsilon) = \mathcal{C}_i(t) + \epsilon \mathbb{M}_{ij} \mathcal{C}_j(t)$ when $\epsilon \rightarrow 0$. Start by discretizing the path integral with N time intervals with length ϵ . Let the whole path integral go from t_0 to $t + \epsilon$. Then we separate the very last interval from the $N - 1$ preceding ones. Then we have

$$\begin{aligned}
\mathcal{Q}_i(\mathbf{u}_f, \bar{\mathbf{u}}_f, \mathbf{u}_0, \bar{\mathbf{u}}_0 | t + \epsilon, t_0) &= \\
&\frac{1}{A_{\mathbf{u}} A_{\bar{\mathbf{u}}}} \int d\mathbf{u}_{N-1} \int d\bar{\mathbf{u}}_{N-1} \exp \left\{ i\frac{\omega}{2} \int_t^{t+\epsilon} ds (\dot{\mathbf{u}}_N^2 - \dot{\bar{\mathbf{u}}}_N^2) \right\} \\
&\times \int_{\mathbf{u}_0}^{\mathbf{u}_{N-1}} \mathcal{D}\mathbf{u} \int_{\bar{\mathbf{u}}_0}^{\bar{\mathbf{u}}_{N-1}} \mathcal{D}\bar{\mathbf{u}} \exp \left\{ i\frac{\omega}{2} \int_{t_0}^t ds (\dot{\mathbf{u}}^2 - \dot{\bar{\mathbf{u}}}^2) \right\} \\
&\times (\mathcal{C}_i(\mathbf{u}, \bar{\mathbf{u}} | t) + \epsilon \mathbb{M}_{ij}(\mathbf{u}_{N-1}, \bar{\mathbf{u}}_{N-1}) \mathcal{C}_j(\mathbf{u}, \bar{\mathbf{u}} | t)) \\
&= \frac{1}{A_{\mathbf{u}} A_{\bar{\mathbf{u}}}} \int d\mathbf{u}_{N-1} \int d\bar{\mathbf{u}}_{N-1} \exp \left\{ i\frac{\omega}{2} \epsilon \left[\left(\frac{\mathbf{u}_N - \mathbf{u}_{N-1}}{\epsilon} \right)^2 - \left(\frac{\bar{\mathbf{u}}_N - \bar{\mathbf{u}}_{N-1}}{\epsilon} \right)^2 \right] \right\} \\
&\times (\mathcal{Q}_i(\mathbf{u}_{N-1}, \bar{\mathbf{u}}_{N-1} | t) + \epsilon \mathbb{M}_{ij}(\mathbf{u}_{N-1}, \bar{\mathbf{u}}_{N-1}) \mathcal{Q}_j(\mathbf{u}_{N-1}, \bar{\mathbf{u}}_{N-1} | t)). \tag{C.3}
\end{aligned}$$

We have used the more compact notation $\mathcal{Q}_i(\mathbf{u}_{N-1}, \bar{\mathbf{u}}_{N-1}|t) = \mathcal{Q}_i(\mathbf{u}_{N-1}, \bar{\mathbf{u}}_{N-1}, \mathbf{u}_0, \bar{\mathbf{u}}_0|t, t_0)$. The normalization factors are

$$A_{\mathbf{u}} = -A_{\bar{\mathbf{u}}} = \frac{2\pi i \epsilon}{\omega} \quad (\text{C.4})$$

Using that $\mathbf{u}_N = \mathbf{u}_f$ we see that the integral over \mathbf{u}_{N-1} is dominated by terms where $\mathbf{u}_f - \mathbf{u}_{N-1}$ is small (same for $\bar{\mathbf{u}}_{N-1}$ and $\bar{\mathbf{u}}_f$). We define new variables through $\mathbf{u}_{N-1} = \mathbf{u}_f + \boldsymbol{\xi}$ and $\bar{\mathbf{u}}_{N-1} = \bar{\mathbf{u}}_f + \boldsymbol{\eta}$ so the integration becomes

$$\begin{aligned} & \mathcal{Q}_i(\mathbf{u}_f, \bar{\mathbf{u}}_f, \mathbf{u}_0, \bar{\mathbf{u}}_0|t + \epsilon, t_0) \\ &= \frac{1}{A_{\mathbf{u}} A_{\bar{\mathbf{u}}}} \int d\boldsymbol{\xi} \int d\boldsymbol{\eta} \exp \left\{ i \frac{\omega}{2\epsilon} (\boldsymbol{\xi}^2 - \boldsymbol{\eta}^2) \right\} \mathcal{Q}_i(\mathbf{u}_f + \boldsymbol{\xi}, \bar{\mathbf{u}}_f + \boldsymbol{\eta}|t) \\ &+ \frac{\epsilon}{A_{\mathbf{u}} A_{\bar{\mathbf{u}}}} \int d\boldsymbol{\xi} \int d\boldsymbol{\eta} \exp \left\{ i \frac{\omega}{2\epsilon} (\boldsymbol{\xi}^2 - \boldsymbol{\eta}^2) \right\} \mathbb{M}_{ij}(\mathbf{u}_f + \boldsymbol{\xi}, \bar{\mathbf{u}}_f + \boldsymbol{\eta}) \mathcal{Q}_j(\mathbf{u}_f + \boldsymbol{\xi}, \bar{\mathbf{u}}_f + \boldsymbol{\eta}|t). \end{aligned} \quad (\text{C.5})$$

Now we Taylor expand \mathcal{Q}_i and \mathbb{M}_{ij} in $\boldsymbol{\xi}$ and $\boldsymbol{\eta}$ in the following way

$$\begin{aligned} f(\mathbf{u}_f + \boldsymbol{\xi}, \bar{\mathbf{u}}_f + \boldsymbol{\eta}|t) &= \left[1 + \boldsymbol{\xi} \cdot \partial_{\mathbf{u}} + \boldsymbol{\eta} \cdot \partial_{\bar{\mathbf{u}}} \right. \\ &\quad \left. + \frac{1}{2} \left(\xi_1^2 \frac{\partial^2}{\partial u_1^2} + \xi_2^2 \frac{\partial^2}{\partial u_2^2} + \eta_1^2 \frac{\partial^2}{\partial v_1^2} + \eta_2^2 \frac{\partial^2}{\partial v_2^2} \right) \right] f(\mathbf{u}_f, \bar{\mathbf{u}}_f|t). \end{aligned} \quad (\text{C.6})$$

After using the normalization factors (C.4) the Gaussian integrals become

$$\begin{aligned} & \frac{1}{A_{\mathbf{u}} A_{\bar{\mathbf{u}}}} \int d\boldsymbol{\xi} \int d\boldsymbol{\eta} \exp \left\{ i \frac{\omega}{2\epsilon} (\boldsymbol{\xi}^2 - \boldsymbol{\eta}^2) \right\} = 1 \\ & \frac{1}{A_{\mathbf{u}} A_{\bar{\mathbf{u}}}} \int d\boldsymbol{\xi} \int d\boldsymbol{\eta} (\boldsymbol{\xi} \cdot \partial_{\mathbf{u}} + \boldsymbol{\eta} \cdot \partial_{\bar{\mathbf{u}}}) \exp \left\{ i \frac{\omega}{2\epsilon} (\boldsymbol{\xi}^2 - \boldsymbol{\eta}^2) \right\} = 0 \\ & \frac{1}{A_{\mathbf{u}} A_{\bar{\mathbf{u}}}} \int d\boldsymbol{\xi} \int d\boldsymbol{\eta} \left(\xi_1^2 \frac{\partial^2}{\partial u_1^2} + \xi_2^2 \frac{\partial^2}{\partial u_2^2} + \eta_1^2 \frac{\partial^2}{\partial v_1^2} + \eta_2^2 \frac{\partial^2}{\partial v_2^2} \right) \exp \left\{ i \frac{\omega}{2\epsilon} (\boldsymbol{\xi}^2 - \boldsymbol{\eta}^2) \right\} \\ &= \frac{i\epsilon}{\omega} (\partial_{\mathbf{u}}^2 - \partial_{\bar{\mathbf{u}}}^2). \end{aligned} \quad (\text{C.7})$$

Going back to (C.5) one can see that after expanding all the terms linear in $\boldsymbol{\xi}$ and $\boldsymbol{\eta}$ are zero. The second term in (C.5) already goes as ϵ , so the integrals quadratic in $\boldsymbol{\xi}$ and $\boldsymbol{\eta}$ give something going as ϵ^2 , and can be discarded. In the end we get

$$\begin{aligned} & \mathcal{Q}_i(\mathbf{u}, \bar{\mathbf{u}}, \mathbf{u}_0, \bar{\mathbf{u}}_0|t, t_0) + \epsilon \frac{\partial}{\partial t} \mathcal{Q}_i(\mathbf{u}, \bar{\mathbf{u}}, \mathbf{u}_0, \bar{\mathbf{u}}_0|t, t_0) \\ &= \left[1 + \frac{i\epsilon}{2\omega} (\partial_{\mathbf{u}}^2 - \partial_{\bar{\mathbf{u}}}^2) \right] \mathcal{Q}_i(\mathbf{u}, \bar{\mathbf{u}}, \mathbf{u}_0, \bar{\mathbf{u}}_0|t, t_0) + \epsilon \mathbb{M}_{ij} \mathcal{Q}_j(\mathbf{u}, \bar{\mathbf{u}}, \mathbf{u}_0, \bar{\mathbf{u}}_0|t, t_0). \end{aligned} \quad (\text{C.8})$$

Gathering all the terms linear in ϵ we get the Schrödinger equation

$$\begin{aligned} & \left[i \frac{\partial}{\partial t} + \frac{\partial_{\mathbf{u}}^2 - \partial_{\bar{\mathbf{u}}}^2}{2\omega} \right] \mathcal{Q}_i(\mathbf{u}, \bar{\mathbf{u}}, \mathbf{u}_0, \bar{\mathbf{u}}_0|t, t_0) - i \mathbb{M}_{ij}(\mathbf{u}, \bar{\mathbf{u}}) \mathcal{Q}_j(\mathbf{u}, \bar{\mathbf{u}}, \mathbf{u}_0, \bar{\mathbf{u}}_0|t, t_0) \\ &= i \mathcal{Q}_i(\mathbf{u}, \bar{\mathbf{u}}, \mathbf{u}_0, \bar{\mathbf{u}}_0|t_0, t_0). \end{aligned} \quad (\text{C.9})$$

Notice that there is a minus sign in front of $\partial_{\bar{u}}^2$. This is something that would only normally appear if the mass is negative. The initial condition is a delta function at the starting point in the transverse plane

$$i\mathcal{Q}_i(\mathbf{u}, \bar{\mathbf{u}}, \mathbf{u}_0, \bar{\mathbf{u}}_0|t_0, t_0) = i\delta(t - t_0)\delta^2(\mathbf{u} - \mathbf{u}_0)\delta^2(\bar{\mathbf{u}} - \bar{\mathbf{u}}_0). \quad (\text{C.10})$$

D The eikonal limit

If the energy of both of the daughter partons is big one can use the eikonal approximation. The eikonal approximation assumes that the partons travel on straight lines through the medium, and neglects the effects of momentum broadening. The medium propagator Eq. (2.1) then reduces to the eikonal propagator Eq. (2.6). The splitting process simplifies greatly in the eikonal approximation. Starting with Eq. (3.1) all of the momentum integrals can be done, and you end up with

$$\begin{aligned} \mathcal{P}_2(\mathbf{k}, \mathbf{q}; \mathbf{p}_0) &= \frac{g^2}{z(1-z)E^2} P_{ba}(z)(2\pi)^2 \delta^2(\mathbf{p}_0 - \mathbf{q} - \mathbf{k}) \text{Re} \int_0^\infty dt_1 \int_{t_1}^\infty dt_2 \\ &\times ((1-z)\mathbf{k} - z\mathbf{q})^2 e^{-i\frac{1}{2\omega}(z\mathbf{q} - (1-z)\mathbf{k})^2(t_2 - t_1)} \mathcal{C}^{(4)}(t_\infty, t_2) \mathcal{C}^{(3)}(t_2, t_1). \end{aligned} \quad (\text{D.1})$$

The objects $\mathcal{C}^{(3)}$ and $\mathcal{C}^{(4)}$ represent Wilson line correlators, given in Eq. (3.20).

After defining $\mathbf{p} = z\mathbf{q} - (1-z)\mathbf{k}$ and $\mathbf{P} = \mathbf{q} + \mathbf{k}$, and integrating out \mathbf{P} we end up with the eikonal analogue of Eq. (3.14)

$$\begin{aligned} (2\pi)^2 \frac{dI}{dz d^2\mathbf{p}} &= \frac{\alpha_s \mathbf{p}^2}{\omega^2} P_{ba}(z) \text{Re} \int_0^\infty dt_1 \int_{t_1}^\infty dt_2 \\ &\times e^{-i\frac{\mathbf{p}^2}{2\omega}(t_2 - t_1)} \mathcal{C}^{(4)}(t_\infty, t_2) \mathcal{C}^{(3)}(t_2, t_1). \end{aligned} \quad (\text{D.2})$$

This is perhaps more conveniently written in terms of the angle θ between the two daughter partons, using the relation $\mathbf{p}^2 \simeq (\theta\omega)^2$. This is accurate for small angles $\theta \ll 1$. Then the emission spectrum is

$$\begin{aligned} \frac{dI}{dz d\theta} &= 2\pi\theta\omega^2 \frac{dI^{\text{in-in}}}{dz d^2\mathbf{p}} \\ &= \frac{\alpha_s}{2\pi} \omega^2 \theta^3 P_{ba}(z) \text{Re} \int_0^\infty dt_1 \int_{t_1}^\infty dt_2 e^{-i\frac{\omega\theta^2}{2}(t_2 - t_1)} \mathcal{C}^{(4)}(t_\infty, t_2) \mathcal{C}^{(3)}(t_2, t_1). \end{aligned} \quad (\text{D.3})$$

This spectrum was calculated for three different processes in [69]. In this paper we will write the spectra in terms of the transverse momentum \mathbf{p} .

Again, we can divide it into the out-out (vacuum), in-out, and in-in contributions. For the vacuum contribution we have $\mathcal{C}^{(4)} = \mathcal{C}^{(3)} = 1$, and we get the same as in the non-eikonal case

$$(2\pi)^2 \frac{dI^{\text{out-out}}}{dz d^2\mathbf{p}} = \frac{2\alpha_s}{\mathbf{p}^2} P_{ba}(z). \quad (\text{D.4})$$

For the out-out spectrum we have $\mathcal{C}^{(4)} = 1$, and we get

$$(2\pi)^2 \frac{dI^{\text{in-out}}}{dz d^2\mathbf{p}} = \frac{\alpha_s \mathbf{p}^2}{\omega^2} P_{ba}(z) \text{Re} \int_0^L dt_1 \int_{t_1}^L dt_2 \times e^{-i \frac{\mathbf{p}^2}{2\omega} (t_2 - t_1)} \mathcal{C}^{(3)}(L, t_1). \quad (\text{D.5})$$

Lastly, the in-in spectrum is

$$(2\pi)^2 \frac{dI^{\text{in-in}}}{dz d^2\mathbf{p}} = \frac{\alpha_s \mathbf{p}^2}{\omega^2} P_{ba}(z) \text{Re} \int_0^L dt_1 \int_{t_1}^L dt_2 \times e^{-i \frac{\mathbf{p}^2}{2\omega} (t_2 - t_1)} \mathcal{C}^{(4)}(L, t_2) \mathcal{C}^{(3)}(t_2, t_1). \quad (\text{D.6})$$

Let us consider the $\gamma \rightarrow q\bar{q}$ process and use the harmonic approximation. The partons travel on straight lines, so $\mathbf{u}^2(t) = (t - t_1)^2 \theta^2$ and $\bar{\mathbf{u}}^2(t) = (t - t_2)^2 \theta^2$. The three-point function is

$$\mathcal{C}^{(3)}(t_2, t_1) = e^{-\frac{1}{12} \frac{\hat{q}\mathbf{p}^2}{\omega^2} (t_2 - t_1)^3}. \quad (\text{D.7})$$

Hence, the in-out contribution is given by

$$(2\pi)^2 \frac{dI^{\text{in-out}}}{dz d^2\mathbf{p}} = -\frac{2\alpha_s}{z(1-z)E} P_{ba}(z) \text{Re} i \int_0^L d\tau e^{-i \frac{\mathbf{p}^2}{2\omega} \tau} e^{-\frac{1}{12} \frac{\hat{q}\mathbf{p}^2}{\omega^2} \tau^3}. \quad (\text{D.8})$$

The four-point function is not trivial to calculate in the eikonal approximation either. However, it can now be calculated through an ordinary differential equation, instead of a more complicated Schrödinger equation

$$\frac{d}{dt} \mathcal{C}_i^{(4)}(t, t_2) = \mathbb{M}_{ij}(t) \mathcal{C}_j(t). \quad (\text{D.9})$$

The matrix in Eq. (4.21) now has a simple time dependence

$$\mathbb{M}(t) = -\frac{\hat{q}\theta^2}{4C_F} \begin{bmatrix} C_F[(t - t_1)^2 + (t - t_2)^2] + \frac{1}{N_c}(t - t_1)(t - t_2) & -\frac{1}{N_c}(t - t_1)(t - t_2) \\ N_c z(1 - z)(t_2 - t_1)^2 & [C_F - N_c z(1 - z)](t_2 - t_1)^2 \end{bmatrix}. \quad (\text{D.10})$$

This can be solved numerically.

In the large- N_c approximation the above matrix simplifies

$$\mathbb{M}(t) = -\frac{\hat{q}\theta^2}{4} \begin{bmatrix} (t - t_1)^2 + (t - t_2)^2 & 0 \\ 2z(1 - z)(t_2 - t_1)^2 & [1 - 2z(1 - z)](t_2 - t_1)^2 \end{bmatrix}. \quad (\text{D.11})$$

The zero in the upper right entry means that $\mathcal{C}_1^{(4)}$ can be solved analytically

$$\mathcal{C}_1^{(4)}(L, t_2) = e^{-\frac{1}{12} \frac{\hat{q}\mathbf{p}^2}{\omega^2} [(L - t_2)^3 + (L - t_1)^3 - (t_2 - t_1)^3]}. \quad (\text{D.12})$$

The physical solution that we need in the emission spectrum is $\mathcal{C}_2^{(4)}$. This can be solved using the solution of $\mathcal{C}_1^{(4)}$ through

$$\mathcal{C}_2^{(4)}(L, t_2) = \mathcal{C}_{2,\text{fac}}^{(4)}(L, t_2) - \frac{1}{2} \frac{\hat{q}\mathbf{p}^2}{\omega^2} z(1 - z)(t_2 - t_1)^2 \int_{t_2}^L ds \mathcal{C}_{2,\text{fac}}^{(4)}(L, s) \mathcal{C}_1^{(4)}(s, t_2), \quad (\text{D.13})$$

where the factorizable solution is

$$\mathcal{C}_{2,\text{fac}}^{(4)}(L, t_2) = e^{-\frac{1}{4}\frac{\hat{q}L^2}{\omega^2}[1-2z(1-z)](L-t_2)(t_2-t_1)^2}. \quad (\text{D.14})$$

This leads to the in-in spectrum

$$(2\pi)^2 \frac{dI^{\text{in-in}}}{dzd^2\mathbf{p}} = \frac{4\alpha_s}{\hat{q}[1-2z(1-z)]} P_{ba}(z) \times \text{Re} \int_0^L d\tau \frac{1}{\tau^2} e^{-i\frac{\mathbf{p}_\perp^2}{2\omega}\tau} e^{-\frac{1}{i2}\frac{\hat{q}\mathbf{p}_\perp^2}{\omega^2}\tau^3} \left(1 - e^{-\frac{1}{4}\frac{\hat{q}L^2}{\omega^2}[1-2z(1-z)](L-\tau)\tau^2}\right). \quad (\text{D.15})$$

References

- [1] J. D. Bjorken, *Highly Relativistic Nucleus-Nucleus Collisions: The Central Rapidity Region*, *Phys. Rev. D* **27** (1983) 140–151.
- [2] R. K. Ellis, W. J. Stirling, and B. R. Webber, *QCD and collider physics*. Cambridge monographs on particle physics, nuclear physics, and cosmology. Cambridge University Press, Cambridge, 2003. Photography by S. Vascotto.
- [3] Y. L. Dokshitzer, V. A. Khoze, A. H. Mueller, and S. I. Troian, *Basics of perturbative QCD*. Editions Frontieres, 1991.
- [4] A. J. Larkoski, I. Moutl, and B. Nachman, *Jet Substructure at the Large Hadron Collider: A Review of Recent Advances in Theory and Machine Learning*, *Phys. Rept.* **841** (2020) 1–63, [[arXiv:1709.04464](#)].
- [5] S. Marzani, G. Soyez, and M. Spannowsky, *Looking inside jets: an introduction to jet substructure and boosted-object phenomenology*, vol. 958. Springer, 2019.
- [6] M. Dasgupta, F. A. Dreyer, K. Hamilton, P. F. Monni, G. P. Salam, and G. Soyez, *Parton showers beyond leading logarithmic accuracy*, *Phys. Rev. Lett.* **125** (2020), no. 5 052002, [[arXiv:2002.11114](#)].
- [7] M. Gyulassy and M. Plumer, *Jet Quenching in Dense Matter*, *Phys. Lett. B* **243** (1990) 432–438.
- [8] M. Gyulassy, I. Vitev, X.-N. Wang, and B.-W. Zhang, *Jet quenching and radiative energy loss in dense nuclear matter*, [nucl-th/0302077](#).
- [9] D. d’Enterria, *Jet quenching*, *Landolt-Bornstein* **23** (2010) 471, [[arXiv:0902.2011](#)].
- [10] S. Peigne and A. V. Smilga, *Energy losses in a hot plasma revisited*, *Phys. Usp.* **52** (2009) 659–685, [[arXiv:0810.5702](#)].
- [11] Y. Mehtar-Tani, J. G. Milhano, and K. Tywoniuk, *Jet physics in heavy-ion collisions*, *Int. J. Mod. Phys. A* **28** (2013) 1340013, [[arXiv:1302.2579](#)].
- [12] J.-P. Blaizot and Y. Mehtar-Tani, *Jet Structure in Heavy Ion Collisions*, *Int. J. Mod. Phys. E* **24** (2015), no. 11 1530012, [[arXiv:1503.05958](#)].
- [13] J. Ghiglieri and D. Teaney, *Parton energy loss and momentum broadening at NLO in high temperature QCD plasmas*, *Int. J. Mod. Phys. E* **24** (2015), no. 11 1530013, [[arXiv:1502.03730](#)].
- [14] L. Apolinário, Y.-J. Lee, and M. Winn, *Heavy quarks and jets as probes of the QGP*, [arXiv:2203.16352](#).

- [15] M. E. Carrington, A. Czajka, and S. Mrowczynski, *Jet quenching in glasma*, *Phys. Lett. B* **834** (2022) 137464, [[arXiv:2112.06812](#)].
- [16] D. Avramescu, V. Baran, V. Greco, A. Ipp, D. I. Müller, and M. Ruggieri, *Simulating jets and heavy quarks in the Glasma using the colored particle-in-cell method*, [arXiv:2303.05599](#).
- [17] J. a. Barata, A. V. Sadofyev, and C. A. Salgado, *Jet broadening in dense inhomogeneous matter*, *Phys. Rev. D* **105** (2022), no. 11 114010, [[arXiv:2202.08847](#)].
- [18] J. a. Barata, A. V. Sadofyev, and X.-N. Wang, *Quantum partonic transport in QCD matter*, [arXiv:2210.06519](#).
- [19] C. Andres, L. Apolinário, F. Dominguez, M. G. Martinez, and C. A. Salgado, *Medium-induced radiation with vacuum propagation in the pre-hydrodynamics phase*, [arXiv:2211.10161](#).
- [20] N. Armesto and E. Scapparini, *Heavy-ion collisions at the Large Hadron Collider: a review of the results from Run 1*, *Eur. Phys. J. Plus* **131** (2016), no. 3 52, [[arXiv:1511.02151](#)].
- [21] M. Connors, C. Nattrass, R. Reed, and S. Salur, *Jet measurements in heavy ion physics*, *Rev. Mod. Phys.* **90** (2018) 025005, [[arXiv:1705.01974](#)].
- [22] H. A. Andrews et al., *Novel tools and observables for jet physics in heavy-ion collisions*, *J. Phys. G* **47** (2020), no. 6 065102, [[arXiv:1808.03689](#)].
- [23] R. Kogler et al., *Jet Substructure at the Large Hadron Collider: Experimental Review*, *Rev. Mod. Phys.* **91** (2019), no. 4 045003, [[arXiv:1803.06991](#)].
- [24] L. Cunqueiro and A. M. Sickles, *Studying the QGP with Jets at the LHC and RHIC*, *Prog. Part. Nucl. Phys.* **124** (2022) 103940, [[arXiv:2110.14490](#)].
- [25] R. Baier, Y. L. Dokshitzer, A. H. Mueller, S. Peigne, and D. Schiff, *Radiative energy loss of high-energy quarks and gluons in a finite volume quark - gluon plasma*, *Nucl. Phys. B* **483** (1997) 291–320, [[hep-ph/9607355](#)].
- [26] P. B. Arnold, *Simple Formula for High-Energy Gluon Bremsstrahlung in a Finite, Expanding Medium*, *Phys. Rev. D* **79** (2009) 065025, [[arXiv:0808.2767](#)].
- [27] P. B. Arnold, *High-energy gluon bremsstrahlung in a finite medium: harmonic oscillator versus single scattering approximation*, *Phys. Rev. D* **80** (2009) 025004, [[arXiv:0903.1081](#)].
- [28] J.-P. Blaizot, F. Dominguez, E. Iancu, and Y. Mehtar-Tani, *Medium-induced gluon branching*, *JHEP* **01** (2013) 143, [[arXiv:1209.4585](#)].
- [29] A. Kurkela and U. A. Wiedemann, *Picturing perturbative parton cascades in QCD matter*, *Phys. Lett. B* **740** (2015) 172–178, [[arXiv:1407.0293](#)].
- [30] F. Domínguez, J. G. Milhano, C. A. Salgado, K. Tywoniuk, and V. Vila, *Mapping collinear in-medium parton splittings*, *Eur. Phys. J. C* **80** (2020), no. 1 11, [[arXiv:1907.03653](#)].
- [31] C. Andres, F. Dominguez, and M. Gonzalez Martinez, *From soft to hard radiation: the role of multiple scatterings in medium-induced gluon emissions*, *JHEP* **03** (2021) 102, [[arXiv:2011.06522](#)].
- [32] B. G. Zakharov, *Radiative parton energy loss and jet quenching in high-energy heavy-ion collisions*, *JETP Lett.* **80** (2004) 617–622, [[hep-ph/0410321](#)].
- [33] S. Caron-Huot and C. Gale, *Finite-size effects on the radiative energy loss of a fast parton in hot and dense strongly interacting matter*, *Phys. Rev. C* **82** (2010) 064902, [[arXiv:1006.2379](#)].

- [34] X. Feal and R. Vazquez, *Intensity of gluon bremsstrahlung in a finite plasma*, *Phys. Rev. D* **98** (2018), no. 7 074029, [[arXiv:1811.01591](#)].
- [35] W. Ke, Y. Xu, and S. A. Bass, *Modified Boltzmann approach for modeling the splitting vertices induced by the hot QCD medium in the deep Landau-Pomeranchuk-Migdal region*, *Phys. Rev. C* **100** (2019), no. 6 064911, [[arXiv:1810.08177](#)].
- [36] C. Andres, L. Apolinário, and F. Dominguez, *Medium-induced gluon radiation with full resummation of multiple scatterings for realistic parton-medium interactions*, *JHEP* **07** (2020) 114, [[arXiv:2002.01517](#)].
- [37] S. Schlichting and I. Soudi, *Medium-induced fragmentation and equilibration of highly energetic partons*, *JHEP* **07** (2021) 077, [[arXiv:2008.04928](#)].
- [38] Y. Mehtar-Tani, *Gluon bremsstrahlung in finite media beyond multiple soft scattering approximation*, *JHEP* **07** (2019) 057, [[arXiv:1903.00506](#)].
- [39] Y. Mehtar-Tani and K. Tywoniuk, *Improved opacity expansion for medium-induced parton splitting*, *JHEP* **06** (2020) 187, [[arXiv:1910.02032](#)].
- [40] J. a. Barata and Y. Mehtar-Tani, *Improved opacity expansion at NNLO for medium induced gluon radiation*, *JHEP* **10** (2020) 176, [[arXiv:2004.02323](#)].
- [41] J. a. Barata, Y. Mehtar-Tani, A. Soto-Ontoso, and K. Tywoniuk, *Revisiting transverse momentum broadening in dense QCD media*, *Phys. Rev. D* **104** (2021), no. 5 054047, [[arXiv:2009.13667](#)].
- [42] J. a. Barata, Y. Mehtar-Tani, A. Soto-Ontoso, and K. Tywoniuk, *Medium-induced radiative kernel with the Improved Opacity Expansion*, *JHEP* **09** (2021) 153, [[arXiv:2106.07402](#)].
- [43] J. H. Isaksen, A. Takacs, and K. Tywoniuk, *A unified picture of medium-induced radiation*, [arXiv:2206.02811](#).
- [44] Y. Mehtar-Tani and K. Tywoniuk, *Radiative energy loss of neighboring subjects*, *Nucl. Phys. A* **979** (2018) 165–203, [[arXiv:1706.06047](#)].
- [45] Y. Mehtar-Tani and K. Tywoniuk, *Sudakov suppression of jets in QCD media*, *Phys. Rev. D* **98** (2018), no. 5 051501, [[arXiv:1707.07361](#)].
- [46] Y. Mehtar-Tani and K. Tywoniuk, *Groomed jets in heavy-ion collisions: sensitivity to medium-induced bremsstrahlung*, *JHEP* **04** (2017) 125, [[arXiv:1610.08930](#)].
- [47] P. Caucal, E. Iancu, and G. Soyez, *Deciphering the z_g distribution in ultrarelativistic heavy ion collisions*, *JHEP* **10** (2019) 273, [[arXiv:1907.04866](#)].
- [48] P. Caucal, A. Soto-Ontoso, and A. Takacs, *Dynamically groomed jet radius in heavy-ion collisions*, [arXiv:2111.14768](#).
- [49] C. Andres, F. Dominguez, R. Kunnawalkam Elayavalli, J. Holguin, C. Marquet, and I. Moult, *Resolving the Scales of the Quark-Gluon Plasma with Energy Correlators*, [arXiv:2209.11236](#).
- [50] B. Zakharov, *Fully quantum treatment of the Landau-Pomeranchuk-Migdal effect in QED and QCD*, *JETP Lett.* **63** (1996) 952–957, [[hep-ph/9607440](#)].
- [51] B. G. Zakharov, *Radiative energy loss of high-energy quarks in finite size nuclear matter and quark - gluon plasma*, *JETP Lett.* **65** (1997) 615–620, [[hep-ph/9704255](#)].
- [52] U. A. Wiedemann, *Gluon radiation off hard quarks in a nuclear environment: Opacity expansion*, *Nucl. Phys. B* **588** (2000) 303–344, [[hep-ph/0005129](#)].

- [53] P. B. Arnold, G. D. Moore, and L. G. Yaffe, *Photon and gluon emission in relativistic plasmas*, *JHEP* **06** (2002) 030, [[hep-ph/0204343](#)].
- [54] L. Apolinário, N. Armesto, J. G. Milhano, and C. A. Salgado, *Medium-induced gluon radiation and colour decoherence beyond the soft approximation*, *JHEP* **02** (2015) 119, [[arXiv:1407.0599](#)].
- [55] J.-P. Blaizot, F. Dominguez, E. Iancu, and Y. Mehtar-Tani, *Probabilistic picture for medium-induced jet evolution*, *JHEP* **06** (2014) 075, [[arXiv:1311.5823](#)].
- [56] P. Arnold and S. Iqbal, *The LPM effect in sequential bremsstrahlung*, *JHEP* **04** (2015) 070, [[arXiv:1501.04964](#)]. [Erratum: *JHEP* 09, 072 (2016)].
- [57] P. Arnold, H.-C. Chang, and S. Iqbal, *The LPM effect in sequential bremsstrahlung 2: factorization*, *JHEP* **09** (2016) 078, [[arXiv:1605.07624](#)].
- [58] P. Arnold, H.-C. Chang, and S. Iqbal, *The LPM effect in sequential bremsstrahlung: dimensional regularization*, *JHEP* **10** (2016) 100, [[arXiv:1606.08853](#)].
- [59] P. Arnold, H.-C. Chang, and S. Iqbal, *The LPM effect in sequential bremsstrahlung: 4-gluon vertices*, *JHEP* **10** (2016) 124, [[arXiv:1608.05718](#)].
- [60] P. Arnold and S. Iqbal, *In-medium loop corrections and longitudinally polarized gauge bosons in high-energy showers*, *JHEP* **12** (2018) 120, [[arXiv:1806.08796](#)].
- [61] P. Arnold, T. Gorda, and S. Iqbal, *The LPM effect in sequential bremsstrahlung: nearly complete results for QCD*, *JHEP* **11** (2020) 053, [[arXiv:2007.15018](#)]. [Erratum: *JHEP* 05, 114 (2022)].
- [62] T. Liou, A. H. Mueller, and B. Wu, *Radiative p_{\perp} -broadening of high-energy quarks and gluons in QCD matter*, *Nucl. Phys. A* **916** (2013) 102–125, [[arXiv:1304.7677](#)].
- [63] J.-P. Blaizot and Y. Mehtar-Tani, *Renormalization of the jet-quenching parameter*, *Nucl. Phys. A* **929** (2014) 202–229, [[arXiv:1403.2323](#)].
- [64] B. Wu, *Radiative energy loss and radiative p_{\perp} -broadening of high-energy partons in QCD matter*, *JHEP* **12** (2014) 081, [[arXiv:1408.5459](#)].
- [65] E. Iancu, *The non-linear evolution of jet quenching*, *JHEP* **10** (2014) 095, [[arXiv:1403.1996](#)].
- [66] J.-P. Blaizot and F. Dominguez, *Radiative corrections to the jet quenching parameter in dilute and dense media*, *Phys. Rev. D* **99** (2019), no. 5 054005, [[arXiv:1901.01448](#)].
- [67] J. a. Barata, F. Domínguez, C. A. Salgado, and V. Vila, *A modified in-medium evolution equation with color coherence*, *JHEP* **05** (2021) 148, [[arXiv:2101.12135](#)].
- [68] P. Arnold, O. Elgedawy, and S. Iqbal, *The LPM effect in sequential bremsstrahlung: gluon shower development*, [arXiv:2302.10215](#).
- [69] J. H. Isaksen and K. Tywoniuk, *Wilson line correlators beyond the large- N_c* , *JHEP* **21** (2020) 125, [[arXiv:2107.02542](#)].
- [70] N. N. Nikolaev, W. Schafer, and B. G. Zakharov, *Nonlinear k (perpendicular)-factorization for gluon-gluon dijets produced off nuclear targets*, *Phys. Rev. D* **72** (2005) 114018, [[hep-ph/0508310](#)].
- [71] B. G. Zakharov, *Color randomization of fast gluon-gluon pairs in the quark-gluon plasma*, *J. Exp. Theor. Phys.* **128** (2019), no. 2 243–258, [[arXiv:1806.04723](#)].

- [72] P. Arnold, *Landau-Pomeranchuk-Migdal effect in sequential bremsstrahlung: From large- N QCD to $N=3$ via the $SU(N)$ analog of Wigner 6- j symbols*, *Phys. Rev. D* **100** (2019), no. 3 034030, [[arXiv:1904.04264](#)].
- [73] M. D. Sievert and I. Vitev, *Quark branching in QCD matter to any order in opacity beyond the soft gluon emission limit*, *Phys. Rev. D* **98** (2018), no. 9 094010, [[arXiv:1807.03799](#)].
- [74] M. D. Sievert, I. Vitev, and B. Yoon, *A complete set of in-medium splitting functions to any order in opacity*, *Phys. Lett. B* **795** (2019) 502–510, [[arXiv:1903.06170](#)].
- [75] T. Altinoluk, N. Armesto, G. Beuf, M. Martínez, and C. A. Salgado, *Next-to-eikonal corrections in the CGC: gluon production and spin asymmetries in pA collisions*, *JHEP* **07** (2014) 068, [[arXiv:1404.2219](#)].
- [76] T. Altinoluk, N. Armesto, G. Beuf, and A. Moscoso, *Next-to-next-to-eikonal corrections in the CGC*, *JHEP* **01** (2016) 114, [[arXiv:1505.01400](#)].
- [77] V. N. Gribov and L. N. Lipatov, *Deep inelastic $e p$ scattering in perturbation theory*, *Sov. J. Nucl. Phys.* **15** (1972) 438–450.
- [78] G. Altarelli and G. Parisi, *Asymptotic Freedom in Parton Language*, *Nucl. Phys. B* **126** (1977) 298–318.
- [79] Y. L. Dokshitzer, *Calculation of the Structure Functions for Deep Inelastic Scattering and $e^+ e^-$ Annihilation by Perturbation Theory in Quantum Chromodynamics.*, *Sov. Phys. JETP* **46** (1977) 641–653.
- [80] F. Dominguez. private communication, 2022.
- [81] M. Attems, J. Brewer, G. M. Innocenti, A. Mazeliauskas, S. Park, W. van der Schee, and U. A. Wiedemann, *The medium-modified $g \rightarrow c\bar{c}$ splitting function in the BDMPS-Z formalism*, [arXiv:2203.11241](#).
- [82] S. Schlichting and I. Soudi, *Splitting rates in QCD plasmas from a nonperturbative determination of the momentum broadening kernel $C(q_\perp)$* , *Phys. Rev. D* **105** (2022), no. 7 076002, [[arXiv:2111.13731](#)].



Graphic design: Communication Division, UIB / Print: Skjipes Kommunikasjon AS



uib.no

ISBN: 9788230859162 (print)
9788230842379 (PDF)